ELECTRIC TRANSPORT INVESTIGATIONS ON THE TRIVALENT–ION DOPED TUNGSTEN BRONZES Y_XWO_3 AND LA_XWO_3 NEAR THE METAL–INSULATOR TRANSITION

Charles Kasl

A thesis submitted to the Faculty of Science, University of the Witwatersrand, Johannesburg, in fulfilment of the requirements for the degree of Doctor of Philosophy.

Johannesburg, 2010

Declaration

I declare that this thesis is my own, unaided work. It is being submitted for the degree of Doctor of Philosophy in the University of the Witwatersrand, Johannesburg. It has not been submitted for any other degree or examination in any other university.

(Signature of candidate)

6 AUGUST 2010

(Date)

Acknowledgement

This research was done under the supervision of Prof. M. J. R. Hoch.

Abstract

Electric transport investigations were performed on the trivalent–ion doped tungsten bronzes Y_xWO_3 ($0.05 \leq x \leq 0.20$) and La_xWO_3 ($0.05 \leq x \leq 0.23$). The range of dopant concentrations includes the cubic phase, as well as the predicted metal–insulator transition occurring in these systems. Polycrystalline samples were prepared by solid state reaction by sintering compressed powder pellets in evacuated quartz ampoules at 1100°C for 72 hr. Characterisation of the samples included powder *x*–ray diffraction, diffuse reflection spectroscopy, specific heat and magnetization measurements. The results are similar to those found in other tungsten bronzes.

An electrical transport station was assembled to measure the transport properties as a function of temperature ($1.6\ \mathrm{K} \leq T \leq 300\ \mathrm{K}$) and magnetic field ($-1.2\ \mathrm{T} \leq B \leq +1.2\ \mathrm{T}$). The standard four–wire method for bar samples and the van der Pauw technique for pellets were both used for dc conductivity and Hall effect measurements.

The conductivity σ versus temperature T plots for a range of x values show a family of curves typical of metal–insulator transition systems and comparable to results for Na_xWO_3 and $Na_xTa_yW_{1-y}O_3$. A change from metallic–type ($d\sigma/dT < 0$) to semiconducting–type ($d\sigma/dT > 0$) behaviour is observed as x is reduced. The metal–insulator transition is found to occur for nominal concentrations between $x = 0.05$ and $x = 0.06$ in both the Y_xWO_3 and La_xWO_3 samples. This corresponds to a critical electron concentration $n_C \sim 3\times10^{21}\ \mathrm{cm}^{-3}$.

Room temperature Hall effect results support the fully ionised donor model for the tungsten bronzes. The Hall concentration decreases on cooling, indicating a partial "freeze–out" of charge carriers, observed previously in cubic single–crystal Na_xWO_3. No evidence is found for local moment formation from magnetization and specific heat measurements at low temperatures. Magnetoresistance effects appeared at low temperatures with small resistivity changes $\lesssim 0.1\%$ in 1 T fields.

For lower x values the Y_xWO_3 and La_xWO_3 samples show very similar behaviour in all their properties, confirming that the donor valence and not donor type is the dominant factor in determining the properties of the tungsten bronzes.

Contents

List of figures

List of tables

Symbols and acronyms

a	lattice constant	6
B	magnetic field	72
E	energy	9
E_F	Fermi energy	24
f	crystal volume fraction	54
n	carrier concentration	15
n_C	critical carrier concentration	26
n_d	donor electron concentration	6
n_H	Hall concentration	13
R_H	Hall coefficient	13
T	temperature	6
x	donor atom concentration	1
x_C	critical donor atom concentration	1
x_{eff}	effective donor atom concentration	5
x_{min} (x_{max})	lower (upper) cubic range limit	11
y	Ta concentration in $Na_xTa_yW_{1-y}O_3$	5
α_{MR}	magnetoresistance coefficient	75
Θ_D	Debye temperature	17
λ	wavelength	20
ρ	resistivity	15
$\rho(E_F)$	Fermi level density of states	24
σ	electrical conductivity	6
σ_0	residual ($T \rightarrow 0$ K) electrical conductivity	23
σ_{min}	Mott minimum metallic conductivity	32

DOS	density of states	24
e–e	electron–electron	23
MI	metal–insulator	1
NMR	nuclear magnetic resonance	4
SEM	scanning electron microscopy	46
VSM	vibrating sample magnetometer	132
XRD	x–ray diffraction	8

Chapter 1: Introduction

In recent years there has been a growth of interest in doped transition metal oxides, such as the doped Cu oxides, exhibiting high T_C superconductivity, and the doped Mn oxides, which are known for colossal magnetoresistance. Many of the properties exhibited by these oxides are not well understood and pose challenging questions. The nature and role of the metal–insulator (MI) transition in these systems is of fundamental importance. A comprehensive review of MI transitions has been given by Imada *et al.*[1] with emphasis on correlation effects occurring in the *d* electrons of the transition atoms. Additional reviews of the MI transition in a variety of systems, including oxides, have been given by Mott[2], Edwards *et al.*[3], Raychaudhuri[4], and Lee and Ramakrishan[5].

The tungsten bronzes are doped transition metal oxides which form a class of non–stoichiometric compounds with the general formula M_xWO_3 ($0 \leq x \leq 1$). The donor ion M represents a metallic atom such as the alkali, alkali earth, transition or rare–earth elements, which is randomly distributed as an interstitial inside a WO_3 lattice. A large variety of metal species are known to form tungsten bronzes, and a general overview of the tungsten bronzes and related compounds has been presented by Dickens and Whittingham.[6] In general the donor atom appears in its natural valence state, with its valence electrons donated to the WO_3 conduction band. The character of these conduction band donor electrons then determines the interesting *x*–dependent properties exhibited by these compounds. The tungsten bronzes undergo a MI transition as the dopant concentration *x* is changed through a non–zero critical concentration x_C. For $x > x_C$ the tungsten bronzes show metallic–type behaviour, while for $x < x_C$ insulating or semiconducting behaviour is encountered. Undoped WO_3, corresponding to $x = 0$, is a charge–transfer insulator, whereas high *x* Na_xWO_3 exhibits metallic conductivity approaching that of Na metal and ReO_3. Although this MI transition has been observed in compensated cubic phase tungsten bronzes such as $Na_xTa_yW_{1-y}O_3$,[7] changes in lattice structure complicate investigations in uncompensated samples. For a range of *x* values, the stable phase is found to be single–phase cubic perovskite with metallic character, and x_C appears to be below the lower end of this range of stability.[7,8] The appearance of additional phases as *x* is reduced towards zero hinders a proper investigation of the MI transition. The MI transition in the tungsten

bronzes has many features in common with other MI systems, such as doped semiconductors.[3] The ABO_3 perovskite class of correlated metallic oxides are receiving significant attention, showing diversity and similarity in the different types of MI transitions observed in these compounds.[4]

Extensive experimental and theoretical investigations of the MI transition have been carried out on the sodium tungsten bronze (Na_xWO_3) and on related systems (such as the compensated $Na_xTa_yW_{1-y}O_3$).[7–12] Much less work has been carried out on the related trivalent–ion doped tungsten bronze system. For monovalent donors, such as Na_xWO_3 and $Na_xTa_yW_{1-y}O_3$, the critical concentration is estimated at $x_C \simeq 0.18$.[7,8] It is to be expected that x_C will be lower for the Y_xWO_3 and La_xWO_3 systems due to the trivalence of the Y and La donors.

Band theory calculations have been carried out for the tungsten bronzes in an effort to understand the effects of electron–electron interactions and disorder in driving the transition.[9] The calculations predict that for sufficiently large electron–electron interaction energies on the tungsten *d* orbitals a pseudogap develops at the Fermi energy. This prediction is in agreement with experimental photoemission spectra and tunnelling current measurements.[10,11] It is suggested that antiferromagnetic correlations play a role in the formation of the pseudogap. Many of the observed properties are consistent with the model which shows that the Fermi surface has strong 2D characteristics linked to the symmetry of the t_{2g} orbital. Localised and extended states in the pseudogap are predicted, consistent with the Friedman anomaly in the temperature dependence of the Hall concentration. Experimental results for the trivalent doped systems, in which the disorder is different to that in the alkali doped tungsten bronzes, will allow for comparison with the earlier studies and with theoretical predictions.

In addition to MI investigations, there is renewed interest in the tungsten bronzes which exhibit interesting physical and chemical properties as *x* is varied. Superconductivity has been observed in some tungsten bronzes[13–16] and the electrochromic properties of WO_3 are of technological interest. They show interesting *x*–dependent optical properties, with application in electrochromic devices[17,18]. Research on the rare–earth tungsten bronzes suggests that they may be used for the storage of radioactive materials due to their

chemical resistance and thermal stability.[19,20] Tungsten bronzes also show possible application in proton exchange membrane fuel cells.[21]

The present work, complementing previous investigations of the tungsten bronzes, has sought to prepare and characterize high quality sintered polycrystalline Y_xWO_3 and La_xWO_3 samples with a range of x values, and to establish the critical concentration x_C for these materials by means of electrical transport measurements made as a function of temperature. No research on the yttrium–doped tungsten bronzes appears to have been published since the early introductory work of Broyde[22] and Shanks[23] in 1967. Previous work[22–25] carried out on La_xWO_3 has provided structural and compositional information, but no systematic investigation of the x–dependent physical properties, specifically the transport properties, has been reported.

1.1 Overview

The research includes the preparation of polycrystalline samples of Y_xWO_3 and La_xWO_3 by solid state reaction for a range of concentrations. The present work confirms that the cubic range for both compounds occurs down to about $x = 0.08$. Previous research has indicated that cubic tungsten bronzes are metallic.[22,26] To observe the predicted MI transition the concentration was extended down to $x = 0.05$. The upper concentration was chosen to include the complete cubic range for both compounds.[22]

The primary objective was the investigation of Y_xWO_3, with most of the research focussing on this compound. The La_xWO_3 investigation followed that of Y_xWO_3 and was initiated to compare the properties of these two trivalent–ion doped tungsten bronzes. As a result, fewer samples were produced and the measurements were not as extensive as for Y_xWO_3.

Extensive characterisation of subsequent samples was performed to ensure a sequence suitable for the intended electrical transport investigations. Characterisation of the samples included powder x–ray diffraction, diffuse reflectance spectroscopy, mass density and volume fraction measurements, room temperature Hall concentration measurements and resistivity measurements down to liquid nitrogen temperatures. These initial electric

transport measurements also served to test and prepare the transport station for the low temperature research.

Electric transport measurements were made down to liquid helium temperatures, focussing on the resistivity and Hall coefficient of these two compounds. The samples exhibited magnetoresistance effects during the Hall carrier concentration measurements, and some magnetoresistance results were obtained as a by–product. Low temperature conductivity measurements were performed on the whole concentration range for both compounds. The dependence of the Hall concentration and magnetoresistance on temperature and donor concentration was investigated, and the results for successful runs are presented.

A general overview of the tungsten bronze properties relevant to this research is presented in chapter 2. Much of the focus is on results for the sodium tungsten bronze Na_xWO_3, which is the most investigated tungsten bronze to date. The MI transition is introduced, and some of the theories available to describe this phenomenon are presented. The results of Dücker *et al.*[9] are presented, and represent the most complete theoretical treatment of cubic tungsten bronzes with regards to the MI transition. Previous experimental results relating to MI transition investigations in the tungsten bronzes are then presented. Chapter 2 concludes with a summary of the previous work done on the Y_xWO_3 and La_xWO_3 tungsten bronzes.

The preparation of the polycrystalline Y_xWO_3 and La_xWO_3 samples is discussed in chapter 3, which also presents the extensive characterisation performed on these samples. This chapter focuses mainly on room temperature investigations. Chapter 4 describes the experimental apparatus used in this research, and the techniques used to investigate the electric transport properties (resistivity and Hall concentration). The main results of this research, consisting of the electric transport measurements down to around 2 K, are presented in chapter 5. The effects of magnetoresistance on Hall effect measurements are also presented. Chapter 6 presents the analysis of the experimental data. The MI transition is investigated using several methods of analysis. The experimental results obtained here for Y_xWO_3 and La_xWO_3 are compared to Na_xWO_3 and $Na_xTa_yW_{1-y}O_3$ data. Additional measurements performed at the Florida State University (U.S.A) are presented, consisting of magnetization, specific heat and nuclear magnetic resonance (NMR) data. The chapter

closes with a summary of the main results of the research. Chapter 7 is the concluding chapter of the thesis.

The appendix provides additional information on certain sections in the thesis. Expressions for the analysis of the powder x–ray diffraction data are presented. The equation used in the analysis of the electric transport results is derived. The function $F(R_1/R_2)$ used in the van der Pauw technique for resistivity measurement is evaluated. Justification is presented for the use of the density–corrected resistivity as a first order estimate of the crystal resistivity from the polycrystalline sample resistivity. Additional results are shown as figures in the appendix gallery. Finally, two publications based on this research are presented. Further publications are in progress.

1.2 Notes

Here are some notes essential to the rest of the thesis to avoid repetition of some minor points throughout the thesis.

1. In some graphs error bars are not present on all the data points. For the data points where the symbol size is larger than the error bar, the error bars have not been shown. The error bars denote the standard error of the mean.

2. The x values listed in this thesis are nominal values determined using the masses of the starting materials, and will be used to denote donor atom concentrations. The matter is discussed further in chapter 3.

3. The effective concentration x_{eff} for Y_xWO_3 and La_xWO_3 will refer to the value $3x$, corresponding to the three electrons donated to the conduction band by the trivalent Y and La dopant. This is useful when comparing the results to monovalent donor systems such as Na_xWO_3 for which $x_{\text{eff}} = x$. The compensated tungsten bronze $Na_xTa_yW_{1-y}O_3$ has $x_{\text{eff}} = x - y$ due to the Ta acceptor.

4. The donor electron concentration $n_d = vx/a^3$ ($= x_{eff}/a^3$) where v is the donor valence and a the lattice constant. It refers to the conduction band concentration assuming full donor ionization ($n_d = x/a^3$ for Na^+; $n_d = 3x/a^3$ for La^{3+},Y^{3+}).

5. Unless stated otherwise, the conductivity in chapters 5 and 6 is the density–corrected conductivity. See chapter 3 and appendix D for further explanations.

6. The standard definition for a metal is $d\sigma/dT < 0$, the conductivity σ decreasing with increasing temperature T due to thermal scattering, whereas a semiconductor has $d\sigma/dT > 0$, with the conductivity increasing with T due to the thermal excitation of charge carriers. This definition will be used for the higher temperature data. For MI transition systems, where the investigations are at low T, a metal is defined by $\sigma(T = 0\ K) > 0$ while an insulator has $\sigma(T = 0\ K) = 0$. The context (in particular the temperature) should make the use of “metallic” clear.

Chapter 2: The tungsten bronzes

This chapter presents a general discussion of tungsten bronzes and their properties. Previous results relevant to the present research are presented. The metal–insulator transition is discussed, including its manifestation in the tungsten bronzes. Most of the results reviewed here are based on the extensively investigated Na_xWO_3 system. The chapter concludes with a summary of the research done on the Y_xWO_3 and La_xWO_3 tungsten bronzes.

2.1 Basic properties

The tungsten bronze M_xWO_3 can be considered as a solution (random distribution) of the electropositive donor atom M as an interstitial in a WO_3 matrix as shown in Fig. 2-1. The donor is fully ionised with the valence electrons entering the WO_3 conduction band. Evidence for this comes from numerous experimental results (Hall effect[13,26–29], Seebeck effect[13], susceptibility[30], Mossbauer[31], and photoemission spectroscopy[12,32]), as well as theoretical band calculations[33–36]. A common preparation method is by the solid state reaction of powders of WO_3, W metal and the donor metal oxide M_nO_m. The reaction involves the oxidation of the tungsten metal and the intercalation of the donor–metal ions into the host WO_3 crystal by thermal diffusion. This procedure produces polycrystalline material, and requires high temperatures and long, temperature–dependent reaction times for complete reaction.[37] Another method commonly employed is the growth of single crystals by electrolysis.[23,38] Polycrystalline Li_xWO_3 has been formed in an electrochemical cell,[17] and $K_{0.4}WO_3$ whiskers have been prepared through hydrothermal reaction.[39] Other preparation techniques have also been described.[19,20,40] The reverse process is also possible. The dissolution procedure for Nd_xWO_3 and Eu_xWO_3 has been shown, leading to the formation of WO_3 and the lanthanide oxide.[20]

2.1.1 Structural and compositional

Fig. 2-1 shows the symmetric cubic–perovskite structure. The basis is a corner shared WO_6 octahedron. Deformation of this structure through lattice variations, WO_6 tilting and W–O bond–length and W–O–W bond–angle changes is characteristic of all the tungsten bronzes. The reduced symmetry occurs with variation of the donor atom, the donor concentration, as well as the temperature.[25,33,38,41,42] Hexagonal tungsten bronzes have also been investigated, and show different behaviour from the cubic–based compounds.[13]

The structural characterisation is usually done by x–ray diffraction (XRD). It should be noted that XRD provides information predominantly on the W positions, being less sensitive to the lower electron density of the O atoms. A more complete structural determination is obtained by neutron diffraction.[25]

WO_3 is not an ionic compound, although the atoms appear in the W^{6+} and O^{2-} oxidation states. The bonding is due to W – O hybridization, with the dominant electronic effect being the W 5*d* and O 2*p* covalent interaction.[34,36] Fig. 2-2 illustrates the formation of the

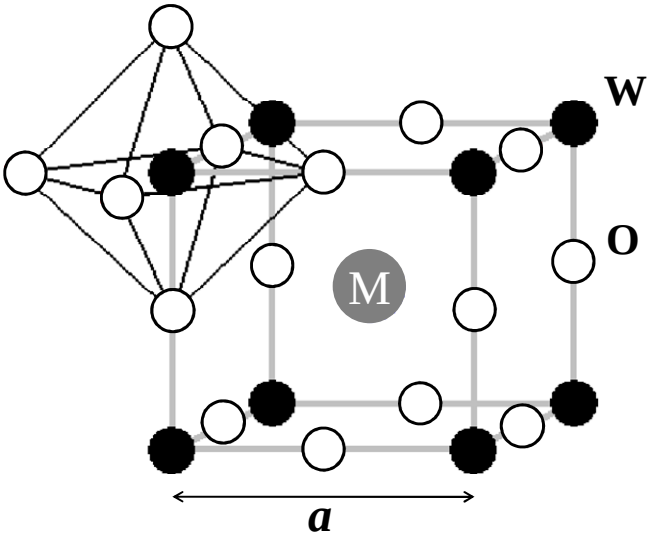

Fig. 2-1. The cubic perovskite structure of tungsten bronzes. Also shown is the corner-shared WO_6 octahedron. The lattice constant *a* ~ 3.8 Å and M occupies the perovskite *A* site in the ABO_3 compound.

energy levels in a cubic WO_3 crystal.[1] Considering first the WO_6 octahedron and then separating the constituent W^{6+} and O^{2-} ions, the formation of the band structure can be described as follows:

A. The valence orbitals of the free W^{6+} ion are the 5–fold degenerate (ignoring spin) 5*d* t_{2g} and e_g states.

B. As the W – O distance is decreased the crystal field due to the six charged O^{2-} ions lifts the t_{2g} and e_g degeneracy. The e_g orbitals lie along the W – O axis in the octahedral environment, and have an enhanced crystal field interaction. The degeneracy of the t_{2g} and the e_g orbitals may be further lifted in non–cubic environments.

C. Further reduction in the W – O separation causes overlap of the W 5*d* and O 2*p* states. This leads to the formation of bonding (σ and π) and anti–bonding (σ* and π*) molecular orbitals. The smaller overlap between the diagonally oriented t_{2g} orbitals and the O 2*p* orbitals leads to a smaller splitting. The lower lying bonding orbitals are mainly O in character, while the anti–bonding states consist predominantly of W orbitals. The O–dominated bonding orbitals are responsible for the ionic W^{6+} and O^{2-} character of WO_3.

D. Bringing together the WO_6 octahedra in a periodic fashion to form the crystal leads to the formation of energy bands from the molecular levels. The valence band is full, and the top of the band consists of the O–dominated $t_{2g}(\pi)$ orbitals. The bottom of the empty conduction band consists of the W–dominated $t_{2g}(\pi^*)$ orbitals. The mainly W5*d* nature of the conduction band states has been shown by NMR[43,44], electron spectroscopy[45], and band structure calculations[33,34], and is responsible for the success of the tight–binding description of this system.[46]

The density of states, calculated for cubic WO_3 from density functional theory, is shown in Fig. 2-3. The top of the valence band (energy $E \lesssim 0$ eV) is shown to consist mainly of O 2*p* orbitals. The bottom of the conduction band is dominated by the W 5*d* orbitals. In WO_3 the conduction band is empty with the valence band full, making WO_3 a band–gap insulator.

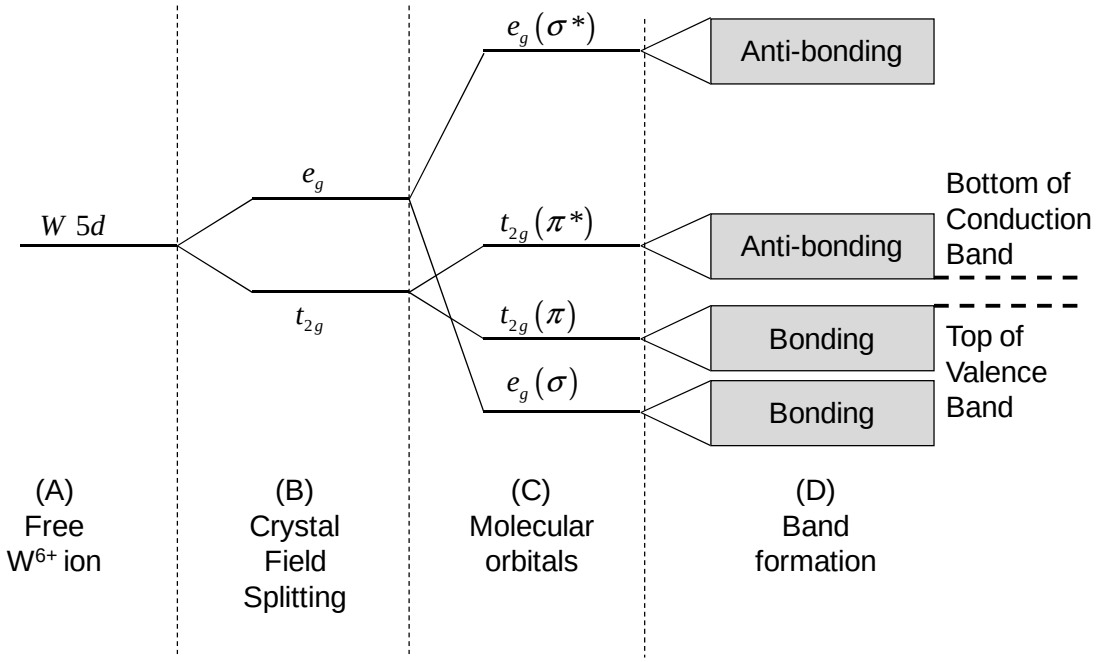

Fig. 2-2. Energy level diagram showing the origins of the WO_3 band structure.

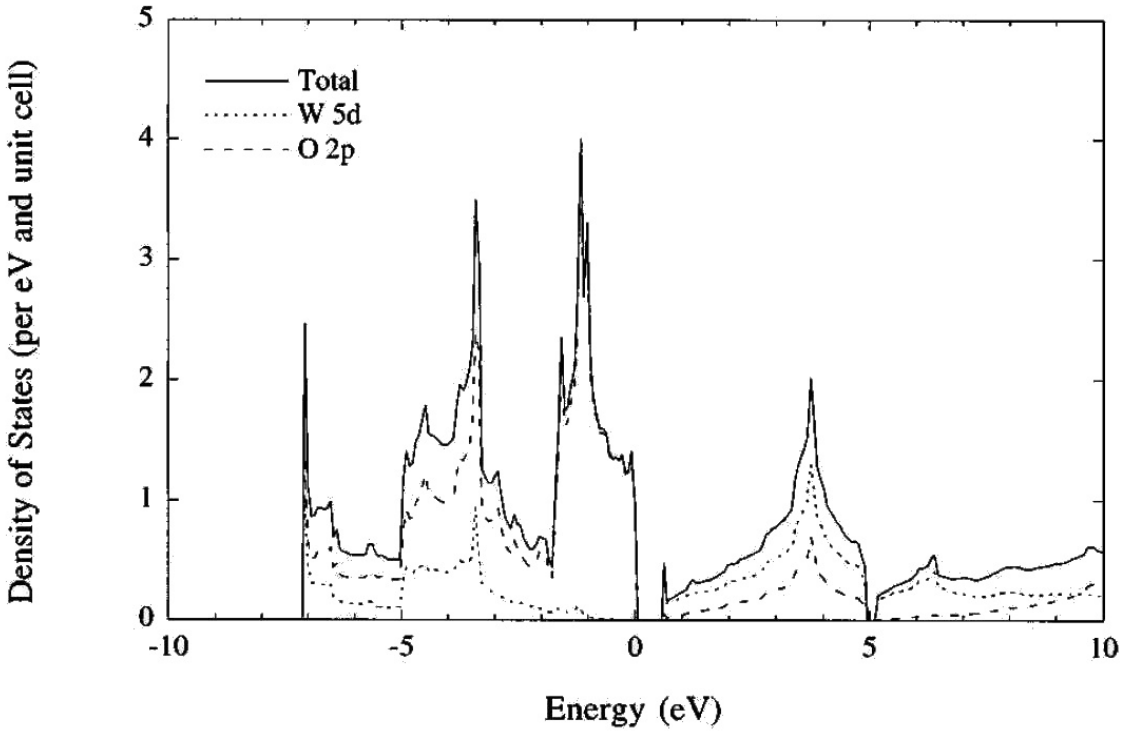

Fig. 2-3. The calculated density of states for WO_3 from Ref. 34. The O 2*p* and W 5*d* projected contributions are included.

Band structure calculations for the tungsten bronzes based on density functional theory give results similar to Fig. 2-3, with the Fermi level lying in the conduction band.[33,34] The tungsten bronzes behave essentially as cubic WO_3 with electrons present in the conduction band. The donor atoms supply their valence electrons, maintain electrical neutrality, and do not appreciably affect the electronic structure. The optical properties of Na_xWO_3 for $x > 0.5$, for example, show a dielectric constant for WO_3 equivalent to that of Na_xWO_3 without the conduction electron contribution.[47] For the higher concentrations, the properties of the tungsten bronzes are sufficiently described by the rigid filling of a band structure based on cubic WO_3.[12,32,48,49] The Seebeck coefficient[50] of metallic Na_xWO_3 and photoemission spectroscopy[12,45] show that the band dispersion is not free–electron parabolic. This accounts for the *x*–dependent free–electron model parameters, such as the effective mass, obtained from analysis of experimental data.[12,45,47,51]

ReO_3 is isostructural and isoelectronic to $NaWO_3$ ($x = 1$). Band structure calculations for ReO_3 produce similar results to those of WO_3 and Na_xWO_3.[35,48,52] ReO_3 and Na_xWO_3 have similar physical properties, and ReO_3 band calculations have been used to interpret Na_xWO_3 data.[32,51,53]

Most of the varied properties of the tungsten bronzes arise from the *x*–dependent conduction band concentration. Although conventional band theory calculations are successful for high donor concentrations, they cannot describe the MI transition occurring in these systems as $x \rightarrow 0$. A rigid band filling would lead to metallic behaviour for all $x > 0$ and a critical concentration $x_C = 0$ (corresponding to insulating WO_3).

The cubic range: $x_{min} < x < x_{max}$

The single–phase cubic range of the tungsten bronzes, as characterised by XRD, does not span the complete range of *x* values (i.e. $x_{min} \neq 0$; $x_{max} \neq 1$). Na_xWO_3 shows the largest cubic range ($0.2 < x < 0.9$)[37,54–56], whereas most other tungsten bronzes show a much smaller range (e.g. 0.085 – 0.16 for Eu_xWO_3 and Gd_xWO_3)[30]. Some tungsten bronzes, such as Ba_xWO_3 and B_xWO_3, do not exhibit a cubic phase.[57,58] The cubic phase represents the most symmetric structure found in the tungsten bronzes.

The cubic lattice constant a_C is observed to increase with increasing x in a near–linear manner,[19,31,37] which is also predicted by calculations.[33] An exception is Li_xWO_3 where a_C decreases with x, attributed to the small ionic size of Li^+.[17] This linear a_C vs x relationship has been used to infer the x values in Na_xWO_3 samples from XRD results.[28,32,47,51,56,59] In hexagonal K_xWO_3 and Rb_xWO_3 the lattice parameters also appear to change linearly with concentration.[14]

The lattice constant also depends on the type of donor, generally increasing with increasing ionic radius. For the rare–earth tungsten bronzes a_C decreases from Ce to Lu, consistent with the ionic lanthanide contraction.[30] Calculations on alkali tungsten bronzes also show a_C decreasing as the donor ion size decreases.[33]

The cubic phase exhibits metallic properties for all tungsten bronzes observed so far.[26]

Above the cubic range: $x > x_{max}$

No single–phase cubic tungsten bronzes with $x = 1$ have yet been observed ($x_{max} < 1$). For $x > x_{max}$ additional phases are observed in XRD traces, usually identified as WO_2 and the donor–atom tungstate.[19,20,22,24,30,31,57,60] The upper cubic limit x_{max} has been attributed to a solubility limit for the donor concentration.[30,57] For a nominal $x > x_{max}$ the compound appears to consist of a cubic tungsten bronze phase with a fixed donor concentration $x = x_{max}$, while the surplus donors that are introduced form the additional compounds detected by XRD. The solubility limit is further discussed in §3.3 and §6.1, and evidenced in Fig. 3-4 (cubic lattice constant) and Fig. 3-11 (Hall carrier concentration).The range of solubility limits is quite varied ($x_{max} \sim 0.15$ for Eu_xWO_3 and Gd_xWO_3; $x_{max} \sim 0.85$ for Na_xWO_3)[30,37], depending on the donor atom and preparation method. The thermodynamic stability of the donor tungstate seems to determine x_{max}.

A solubility limit for Na_xWO_3 is suggested for $x \sim 0.85$.[37] For $x \gtrsim 0.85$ additional phases appear, and the cubic lattice constant lies below the extrapolation of the linear form on the cubic range. This has been attributed to a reduced Na^+ concentration in the tungsten bronze phase. For Eu_xWO_3 solubility limits of $x_{max} = 0.125$ and 0.15 have been separately reported, showing that the solubility limit is affected by preparation conditions.[30,31] B_xWO_3

and Ba_xWO_3 reach their solubility limits (x_{max} ~ 0.09 and 0.13 respectively) in the tetragonal phase, thereby not exhibiting a cubic structure.[57,58]

Below the cubic range: $x < x_{min}$

The appearance of additional phases as $x \rightarrow 0$ is expected as the system approaches the non–cubic WO_3 (corresponding to $x = 0$). For $x < x_{min}$ structural changes with tetragonal, orthorhombic and monoclinic variations are detected.[6,17,31,38,58,60] Additional compounds are not detected for $x < x_{min}$, which suggests that lowering x only causes structural changes. A reduction in the crystal symmetries follows the usual sequence of transformations: cubic → tetragonal → orthorhombic → monoclinic.

Density functional calculations show that the observed structural transformations are driven primarily by electronic factors.[36] The conduction band concentration, which decreases with a reduction in x, is shown to determine the lattice structure. The calculations, which assume a homogeneous positively charged background due to the donor cations, predict well defined phase boundaries. Experimental observation show overlapping phases in the tungsten bronzes as $x \rightarrow 0$.[17,22,31,60,61] The neutralising positive charges are localised on the donor cations, which are randomly distributed. This would introduce local variations in the electronic density and could account for the observed overlapping phases.

The cubic phase of M_xWO_3 with $x > x_{min}$ is metallic in nature, while WO_3 ($x = 0$) is an insulator. The MI transition in uncompensated tungsten bronzes would therefore occur for $0 < x < x_{min}$. The appearance of non–cubic phases makes a description of the transition more difficult. The production of single crystal Na_xWO_3 samples in this range has also proved to be difficult.[16] Phase separation into high–x cubic and low–x tetragonal forms has also been observed in Eu_xWO_3 for $x < x_{min} \simeq 0.085$.[31] The MI transition has been observed in cubic $Na_xTa_yW_{1-y}O_3$ (see §2.4), where the Ta substitution stabilises the cubic phase.

2.1.2 Hall effect and resistivity

The Hall concentration $n_H = 1/R_He$, where R_H is the measured Hall coefficient, gives a direct indication of the conduction band carrier concentration. The sign of R_H for Na_xWO_3

confirms the expected negative charge carriers.[27] Fig. 2-4 shows n_H vs x for single crystal Na_xWO_3 at room temperature. Also shown is the temperature dependence for $x = 0.22$.

The monotonic increase in n_H with increasing x, and the proximity of the room temperature data to the $n_H = n_d$ line lends support to the fully–ionised donor model. The majority of charge carriers appear to participate in the conduction process. Photoemission spectroscopy on Na_xWO_3 also supports a conduction electron concentration equal to the Na concentration.[12,32] A linear fit of the 300 K data gives $n_H = 1.22n_d$. Assuming that n_d does give the carrier concentration, this leads to a scattering factor $A = n_d/n_H = 0.82 \sim 1$ as found for alkali metals ($A_{Li} \simeq 1.28$; $A_{Na} \simeq 0.88$; $A_K \simeq 0.95$; $A_{Rb} \simeq 0.93$) and other monovalent metals ($A_{Cu} \simeq 0.73$; $A_{Ag} \simeq 0.84$; $A_{Au} \simeq 0.68$).[62] The values of A are generally close to unity, with the exact value depending on many parameters (e.g. temperature, magnetic field, and mechanical stress).[63]

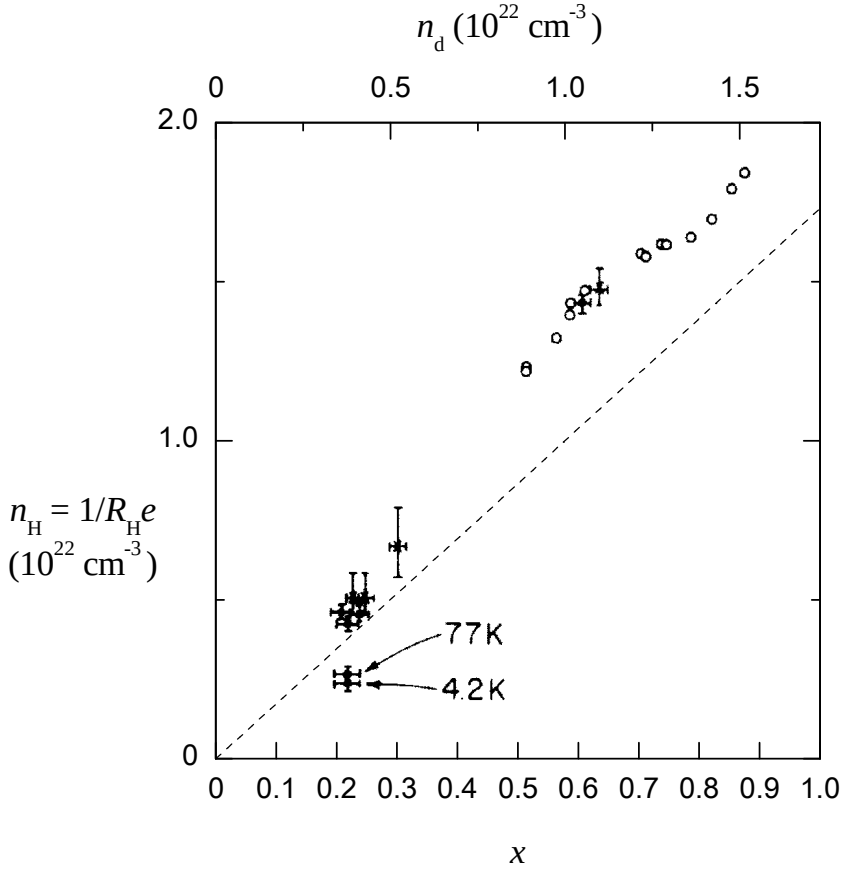

Fig. 2-4. The Hall concentration n_H vs x for Na_xWO_3 at room temperature, reproduced from Ref. 26. Also shown are 77 K and 4.2 K results for $x = 0.22$. The top scale shows the donor-electron concentration $n_d = x/a^3$, and the dashed line is $n_H = n_d$.

For $x > 0.4$ the Hall concentration appears to be temperature independent down to ~4 K, consistent with the typical metallic behaviour expected at the higher concentrations.[26–28,55] The reduction in n_H with decreasing temperature observed for $Na_{0.22}WO_3$ points to a "freezing–out" or localization of charge carriers. This thermal effect on the charge carriers is also evidenced in the temperature dependence of the low x conductivity, leading to semiconducting–type behaviour (Fig. 2-7). The carrier "freeze–out" at lower donor concentrations is attributed to the formation of localized states inside a pseudogap at the Fermi energy (see §2.3 and §2.4).

The Hall effect in the hexagonal tungsten bronzes shows similar behaviour to that of the cubic phase. Room temperature measurements on hexagonal Rb_xWO_3 are consistent with the Rb atoms donating their s electrons to the WO_3 conduction band. Both $Rb_{0.18}WO_3$ and $K_{0.20}WO_3$ show a reduction in the Hall concentration on cooling, as found for $Na_{0.22}WO_3$ in Fig. 2-4.[13,14]

The room temperature resistivity ρ of some cubic and tetragonal alkali tungsten bronzes is shown in Fig. 2-5. The decrease in ρ with increasing x is consistent with the increased carrier concentration shown in Fig. 2-4. The conductivity can be expressed as $\sigma = ne\mu$, where the carrier concentration $n \sim x$ and μ is the electron mobility. The dashed line in Fig. 2-5 shows this form for a constant mobility ($\rho \propto x^{-1}$), giving a satisfactory description of the x–dependence for $x \gtrsim 0.6$. This again highlights the typical metallic behaviour observed in the higher concentration tungsten bronzes. The deviation between the curve and the data on lowering x indicates a dramatic reduction in the electron mobility. As x is reduced the carrier concentration decreases, thereby reducing the screening effects of the itinerant electrons. The disorder due to the randomly positioned Na cations, and disorder–enhanced correlation effects, become more pronounced and reduce the carrier mobility, eventually leading to the MI transition.

The room temperature resistivity of crystalline WO_3 ranges from $10^5 - 10^7$ $\mu\Omega$ cm, depending on the purity.[16] This is several orders of magnitude larger than the resistivity shown in Fig. 2-5, indicating the dramatic transport changes when doping WO_3.

The ρ vs x data in Fig. 2-5 are all for monovalent alkali donors in cubic and tetragonal phases. The coincidence of the data, taking into account the significant fluctuations in the

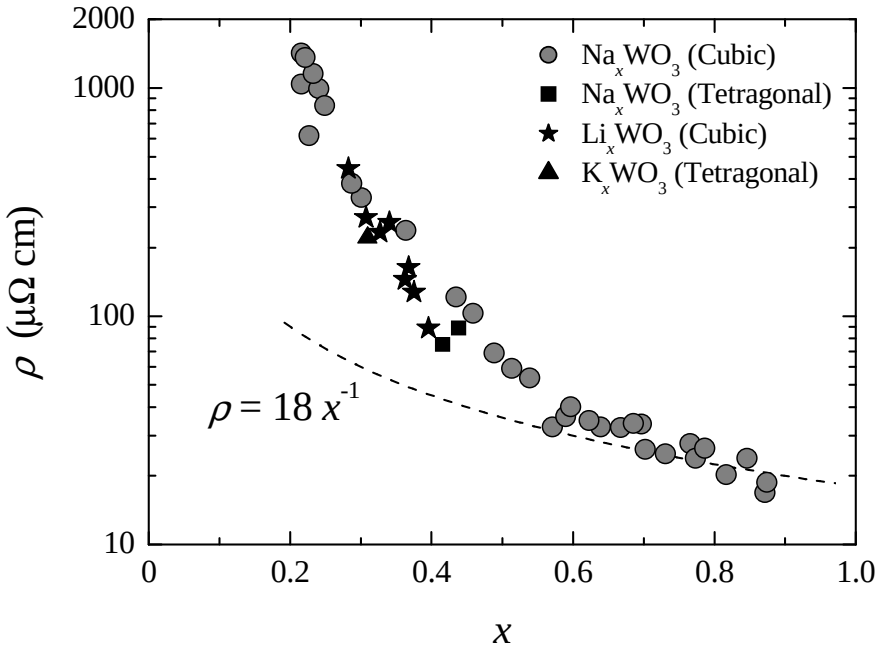

Fig. 2-5. The room temperature resistivity ρ of cubic and tetragonal samples of alkali tungsten bronzes vs x in a log-linear plot. The data was obtained from Refs. 16 and 26. The dashed line is the expression $\rho = 18/x$ matched to the high-x data.

absolute resistivity for Na_xWO_3, suggests that the crystal phase and the type of ion do not significantly affect the resistivity. The valence of the donor atom appears to be the dominant factor. This also indicates that the phase changes observed in the tungsten bronzes as $x \rightarrow 0$ should not interfere significantly with the MI transition. The MI transition is not believed to be driven by structural transitions.[9]

The temperature dependence of the resistivity for higher concentration samples of Na_xWO_3 and La_xWO_3 is shown in Fig. 2-6. Since La is trivalent the effective concentration is $x_{eff} = 0.3$. The resistivity shows the behaviour typically found in metals. For $T \rightarrow 0$ K the resistivity levels off to its residual value, while at the higher temperatures the near–linear behaviour is attributed to phonon scattering. Both Na_xWO_3 and La_xWO_3 show similar thermal changes ~30 μΩ cm in Fig. 2-6, and exhibit a positive temperature coefficient of resistivity characteristic of thermal scattering in metals.[27] This linear ρ vs T behaviour was observed in single crystal Na_xWO_3 ($0.527 \leq x \leq 0.852$) up to 360°C.[59] The hexagonal

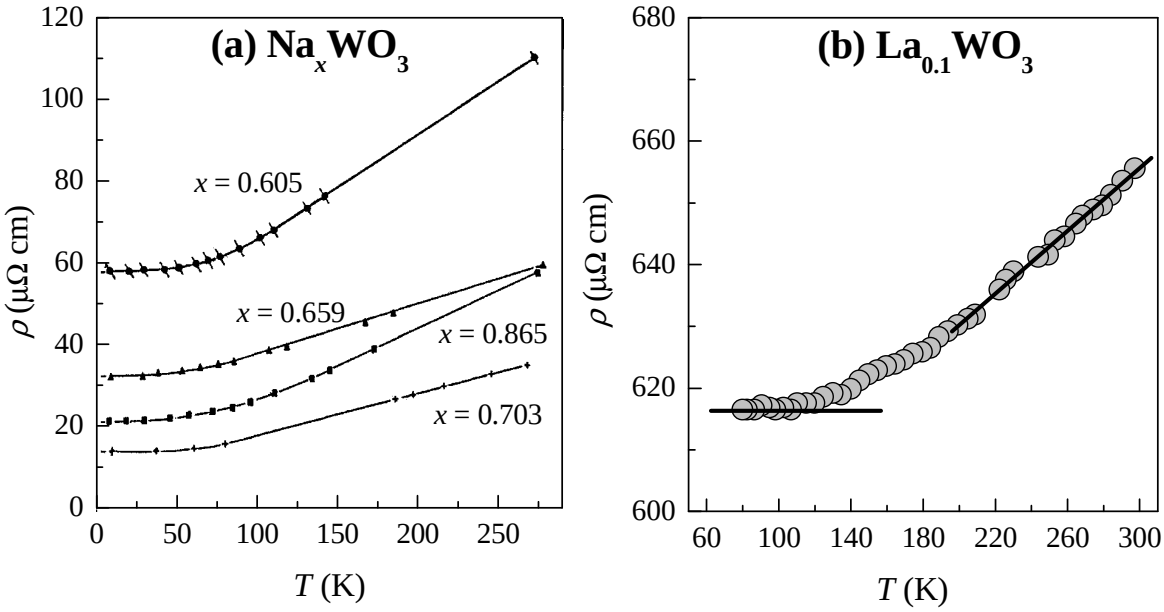

Fig. 2-6. The resistivity ρ vs the temperature T for single crystal samples of (a) Na_xWO_3 (x = 0.605 – 0.865) and (b) La_xWO_3 (x = 0.1). The straight lines in (b) indicate the asymptotic high and low temperature behaviour. The data is from Ref. 28 (a) and Ref. 23 (b).

tungsten bronzes also show this near–linear resistivity behaviour at the higher temperatures.[13] The linearity in ρ is expected for $T \gtrsim \Theta_D$ where the Debye temperature $\Theta_D \sim 300$ K for Na_xWO_3.[51]

The conductivity $\sigma(T)$ of $Na_xTa_yW_{1-y}O_3$ is shown in Fig. 2-7 for a series of samples spanning the MI transition. The change in the effective carrier concentration $x_{eff} = x - y$ from 0.44 to 0.11 leads to a reduction in σ by seven orders of magnitude at the lowest temperatures. The MI transtition occurs for $x - y \simeq 0.18$ (see Fig. 2-13). The highest concentrations show the typical metallic–type behaviour shown in Fig. 2-6 ($d\sigma/dT < 0$). A reduction in the donor concentration then leads to semiconducting–type behaviour with $d\sigma/dT > 0$. The crossover, where $d\sigma/dT$ changes sign, was previously believed to indicate the MI transition. However, the semiconductor-like behaviour does not necessarily indicate insulating samples, as evidenced by the results in Fig. 2-13. The $Na_{0.35}Ta_{0.16}W_{0.84}O_3$ sample is just–metallic ($\sigma \simeq 10$ S/cm as $T \rightarrow 0$ K) but σ increases monotonically with increasing temperature. This behaviour is suggestive of thermally activated charge carriers,

possibly linked to a pseudogap in the density of states,[9] and consistent with the Hall concentration results for $Na_{0.22}WO_3$ in Fig. 2-4. The increase in σ with temperature can also arise from electron–electron interactions in disordered metals (see Eq. 2.10 in §2.2.1).[64]

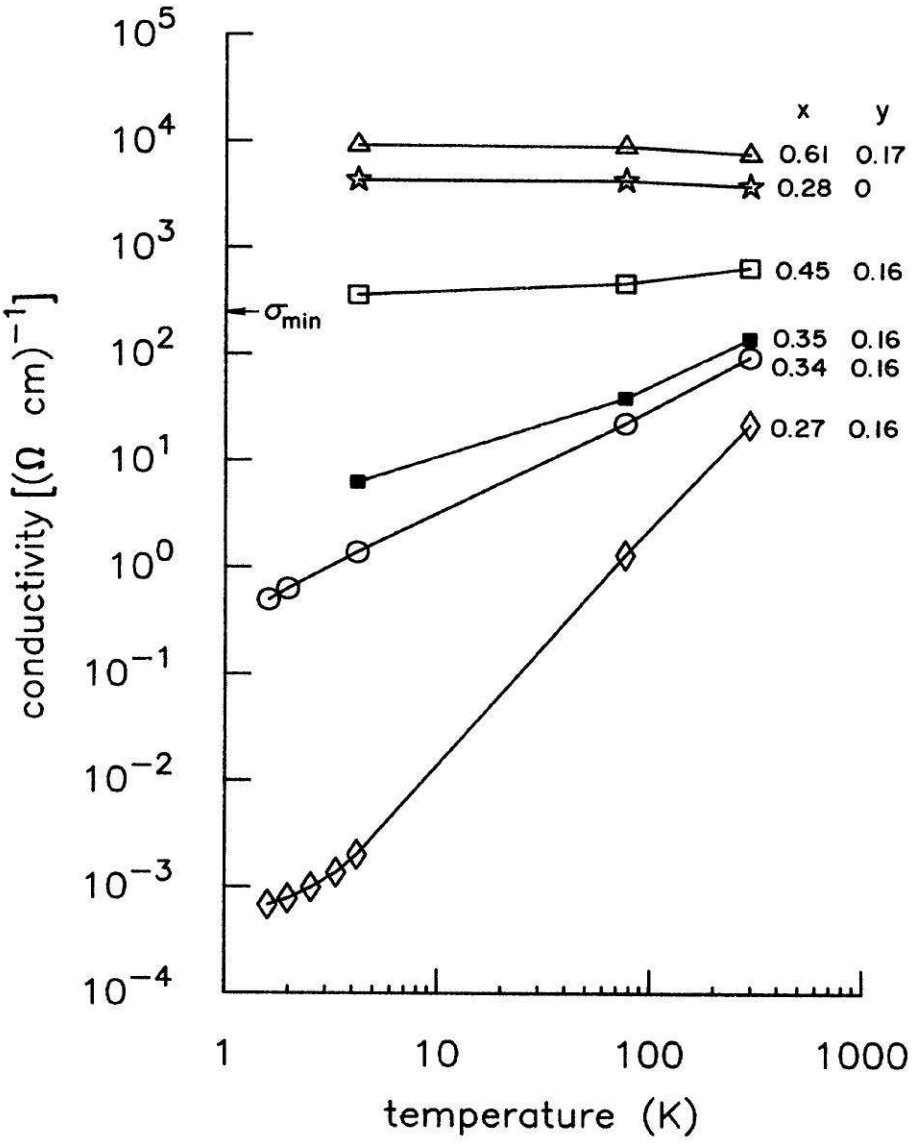

Fig. 2-7. The conductivity σ vs the temperature T for a sequence of $Na_xTa_yW_{1-y}O_3$ samples. One sample of Na_xWO_3, corresponding to $y = 0$, is also included. The Mott minimum metallic conductivity $\sigma_{min} \simeq 250$ S/cm is shown. The effective carrier concentration is $x_{eff} = x - y$. The figure was reproduced from Ref. 8.

2.1.3 Diffuse reflectance

The sodium tungsten bronzes undergo dramatic colour changes as the Na concentration x is varied. For $x = 0$, WO_3 shows a yellow–green colour at room temperature, apparently becoming transparent as $T \rightarrow 0$ K.[65] In addition to more metallic lustre, an increase in x is accompanied by a range of colour changes: yellow–green; blue–black; blue; violet; red–violet; red–orange; orange; golden–yellow.[12] The colour of a Na_xWO_3 sample may be used to infer the Na concentration, as well as indicate sample homogeneity. The x–dependent conduction band concentration is responsible for the chromatic character of the tungsten bronzes. Optical studies have formed a significant part of tungsten bronze investigations.[18,34,37,41,47,53,65]

Fig. 2-8 gives diffuse reflectance results for Na_xWO_3 and Li_xWO_3. The yellow–green colour of WO_3 is attributed to interband transitions resulting in the peak around 470 nm in Fig. 2-8a. (See Fig. E-6 in appendix E.) This wavelength corresponds to the experimentally determined value of 2.6 eV for the indirect band gap.[34,45] For $x > 0$ the reflectance in the visible and infrared range shows a strong dependence on x. This is due to the metallic–type

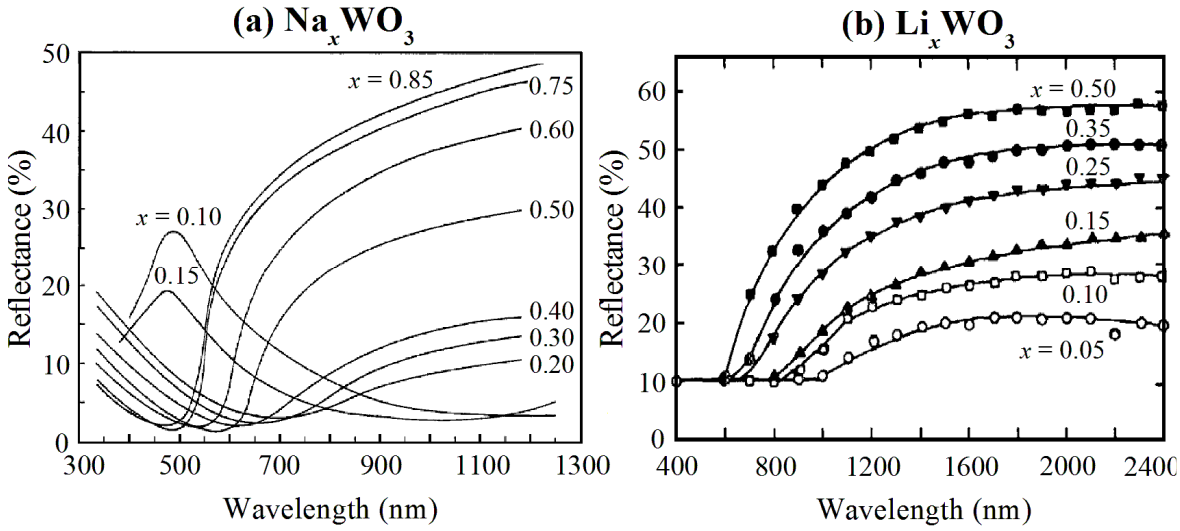

Fig. 2-8. Diffuse reflectance results for polycrystalline samples of Na_xWO_3 and Li_xWO_3 for various x values. The figures are modified extracts from Ref. 37 (a) and Ref. 18 (b).

reflection from the donor electrons in the conduction band. The reflection is similar in form to that of typical metals such as copper and gold.[66] In metals the reflectivity is greatly enhanced below the plasma frequency $\omega_P \propto n^{1/2}$, with n the free carrier concentration.[65] Increasing x leads to an increase in n and hence an increased ω_P. This accounts for the shift in the onset of the metallic–type reflection observed in Fig. 2-8. Fig. 2-8a gives a hint of the MI transition in Na_xWO_3, with the metallic–like reflection disappearing with decreasing x, being replaced with the reflection of insulating WO_3. The expected critical concentration $x_C \sim 0.18$ for Na_xWO_3 fits well with the results in Fig. 2-8a. The reflectivity results for Li_xWO_3 in Fig. 2-8b are similar to those of Na_xWO_3 in Fig. 2-8a. A lack of resolution in the Li_xWO_3 data may account for the absence of the short–wavelength low–x features observed in Na_xWO_3 results.

The longer wavelength reflection observed in Fig. 2-8 arises from the metallic–type donor electron concentration. The optical properties of the tungsten bronzes may therefore be modulated by varying the donor concentration x. This accounts for the interest in tungsten bronzes for use in chromatic devices. For a good conductor the reflectivity R for normal incidence can be approximated by[67]

$$R = 1 - \kappa\sqrt{\frac{\rho(x)}{\lambda}} \qquad 2.1$$

where κ is a constant, λ the wavelength and ρ the x–dependent crystal resistivity. Decreasing λ reduces the reflectivity, accounting for the 'tail' in the visible region. Increasing x leads to a reduction in ρ (Fig. 2-5), accounting for the increased reflectivity observed in Fig. 2-8. The total reflectivity in the visible range therefore increases with x and accounts for the more metallic lustre observed in the higher x samples. The long wavelength reflection is predicted to approach 100%, which is observed in high concentration single crystal Na_xWO_3.[53] The reduced values observed in Fig. 2-8 are attributed to the samples being polycrystalline. The porous nature and varying surface orientations need consideration. The overall low reflectivity in the visible range accounts for the dark appearance of the lower x tungsten bronzes.

The above expression gives only a qualitative description of the low x tungsten bronze metallic reflectivity. For the higher concentrations rigid band models do become

appropriate. Calculations based on the free–electron Drude model are then more successful in quantitatively describing the intraband contribution to the reflectivity.[34,47,53] Recent calculations provide a quantitative description of the systematic colour changes with x observed in Na_xWO_3.[65] The intraband response was modelled by the Drude model, while the dielectric function due to interband transitions was determined by first–principle electronic structure techniques using density functional theory. The interplay between the interband and intraband contributions is shown to be important.

2.1.4 Specific heat and magnetization

Fig. 2-9 shows the electronic susceptibility χ_e and specific heat coefficient γ of Na_xWO_3 as a function of the sodium concentration x.[51] The measured susceptibility near room temperature is constant (also observed for $Ba_{0.12}WO_3$),[51,57,68] attributed to the WO_3 and Na^+ diamagnetism ($\chi_{WO_3} + x\chi_{Na^+} = (-13.9 - 6.1x)\times 10^{-6}$ emu / mol) and the paramagnetic susceptibility χ_e of the donor electrons in the conduction band. The Curie–type susceptibility occurring at low temperatures is attributed to impurities. At low temperatures ($T \lesssim 5$ K) the specific heat shows behaviour typical of metals ($C = \gamma T + \beta T^3$, with βT^3 the phonon contribution).

The Hall concentration suggests a conduction band concentration $n \propto x$, and band theory gives χ_e, $\gamma \propto \rho(E_F)$, the Fermi–level density of states. The linear dependence observed in Fig. 2-9 for $x > 0.4$ therefore suggests $\rho(E_F)$ is linearly dependent on the conduction band concentration. This has been experimentally observed.[12,45] The failure of the free–electron model, which predicts an $x^{1/3}$ dependence, is evident in Fig. 2-9. Use of the free–electron predictions requires a varying effective mass parameter. Photoemission spectroscopy[12,45] and optical measurements[47] show a strictly increasing effective mass for $x > 0.5$. Band theory calculations on ReO_3 (which give similar results to the alkali tungsten bronzes)[35] predict the required linear form for $\rho(E_F)$ vs x, as shown in Fig. 2-9.[51] This follows from a density of states $\rho(E) \sim \exp(E/E_0)$, and this form is noticed in Fig. 2-3 for the lower part of the conduction band at sufficient concentrations ($1\text{ eV} \lesssim E \lesssim 3.5$ eV).

The deviation between χ_e and γ in Fig. 2-9 for $x < 0.4$ is not unexpected. There is ample evidence that the rigid–band models (based on cubic WO_3 with conduction band filling) give a sufficient description of the tungsten bronzes at the higher concentrations. However,

as the MI transition is approached ($x \rightarrow x_C$), conventional band theory breaks down. In this metallic regime carrier localization is suggested (Fig. 2-4), conductivity with $d\sigma/dT > 0$ is observed (Fig. 2-7), and the formation of a pseudogap occurs (§2.3 and §2.4 below). At the lower concentrations the disorder (from the randomly situated donors) and electron interaction effects become more pronounced, and need to be considered in theoretical descriptions of these systems.

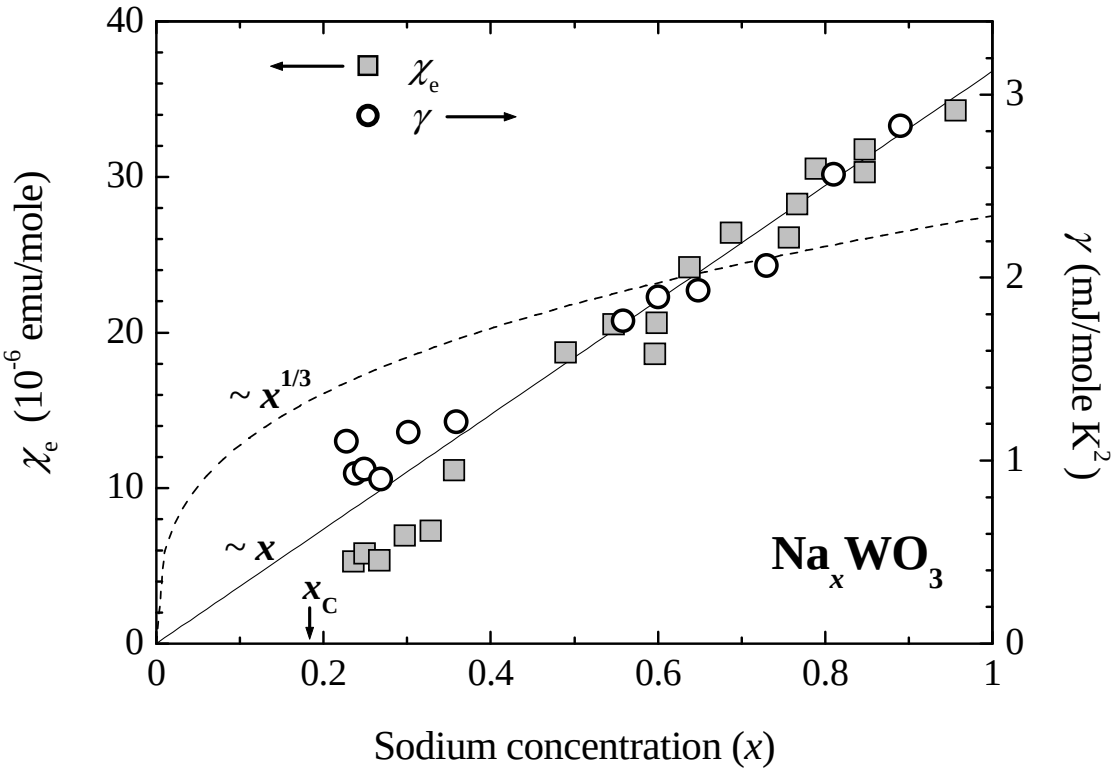

Fig. 2-9. Na_xWO_3 electronic susceptibility χ_e and specific heat coefficient γ reproduced from Ref. 51. The vertical scales were chosen for coincidence of the high x data. The dashed line is a free-electron prediction ($\propto x^{1/3}$). ReO_3 band theory applied to the high-concentration data produces the solid straight line ($\propto x$). The critical concentration $x_C \sim 0.18$ is shown.

2.2 The metal–insulator transition

By varying a physical parameter the conductivity of some systems may be changed over many orders of magnitude, changing insulating materials into metallic–type conductors. An example of this is shown in Fig. 2-7, where the conductivity of $Na_xTa_yW_{1-y}O_3$ changes by seven orders of magnitude at low T by small variations of the Na and Ta doping. The compositionally controlled MI transition is the most commonly observed case, although factors such as stress (pressure) and magnetic field may also be used to drive the transition.[3] The MI transition is observed in a variety of systems such as transition–metal oxides ($Na_xTa_yW_{1-y}O_3$, $LaNi_xCo_{1-x}O_3$, $LaNi_{1-x}Mn_xO_3$, $La_{1-x}Sr_xCoO_3$), doped semiconductors (Si:P, Ge:Ga, C:B) and metal–ammonia solutions.[3,4,69–72] A complete theoretical description of the MI transition is still lacking, as a variety of coupled mechanisms need to be considered. In addition to band structure considerations, effects such as disorder, electron–electron (e–e) interactions and screening need to be included. Several references on the MI transition have been mentioned at the start of chapter 1. Further information may also be found in the books by Shklovskii and Efros[73] and Edwards and Rao[74].

A strict definition of what is meant by an insulator and a metal can only be made at absolute zero. Insulators are defined by a vanishing residual conductivity $\sigma_0 = \sigma(T = 0\ \mathrm{K})$, while metals conduct electricity at absolute zero ($\sigma_0 > 0$). As the donor concentration in the tungsten bronzes is increased from $x = 0$, we find that (for $T \rightarrow 0$ K) a critical value x_C is reached at which the material starts to conduct electricity. Since absolute zero cannot be reached, the exact determination of the MI transition is problematic, and requires certain assumptions in determining σ_0 from the analysis of finite T data in order to classify a system as insulating or metallic. It has been shown that very low temperatures are required for a proper investigation of the low T conductivity data.[7,69,75]

Materials in which the top of a filled valence band is separated from the bottom of an empty conduction band by an energy gap are called band–gap insulators. Thermal excitation of carriers into the conduction band is required for electrical conductivity. Doping a material or applying stress can change the internal electronic structure, thereby creating or eliminating band gaps and inducing an MI transition. The Mott–Hubbard transition (discussed in §2.2.1) arises from the formation of a gap due to electron interactions. The conductivity of a material can also vanish in the presence of sufficient

disorder. Anderson localisation (discussed in §2.2.2) leads to a disorder–induced MI transition without the presence of any band gaps.

Using the Einstein relation

$$\sigma_0 = e^2 \rho(E_F) D \qquad 2.2$$

where $\rho(E_F)$ is the density of states (DOS) at the Fermi energy E_F and D the electron diffusivity, a metallic system stops conducting if either $\rho(E_F) \to 0$ or $D \to 0$. The first can occur if a gap opens up at E_F (such as in a band–gap material or the Mott–Hubbard transition), while the second occurs if the states at E_F become localized (such as Anderson localization). In real systems it is generally found that both occur as the MI transition is approached.[3]

WO_3 (with $x = 0$) is a band–gap insulator (Fig. 2-2 and Fig. 2-3) with a semiconducting behaviour at finite temperatures.[41] The cubic tungsten bronzes ($x \geq x_{min}$) show metallic behaviour and hence $x_C < x_{min}$.[26] For the much researched Na_xWO_3 the critical concentration is estimated at $x_C \sim 0.18$, corresponding to an electron concentration around 3×10^{21} cm^{-3}.[7,8] For $0 \leq x < x_C$ the tungsten bronzes are therefore insulating with a diverging $T \to 0$ K resistivity, while for $x > x_C$ they exhibit a finite residual resistivity (or conductivity).

The tungsten bronzes are tight–binding materials.[9,46] The WO_3 lattice is the host while the donor atoms provide electrons that fill the WO_3 conduction band (§2.1.1). The WO_3 tight binding Hamiltonian in the site representation is

$$\hat{H}_{TB} = \sum_{i,\mu} \varepsilon_{0i} \hat{n}_{i\mu} + \sum_{i\,j,\mu} t_{ij} \hat{c}^{\dagger}_{i\mu} \hat{c}_{j\mu} \ . \qquad 2.3$$

The number operator $\hat{n}_{i\mu} = \hat{c}^{\dagger}_{i\mu} \hat{c}_{i\mu}$ where $\hat{c}^{\dagger}_{i\mu}$ ($\hat{c}_{i\mu}$) is the creation (annihilation) operator for site i (i and j run over W or O sites) with spin μ. For large atomic separations the transfer integral $t_{ij} = 0$ and the solutions to $\hat{H}_{TB}$ are the atomic site states $|i\rangle$ with orbital energies ε_{0i}. As the atoms are brought closer, the overlap of orbitals makes $t_{ij} \neq 0$ and leads

to the formation of the band structure in WO_3 (Fig. 2-2 and Fig. 2-3). For the periodic WO_3 lattice the solutions to $\hat{H}_{TB}$ are then the Bloch states

$$\left|\vec{k}\right\rangle \equiv \sum_i a_i \left|i\right\rangle \equiv \sum_i e^{\vec{k}\cdot\vec{r}_i} \left|i\right\rangle \qquad 2.4$$

where $\vec{k}$ is the wavevector and $\vec{r}_i$ the vector position of site *i*. For the valence band the sum in Eq. 2.4 is dominated by O sites, while for the conduction band the sum is mainly over W sites. The Bloch states have equal amplitudes on equivalent sites ($|a_i|^2 = |a_j|^2$) and hence extend over the whole crystal. The quasi–continuous nature of the conduction band, which is partially filled for $x > 0$, then allows for electronic transitions by an external electric field. This leads to the metallic behaviour observed in the higher *x* tungsten bronzes.

The model of filling a rigid WO_3 conduction band by donor atom electrons is very successful in describing the tungsten bronze properties at higher concentrations, as discussed in earlier sections, but starts to fail as $x \rightarrow 0$. The most notable is the fact that in a rigid–band filling the conductivity will only disappear for $x = 0$, making WO_3 the only insulating system (i.e. $x_C = 0$). Referring to Fig. 2-3 and Eq. 2.2 the MI transition would occur since $\rho(E_F) \rightarrow 0$ as $x \rightarrow 0$. The conduction band states are all of extended Bloch nature, so *D* remains finite. As discussed below, mechanism such as e–e interactions and disorder can have profound effects on the properties of materials. These effects are found to be important in the low *x* tungsten bronzes, and are eventually responsible for the MI transition at finite concentrations. At the higher concentrations the conduction electrons screen out the effects of disorder and e–e interactions, accounting for the success of the band theory description.

2.2.1 Interactions: the Mott–Hubbard transition

In a good metal the success of the free–electron model arises from the collective screening effects involving the conduction electrons. The high concentration and high mobility of the carriers are very effective in shielding the fields due to external charges (such as the core cations).[62,76] Each electron therefore experiences only a weak periodic potential. The screened potential of the cations does not support bound states. As the

carrier concentration decreases, by increasing the lattice constant say, the screening length increases. At some critical concentration n_C the screening length is large enough for the cation to support bound states. For concentrations below n_C the material will be insulating with the valence electrons in bound states with a Bohr radius a_B. A MI transition therefore occurs based on the screening of Coulombic centres. Using the Thomas–Fermi screening length, Mott[2] quantified this argument as

$$n_C^{1/3} a_B \sim 0.24 \qquad 2.5$$

Many diverse MI systems follow the above Mott criterion, as evidenced by the $n_C^{1/3}$ vs a_B plot of Fig. 6 in Ref. 3. A similar expression can also be obtained for disordered systems from percolation theory. Noticing that $n_C^{-1/3}$ gives a measure of the average spacing between orbitals in the insulating state, the above relation can also be viewed as defining a percolation threshold concentration related to the orbital size a_B.[77]

In typical metals it is difficult to vary the carrier concentration significantly to observe the above transition. In the tungsten bronzes, however, the carrier concentration can be systematically varied by selecting the donor concentration x. For $x \lesssim 1$ it has been shown that the tungsten bronzes have typical metallic properties. The idealised MI transition outlined above would probably occur in the tungsten bronzes as $x \rightarrow 0$ if the donor cations were distributed periodically in the WO_3 host lattice.

The random distribution of the donors, however, introduces disorder which has profound effects on the properties as the MI transition is approached. For large x the effects of the disorder is mainly to introduce scattering centres and reduce the conductivity of the system. The reduced mobility of the carriers, combined with a reduction in the carrier concentration as x is reduced, leads to a reduction in the effective screening abilities of the conduction electrons. Electron–electron interactions then become important. These disorder–enhanced correlation effects are manifested in the physical properties of the tungsten bronzes in the metallic phase near the MI transition. Interaction effects are also observed in the insulating phase. This is further discussed in §2.3 and §2.4.

The next section (§2.2.2) discusses how disorder alone can lead to an MI transition. Below it is shown that introducing e–e interactions into band theory can also have a similar

effect. In the tungsten bronzes and many other MI systems, however, band structure, screening effects, disorder and e–e interactions all have to be considered in order to adequately describe the properties near the MI transition.

Fig. 2-10 demonstrates how e–e interactions can produce a MI transition in an otherwise metallic system. Considering a periodic collection of monovalent atoms with lattice constant a, band theory will predict a metallic half–filled conduction band due to the spin degeneracy. The bandwidth B decreases as a increases. The system will remain metallic as $a \rightarrow \infty$, although the effective mass will diverge with the mobility vanishing exponentially.

In reality, for a sufficiently large a, the electrons will eventually occupy the individual atomic orbitals with energy E_0. A second electron of opposite spin, when placed into this orbital, will have a larger energy due to the Coulombic interaction with the first electron. The orbital spin degeneracy is lifted by an energy $U \sim e^2/a_B$. The energy U, referred to as the Hubbard energy, is manifested in the different ionization energies required to remove the two electrons from a divalent atom.

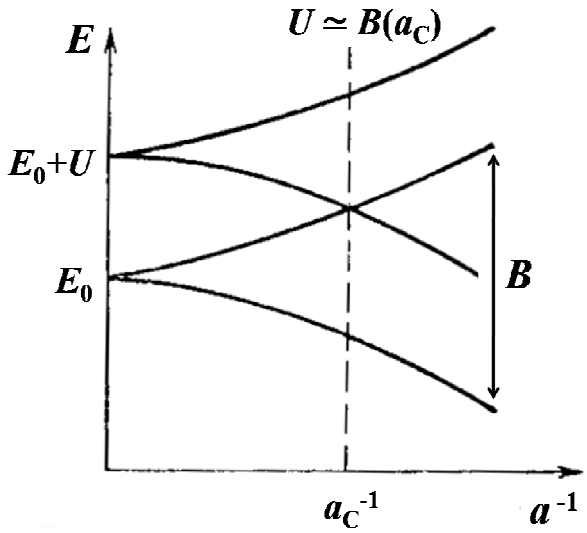

Fig. 2-10. The electronic bandwidth B as a function of the lattice constant a. The atomic level spin degeneracy is split by the electron-electron interaction U. Band-gap formation occurs for $a > a_C$. (Modified from Ref. 73.)

As the lattice spacing is reduced, the orbital overlap causes the two levels to form bands (the upper and lower Hubbard bands), as shown in Fig. 2-10. Initially the bands are separated by a gap (for $U > B$) leading to a band–gap insulator. When a is further reduced below a critical value a_C, the upper and lower Hubbard bands overlap (for $U < B$). This leads to two partially filled bands, each one contributing to the conductivity, thereby making the system metallic. A MI transition, called the Mott–Hubbard transition, therefore occurs when the varied bandwidth $B \simeq U$. The Hubbard energy is important in narrow bands, while in typical metals $B \gg U$ and interaction effects are less evident.

Quantitatively the e–e interactions are accounted for in the Hubbard model Hamiltonian[78]

$$\hat{H}_U = \hat{H}_{\mathrm{TB}} + \frac{1}{2} U \sum_{i,\mu} \hat{n}_{i\mu} \hat{n}_{i-\mu} \,. \qquad 2.6$$

The interaction term is added to the tight–binding Hamiltonian $\hat{H}_{\mathrm{TB}}$ in Eq. 2.3. In the Hubbard model the electron interaction is only considered for electrons on the same site with opposite spin (due to the Pauli exclusion principle). The Hubbard energy U quantifies this interaction, and is usually treated as a parameter. The Hamiltonian $\hat{H}_U$ favours states with sites occupied by a single electron. The Coulombic interaction in this case is therefore more restrictive than the Pauli exclusion principle, which allows for two electrons per site.

As discussed above, the general effect of e–e interactions is to shift bands which may lead to a depletion of the DOS at E_F and the possible formation of a band gap. On the insulating side, Efros and Shklovskii[79] have shown that the long range Coulomb interactions between localized states lead to the formation of a soft gap near E_F, with a parabolic DOS

$$\rho(E) \propto \left| E - E_F \right|^2 \,. \qquad 2.7$$

The gap is soft since $\rho(E) = 0$ only at E_F. The resultant hopping conductivity is of the form

$$\sigma(T) \propto \exp\left(-\left(\frac{T_0}{T}\right)^{1/2}\right) \qquad 2.8$$

where $k_B T_0 = e^2/\kappa\eta$ defines a characteristic temperature T_0 with κ the dielectric constant and η the localization length. Eq. 2.8 is valid for $T \ll T_0$. The Efros–Shklovskii exponent $p = 1/2$ is different from the Mott variable range hopping exponent $p = 1/4$, which considers non–interacting localized states with $\rho(E_F) \neq 0$.[2]

On the metallic side, Altshuler and Aronov[80] have shown that in disordered (dirty) metals a pseudogap forms due to e–e interactions. The DOS near E_F exhibits a square–root cusp with

$$\rho(E) \equiv \rho(E_F) + \alpha_1 |E - E_F|^{1/2} \qquad 2.9$$

while the low temperature conductivity is predicted to be of the form

$$\sigma(T) = \sigma_0 + \alpha_2 T^{1/2} \ . \qquad 2.10$$

(α_1 and α_2 are constants in the above two expressions.)

The e–e interactions are therefore manifested in the physical properties on both sides of the MI transition, as evidenced in §2.4. Experimental results suggest that the pseudogap in the metallic phase (Eq. 2.9) evolves as the MI transition is approached and eventually becomes a Coulomb gap in the insulating phase (Eq. 2.7). (i.e. $\rho(E_F) \rightarrow 0$ and the exponent changes from 1/2 to 2.) The conductivity, which is coupled to the DOS at E_F, also evolves from the form in Eq. 2.10 to the hopping conduction in Eq. 2.8 as the system is driven from a metallic to insulating state. The Anderson–Mott–Hubbard model (discussed in §2.3) shows that the observed pseudogap in the metallic state is related to the strength of the e–e interactions via the Hubbard parameter U in Eq. 2.6. In addition to correlation effects, the effects of disorder (discussed next) are also essential to a proper description of these observations.

2.2.2 Disorder: Anderson localization

An ideal metal has no residual resistivity. The finite T = 0 K conductivity (as in Fig. 2-6) arises from deviations of the lattice periodicity, mostly attributed to impurities. Lattice vibrations cause the resistivity to increase with temperature. For $T > \Theta_D$ the number of phonons $\propto T$, accounting for the linear ρ vs T relationship observed in metals (Fig. 2-6).When the impurity concentration is small the conductivity can be modelled as the scattering of Bloch waves. In the weak scattering regime Boltzmann transport theory may be used. In the relaxation time approximation (also called the Drude formula)

$$\sigma = \frac{ne^2\tau}{m_{\text{eff}}} \qquad 2.11$$

where n is the carrier concentration, m_{eff} the effective mass, and τ the relaxation time. The effective mass is given by the curvature of the dispersion relation ($\hbar^2/m_{\text{eff}} = d^2E(k)/dk^2$) and hence depends on the underlying band structure. The relaxation time gives the average time between scattering events, and will depend on the extent of the disorder. The carrier mobility $\sigma/ne \propto \tau$ and the mean free path $l = v_F \tau$ (v_F the Fermi velocity) therefore both decrease with increasing disorder. Experiments show that τ decreases with decreasing x for the higher concentration Na tungsten bronzes.[47] Using the free–electron model relation $k_F^3 = 3\pi^2 n$ for the Fermi–level wavevector, with $n = x/a^3$, gives the Drude formula for Na_xWO_3 (with $a \simeq 3.8$ Å and $x_C \simeq 0.18$):

$$\sigma = 695 \left(\frac{x}{x_C}\right)^{2/3} \left(\frac{l}{a}\right) \text{ S/cm.} \qquad 2.12$$

Considering, for example, the $Na_{0.28}WO_3$ sample in Fig. 2-7 with $x/x_C \simeq 1.5$ and $\sigma \sim 4\times10^3$ S/cm gives $l \sim 4a$. Extrapolation of the Boltzmann transport theory into the strong scattering regime therefore becomes questionable, particularly when l approaches the lattice spacing as it does in Na_xWO_3 when $x \rightarrow x_C$.

In a lattice with sufficient disorder, Anderson[81] showed that the electronic wavefunction could become localized. This disorder-induced localization is called Anderson localization, and is a crucial aspect of the MI transition. The tight-binding Anderson model Hamiltonian

$$\hat{H}_{\mathrm{A}} = \sum_{i,\mu} \varepsilon_i \hat{n}_{i\mu} + \sum_{i\,j,\mu} t_{ij} \hat{c}^{\dagger}_{i\mu} \hat{c}_{j\mu} \qquad 2.13$$

is similar to the Hamiltonian $\hat{H}_{\mathrm{TB}}$ for a periodic lattice in Eq. 2.3. The difference is that due to disorder the energies ε_i (and possibly t_{ij}) are now random variables. The matrix of $\hat{H}_{\mathrm{A}}$ therefore has diagonal (and off–diagonal) disorder. The Bloch states in Eq. 2.4, which are solutions of $\hat{H}_{\mathrm{A}}$ in the absence of disorder, are extended throughout the crystal. For a sufficient amount of disorder, the solutions of $\hat{H}_{\mathrm{A}}$ will include states which are only a finite sum of site states $|i\rangle$, and hence finite in spatial extent (or the envelope of the wavefunction decays exponentially from some region in space). These are the disorder–induced Anderson localized states.

Fig. 2-11 gives an example of the DOS of a band in the presence of disorder–induced Anderson localization. States with a low $\rho(E)$ are more susceptible to localization, accounting for the band tail states being localized (see Ref. 73 for an elucidation). Band state localization depends on the parameter W/B, where B is the bandwidth and W the range of fluctuations in the site energies ε_i (and t_{ij}) due to disorder. For small W/B no Anderson localization occurs in the band, and the disorder has a perturbative effect on the band structure. As W/B increases, the localization starts to occur where the DOS is the smallest, such as the band tail states. For a sufficiently large W/B all the band states will eventually be localized.

The mobility edge E_{C} is the energy that separates the region of localized states from the region of extended states. If the Fermi energy E_{F} falls inside the extended state region (as in Fig. 2-11), the system will be metallic. For $E_{\mathrm{F}} < E_{\mathrm{C}}$ the system will be insulating (referring to Eq. 2.2, $\rho(E_{\mathrm{F}}) \neq 0$ but $D = 0$). For $k_{\mathrm{B}}T \ll E_{\mathrm{C}} - E_{\mathrm{F}}$ the conductivity will then be due to thermally activated variable range hopping as in Eq. 2.8 (with an exponent possibly different from 1/2). For the DOS shown in Fig. 2-11 an MI transition will therefore occur as the Fermi energy crosses the mobility edge. This is known as the Anderson transition.

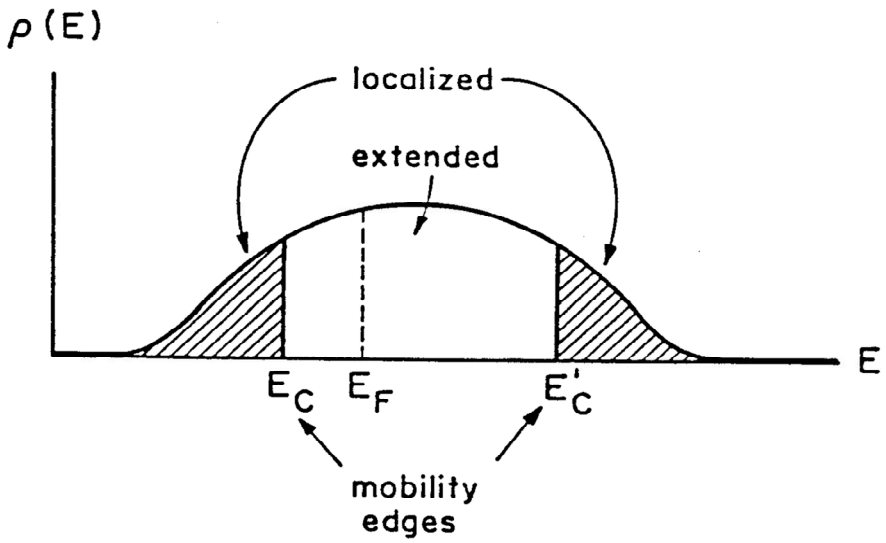

Fig. 2-11. The density of states in the presence of disorder-induced Anderson localization. (Reproduced from Ref. 77.)

In the case of the tungsten bronzes, E_F increases as the conduction band is filled by increasing the donor concentration x. Calculations by Dücker *et al.*[9,52] suggest that, in the absence of e–e interactions, the Anderson transition will occur for $x \simeq 0.1$ (see §2.3). This critical concentration is significantly lower than the experimental estimate $x_C \simeq 0.18$. Incorporating e–e interactions, Dücker *et al.*[9] find that the MI transition is shifted to larger concentrations.

2.2.3 The critical region

The critical region refers to the just–metallic phase for concentrations very near the MI transition ($0 < n/n_C - 1 \ll 1$). Of interest is the behaviour of the residual conductivity σ_0 as the MI transition is approached from the metallic side. The way that $\sigma_0 \rightarrow 0$ as $n \rightarrow n_C$ has received significant theoretical and experimental investigation.

Mott[2] proposed that σ_0 vs n undergoes a discontinuity at the MI transition, and that there is a minimum metallic conductivity σ_{min} (i.e. $\sigma > \sigma_{min}$ for $n > n_c$). The Drude formula (Eq. 2.11) from Boltzmann transport theory can be rewritten as $\sigma = (e^2/3\pi^2\hbar)k_F^2 l$, with k_F the Fermi–level wavevector. The expression, which is valid in the weak scattering regime,

is then extrapolated to the MI transition. (Extrapolations to n_C of theories which are valid far from the MI transition are often encountered, and are only justified in the success of the results they produce.) The mean free path l cannot be shorter than the Fermi wavelength λ_F ($\sim k_F^{-1}$), which itself must be larger than the lattice spacing (k_F is limited to the first Brillouin zone). These ideas place a lower bound on the conductivity with

$$\sigma_{\min} = C_{Mott}\left(\frac{e^2}{\hbar}\right) l_C^{-1} \qquad 2.14$$

where l_C is the mean distance between scattering centres (~ donor separation in the tungsten bronzes ~ 7 Å ~ 2 lattice spacings), and C_{Mott} is a constant in the range 0.01 – 0.05.[3]

Experimental evidence, however, suggests that σ_0 vanishes continuously at the MI transition.[75] Several systems, including $Na_xTa_yW_{1-y}O_3$, exhibit metallic behaviour with $\sigma_0 \ll \sigma_{min}$.[7,69,75] The Mott minimum metallic conductivity $\sigma_{min} \sim 250$ S/cm for $Na_xTa_yW_{1-y}O_3$ is included in Fig. 2-7. Fig. 2-13 in §2.4 shows the conductivity for a just–metallic sample of $Na_xTa_yW_{1-y}O_3$ with $\sigma_0/\sigma_{min} \sim 0.02$. The Mott minimum metallic conductivity, however, remains a useful quantity in that metallic samples with $\sigma < \sigma_{min}$ are believed to be in the critical region.[4,8]

The scaling theory of localization looks at the behaviour of the conductance with respect to the system size scaling. Considering the conductance $g(L)$ of a cube of length L, the main assumption is that the conductance $g(2L)$ of a cube with its sides doubled should only depend on the original conductance $g(L)$ and not the length L. This may be formally expressed as $d(\ln g)/d(\ln L) = \beta(g)$, where β is the scaling function. A detailed description of the scaling theory has been presented by Lee and Ramakrishan.[5] The main result relevant to this section is that in the critical region scaling theory predicts σ_0 has the form

$$\sigma_0 \propto (n - n_C)^{\nu_C} \ . \qquad 2.15$$

In contrast to the Mott minimum metallic conductivity, scaling theory predicts that σ_0 vanishes continuously as $n \rightarrow n_C$. The above expression is usually used to obtain the critical concentration n_C from extrapolated values of the finite temperature conductivity.

The extent of the critical region is very important and, as mentioned above, σ_{min} may be used as a rough estimate for the range of validity of Eq. 2.15 for a particular MI system. The critical region is found to be unusually large in some systems. The expectation for the critical range is usually $n/n_C - 1 < 0.01$.[75] For Si:P and Ge:Ga, for example, Eq. 2.15 is observed for $0.001 \lesssim n/n_C - 1 \lesssim 1$ and $0.004 \lesssim n/n_C - 1 \lesssim 0.3$ respectively.[69,75]

The values of the critical exponent ν_C are still under debate. Theoretical predictions show that $\nu_C \simeq 1$ and this is indeed observed in many systems.[3,69] Systems such as Si:P and Ge:Ga clearly show $\nu_C \simeq 0.5$.[69,75] Values of $\nu_C \sim 2$ have also been proposed for some compounds.[70,72] A general consensus between experimental results and theory regarding the critical exponent is still to be reached. Crucial in determining ν_C is the proper determination of σ_0 from finite temperature data (i.e. very low T conductivity data), and sample concentrations sufficiently close to the MI transitions (i.e. to ensure the validity of Eq. 2.15).

Percolation theories have also been used to describe the properties of the tungsten bronzes and predict the value of the critical concentration x_C. A quick summary of the results is given by Doumerc *et al.*[74] Using site percolation with first, second and third nearest neighbour percolation paths, Lightsey[54] obtained a value of $x_C = 0.16 \pm 0.03$ for Na_xWO_3. This is surprisingly close to the experimental estimate $x_C \simeq 0.18$. Likalter[71] used a microscopic percolation model and estimated $x_C \simeq 0.08$ for Na_xWO_3. This is close to the value $x_C \simeq 0.1$ obtained by Dücker *et al.*[52] using the Anderson model. It is noted that percolation theories also predict Eq. 2.15 near the critical concentration, with the critical exponent in the range 1.5 – 2.5.[70] Holcomb[70] has proposed experiments on selected transition metal oxides to check for the appropriateness of using percolation ideas to supplement other models.

2.3 The Anderson–Mott–Hubbard model

An extensive theoretical study relating to the MI transition in the cubic tungsten bronzes Na_xWO_3 and $Na_xTa_yW_{1-y}O_3$ has been presented by Dűcker *et al*.[9,52] The Anderson–Mott–Hubbard model Hamiltonian for the tungsten bronze M_xWO_3, which allows for the effects of band structure, disorder and e–e interactions, is taken as

$$\hat{H} = \sum_{i,\mu} \varepsilon_{0i} \hat{n}_{i\mu} + \sum_{i\,j,\mu} t_{ij} \hat{c}^{\dagger}_{i\mu} \hat{c}_{j\mu} + \sum_{i,\mu} V_{Ci} \hat{n}_{i\mu} + \frac{1}{2} U \sum_{i,\mu} \hat{n}_{i\mu} \hat{n}_{i-\mu} \quad . \qquad 2.16$$

The first two terms represent the tight–binding Hamiltonian for the WO_3 periodic lattice shown in Eq. 2.3. The transfer integral tij arising from the orbital overlap is only considered for nearest–neighbour W and O sites. The first two terms lead to the usual tight–binding band structure of crystalline materials with the Bloch states as solutions, as discussed in §2.2.

The effects of disorder are incorporated into the third term of Eq. 2.16. The disorder arises from the random distribution of the donor ions at interstitial sites. The positive charge on the donor cation results in an attractive potential causing a lowering of the neighbouring W and O site energies ε_{0i}. The term $V_{Ci} = N_i V_C$ gives the energy shift at site i due to the random number N_i of neighbouring donor cations. The shift per donor ion was taken as $V_C = -0.3$ eV corresponding to the binding energy of a Coulombic donor in WO_3. The first three terms in Eq. 2.16 (letting $U = 0$ in the Hamiltonian) therefore resemble the Anderson model Hamiltonian in Eq. 2.13, with the energy $\varepsilon_i = \varepsilon_{0i} + V_{Ci}$. Disorder appears in the randomly valued Coulomb term V_{Ci}. In $Na_xTa_yW_{1-y}O_3$ the random substitution of W by Ta leads to additional disorder in both the energies ε_{0i} and t_{ij} (i.e. diagonal and off–diagonal disorder). The Ta 5*d* states lie at a higher energy than the W 5*d* states. Ta supplies additional scattering centres, accounting for the reduced conductivity of $Na_xTa_yW_{1-y}O_3$ relative to Na_xWO_3.[7]

Electron–electron interactions are included using a Hubbard U (Eq. 2.6) that is treated as a parameter ($0 \leq U \leq 10$ eV) in the unrestricted Hartree–Fock numerical calculations used to obtain the conduction band DOS and localization properties of the model system. Since W t_{2g} and O 2*p* orbitals lying in a plane are coupled, the conduction band states are

essentially 2D in character, and this feature is used in the model. The Hamiltonian in Eq. 2.16 does not allow for single–particle solutions due to the two–particle operator $\hat{n}_{i\mu}\hat{n}_{i-\mu}$. The unrestricted Hartree–Fock approach effectively replaces $\hat{n}_{i-\mu}$ by its expectation value $\langle \hat{n}_{i-\mu} \rangle$, and reduces the Hamiltonian into two coupled additive one–particle operators ($\hat{H} = \hat{H}_{\uparrow} + \hat{H}_{\downarrow}$). The Hamiltonians $\hat{H}_{\uparrow}$ and $\hat{H}_{\downarrow}$ are then solved self–consistently by matrix diagonalization for the single–particle DOS. Fig. 2-12 gives the results for a range of concentrations using U = 6.5 eV and V_C = –0.3 eV.

The results of Dücker *et al.* show that for small interaction strengths (U < 5 eV) the effects of the disorder on the single–particle DOS are to broaden the band and round van Hove singularities. No gap or pseudogap is found to arise for any x. The band tail states are strongly localised by disorder, with a crossover to extended states for higher energies (i.e. a mobility edge is formed). The picture is that of the Anderson transition discussed in §2.2.2 (corresponding to U = 0). The MI transition is found to occur for $x \simeq 0.1$.

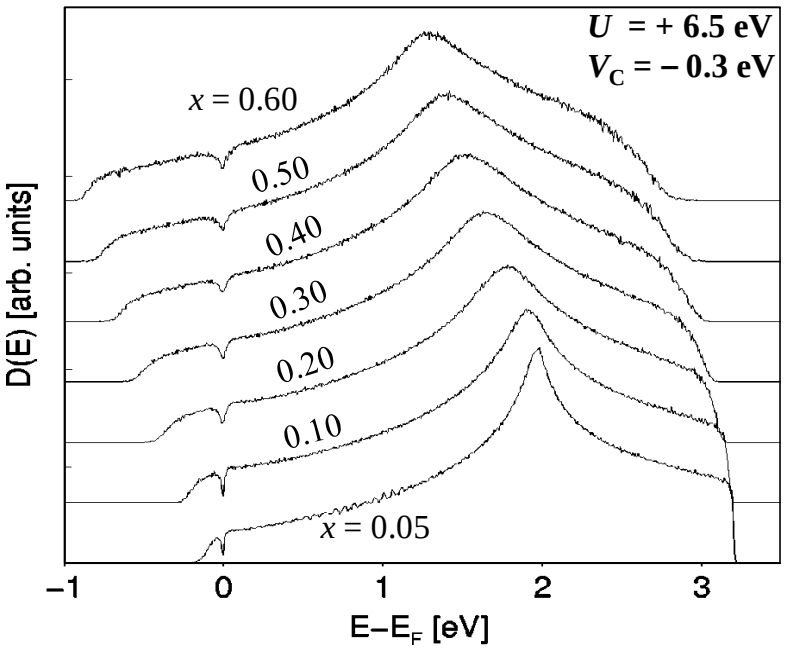

Fig. 2-12. The conduction band density of states obtained from the 2D Anderson-Mott-Hubbard model for Na_xWO_3. (Reproduced from Ref. 9.)

For sufficiently large e–e interactions ($U > 5$eV) a pseudogap in the DOS is found at the Fermi energy E_F for all x considered (see Fig. 2-12). The pseudogap evolves with increasing U (broadening and deepening) and is associated with the localization properties of the system. The results are in semi–quantitative agreement with experimental tunnelling conductance measurements.[10] The microscopic origin of the pseudogap is attributed to antiferromagnetic electron correlations that give rise to repulsion between occupied states and unoccupied states on either side of E_F.

The effects of disorder are shown to lead to increased electron interactions in localized single particle states. By considering $Na_xTa_yW_{1-y}O_3$, in which disorder effects are increased by the random distribution of Ta on W sites, it is confirmed that localization effects are enhanced by disorder. It is, however, concluded that interactions are of dominant importance in determining the critical concentration for the MI transition. The details of the disorder are found to be relatively unimportant, with the local charges essentially screening the disorder.

An important prediction of the model is that strongly localized states near the lower conduction band edge are essentially 2D. Similarly states in the pseudogap are strongly 2D with the existence of strongly localized states in the vicinity of E_F. These findings are used to account for the observed Friedman anomaly in the temperature dependent Na_xWO_3 Hall effect measurements (Fig. 2-4) in terms of localization of states in the pseudogap. Extended states close to E_F are populated as T is increased, leading to an increase in the Hall concentration.

The value of $U = 6.5$ eV is stated as being the most relevant for the tungsten bronzes. For this interaction strength the critical concentration is found to occur for $x_C \simeq 0.3$, larger than the experimental value $x_C \lesssim 0.2$. The discrepancy may be accounted for by including screening effects, invoking a U which depends on x (with $U \rightarrow 0$ as $x \rightarrow 1$ due to increased screening effects). The important point is that the e–e interactions are shown to increase the critical concentration from the non–interacting Anderson model value of $x_C \simeq 0.1$. The correlation effects also account for the pseudogap and temperature dependent Hall concentration observed in the tungsten bronzes.

2.4 The metal–insulator transition in the tungsten bronzes

Correlation effects are essential to understanding the properties of the tungsten bronzes near the MI transition. The Coulomb interactions in the tungsten bronzes are stronger (larger Hubbard U) compared to doped semiconductors which have low concentrations near n_C and large Bohr radii (~10^{18} cm^{-3} and ~17 Å for SiP)[3]. The tungsten bronzes have an inter–particle separation of the order of the lattice spacing (~3.8 Å) and electron concentrations ~10^{21} cm^{-3}. The high electron densities and low conductivity ($\sigma \ll \sigma_{min}$ near x_C) point to a low diffusivity (see Eq. 2.2) which is expected to enhance correlation effects. Combined with disorder, as in the Anderson–Mott–Hubbard model of the previous section, e–e interactions have a pronounced effect on the compound near x_C. This is manifested in physical properties such as photoelectron spectroscopy, tunnelling conductance and electrical conductivity.

Photoelectron spectroscopy investigates the band structure of materials, and hence probes the electronic DOS. High–resolution electron spectroscopy on polycrystalline Na_xWO_3 shows evidence for the formation of a pseudogap at E_F for lower x samples. The pseudogap disappears as $x \rightarrow 1$.[45] High–resolution angle–resolved photoemission spectroscopy (ARPES) on an insulating sample of single–crystal orthorhombic $Na_{0.025}WO_3$ shows no DOS at E_F, with the states near E_F localized.[12] Photoelectron spectroscopy studies on single crystal Na_xWO_3 and $Na_xTa_yW_{1-y}O_3$ near the MI transition show no detectable DOS at E_F for low concentrations ($Na_{0.1}WO_3$ and $Na_{0.25}Ta_{0.20}W_{0.8}O_3$).[82] Higher concentrations show a finite DOS at E_F within a pseudogap. The suggestion of Coulomb gap formation in the insulating samples was later supported by calculations of the DOS for a classical model of $Na_xTa_yW_{1-y}O_3$.[11] The long–range Coulomb interactions are shown to account for the experimental features.

Tunnelling conductance measurements at low temperatures ($T \leq 4.2$ K) have been performed on single crystals of Na_xWO_3 and $Na_xTa_yW_{1-y}O_3$ ($x - y$ = 0.18, 0.3, 0.5 and 0.6).[10,83] The tunnelling conductance $G(V)$ at low voltages (V) is generally assumed to be a measure of the single–particle DOS. The results show a depletion in the DOS at E_F for all samples investigated with $G(V)$ given by

$$G(V) = G_0\left(1 + \left|V / V_0\right|^k\right) \ . \qquad 2.17$$

The dip in $G(V)$ becomes weaker with increasing x, consistent with the disappearance of the pseudogap as $x \rightarrow 1$ observed by photoemmision spectroscopy.[45,83] The dip is also found in $Na_{0.6}WO_3$. The pseudogap is therefore evident in large x samples where rigid–band theory is found to be succesfull. For this $x = 0.06$ sample the exponent $k \simeq 0.5$, consistent with the square–root–cusp prediction in the weak–localization region for correlated systems (see Eq. 2.9, with $V \equiv E - E_F$). As the MI transition is approached from the metallic side the tunnelling exponent increases from 1/2 to 1, and the pseudogap becomes deeper ($G_0 \rightarrow 0$). It eventually forms a Coulomb gap in the insulating region (with $k = 2$ and $G_0 = 0$, but $G_0/V_0^k \neq 0$).

The photoemission spectroscopy and tunnelling conductance studies therefore show clear evidence for the depletion of the DOS at the Fermi energy, both in metallic (forming a pseudogap) and insulating samples (forming a Coulomb gap). Evident are the signatures of e–e interactions in the tungsten bronzes near the MI transition. The formation of a pseudogap in the DOS at E_F for barely metallic and insulating samples of $Na_xTa_yW_{1-y}O_3$ is also suggested by NMR investigations.[77]

In the metallic phase, disordered solids with strong e–e interactions can show a low temperature $T^{1/2}$ contribution to $\sigma(T)$ as in Eq. 2.10. It is standard to fit the low T conductivity data in the metallic phase with the expression

$$\sigma(T) = \sigma_0 + \alpha T^m \qquad 2.18$$

where α is a constant and the exponent m is treated as a parameter. This expression is often used to determine the residual conductivity σ_0. The exponent is expected to change from $m = 1/2$ as the MI transition is approached (as is observed in the tunnelling exponent k above). In Ge:Ga, for example, the $T^{1/2}$ dependence becomes a $T^{1/3}$ dependence as $n \rightarrow n_C$.[69] Similar behaviour is observed in metallic samples of boron–doped diamond and some of the transition metal oxides.[4,72] The $T^{1/3}$ dependence is consistent with theory for disordered interacting systems in the critical region.[7]

At sufficiently low temperatures in insulating samples transport occurs between distinct localized states and can be described by the hopping law expression

$$\sigma(T) \propto \exp\left[-(T_0 / T)^p\right] \qquad 2.19$$

where T_0 is a characteristic temperature scaling inversely with the localization length, and p is the hopping exponent, treated as a parameter. For variable–range hopping p = 1/4 (Mott) or p = 1/2 (Efros–Shklovskii, which occurs for correlated systems as in Eq. 2.8). For activated conduction p = 1 with $k_B T_0 = \Delta E$, the activation energy. The exponent p is therefore an indicator of the type of system investigated. In Ge:Ga, for example, p = 1/2 for $n < n_C$, indicating correlated hopping conduction, with p decreasing rapidly as $n \rightarrow n_C$ due to the collapse of the Coulomb gap.[69] A change from p = 1/2 to p = 1/4 as T is increased is also observed in boron–doped diamond and boron–doped silicon, signifying a change from a low temperature Efros–Shklovskii hopping to a high temperature Mott hopping conduction.[72, 84]

Direct evidence for the MI transition in the tungsten bronzes comes from $Na_xTa_yW_{1-y}O_3$ in which the structural transition is suppressed and the doping degree is $x - y$ (= x_{eff}). Strong interaction effects are evident in the temperature dependence of the conductivity in both insulating and metallic samples. Fig. 2-13 shows the conductivity for two samples of $Na_xTa_yW_{1-y}O_3$ on either side of the MI transition for 0.4 K < T < 300 K.[7] (These samples are from the same batch as shown in Fig. 2-7.) The just–metallic sample of $Na_{0.35}Ta_{0.16}W_{0.84}O_3$ ($x - y \simeq 0.19$) in Fig. 2-13 shows a low T conductivity $\sigma(T) = \sigma_0 + \alpha T^{1/3}$ ($\sigma_0 \sim 6$ S/cm $\ll \sigma_{min} \sim 250$ S/cm). This corresponds to the form in Eq. 2.18 with the exponent m = 1/3, and is consistent with metallic behaviour in the critical region, as discussed above. The insulating sample of $Na_{0.34}Ta_{0.16}W_{0.84}O_3$ ($x - y \simeq 0.18$) in Fig. 2-13 shows the low T hopping relation in Eq. 2.19 with T_0 = 50 K and $p \simeq 0.42$. The value of p is close to the Efros–Shklovskii value p = 1/2. A plot of log σ vs $T^{-1/2}$ gives a good linear form for T < 4 K ($\ll T_0$ as it should be for Eq. 2.19 to be valid). This conductivity indicates hopping controlled by correlation effects, and also suggests that a Coulomb gap opens up in the single–particle density of states. This would be consistent with the tunnelling conductance and photoemission results.

Two of the insulating samples of $Na_{0.34}Ta_{0.16}W_{0.84}O_3$ showed a $\sigma(T) \propto T^m$ behaviour with m = 1.24 and 1.55 respectively.[7] A $\sigma(T) \propto T$ behaviour (m = 1) was observed on the whole temperature range (1.6 K < T < 300 K) for the $Na_{0.34}Ta_{0.16}W_{0.84}O_3$ sample in Fig. 2-7.[8] From Eq. 2.18 this behaviour implies $\sigma_0 = 0$ (i.e at the critical concentration). It should be noted that very close to the critical concentration small fluctuations in the sample composition can have pronounced effects on the conductivity behaviour. This would account for the different behaviour found in the various samples of $Na_xTa_yW_{1-y}O_3$ for $x - y$ = 0.18. The larger values of m ($m \gtrsim 1$ compared to the values $m \sim 1/2$ and 1/3 discussed above) have been observed in just–metallic samples of other transition metal oxides.[4] The $Na_xTa_yW_{1-y}O_3$ samples with $x - y = 0.18$ therefore appear to be very near the MI transition. It has been mentioned[7] that for these samples the hopping relationship in Eq. 2.19 may occur at even lower temperatures, with T_0 lower than for the sample shown in Fig. 2-13 ($T_0 \rightarrow 0$ as $x \rightarrow x_C$ from the insulating side). For T > 2 K the sample in Fig. 2-13 has $\sigma(T) \propto T^m$ with $m \simeq 1.2$, similar to the other samples with this concentration. The classification of the $x - y = 0.18$ samples as being just–insulating therefore appears to be reasonable.

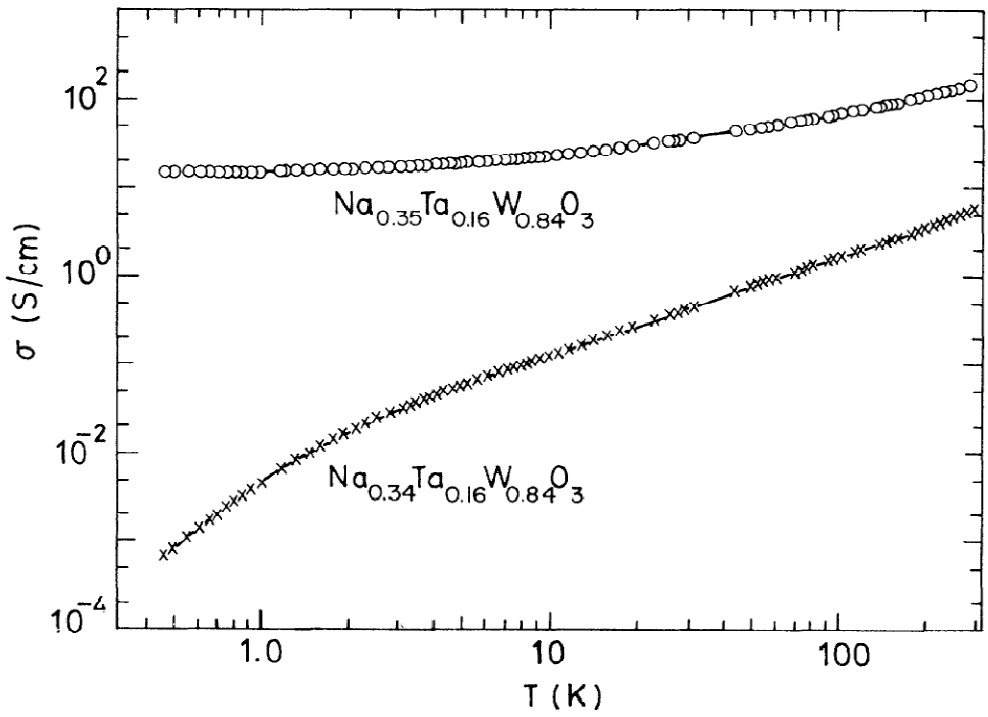

Fig. 2-13. The conductivity of a just-metallic ($x - y$ = 0.19) and just-insulating ($x - y$ = 0.18) sample of $Na_xTa_yW_{1-y}O_3$. (Reproduced from Ref. 7.)

2.5 The yttrium and lanthanum tungsten bronzes

This chapter concludes with a brief summary of previous results on Y_xWO_3 and La_xWO_3. Very little research has been done on these two compounds. The results do suggest, however, that they have properties similar to the other tungsten bronzes.

The first report on the yttrium and lanthanum tungsten bronzes was presented by Broyde[22] in 1967, and that recipe was used to produce the samples in this research. Powders of W metal, WO_3, and the metal oxide (La_2O_3 or Y_2O_3) were mixed, pelletized, and sealed in quartz tubes under 5×10^{-4} torr. The tubes were heated at 1100°C for 72 hr, and then cooled under ambient conditions (taking ~20 min). Homogeneous cubic perovskite structures were found for Y_xWO_3 ($0.09 \leq x \leq 0.15$) and La_xWO_3 ($0.08 \leq x \leq 0.19$). The lattice parameters for La_xWO_3 increased in a non–linear manner with x from 3.829 to 3.845 Å, while for Y_xWO_3 they varied from 3.800 to 3.815 Å. (All other tungsten bronzes, including the La_xWO_3 and Y_xWO_3 samples studied here, do suggest a linear behaviour for the lattice parameter.) For lower x an additional tetragonal structure appeared, having the same lattice parameters in both compounds, indicating similar structural evolution as $x \rightarrow 0$. No additional compounds appeared. For higher x, La tungstate and WO_2 appeared in La_xWO_3, consistent with a solubility limit. Y_xWO_3 was unusual in that no yttrium tungstate was observed up to $x = 0.2$, with only WO_2 present. The colours of La_xWO_3 were green ($x = 0.02$), blue ($x = 0.10$), and red–purple ($x = 0.19$), varying in a similar way to other tungsten bronzes.

In the same year, Shanks and Danielson[23] produced single crystals of $Y_{0.1}WO_3$ and $La_{0.1}WO_3$, grown by electrolysis at 1000°C. The resulting samples were blue–black cubes with sides $\lesssim$ 1 mm. XRD results showed a single phase cubic structure with lattice constants a_Y = 3.800 Å and a_{La} = 3.835 Å, consistent with the results of Broyde[22]. Resistivity measurements suggested both compounds to be metallic (Fig. 2-6.), with resistivity coefficients typical of cubic tungsten bronzes.

Powder neutron diffraction studies were performed by Wiseman and Dickens[25] on $La_{0.14}WO_3$. The samples were prepared by solid state reaction resulting in a blue–violet product. XRD showed a pure cubic phase with lattice constant a = 3.833 Å. The neutron diffraction results showed $La_{0.14}WO_3$ had a simple cubic perovskite structure, with no tilt

of WO_6 octahedra, and the random distribution of the donor La atoms was confirmed. The other cubic tungsten bronzes investigated ($Na_{0.54}WO_3$, $Na_{0.73}WO_3$, and $Li_{0.36}WO_3$) did show slight tilting of the WO_6 octahedra.

Rare earth tungsten bronzes, including La_xWO_3, were investigated for $0.1 \leq x \leq 0.3$ by Grenthe and Sundberg[24] using powder XRD, electron diffraction and high–resolution TEM. Samples were formed by conventional solid state synthesis of the rare earth oxide, WO_3 and W. The samples were dark blue to black with a metallic lustre. Samples with $x \leq 0.15$ appeared single cubic phase, with a lattice constant $a \sim 3.8$ Å, apart from a small amount of WO_3. (The appearance of WO_3 is most likely a result of incomplete reaction due to the shorter heating times.) For $x > 0.15$ rare–earth tungstate and WO_2 was detected, increasing with x, and consistent with results for other tungsten bronzes above the solubility limit. The location of the La^{3+} ions was in the interstices of the WO_3 structure with a random distribution. An increase in rare–earth content decreased the oxidation state of tungsten, consistent with the transfer of valence electrons to the predominantly W 5*d* conduction band. Further structural and compositional research on lanthanum tungsten bronzes by Grenthe *et al.*[85] and Filonenko *et al.*[86] involved the formation of non–perovskite compounds under high pressure.

As is evident, there is a lack of experimental research on the perovskite yttrium and lanthanum tungsten bronzes. Most of the research has focussed on the structural aspects with no systematic investigations of the electric transport properties. The research here is therefore important in providing further information on the behaviour of these two compounds, and expands the knowledge base of the tungsten bronzes.

Chapter 3: Sample preparation and characterisation

This chapter describes the preparation and characterisation of the Y_xWO_3 and La_xWO_3 tungsten bronze samples. Extensive characterisation was performed to ensure a good sequence of homogeneous tungsten bronze samples suitable for the low temperature investigations. The first section (§3.1) presents the details of the sample preparation. The second section (§3.2) gives a description of the characterisation experiments and presents the data obtained. The last section (§3.3) gives a brief discussion of the results, with comparison to other tungsten bronzes, in order to establish that the material prepared is of the required quality.

3.1 Sample preparation

The solid state reaction used for the preparation of Y_xWO_3 and La_xWO_3 ($0 \leq x \leq 1$) is given by[22]

$$\left(\frac{x}{2}\right)M_2O_3 + \left(\frac{x}{2}\right)W + \left(1-\frac{x}{2}\right)WO_3 \rightarrow M_xWO_3 \qquad 3.1$$

where M = Y or La. The reaction equations differ only in the use of the donor-metal oxides Y_2O_3 and La_2O_3. The recipe presented by Broyde[22] was used. The reactants, obtained from Cerac Incorporated (La_2O_3: 99.999%, ~325 mesh, W: 99.95%, ~1 μm, and WO_3: 99.99%, ~325 mesh) and H.C. Starck (Y_2O_3: Grade C, purity 99.95%, size ~1 μm), were passed through a 32 μm sieve before use. These particle sizes appeared too large for pellet production, and further grinding in the mortar during the mixing of the reactant powders was required. The masses of the starting powders are determined from Eq. 3.1 above. The density of the Y_xWO_3 and La_xWO_3 crystal (in g/cm^3), based on the perovskite structure in Fig. 2-1, is

$$\rho_{Y_xWO_3}(x) = \frac{231.85 + 88.91x}{0.602\ a(x)^3} \qquad \rho_{La_xWO_3}(x) = \frac{231.85 + 138.91x}{0.602\ a(x)^3} \qquad 3.2$$

where $a(x)$ is the cubic lattice constant in units of Angstrom.

The mixed reactant powders were pelletized in a 13 mm die (Lightpath Optical Company Ltd.) at 6 tons using a hydraulic press. Although the die had a working pressure of 10 tons, this load produced pellets with flakes and cracks. Samples were produced in batches of 5 g, creating 3 to 4 pellets of about 2 mm thickness. The pellets were placed in quartz tubes (20 mm OD; 1.5 mm thickness; length ~140 mm) that were then outgassed under vacuum at 300°C for 30 min (Y_xWO_3) and 40 min (La_xWO_3), followed by evacuation to below 10^{-5} torr before sealing. The additional 10 min required for La_xWO_3 is attributed to the outgassing of the hygroscopic pellets (see below). Sintering was carried out in a programmable Carbolite STF1500 tube furnace at 1100°C for 72 h. The temperature stability and gradients across the ampoules are estimated to be ~10°C. (The temperature profile of the furnace is shown in Fig. E-4 of appendix E.) A ramp rate of 300°C/hr was used for the heating and cooling cycles. The cooling rate was a restriction on the furnace control, and this was the only deviation from the Broyde recipe where the ampoules were cooled under ambient conditions, taking about 20 min. All the pellets from a single batch were placed in the same ampoule to ensure homogeneity and compositional integrity.

The samples have a range of x values ($0.05 \leq x_Y \leq 0.2$ and $0.05 \leq x_{La} \leq 0.23$) that includes the cubic perovskite phase.[22] The sintered samples were typical of the tungsten bronzes, with a bluish-black appearance. The Y_xWO_3 and La_xWO_3 samples were optically indistinguishable for the same x value. The low x material had a navy-blue colour, which darkened as x increased, and eventually became deep violet for the highest concentrations (for La_xWO_3). The lustre also increased with x showing the higher donor concentrations to be more metallic as expected. The colour changes are similar to those of Na_xWO_3 for x in the range of ~0.3 – ~0.7,[16] corresponding to a similar donor electron concentration range. (The effective carrier concentration for the trivalent Y_xWO_3 and La_xWO_3 tungsten bronzes is $3x$ per W.) The uniform colour of the samples is a good indication of sample homogeneity, consistent with the complete reaction of the starting materials (which is confirmed by the powder XRD results). A significant hardening occurs for both the La_xWO_3 and Y_xWO_3 samples with increasing x. An expansion of ~15% in the linear dimensions was found following the sintering, with slight warping of some pellets. Following sintering, all of the samples were stable and showed no changes in physical

properties with time. No post-sintering procedures were performed, such as the washing, re-grinding and re-heating done in the production of some other tungsten bronzes.[24,30,56,57]

Grain size analysis was performed using a JEOL – JSM 840 scanning electron microscope (SEM). Two SEM images are shown in Fig. 3-1, indicating a variety of grain structures for both Y_xWO_3 and La_xWO_3, with grain sizes ~10 μm. The SEM pictures show a similar polycrystalline structure for both compounds, as expected from the similar production methods, and the fact that Y and La are in the same group of the periodic table having similar chemical properties. The formation of rods is observed in some samples, clearly evident in Fig. 3-1a. $Na_{0.3}WO_3$ nanorods have recently been synthesized and investigated.[87] (X-ray microscopy results are shown in Fig. E-2 of appendix E.)

La_2O_3 powder is hygroscopic (see Fig. E-3 in appendix E), and this property produced some difficulties in La_xWO_3 sample production. Measurable expansion is observed in pre-sintered pellets when exposed to air for several hours, and this process can eventually lead to disintegration back into powder form. Y_2O_3 is not hygroscopic and hence this was not a problem for Y_xWO_3 production. To minimize moisture uptake during the La_xWO_3 production, the pellets were kept under vacuum prior to sintering. Exposure of the starting La_2O_3 powder to air was also minimised, as the H_2O absorption would create uncertainties in the actual mass of La_2O_3 (and hence x) in Eq. 3.1. As indicated in Fig. E-3, significant H_2O absorption only occurs for exposure times of several hours. The reduction in x due to the hygroscopic nature of La_2O_3 should therefore be minimal. For samples with high x values, the hygroscopic swelling effect becomes more pronounced due to the higher La_2O_3 content. This complicated good sample production above $x = 0.19$. While the absorbed moisture was driven off during outgassing, the pellets with $x = 0.21$ and $x = 0.23$ disintegrated back into powder form inside the ampoules during handling. For these two concentrations, soft sintered-powder blocks emerged after heating to 1100°C, and only XRD measurements were made on these samples to determine structural information.

Whiskers were formed in some cases, with colours similar to the sample colours, suggesting that these are tungsten bronze whiskers. For La_xWO_3 at the lowest concentrations ($x \leq 0.080$), soft, hairlike navy-blue whiskers appeared on some pellets, and harder whisker "nests" appeared at the bottom of the quartz tubes. For the larger concentrations, violet hairlike whiskers appeared on a few pellets. For the Y_xWO_3 samples,

(a) $Y_{0.104}WO_3$

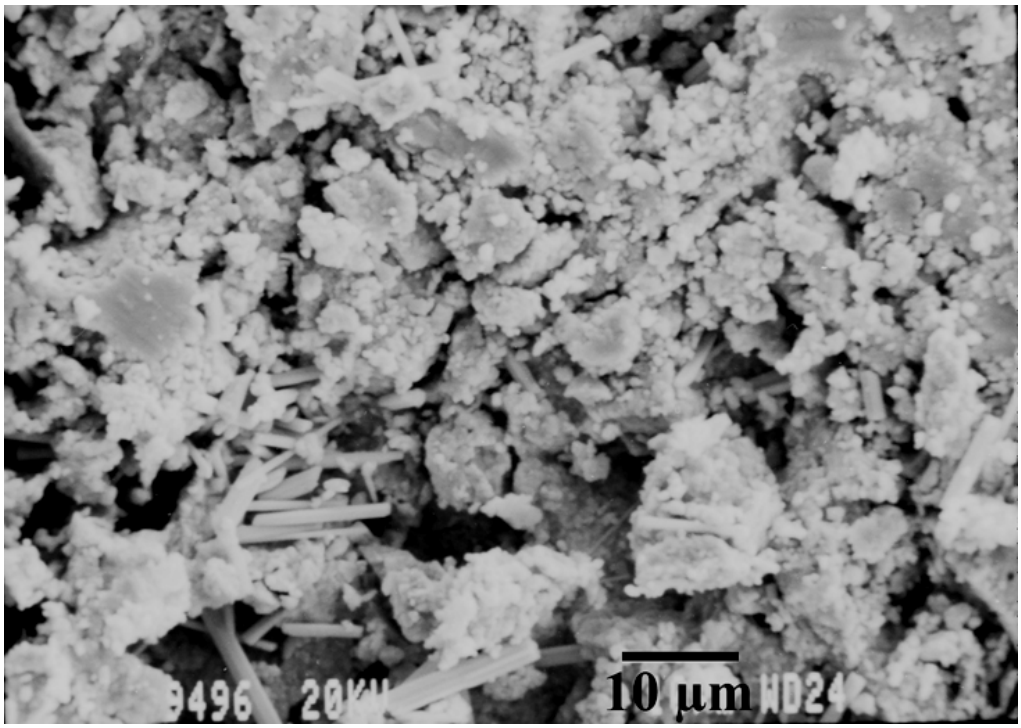

(b) $La_{0.100}WO_3$

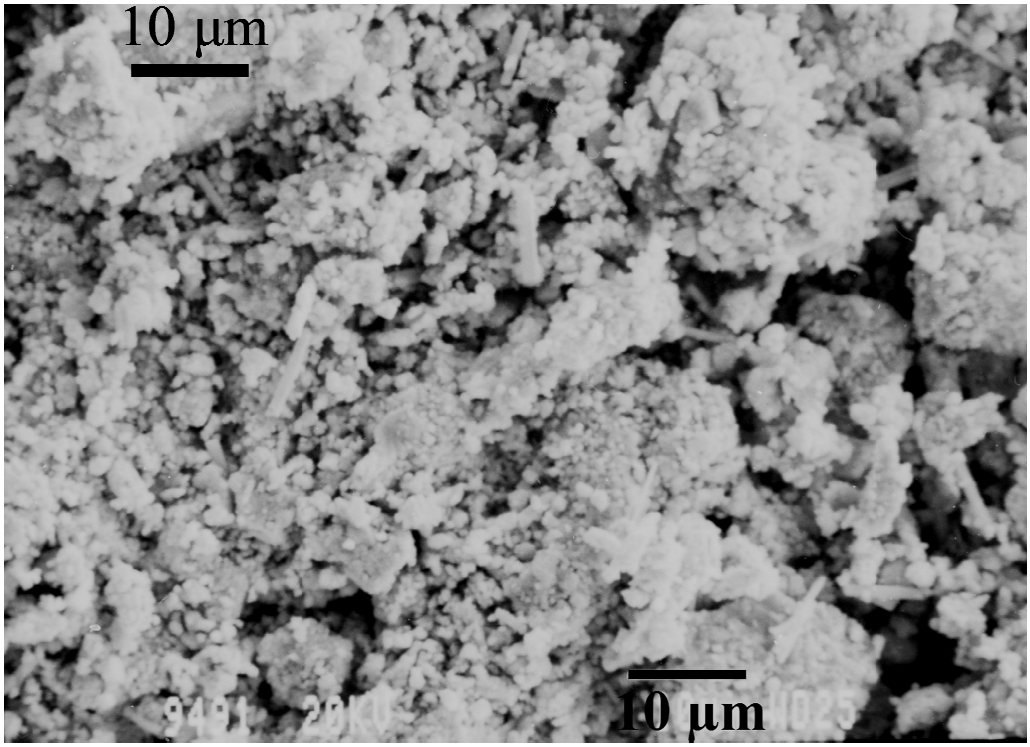

Fig. 3-1. Scanning electron microscope images of Y_xWO_3 and La_xWO_3 samples.

whisker formation was also present for some of the lower concentration samples ($x \leq 0.091$). Whisker-like formations also appear on Na_xWO_3 when sintering above 930°C.[77] Structural investigations have been reported on single crystal $K_{0.4}WO_3$ whiskers grown at 360°C through a hydrothermal reaction.[39] Fine golden metallic particles were observed on some of the higher concentration samples ($x_Y \geq 0.14$ and $x_{La} = 0.23$). These could be high-concentration tungsten bronze particles, with colours similar to high-x Na_xWO_3. There was some evidence of a local reaction between the pellets and the quartz tubes at the points of contact for both the Y_xWO_3 and La_xWO_3 samples. This is also observed with the sodium tungsten bronzes.[16,37,77] All the quartz ampoules for La_xWO_3 production also showed blue-white film-like deposits on nearly the whole interior after sintering. For Y_xWO_3 the quartz ampoules were clear after sintering.

The ampoule deposits for La_xWO_3 and whisker formations may introduce small compositional uncertainties in the samples, and hence possible shifts in the intended x values. For Y_xWO_3 the anomalies were of such low mass that the sample composition should be very close to the nominal values. Previous investigations have shown that for homogeneous products the nominal x values obtained from the starting composition are close to values obtained by analytical methods.[25] Comparison of the XRD and diffuse reflectance results for the two compounds suggest that the possible shifts in x for La_xWO_3 are not significantly large, with the nominal x close to the actual composition. Comparison of the Y_xWO_3 and La_xWO_3 resistivity results suggests that the actual x for the La_xWO_3 samples could be up to 0.005 below the nominal value. Collectively the results show an uncertainty Δx not more than 0.01.

3.2 Experimental

The following experiments were performed to characterise the samples:

- Powder XRD measurements were performed at room temperature to determine the crystal structure and cubic lattice constant. Measurements at 110 K were done on a few Y_xWO_3 samples to check for structural stability, and also allowed for the determination of the average thermal expansion coefficient. After visual inspection (of homogeneity for example), the powder XRD and room temperature resistivity were the first tools used for checking the samples.

- The mass density for known geometries was calculated from which the crystal volume fraction could be determined. This was required to explain some anomalies encountered in other results, particularly room temperature resistivity results for La_xWO_3.

- Diffuse reflectance measurements were done at room temperature. Reflectivity is strongly dependent on *x*, as evident from the colour chnges in the tungsten bronzes. Comparison between Y_xWO_3 and La_xWO_3 results suggest that the nominal *x* used for La_xWO_3 appears valid (referring to the quartz deposits for La_xWO_3 production mentioned in the previous section).

- Resistivity measurements were done from room temperatures down to 64 K. The results show a dependence on *x* and *T* that is typical of other bronzes, and confirms the samples to be a suitable sequence of tungsten bronze compounds. These measurements were also used to test and refine the functioning of the transport station prior to the low temperature measurements.

- Hall effect measurements were done at room temperature to obtain the *x* dependence of the Hall concentration.

3.2.1 Powder x-ray diffraction

Powder XRD patterns were obtained for all the Y_xWO_3 and La_xWO_3 samples at room temperature using a Philips diffractometer with Cu Kα radiation (λ = 1.54 Å). Some XRD measurements were performed on Y_xWO_3 samples at 110 K (using a cold-finger with liquid nitrogen) to check for possible temperature induced phase changes, as is observed for WO_3.[41] Expansion coefficient values for the cubic phase of Y_xWO_3 were obtained from these measurements.

Room temperature powder XRD traces are shown in Fig. 3-2 for Y_xWO_3 and Fig. 3-3 for La_xWO_3. The lowest concentration results are shown in Fig. 3-2a and Fig. 3-3a, while the highest concentration results are shown in Fig. 3-2b and Fig. 3-3b. Intermediate concentrations ($0.091 < x_Y < 0.132$ and $0.086 < x_{La} < 0.150$) have single-phase cubic perovskite XRD spectra similar to that of $x_Y = 0.091$ in Fig. 3-2a and $x_{La} = 0.086$ in

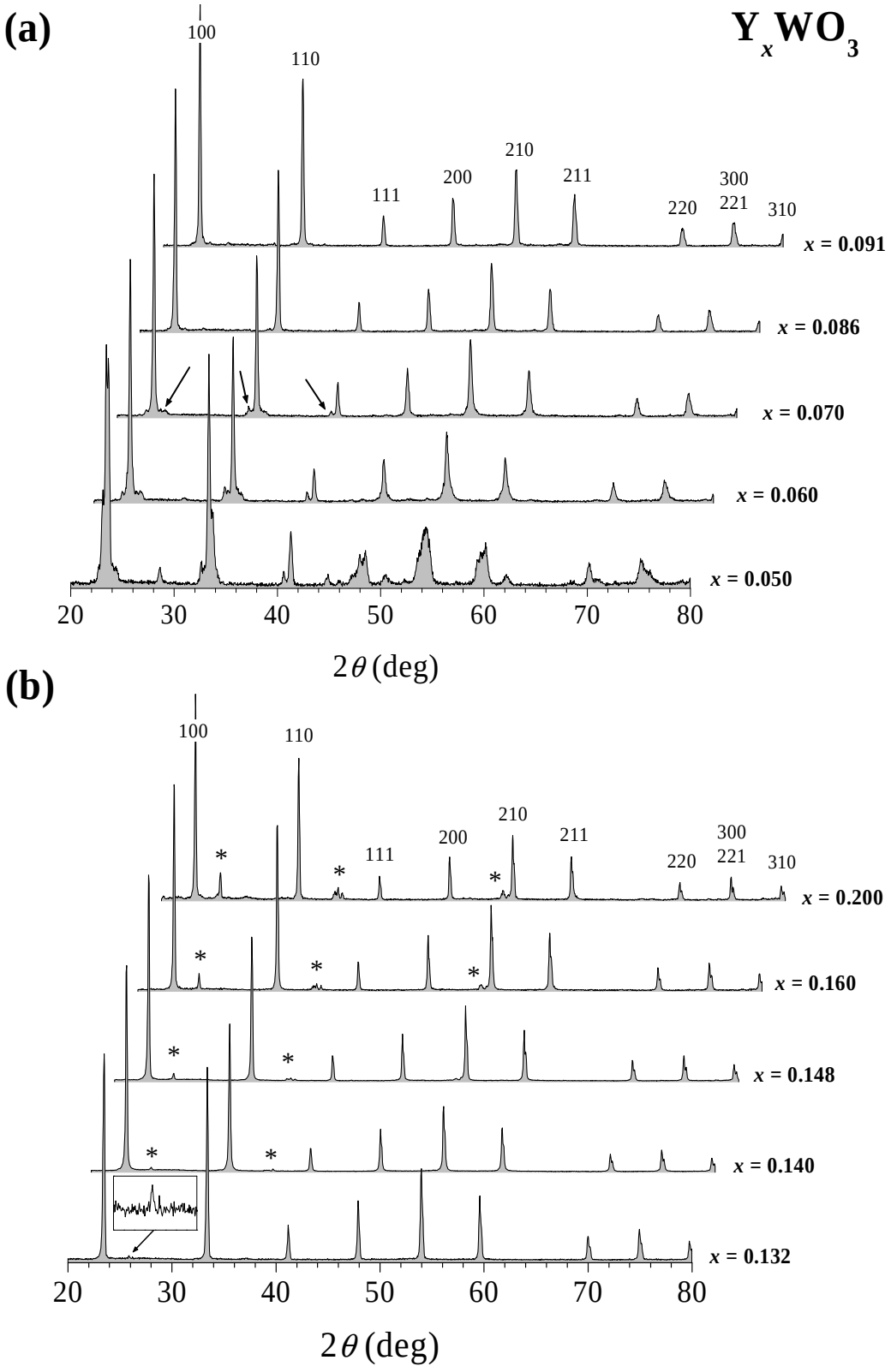

Fig. 3-2. Powder XRD results for the lowest and highest concentration Y_xWO_3 samples. The cubic phase peaks are labelled by their Miller indices. The onset of additional phases with decreasing x is indicated by the arrows for x = 0.070 in (a). The evolution of some additional peaks is indicated by * and the expanded view for x = 0.132 in (b).

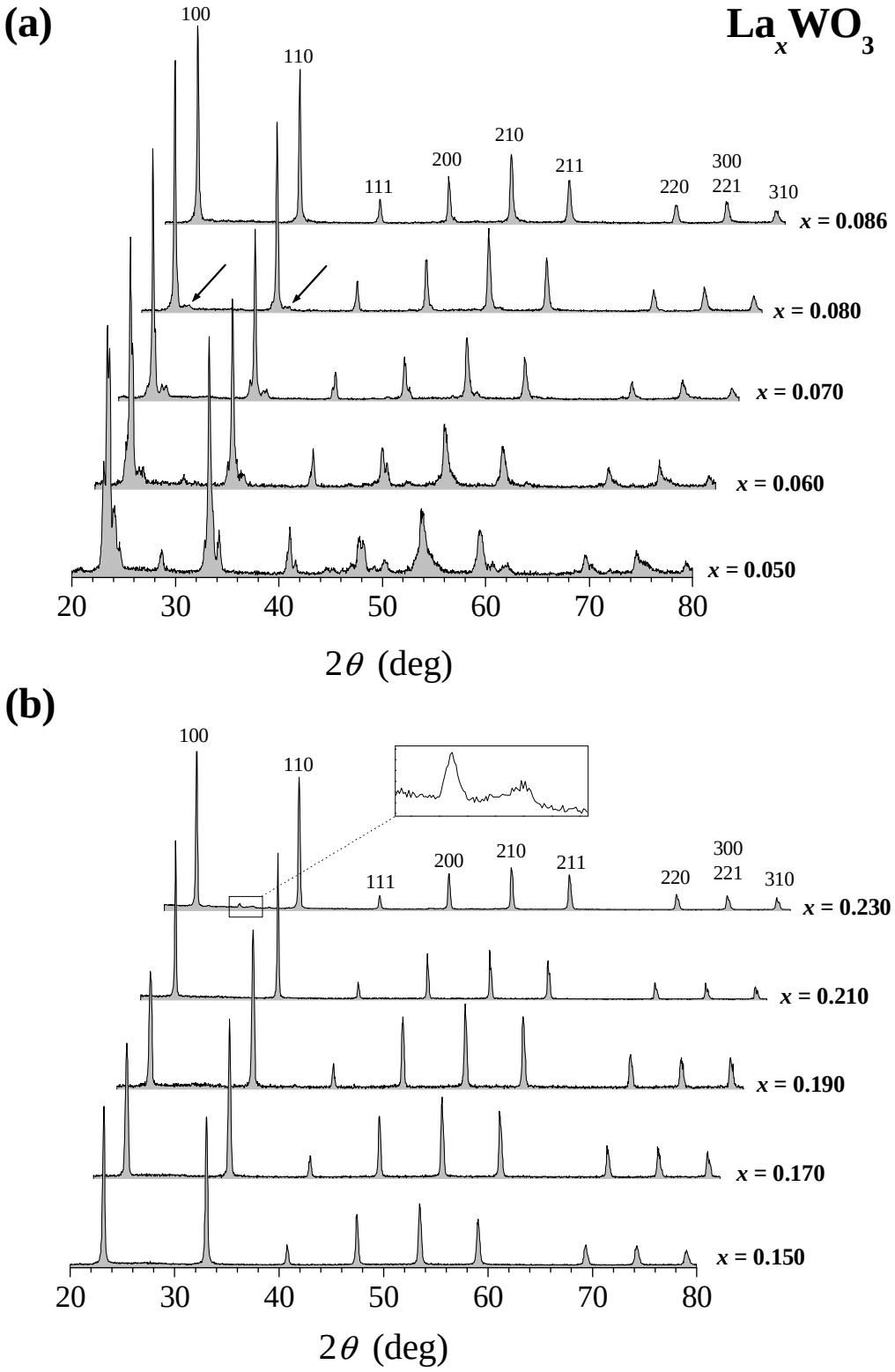

Fig. 3-3. Powder XRD results for the lowest and highest concentration La_xWO_3 samples. The cubic phase peaks are labelled by their Miller indices. The onset of additional phases with decreasing *x* is indicated by the arrows for *x* = 0.080 in (a). The appearance of additional peaks in (b) is detected only for *x* = 0.23, and the inset shows two of these peaks on an expanded scale.

Fig. 3-3a. (See Fig. E-1 in appendix E for these XRD results.) Miller indices for the cubic phase peaks are shown in the figures, as well as indications to the appearance of additional phases.

Lattice constants for the cubic phase of the Y_xWO_3 and La_xWO_3 samples were obtained from the cubic XRD peaks (see appendix A for the theory) and the results are shown in Fig. 3-4. The cubic lattice constant for x = 0.05 was not determined with sufficient accuracy due to the significant presence of additional phases. The relative peak positions were used in the analysis to eliminate zero offset effects in the XRD traces. The Na tungsten bronzes have a cubic lattice parameter which is linear in x over the cubic range.[37] The La and Y tungsten bronzes also appear to follow this trend. The dashed lines in Fig. 3-4 are linear fits to the data on the cubic range of each compound, with lattice constants $a_C(\text{La}) = 3.807 + 0.21x$ and $a_C(\text{Y}) = 3.766 + 0.34x$.

Powder XRD measurements were performed on three samples of Y_xWO_3 (x = 0.07, 0.110, 0.148) at 300 K and 110 K. The XRD traces at 110 K are very similar to those at 300 K, indicating no phase changes, as evidenced by the results for x = 0.148 in Fig. 3-5a. Peaks for both the K_α and K_β radiation are present due to the absence of the Ni filter for the

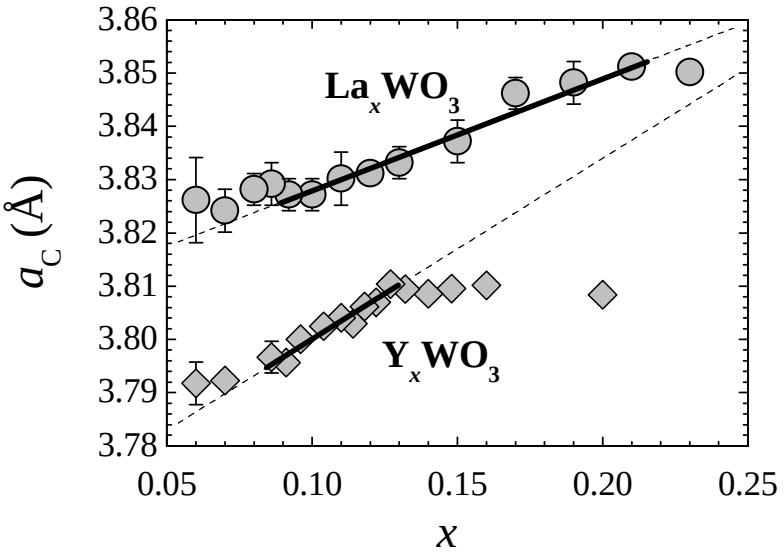

Fig. 3-4. The cubic lattice constant a_C vs x for the Y_xWO_3 and La_xWO_3 samples. The dashed lines are linear fits on the cubic ranges (indicated by solid lines).

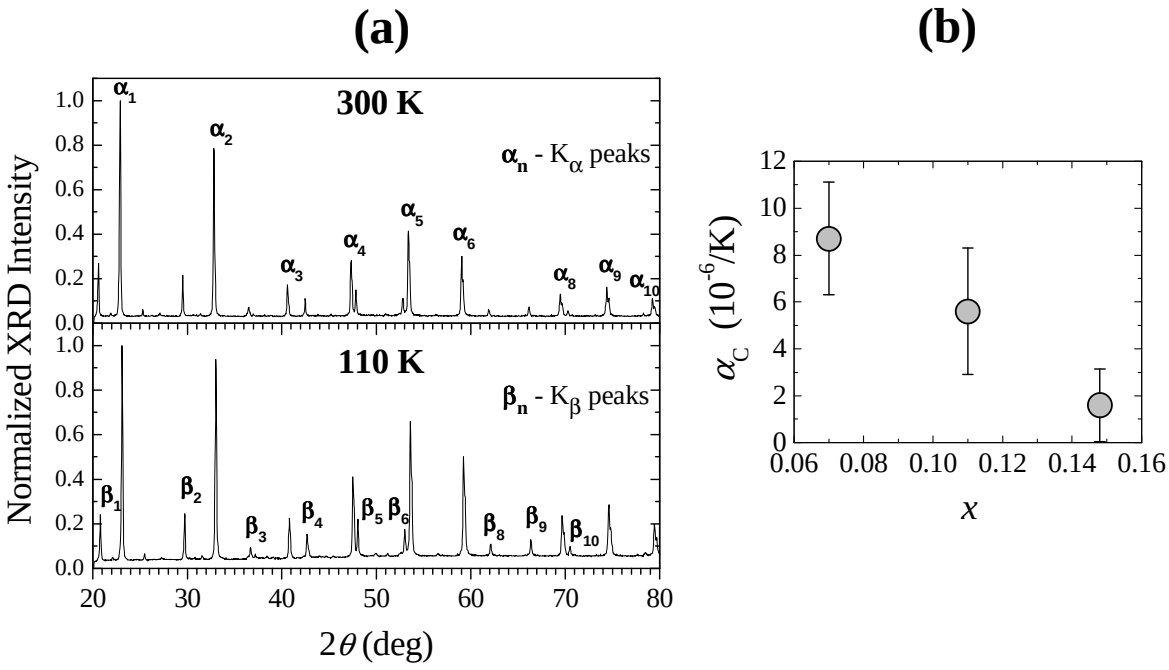

Fig. 3-5. (a) Powder XRD results for a sample of $Y_{0.148}WO_3$ at 300 K and 110 K. (b) The average cubic phase expansion coefficient α_C vs x for the three Y_xWO_3 samples.

K_β radiation in these runs. Fig. 3-5b shows the average cubic phase expansion coefficient α_C obtained by calculating the change in lattice constant, and also by investigating (to get a better average) the shifts in the K_α and K_β peaks between 300 K and 110 K. (See appendix A for the theory.) The large uncertainties in α_C are due to fact that the observed thermal changes are similar to the uncertainties encountered in the XRD data.

3.2.2 Density and crystal volume fraction

Sample mass densities were measured on bar and disk samples and are shown in Fig. 3-6. The predicted density of cubic crystalline Y_xWO_3 and La_xWO_3 (Eq. 3.2), calculated using the lattice constant values from Fig. 3-4, is shown by the dashed lines. The density of the pellets prior to sintering was about 5 g/cm^3, and the expansion of the pellets during sintering is consistent with the observed reduction in pellet density to about 3.3 g/cm^3.

From the sample density and the calculated crystal density it is possible to determine the crystal volume fraction f = (crystal volume)/(sample volume) = (sample density)/(crystal density), which is also shown in Fig. 3-6. The porous nature of the sintered polycrystalline samples is evident from these values (the crystal occupies ~45% of the sample space). The densities for the largest La_xWO_3 concentrations (x = 0.21 and 0.23) are not shown. These samples were soft sintered-powder blocks (§3.1), which had much lower densities. The crystal volume fraction is presented since its value (and in particular its x dependence) does affect certain physical properties of the samples. Sample resistivity and reflectance, for example, will be strongly dependant on f. The values were used to determine the density–corrected resistivity from the sample resistivity as a first order approximation to the crystal resistivity (see appendix D).

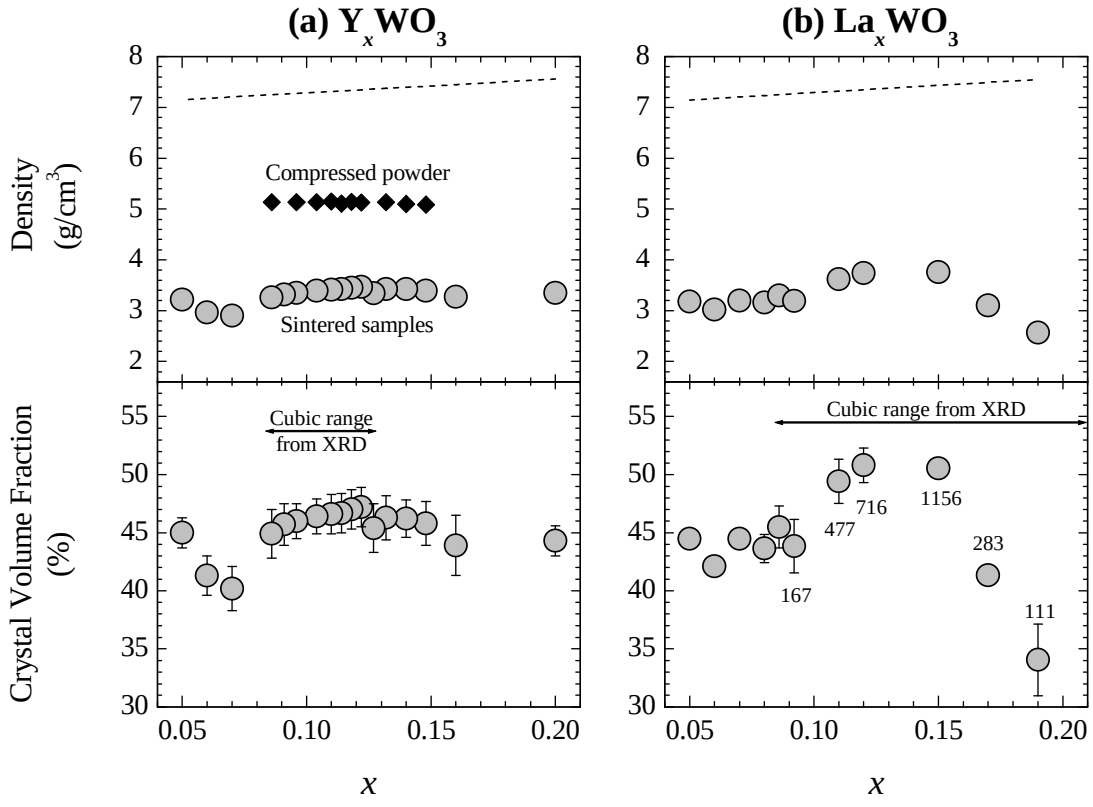

Fig. 3-6. The mass density and crystal volume fraction of the Y_xWO_3 (a) and La_xWO_3 (b) samples. Also shown is the mass density of the pre-sintered Y_xWO_3 pellets. The dashed lines show the predicted crystal density. Data labels in (b) give an indication of sample hardness, specifying cutting-wheel revolutions to cut equivalent sized pieces of material.

3.2.3 Diffuse reflectance

The Na tungsten bronzes show dramatic colour changes as x is varied, and the appearance of Na_xWO_3 samples can be used to estimate x and also check for inhomogeneities. Diffuse reflectance spectroscopy can therefore be used as an analytical tool to investigate the donor concentrations in the tungsten bronzes. To further check the validity of the nominal x values used for La_xWO_3, diffuse reflectance investigations were done to compare the chromic character of the La_xWO_3 and Y_xWO_3 samples.

Diffuse reflectance measurements were performed in the visible and infrared range on a selection of samples using a Cary Scan 500 UV-VIS-NIR spectrophotometer. The results are shown in Fig. 3-7. Fig. 3-7a shows the percentage reflectance R vs the wavelength λ for cubic samples of Y_xWO_3 and La_xWO_3. Fig. 3-7b shows the reflectance in the visible range, normalised to the value at λ = 750 nm, of lower x samples of Y_xWO_3 and La_xWO_3 to show the colour changes associated with changes in x.

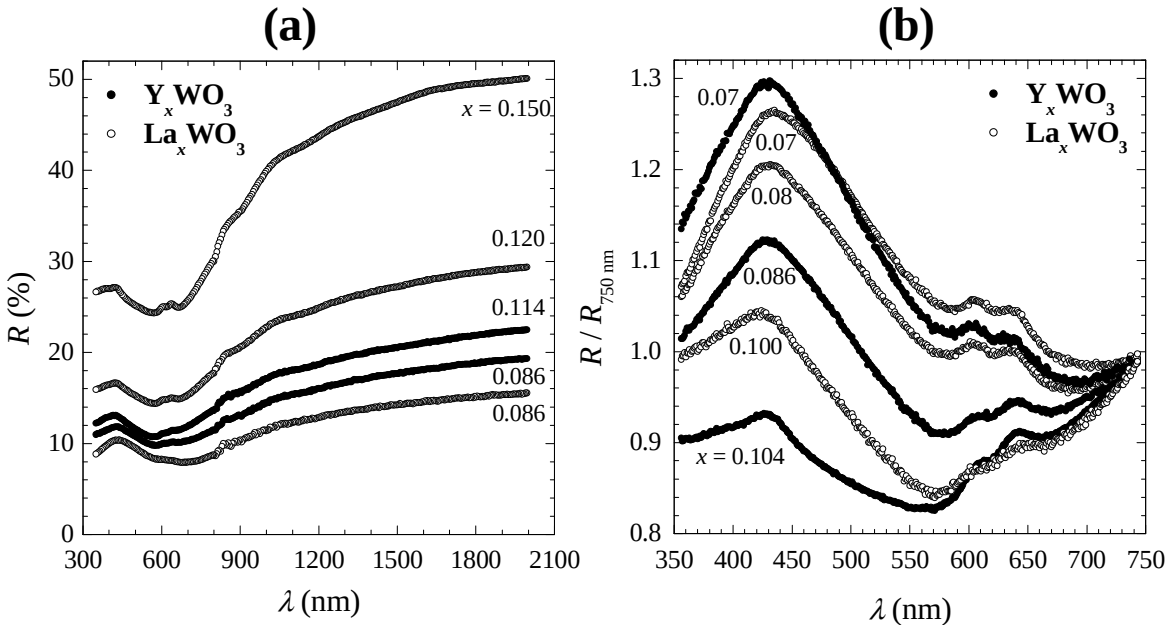

Fig. 3-7. (a) Diffuse reflectance results for selected Y_xWO_3 and La_xWO_3 cubic phase samples showing the percentage reflectance R vs the wavelength λ. (b) The reflectance, normalized at 750 nm, in the visible range of wavelengths to indicate the colour evolution of the lower x samples.

As the figures show, there is a monotonic change in the reflectance as x is varied. Performing reflectance measurements on more samples, however, produced variations. Reflectance measurements on different parts of the same sample, for example, show differences of up to 3% in R. This is attributed to surface variations from the sample cutting. This could explain the difference (~4%) in R for the same x = 0.086 samples of Y_xWO_3 and La_xWO_3 in Fig. 3-7a.

The relative reflectance, shown in Fig. 3-7b, is therefore a better quantity when comparing the two compounds. The results in this figure suggest that the deposits observed inside the quartz ampoules after La_xWO_3 production do not appear to significantly change x from the nominal values. The position of the La_xWO_3 data in Fig. 3-7b is as expected relative to the Y_xWO_3 data, and also shows that the Y_xWO_3 and La_xWO_3 samples are optically indistinguishable for the same x.

3.2.4 Resistivity

Resistivity measurements were performed on the whole range of donor concentrations using the van der Pauw method.[88,89] Samples were cut into discs with thicknesses varying from 0.75 mm to 2 mm, with diameters ranging from 11 mm to 15 mm. The measurements were made between 64 K (pumped liquid nitrogen) and 300 K. The leads were attached to the sample edges using silver paste (at ~90° intervals), with excitation currents ranging from 10 mA to 200 mA (depending on the sample resistivity). These preliminary higher temperature runs were performed to ensure a good sequence of samples suitable for the low temperature investigations, and to fine-tune the operation of the transport station. (See chapter 4 for further details on the resistivity measurements.)

The resistivity results are summarised in Fig. 3-8, Fig. 3-9 and Fig. 3-10. The room temperature sample resistivity ρ_S is shown in Fig. 3-8. Each value corresponds to an average of measurements made on all the available samples. Both the Y_xWO_3 and La_xWO_3 sample resistivity shows a resistivity minimum at $x \sim 0.13$. For the La_xWO_3 samples the resistivity minimum appears to be due to the x-dependent fluctuations in the crystal volume fraction f (Fig. 3-6b). To account for the varying polycrystalline nature of the samples with x, a first order estimate of the actual crystal resistivity ρ_C, which is the quantity of interest, can be made by the equation $\rho_C = f\,\rho_S$ (see appendix D). The density-corrected resistivity

ρ_C, using the values for f from Fig. 3-6, is included in Fig. 3-8. For La_xWO_3 the anomaly seems to be accounted for. For Y_xWO_3 the fluctuations in f do not account for the resistivity minimum. The minima occurs near the upper cubic limit $x_{max} \sim 0.13$, and is discussed further in §3.3. The dashed curves in Fig. 3-8, with $\rho = c/x$, show metallic-type behaviour with the conductivity proportional to the dopant (carrier) concentration. The proportionality constant c (0.094 and 0.155 for Y_xWO_3 and La_xWO_3 respectively) was chosen to fit the curve through the $x = 0.12$ data. The curve does describe the La_xWO_3 data for $x \geq 0.12$, indicating possible metallic-type behaviour for higher x. However, as will be shown in §3.3, grain-boundary scattering is a more plausible explanation for the high x data. As expected from the behaviour of other tungsten bronzes (Fig. 2-5), both Y_xWO_3 and La_xWO_3 show a similar non-metallic behaviour for low x.

Fig. 3-9 and Fig. 3-10 shows the temperature dependence of the conductivity for selected samples. The density-corrected conductivity $\sigma_C = \sigma_{sample} / f$ is shown in these

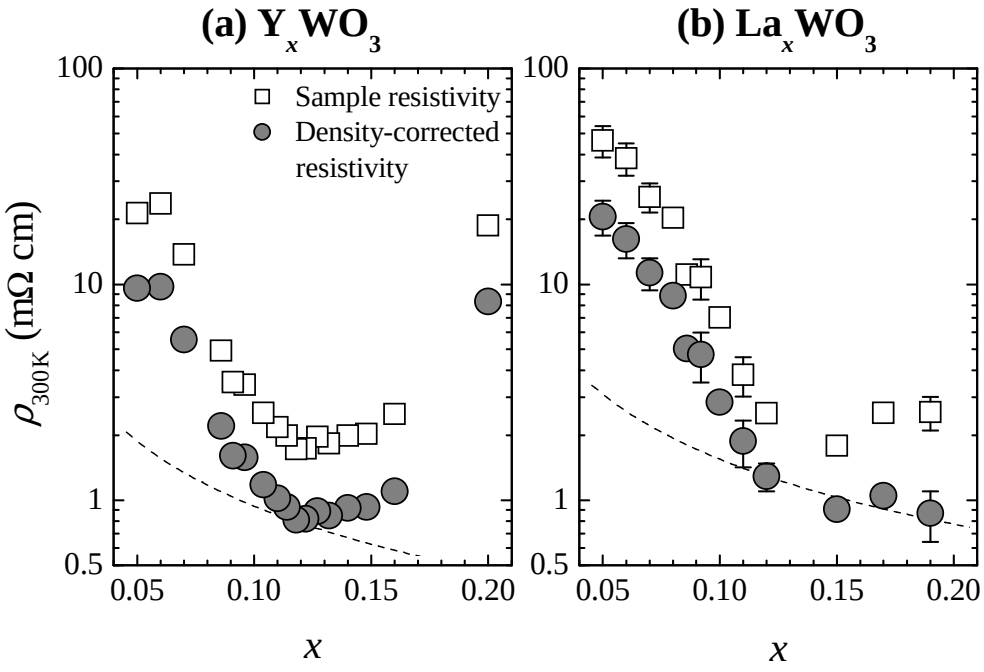

Fig. 3-8. Room temperature resistivity results for the Y_xWO_3 (a) and La_xWO_3 (b) samples. The x-dependence of the sample resistivity ρ_S and density-corrected resistivity $\rho_C = f\rho_S$, using the f values in Fig. 3-6, is shown in a semi-log plot. The dashed line shows metallic-type behaviour with $\rho \propto 1/x$.

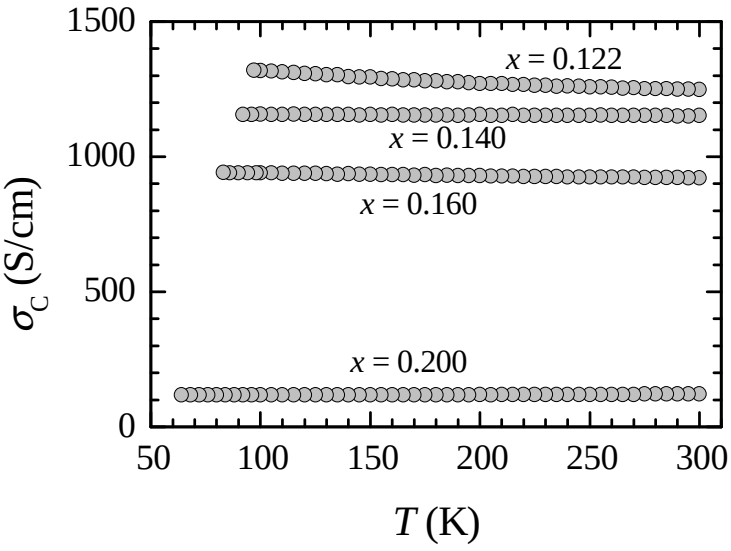

Fig. 3-9. The density-corrected conductivity $\sigma_C = \sigma_{sample} / f$ of the Y_xWO_3 samples vs the temperature T for the higher donor concentrations ($x > 0.12$).

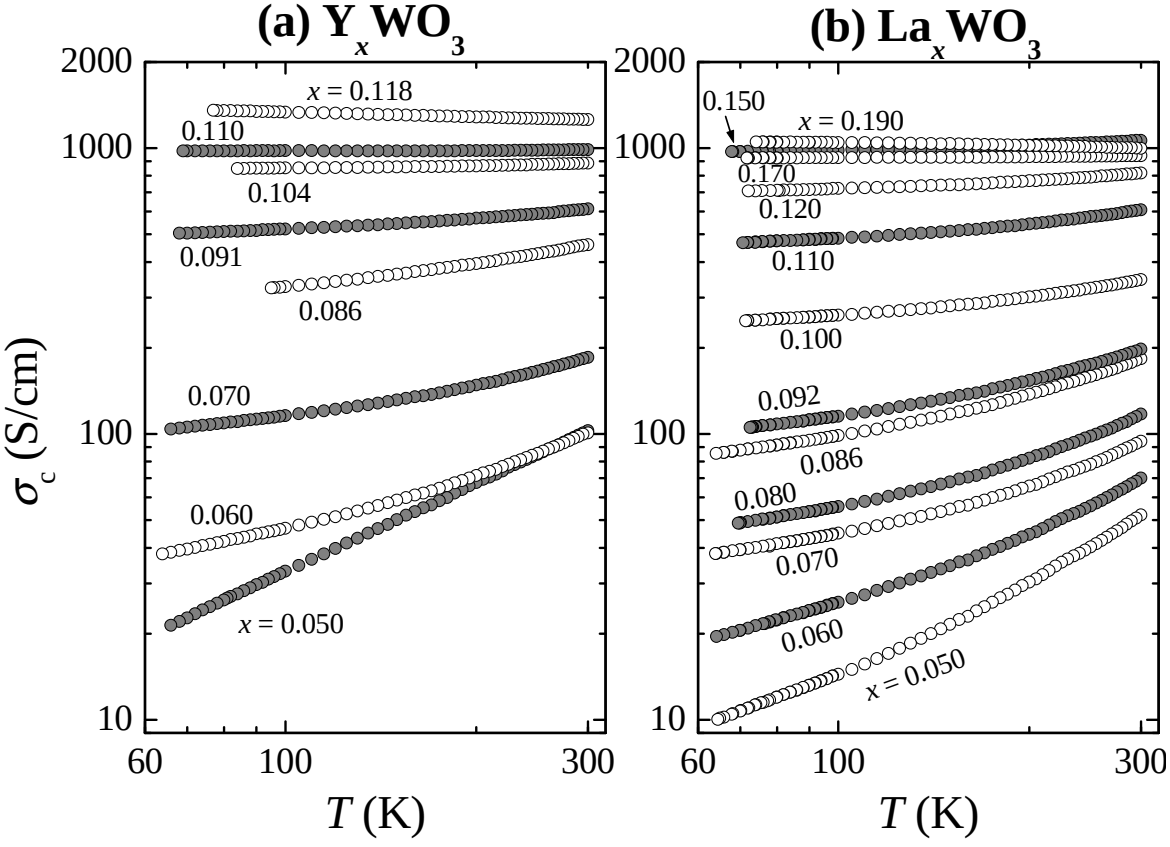

Fig. 3-10. The conductivity results for the Y_xWO_3 (a) and La_xWO_3 (b) samples in a logarithmic plot of the density-corrected conductivity $\sigma_C = \sigma_{sample} / f$ vs the temperature T for various donor concentrations x.

figures. The transformation only shifts the absolute value and does not affect the temperature dependence. The uncertainties are estimated at ~7%, mainly due to uncertainties in sample dimensions and finite contact size. Fig. 3-9 shows the Y_xWO_3 results for concentrations above the resistivity minimum ($x > 0.12$). Fig. 3-10 shows the lower concentration ($x < 0.12$) results for Y_xWO_3 and the complete range of results for La_xWO_3. Both compounds show a family of curves that gradually evolve from metallic-type ($d\sigma/dT < 0$) to semiconducting-type ($d\sigma/dT > 0$) behaviour as x is reduced, typical of the low x tungsten bronzes (Fig. 2-7). Although the $x = 0.150$ curve for La_xWO_3 has a higher conductivity than expected, the temperature dependence, which is of particular interest, is consistent with the sequence. This is also the case for the $Y_{0.050}WO_3$ curve.

3.2.5 Hall effect

Measurements of the Hall coefficient R_H were done at room temperature using a dc Hall configuration. The samples were disc and bar shaped with thicknesses ~1 mm. For the bar samples (length ~ 10 mm and width ~ 7 mm) the width to thickness ratio was made large to optimize the Hall voltage detection. Currents of 100 mA and 200 mA were used which produced Hall voltages ~0.1 μV. The details for each sample are shown in Table 5-3 of §5.4. A Varian magnet supplied bi-directional magnetic fields up to 1.2 T. The two current contacts were attached with silver paint. The voltage leads, which need to be as small as possible, were initially attached to the samples using silver paste. Successful runs were intermittent, mainly attributed to the poor contact properties between the small silver paste electrode and sample. Gold-coated pins with pressure contact provided a more consistent method for the voltage lead connections. (Refer to chapter 4 and §5.2 for the experimental details.) Magnetoresistance effects were not detected in the room temperature measurements.

The results of the room temperature Hall effect measurements on the Y_xWO_3 and La_xWO_3 samples are shown in Fig. 3-11. The Hall concentration $n_H = 1/R_He$ is shown and the dashed lines correspond to $n_H = n_d$, with $n_d = 3x/a^3$ the donor electron concentration assuming trivalent Y^{3+} and La^{3+} donor states (a is the lattice constant). The sign of the Hall coefficient indicates negative charge carriers for both compounds. Each datum in Fig. 3-11 is the average of several runs on a sample, with each run performed in several magnetic field cycles (see Fig. 5-4).

The significant fluctuations in n_H, particularly noticeable in the Y_xWO_3 data for $x \geq 0.12$ in Fig. 3-11a, are not random, as repeated measurements on these samples produced the same values. These fluctuations are attributed to systematic errors in the sample thickness values used in the expression for R_H. The sample cutter did not produce sufficiently parallel surfaces for these samples, and surface damage or internal cracks may also be a factor. Closer inspection of several samples showed thickness variations of up to 10% along the surface, consistent with the magnitude of the fluctuations seen in Fig. 3-11a. This is also an explanation for the apparent constancy in the La_xWO_3 Hall concentration for $x \geq 0.12$ in Fig. 3-11b. Further investigations suggest that this is indeed due to systematic experimental fluctuations (see Fig. 6-1).

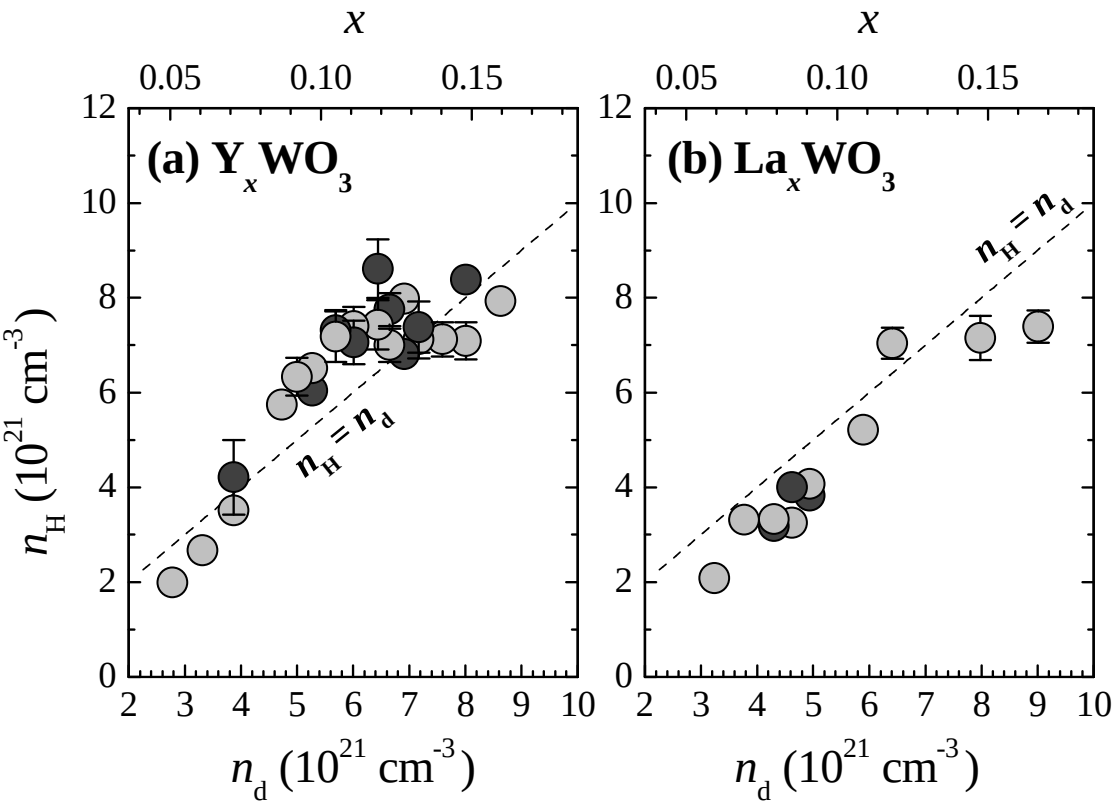

Fig. 3-11. The results of the room temperature Hall coefficient R_H measurements on the Y_xWO_3 (a) and La_xWO_3 (b) samples, showing the Hall concentration $n_H = (R_H e)^{-1}$ vs the donor electron concentration n_d. Values of x are shown on the top scale. The dashed lines correspond to $n_H = n_d$. (Darker symbols in both figures represent a second sample set.)

3.3 Discussion

The powder XRD traces in Fig. 3-2 and Fig. 3-3 are typical of the tungsten bronzes.[19,20,40,60,90] The single-phase cubic range for Y_xWO_3 and La_xWO_3 occurs for $0.086 \leq x \leq 0.127$ and $0.086 \leq x \leq 0.21$ respectively, consistent with previous results.[22] Outside these ranges additional phases appear. The additional XRD peaks in Y_xWO_3 for $x > 0.13$ (shown by * in Fig. 3-2b) coincide with the non-cubic peaks observed for Ce_xWO_3 and Nd_xWO_3, which were attributed to WO_2.[19,20] The appearance of WO_2 was also previously observed in Y_xWO_3 above the solubility limit.[22] The presence of the tetragonal form in Y_xWO_3 and La_xWO_3 for $x \lesssim 0.08$ was reported, both having the same lattice constants.[22] The XRD traces in Fig. 3-2 and Fig. 3-3 do show a similar evolution as $x \rightarrow 0$. The additional peaks in Y_xWO_3 and La_xWO_3 for $x = 0.05$ are also observed in the tetragonal phase of Ca_xWO_3 ($x \leq 0.11$).[60] There are signs of the tetragonal peak-doublets, but the traces for Y_xWO_3 and La_xWO_3 suggest a mixed-phase with the cubic structure. Overlapping phases for lower x are also observed in other tungsten bronzes.[17,31,61] The results here are therefore consistent with the structural behaviour observed in the tungsten bronzes.

The presence of the mixed phases is particularly important at the low dopant concentrations where the MI transition occurs. Investigations show that the cubic phase of the tungsten bronzes is metallic, and the transition to the insulating state is preceded by lattice instability in the cubic Na_xWO_3 system.[26] Adopting a similar criterion implies a critical concentration $x_C < 0.086$ for Y_xWO_3 and La_xWO_3.

The lower cubic limit $x_{min} \sim 0.086$ is the same for both compounds, consistent with previous results.[22] This value is also found for other trivalent-donor tungsten bronzes.[30,31] Calculations suggests that the crystal structure is primarily determined by the conduction band electronic density.[36] Fig. 3-12 plots x_{min} vs the donor valence v for the trivalent systems ($x_{min} \sim 0.086$), the divalent Ca_xWO_3 ($x_{min} \sim 0.12$)[60] and the monovalent Na_xWO_3 ($x_{min} \sim 0.26 \pm 0.04$)[12,37,45,51,54]. The linear fit gives $x_{min}\, v = 0.25$, indicating that the donor-electron concentration $n_d = x_{min}\, v/a^3 \simeq 4.5\times10^{21}$ cm^{-3} appears to be the determining factor for x_{min} (variations in the lattice constant $a \sim 3.8$ Å are small at ~1 %).

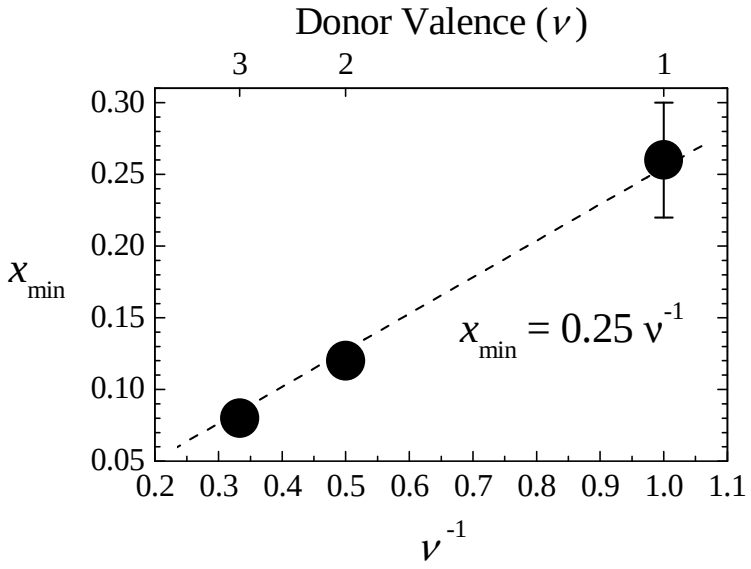

Fig. 3-12. A plot of the lower cubic limit x_{min} vs the valence ν of the donor atom (upper scale). The line is a linear fit of the x_{min} vs ν^{-1} data (forced through the origin).

The upper cubic limit $x_{max} \simeq 0.13$ for Y_xWO_3 is smaller than previously obtained ($x_{max} \simeq 0.15$).[22] Different values for x_{max} were also reported for Eu_xWO_3 ($x_{max} \simeq 0.125$ and 0.16).[30,31] This was attributed to the differences in the preparation procedure.[31] This could also explain the difference in x_{max} for Y_xWO_3 (the samples here were more slowly cooled – §3.1). It has been shown that the preparation of Na_xWO_3 is sensitive to conditions such as temperature and reaction time.[37] Metastable cubic structures of Na_xWO_3 have been obtained for lower x by quenching heated samples to room temperature.[54] The large range of x_{max} values observed for the various tungsten bronzes ($x_{max} \simeq 0.9$ for Na_xWO_3)[37] has been attributed to the thermodynamic stability of the corresponding donor-metal tungstate.[57]

The cubic lattice constant a_C for Y_xWO_3 and La_xWO_3 (Fig. 3-4) gives results consistent with previous investigations.[22–25] Although Broyde[22] obtained a non-linear a_C vs x relationship for La_xWO_3, the data here do appear to follow a linear form. The straight-line fits on the cubic range give a good description of the a_C results for both Y_xWO_3 and La_xWO_3. This linear a_C vs x behaviour for the cubic phase is also observed in Na_xWO_3,[37] Eu_xWO_3,[30,31] and Ce_xWO_3,[19] and is also predicted by calculations.[33]

The solubility limit for Y_xWO_3, occurring at the upper cubic limit $x_{max} \simeq 0.13$, is clearly visible in Fig. 3-4. Since the lattice constant depends on the donor electron concentration,[36] the constancy of a_C for $x > x_{max}$ indicates saturation of the donor concentration in the cubic tungsten bronze phase. The concentration of the additional phase(s) then grows with increasing $x - x_{max}$ (Fig. 3-2b). Furthermore, the saturation of the Y_xWO_3 tungsten bronze phase for $x \gtrsim 0.13$ is suggested by the levelling of the Hall concentration data in Fig. 3-11a, and may also be responsible for the upturn in the resistivity data in Fig. 3-8a (discussed below). The La_xWO_3 lattice constant appears to level for $x \geq 0.21$ suggesting an upper cubic limit $x_{max} \simeq 0.21$.

Fig. 3-13 compares the Y_xWO_3 cubic lattice constant to that of Eu_xWO_3.[31] The cubic-phase range is the same, with a_C having a similar magnitude and slope. Both donor ions are trivalent with similar ionic radii. The Eu_xWO_3 results also suggest a saturated tungsten bronze phase for $x > x_{max}$. This is also observed in Na_xWO_3 for $x \gtrsim 0.9$.[37] For $x < x_{min}$ the Eu_xWO_3 lattice constant shows increased values. Phase separation into cubic ($x_{min} < x < x_{max}$) and tetragonal ($x \sim 0.05$) structures was observed by XRD and optical microscopy.[31] This does not appear to occur for Y_xWO_3 and La_xWO_3. All the measured quantities (apart from the crystal volume fraction in Fig. 3-6) show gradual changes as x crosses the lower cubic-phase boundary.

Optical microscope images of cubic $Y_{0.091}WO_3$ and $La_{0.092}WO_3$ are very similar, as expected for equivalent concentrations. The images, however, do not show a uniform colour at the microscopic level, even though both these samples are single-phase. The polycrystalline nature of the surface produces chromatic variations. Comparing, for example, the multiphase $Y_{0.050}WO_3$ and single-phase $Y_{0.091}WO_3$ images shows the expected overall colour changes, but otherwise look very similar. Optical microscope images of the range of Y_xWO_3 and La_xWO_3 samples do not give an indication of any phase separation. The nature of the multiphase region therefore requires further investigation.

The 110 K XRD results show no crystallographic structure changes in cooling from 300 K (Fig. 3-5a). This is consistent with the conductivity, which shows smooth σ vs T curves down to 64 K (Fig. 3-10). The phase transitions observed at lower T in WO_3 are suppressed,[41] although the WO_6 octahedral basis may be tilting and deforming.[25,42] The cubic phase expansion coefficient α_c for Na_xWO_3 has produced a large range of values

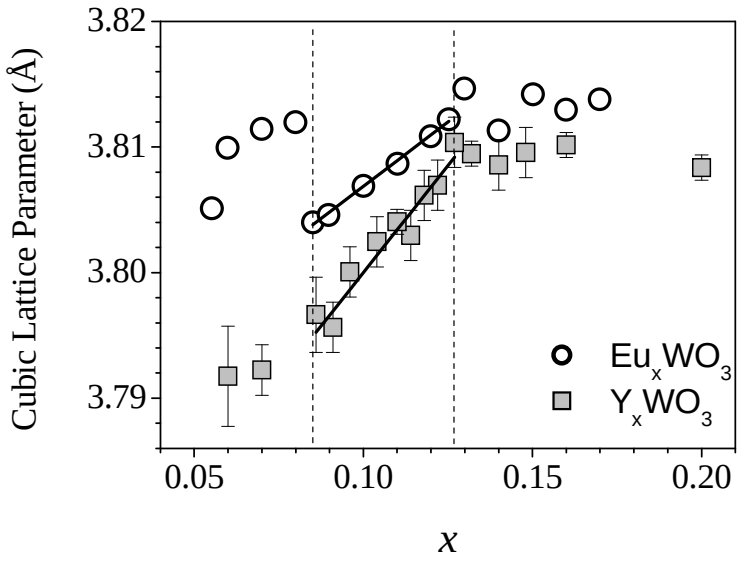

Fig. 3-13. The cubic lattice constants of Y_xWO_3 and Eu_xWO_3 vs x. The dashed lines indicate the common single-phase cubic range, and the full lines are linear fits.

($0.2 – 17\times10^{-6}$ /K) for $T > 0$°C ($\alpha_c \simeq 14\times10^{-6}$ /K for WO_3).[42,91,92] A small reduction in α_c with increasing x is also observed in Na_xWO_3.[91] The lower-temperature values for Y_xWO_3 are of similar magnitude, but show a significantly stronger reduction with x (Fig. 3-5b). There is an appreciable sample hardening in both Y_xWO_3 and La_xWO_3 with increasing x, and the multiphase nature of these materials may also be responsible for the larger changes observed in α_c.

From Fig. 3-6, both Y_xWO_3 and La_xWO_3 show similar magnitudes for the sample density (~3.3 g/cm^3) and crystal volume fraction (~45%). This is expected, as the SEM results (Fig. 3-1) show a similar polycrystalline structure for both compounds. The density of Y_xWO_3 increases gradually on the cubic range, with a slope near that of the calculated value for a single crystal. The multiphase regions obtained by the XRD results ($x < 0.08$, $x > 0.13$ for Y_xWO_3) are also revealed in the density and volume fraction by the deviation of the data from the near-linear form on the cubic range.

The significant decrease in f for La_xWO_3 when $x > 0.15$ (Fig. 3-6b) is attributed to the hygroscopic nature of La_2O_3. The larger La_2O_3 content for higher x samples causes a greater expansion of the pellets prior to sintering. The results reveal the importance of

preparing La-doped samples in a dry atmosphere, particularly for larger x values. There is a variation in the nature of the samples, such as sample strength and texture, related to f and x. The sample hardness, for example, is dependent on both f and x (Fig. 3-6b).

The diffuse reflectance results in Fig. 3-7a show two main features. The first is the broad infrared contribution, with its tail in the visible range ($350 \lesssim \lambda \lesssim 750$ nm), which grows with increasing x. The form and evolution is the same as that observed in cubic polycrystalline Na_xWO_3 and thin-film crystalline Li_xWO_3 (Fig. 2-8). This contribution is attributed to the metallic-type reflection due to the x-dependent conduction band concentration. The maximum long-wavelength reflection is also ~50%. Typical metals and high-x single-crystal Na_xWO_3 have long wavelength reflections approaching 100%.[53,66] The effective reflection area for polycrystalline samples, for example, will be of the order of the crystal volume fraction (~45% from Fig. 3-6), and could account for this reduced reflection.

The second feature is the small "blue" peak observed for $\lambda \simeq 430$ nm, emphasized in Fig. 3-7b, which appears to give a contribution independent of x. This enhanced contribution in the visible range gives the low x samples their bluish appearance. The yellow-green colour of WO_3 is attributed to interband transitions which give rise to a reflection peak at $\lambda \sim 470$ nm (see Fig. 2-8a, and Fig. E-6 in appendix E). The reflectivity results for Na_xWO_3 at equivalent concentrations ($x \sim 0.20 - 0.50$) do not show such a peak (Fig. 2-8a). Calculations of the reflectivity for Li_xWO_3 and Na_xWO_3 do predict a small peak at $\lambda \sim 400$ nm for $x = 0.25$ ($x_{eff} \sim 0.08$ for Y_xWO_3 and La_xWO_3), consistent with the results here.[34] The shorter wavelength, compared to WO_3, is attributed to the Fermi level rising with x. There appears to be no systematic shift in the "blue" peak position with x, as would be expected in the filling of a rigid band. It should be noted, however, that the dominant x-dependent metallic-type contribution will influence the observed peak position. The plasma frequency $\omega_P \propto n^{1/2}$, with $n \sim x$, moves to lower wavelengths as x is increased. The colour changes in Na_xWO_3 have been attributed to the free-electron plasma edge moving through the visible spectrum.[16,45,65] The classification of the "blue" peaks as interband transition requires further investigations, considering their absence in the Na_xWO_3 reflectivity.

Fig. 3-14 compares the Y_xWO_3 and La_xWO_3 conductivity results. Fig. 3-14a shows the room temperature density-corrected conductivity σ_C vs x. Fig. 3-14b compares the evolution of the temperature dependence by plotting the ratio σ(100 K)/σ(300 K). There are three regions of interest for the Y_xWO_3 results: $x \lesssim 0.11$, $0.11 \lesssim x \lesssim 0.13$, and $x \gtrsim 0.13$.

The region $x \lesssim 0.11$, which is of interest for the MI transition investigations, shows both compounds with a similar exponential dependence on x, as indicated by the parallel dashed lines (Fig. 3-14a). This behaviour is also observed in the alkali tungsten bronzes at the lower concentrations (Fig. 2-5). As shown in Fig. 3-14b, the slope of the $\sigma - T$ curves evolve monotonically in a similar fashion, indicating the stronger T-dependence as x is reduced. The conductivity is consistent with Na_xWO_3 and $Na_xTa_yW_{1-y}O_3$ results (comparing Fig. 3-10 and Fig. 2-7), showing the change from metallic ($\sigma_{100K}/\sigma_{300K} > 1$) to semiconducting-type ($\sigma_{100K}/\sigma_{300K} < 1$) behaviour as x is reduced. The crossover ($\sigma_{100K}/\sigma_{300K} = 1$) occurs at similar conductivities (~1000 S/cm, see Fig. 3-10), all within the single-phase cubic range. For Na_xWO_3 this occurs at $x \sim 0.3$ with a similar conductivity (~2000 S/cm)[7,26], while $x \simeq 0.11$ for Y_xWO_3 ($x_{eff} \simeq 0.33$ is similar). For La_xWO_3 the

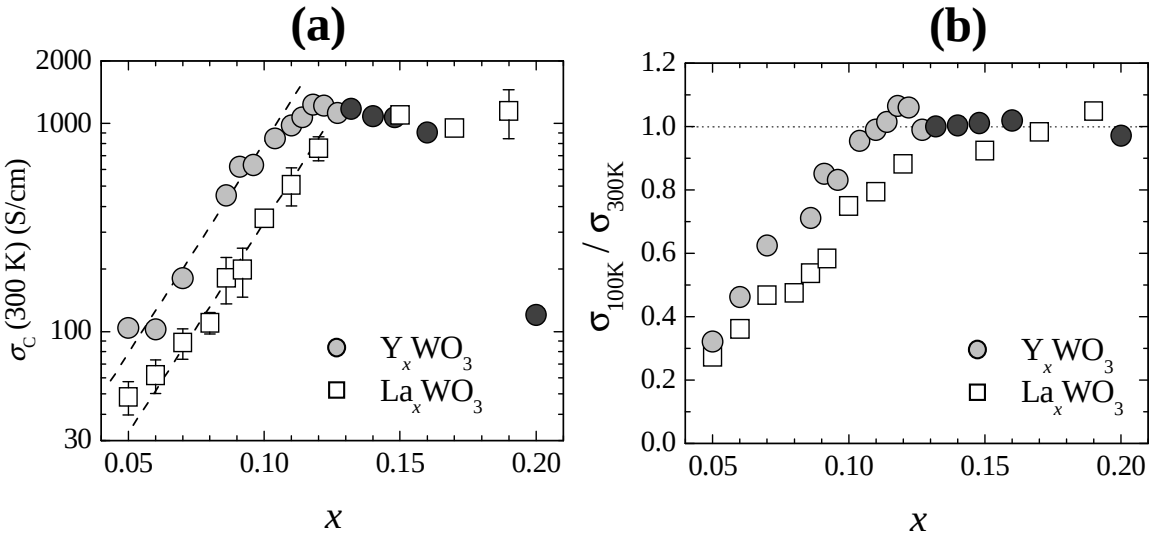

Fig. 3-14. Comparison of the Y_xWO_3 and La_xWO_3 conductivities. (a) The room temperature density-corrected conductivity σ_C vs x. The dashed lines are two parallel straight lines. (b) The relative conductivity $\sigma_{100K}/\sigma_{300K}$ vs x. The darker symbols correspond to concentrations above the Y_xWO_3 solubility limit ($x > 0.13$).

crossover occurs at a larger value with $x \simeq 0.17$. For $x < 0.11$ the Y_xWO_3 and La_xWO_3 samples therefore show behaviour typical of the tungsten bronzes.

The Na_xWO_3 and $Na_xTa_yW_{1-y}O_3$ conductivity shows a near-linear temperature dependence for $T > 10$ K near the MI transition ($x - y \simeq 0.18$).[7] The conductivity follows a relation $\sigma(T) = a_0 + a_1T^k$, with the exponent $k \in (0.9, 1.3)$ and $a_1 > 0$. The Y_xWO_3 and La_xWO_3 conductivity for the lower x samples can also be described by this equation with k in the same range. The conductivity of the $Y_{0.05}WO_3$ sample in Fig. 3-10a shows a distinctly different behaviour in that the slope $d\sigma/dT$ appears constant over the shown temperature range, with $\sigma_C = 0.286T^{1.03}$. This T-dependence is also observed near the MI transition for $Na_xTa_yW_{1-y}O_3$ ($x = 0.34$ and $y = 0.16$ in Fig. 2-7; see also §2.4).

The La_xWO_3 conductivity in Fig. 3-14a is about half that of Y_xWO_3 for $x \lesssim 0.11$, which is unexpected. Referring to the anomalous behaviour observed in the La_xWO_3 preparation (§3.1 – film deposits on the quartz ampoule walls) a shift of $\Delta x \sim -0.02$ for La_xWO_3 would make the σ vs x data for La_xWO_3 and Y_xWO_3 coincide. This required shift in x is larger than appears likely based on the small amount of material of unknown composition detected on the ampoule walls. It would also introduce similar problems for the other measured quantities. The specific heat results presented in §6.4.2 show equivalent results for $Y_{0.050}WO_3$ and $La_{0.050}WO_3$ (Fig. 6-17), indicating no significant deviation from the nominal x value used for La_xWO_3.

The second region ($0.11 < x < 0.13 \sim x_{max}$) corresponds to the upper part of the Y_xWO_3 single-phase cubic range. The conductivity in Fig. 3-14a appears to reach a plateau value, and this is also observed for La_xWO_3 before reaching its upper cubic limit $x_{max} \sim 0.21$. For La_xWO_3 metallic-type behaviour (with $\sigma \propto x$) does describe the results for $x \geq 0.12$ (Fig. 3-8b). Room temperature results for single crystal Na_xWO_3 (Fig. 2-5), however, indicate a stronger x-dependence for equivalent concentrations. SEM indicates a similar polycrystalline structure (Fig. 3-1), and both conductivities in Fig. 3-14a level off to about the same value (~1000 S/cm). This rather suggests that the grain-boundary resistance is responsible in limiting the total conductivity. Evidence of large grain-boundary contributions was also evident in earlier studies of high concentration polycrystalline Na_xWO_3.[56] For this reason research focussed primarily on single-crystal samples. As

evidenced here, both the crystal volume fraction and the grain-boundary resistance need to be considered in the higher-concentration polycrystalline samples.

In the third region ($x > 0.13 \sim x_{max}$) the Y_xWO_3 conductivity is expected to be limited by the grain-boundary resistance. The carrier concentration within the crystallites is also saturated due to the solubility limit, and further increase in crystallite conductivity is not expected. The XRD results, however, show the appearance of impurities for $x > 0.13$, resulting in increased scattering centres with increasing x. This would account for the observed reduction in conductivity. The same behaviour is expected for La_xWO_3 when $x > 0.21$.

The dominance of the grain-boundary and impurity scattering in Y_xWO_3 is also apparent in the temperature dependence of the conductivity. The conductivity curves for $x \geq 0.140$ in Fig. 3-9 show very little temperature dependence. This is also evident in Fig. 3-14b with $\sigma_{100K}/\sigma_{300K} \simeq 1$ for $x \gtrsim 0.13$. This is indicative of dirty metal behaviour where temperature dependent contributions, such as phonon scattering, get swamped by impurity scattering.

The anomalies in the sample resistivity for Y_xWO_3 and La_xWO_3 in Fig. 3-8 are therefore summarised as follows:

- In La_xWO_3 the upturn in the resistivity for $x \geq 0.15$ is due to the large crystal volume fraction reduction.

- For Y_xWO_3 and La_xWO_3 the resistivity levels (to ~1 mΩ cm) within the cubic range due to the grain-boundary resistance.

- In Y_xWO_3 the carrier concentration in the conducting cubic phase is saturated for $x > 0.13$. Increasing x leads to more impurity scattering centres, accounting for the increased resistivity.

The room temperature Y_xWO_3 and La_xWO_3 Hall concentration in Fig. 3-11 is similar to the results of Na_xWO_3 (Fig. 2-4) for $x \lesssim 0.12$. Refer to §6.3 for further discussion and comparisons. The Hall concentration for Y_xWO_3 appears to plateau for the higher

concentrations, and this is attributed to the solubility limit of Y in the tungsten bronze phase. For $x > x_{max} \sim 0.13$ the Y concentration becomes saturated, leading to a constant carrier concentration. The apparent constancy in the La_xWO_3 Hall concentration for $x \geq 0.12$ is due to experimental fluctuations, evidenced in §6.1, and does not represent a concentration limit.

In conclusion, the characterisation of the Y_xWO_3 and La_xWO_3 samples shows results that are typical of other investigated tungsten bronzes, such as the much investigated Na_xWO_3. The results confirm that the two compounds are homogeneous tungsten bronzes, and point to a sequence of Y_xWO_3 and La_xWO_3 samples suitable for this investigation. The grain-boundary resistance makes the measured absolute resistivity somewhat uncertain for $x > 0.1$, although the temperature dependence should still be accurate. The region of interest for the MI transition is at the lower concentrations (with $x_C < 0.086$). Due to the larger crystallite resistance in this range, the interfering grain-boundary effect will be less evident.

Chapter 4: The electric transport station

This chapter discusses the details of the electric transport station for the low temperature resistivity and Hall coefficient measurements. The van der Pauw technique and the bar-sample method used in the transport investigations are discussed. The experimental setup and the apparatus used in the transport station are then presented. The chapter concludes with the tests performed on the transport station to ensure proper functionality.

4.1 Measurement techniques

4.1.1 The van der Pauw method

The van der Pauw method[88] provides a way of measuring the resistivity ρ and Hall coefficient R_H of a sample having an arbitrary surface shape provided that the following conditions are satisfied:

- The sample is sufficiently thin with a uniform thickness d.
- The sample should be simply-connected with a uniform resistivity ρ.
- The contacts used for supplying the current I and measuring the voltage V must be on the periphery of the sample.

If the above conditions are satisfied then the van der Pauw technique states that the resistivity is

$$\rho = \frac{\pi d}{\ln 2}\left(\frac{R_1 + R_2}{2}\right) F\left(\frac{R_1}{R_2}\right) \quad . \tag{4.1}$$

Fig. 4-1 shows the setup for this method. The resistances R_1 and R_2 in Eq. 4.1 are determined by placing the two switches at positions 1 and 2 respectively. In position 1 the current I_{AB} and voltage V_{DC} are measured to determine $R_1 = V_{DC}/I_{AB}$, while in position 2 the current I_{AD} and voltage V_{BC} gives $R_2 = V_{BC}/I_{AD}$. The function F in Eq. 4.1 depends only on the ratio of the measured resistances R_1 and R_2. This function is plotted in Fig. C-1 of appendix C, which also describes a numerical method of evaluating F for use in the transport station software.

This technique is well suited to very thin (such as thin-film), arbitrarily shaped samples, with the contacts placed anywhere on the periphery. The thickness-to-diameter ratio of sintered pellets can be ~10%. The validity of using the van der Pauw method on these "thick" samples has not been previously addressed. To confirm that the van der Pauw method is also suitable for use on thick samples, an independent investigation was performed and the results have been published.[89] (See Appendix F for the publication.) The results indicate that the technique may be used for samples of arbitrary thickness, provided that a two-dimensional current distribution is maintained inside the sample (i.e. the current distribution at any depth is the same as that on the surface). For this reason the current and voltage contacts were placed on the sides of the samples, as shown in the inset of Fig. 4-1.

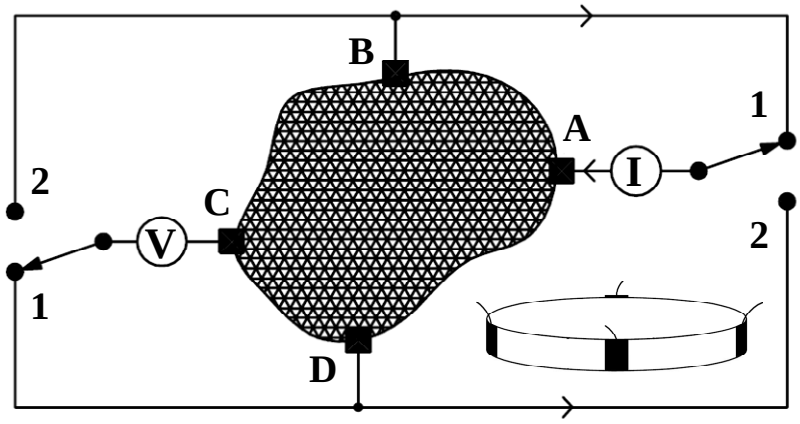

Fig. 4-1. The setup for the van der Pauw technique for resistivity measurements. The voltmeter and current source with ammeter are labelled by 'V' and 'I' respectively. The inset indicates contact placements for sample pellets.

The van der Pauw technique also allows for the measurement of the Hall coefficient, with

$$R_H = d\frac{\Delta R_3}{B}. \qquad 4.2$$

Referring to Fig. 4-1, a current I_{AC} is passed through AC, and the voltage V_{BD} is measured across BD, with the resistance $R_3 = V_{BD}/I_{AC}$. ΔR_3 in is the change in this resistance (due to the induced Hall voltage) when the sample is placed in a uniform magnetic field B that is perpendicular to the sample's surface.

4.1.2 The bar-sample method

The simplest way to do transport measurements is on bar-shaped samples. Fig. 4-2 shows the setup for this method on a sample with thickness d and width w. The voltage leads are placed at points A and B with a separation l. The current electrodes are placed on the entire end surfaces. With a current I this ensures a uniform current density $J = I/A$ through the sample's cross-sectional area $A = wd$. The uniform current and well-defined geometry simplifies the theory. Measuring the voltage V_{AB} gives the resistance $R_{AB} = V_{AB}/I$, and referring to Eq. B.13, the resistivity is then

$$\rho = \frac{R_{AB} wd}{l}. \qquad 4.3$$

The Hall coefficient is determined by using the contacts B and C for voltage measurements. Contact C is placed directly opposite to contact B so that no voltage appears in the absence of a magnetic field (i.e. the contacts are balanced). Referring to Eq. B.14, when a uniform magnetic field B is applied perpendicular to the surface, the voltage $V_{BC} = R_H BI/d$. This is the induced Hall voltage, and hence the Hall coefficient is

$$R_H = \frac{V_{BC} d}{BI}. \qquad 4.4$$

This expression is equivalent to Eq. 4.2 for the van der Pauw method.

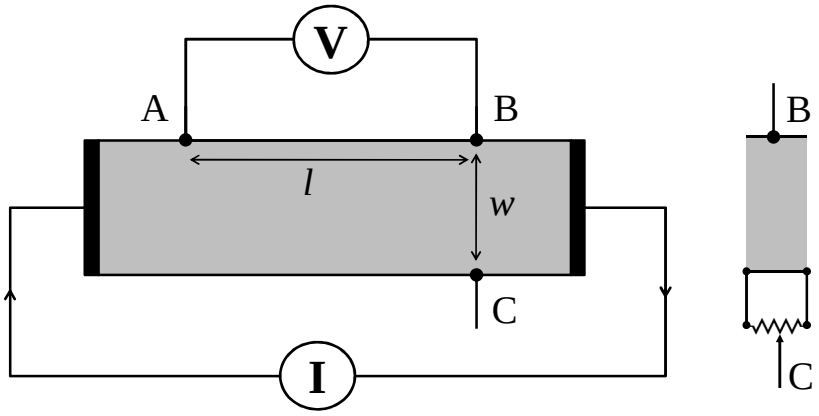

Fig. 4-2. The setup for resistivity and Hall coefficient measurements on bar-shaped samples. The voltmeter and current source with ammeter are labelled by 'V' and 'I' respectively. The inset shows a way to balance the points B and C using a potentiometer.

4.1.3 Additional notes

Eqs. 4.1 – 4.4 provide the expressions for the two quantities (ρ and R_H) that are the target of this investigation. Both methods described above use a 4-wire approach to eliminate the effects of contact resistance when measuring the resistivity. The 2-wire method (such as placing points A and B in Fig. 4-2 on the current line) would not be suitable here, as the sample resistance is significantly smaller than the contact resistances encountered in this research (see §5.1). Achieving good electrical contacts in the tungsten bronzes is a challenge.

Due to the finite resistance R of the samples, the applied current I will generate heat (power ~ I^2R) which could significantly change the sample's temperature. The large contact resistances found in the tungsten bronze samples is also a source of heat. Heating effects were noticed in the more resistive low x samples. To minimise this heating effect the current was only switched on during measurements (with a sufficient delay of about 1 s to allow for signal relaxation). The current magnitude was also varied to observe possible heating effects (see §5.1). Heating effects will manifest themselves by producing a current-dependent resistivity, particularly when the ρ vs T curve is not flat.

The voltmeter in Fig. 4-1 and Fig. 4-2 measures the signal voltage V_{signal} due to the current in the sample, as well as stray voltages V_{ext} appearing on the lines leading from the sample to the meter. The measured voltage $V = V_{signal} + V_{ext}$ therefore has a systematic error due to the stray voltages. This stray voltage can be eliminated by using current reversal. V_{ext} does not depend on the sample current, whereas V_{signal} reverses sign on reversing the current. The measured voltages for the two current directions is therefore $V_+ = V_{signal} + V_{ext}$ and $V_- = -V_{signal} + V_{ext}$. The signal voltage is then $V_{signal} = ½(V_+ - V_-)$. Current reversal for stray voltage elimination was used in all the resistivity measurements.

Two additional practical problems that can occur in resistivity measurements are contact slipping and contact creep. Contact creep occurs for finite sized voltage contacts (such as when using silver paste), and represents a change in the effective position on the sample at which the voltage is probed. This occurs due to non-uniform changes in the contact resistance when the temperature is varied. For this reason the voltage contacts need to be as small as possible. Contact slipping may occur when using pressure-applied voltage contacts. Both effects occur due to thermal changes in the environment. Although finite contact size does introduce quantifiable errors in the van der Pauw technique,[88] this method is not affected by contact creep or slip, since the results are independent of the contact placement. The bridge technique suffers from both contact creep and slipping, which affects the effective separation of the voltage leads (l in Eq. 4.3). Contact slipping and contact creep were apparent in several runs, but the effect was small. An example of significant contact slipping is shown in Fig. 6-2 by the "bump" in the resistivity data of $La_{0.19}WO_3$ for $T \sim 200$ K. These effects could also account for the slight differences in the resistivity data for the cooling and heating measurement cycles.

All four equations (Eqs. 4.1 – 4.4) contain sample dimensions (thickness d and width w) which change with temperature. For temperature changes of 300 K and an expansion coefficient $\sim 5\times10^{-6}$/K (Fig. 3-5) the sample dimension change is ~0.2%. The uncertainty in the measured sample dimensions is a few percent, and the thermal changes may therefore be ignored in comparison with other sources of uncertainty.

The derivation of Eq. 4.2 for the Hall coefficient is given in appendix B. It should be noted that this expression (reproduced from literature) is only valid in the absence of magnetoresistance effects. The expression is correct if the resistivity is independent of the

magnetic field, or if the voltage contacts (B and D in Fig. 4-1) are balanced (lie on an equipotential line with $V_{BD} = 0$ for $B = 0$). This is also the case for the bar-sample Eq. 4.4. If the contacts in Fig. 4-2 are not balanced, such as using contacts A and C, then magnetoresistance effects could appear in the measured voltage. The effects of magnetoresistance and the breakdown of the two expressions are illustrated in Fig. 5-4 of §5.2. See Eq. B.19 in appendic B for the corrections to Eq. 4.2 and Eq. 4.4 in the presence of magnetoresistance.

It is possible to eliminate magnetoresistance effects and create balanced voltage lines by using a 3-point voltage setup. This is illustrated in the inset of Fig. 4-2. The potentiometer is varied until the zero-field voltage across BC vanishes. This technique can also be implemented in the van der Pauw setup of Fig. 4-1. It is also possible to numerically balance the lines by measuring the two voltages across the sample (with the potentiometer in Fig. 4-2 removed). From Eq. B.19 the two voltages V_1 and V_2 are

$$V_k = V_{0k}\left(1 + \alpha_{MR}\left|B\right|\right) + \frac{R_H I}{d} B \qquad (k = 1, 2) \tag{4.5}$$

where V_{01} and V_{02} are the zero-field values. (α_{MR} is the magnetoresistance coefficient.) Calculating the ratio $\eta = -V_{02}/V_{01} > 0$ from the $B = 0$ measurements (which depends only on the positioning of the three voltage contacts), gives

$$V_2 + \eta V_1 = \left(1 + \eta\right)\frac{R_H I}{d} B \tag{4.6}$$

which eliminates the magnetoresistance term and allows for a direct determination of the Hall coefficient R_H. Eq. 4.6 is then equivalent to Eq. 4.2 and Eq. 4.4 apart from the geometrical balancing factor η.

Both of the balancing methods were applied to the 3-point voltage platforms used in this research (see Fig. 4-6 in §4.2.3). The results, however, indicated no additional improvement in measurement accuracy from the simpler 2-point measurements. When bi-directional magnetic field capability is available, the magnetoresistance can be easily separated from the Hall effect for unbalanced 2-point lines, as is shown in Fig. 5-4 of §5.2. For the 3-point platforms, two independent 2-point Hall effect measurements were

performed (with one common contact, such as contact B in Fig. 4-2). The second measurement served as a check on the first measurement, and also served to improve the precision by averaging the two results.

4.2 Experimental setup

From the previous section the basic requirements for the transport measurements are

- Variable magnet to generate a magnetic field perpendicular to the sample surface.
- Cryostat to control the sample temperature.
- Power supply to source a current, and a meter for current measurements.
- Meter for voltage measurements.
- Switches for current supply and voltage measurement control.

4.2.1 The magnet and cryostat

A Varian Fieldial Mark II water-cooled magnet provided bi-directional magnetic fields which could be continuously varied from 0 – 1.2 T. A Lakeshore 450 gaussmeter measured the field strength and direction. The sample was always oriented with its surface perpendicular to the field.

An Oxford CF1200 series continuous flow cryostat was used to control the thermal environment of the samples. An Oxford GFS650 transfer tube, Oxford VC31 gas flow controller and Oxford GF3 pump were used to promote the flow of the cryogen through the cryostat. Liquid helium and liquid nitrogen were used as cryogens in this research. An Oxford ITC503 temperature controller monitored the cryostat temperature (by means of a thermocouple). A set-point temperature could be maintained by the controller using the heater inside the cryostat.

The cryostat was placed in a vertical position inside the magnet. In this position the cryostat could be flooded with the cryogen and pumping on the cryostat with a rotary pump allowed for lower temperatures to be attained (1.6 K for liquid helium; 64 K for liquid nitrogen). The level of the cryogen during flooding was monitored by a 100 Ω Allen-Bradley carbon resistor at an appropriate level inside the cryostat (see Fig. 4-3 in the next section). A Fluke 8840A multimeter measured its 4-wire resistance. A distinctive behaviour in the resistance is observed when the resistor comes into contact with the rising cryogen.

A cryostat insert (see next section) was designed to accommodate the sample and all the electrical lines. The cryostat insert had a copper sample chamber attached to its end, which housed the various sample platforms used in the research (discussed in §4.2.3), as well as a heater and a Lakeshore CGR-1-500 carbon glass resistance thermometer. A Lakeshore 234D temperature monitor measured the temperature of the CGR thermometer.

4.2.2 The cryostat insert

Fig. 4-3 shows the schematics of the cryostat insert. (The bracketed numbers that follow refer to the labels in the figure.) The brass plug [1] seals the sample space by means of an o-ring inside the cryostat. The two small posts on the top are for magnetic field alignment, to ensure that the sample surface is perpendicular to the field. Also shown is the housing for the two Oxford 10-pin male connectors, which provide access to the 20 electrical leads. Joined to the plug is a thin-walled 6.35 mm stainless steel tube [2], with holes for gas exchange and three stainless steel spacers [3], which also act as radiation baffles. The holes in the spacers promote the flow of the cryogen gas from the bottom of the cryostat to the exhaust at the top.

Protective plastic tubing [4] was used for the electrical leads connected to the Oxford 10-pin connectors. Each tube contains ten insulated 0.19 mm copper wires, which are twisted-pairs to reduce noise pickup. The tubing is wound around the stainless steel tube to increase the length of the wires and reduce the heat load to the sample chamber. The two stainless steel tubes [5] act as guides to the two sets of copper wires. Sections of these tubes were removed to expose the copper wires directly to the cryogen gas and further reduce the heat load to the sample chamber.

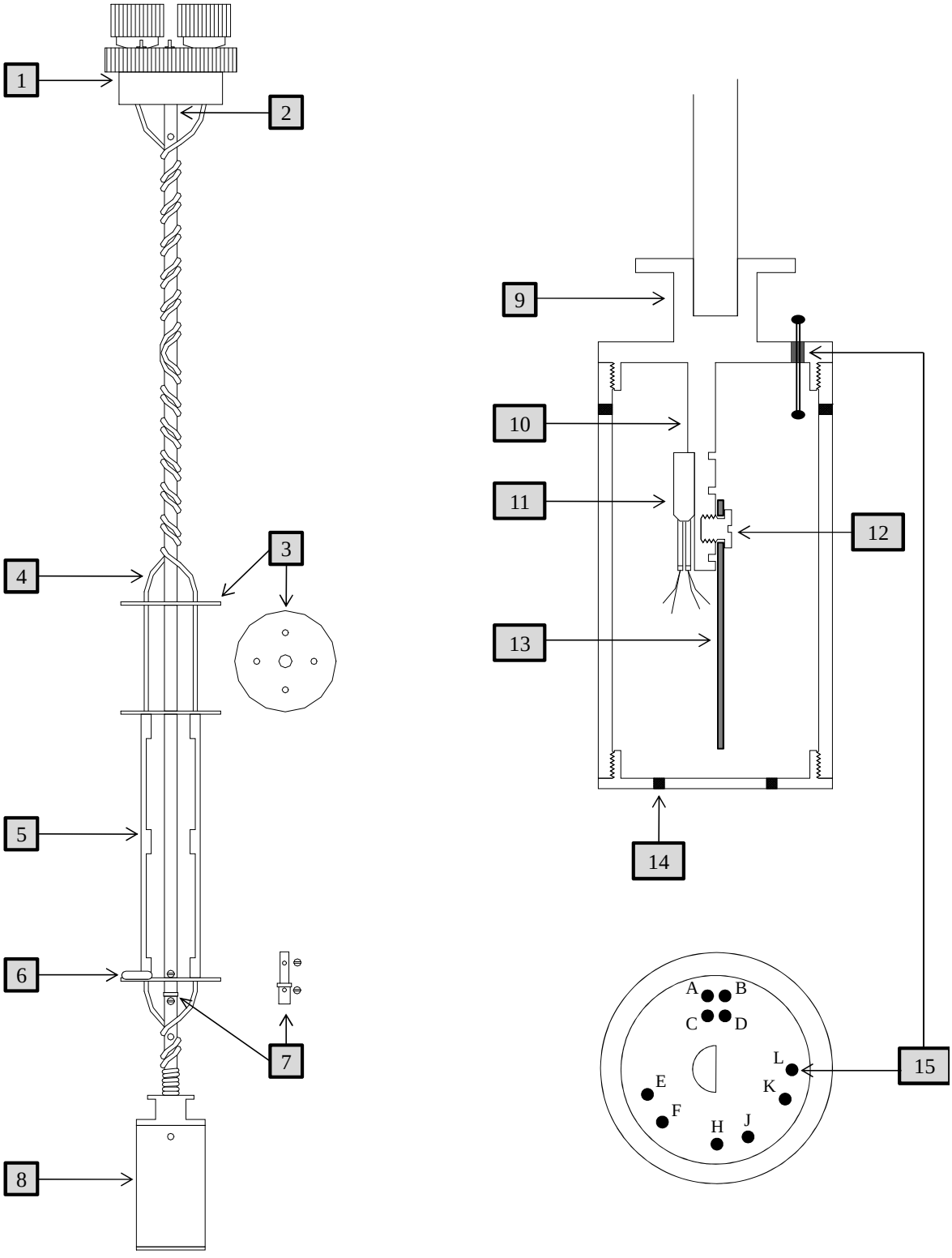

Fig. 4-3. A schematic of the cryostat insert (drawn to scale). Also shown is a vertical cross-section of the sample chamber. The horizontal cross-section indicates the positions of the electrical posts. (See the text for a description of the labels.)

The Allen-Bradley carbon resistor [6] was used to monitor the cryogen level. A stainless steel connector [7] joined the sample chamber assembly to the insert (using the two screws shown). The connector also acts as radiation baffle, and allows for different chambers to be used with the cryostat insert.

The sample chamber [8] was constructed from copper to create a constant-temperature environment for the samples. The two insets in Fig. 4-3 show cross-sections of the sample chamber. Oxford heater wire (0.19 mm nichrome) was wound around the copper spool [9] and anchored with Oxford GE varnish. About 3 m of twisted-pair wire was used with a heater resistance $R \simeq 105\ \Omega$. A copper post [10] was used for the attachment of the CGR thermometer [11], and a screw [12] secured the sample platform [13]. The grooves in the post are for the thermometer wires, which were wound around the post and anchored with GE varnish (to ensure proper measurement of the sample chamber temperature). The sample platforms are discussed in the next section (§4.2.3). Several holes [14] were placed in the sample chamber for gas exchange to minimise the occurrence of CO_2 or H_2O solidification.

Ten pieces of insulated 0.5 mm copper wire [15] were used for the electrical access to the sample chamber interior. The wire-posts were anchored with Oxford epoxy resin, which also provided further electrical insulation. The positions of the wire-posts are shown in Fig. 4-3 (the letters refer to the Oxford connector pin labels for easy identification). Four posts (A → D) were used for the electrical connections to the CGR thermometer. The remaining three pairs of posts (E → L) were used as the transport lines to the samples (current supply and voltage measurements).

4.2.3 The sample platforms

Fig. 4-4 shows the 1 mm thick copper disc (ϕ28 mm) used as a base-plate. A dual cigarette-paper layer was placed on the surface with diluted GE varnish. This provided good thermal contact between the sample and copper disc while maintaining electrical insulation. The larger screw connects the disc to the copper post in the sample chamber. The two smaller screws are affixed by a pair of nuts. The second pair of nuts keeps the samples in place by means of the attachments. See Fig. 4-5a for an example of a complete assembly.

The attachments consist of 25×2.5×0.5 mm phosphor-bronze strips which press the Teflon members against the samples. Attachment I was used in the van der Pauw method to position the sample pellets, and the four electrical wires were attached to the edges using silver paste (as in Fig. 4-1). Attachment II was used for single bar-shaped samples. It has a 13×ϕ5 mm Teflon cylinder with 1 mm spaced grooves for the 0.25 mm gold wires used as the voltage contacts (a 4 mm spacing was used). Attachment III, used for a dual bar-sample setup, has two 6×ϕ3 mm Teflon cylinders with 4 mm spaced grooves for the gold wires. Contact pressure between the gold wires and sample was controlled by the two nuts. The voltage leads were attached to the gold wires using silver paste. The two sides of the bar samples were painted with silver paste which also connected the current leads (as in Fig. 4-2). Fig. 4-9 in §4.2.4 shows the circuit diagrams for the three types of resistivity measurements.

The van der Pauw setup for Hall effect measurements is shown in Fig. 4-5a. Two other sample geometries used with this platform are indicated by Fig. 4-5b and Fig. 4-5c. The electrical wires were connected to the sample with silver paste. The small silver paste

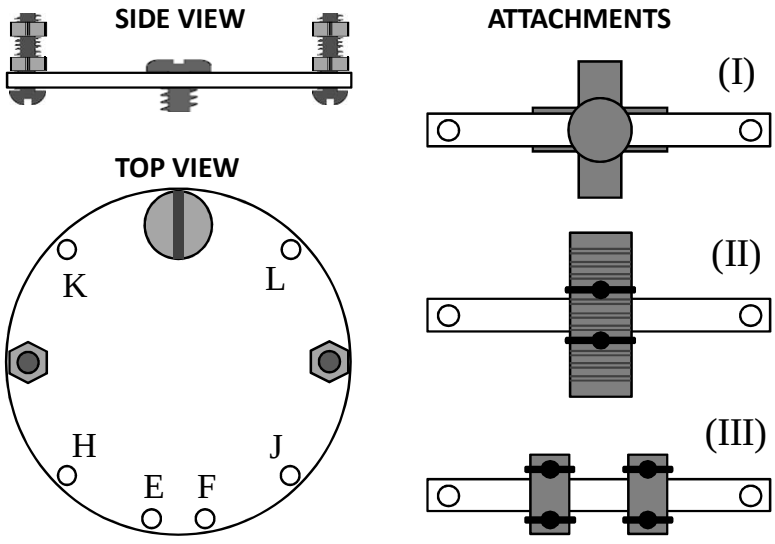

Fig. 4-4. The left side shows the copper disc used as a base-plate for the sample platforms. The labels refer to the Oxford connector pin labels, and indicate holes in the disc for the electrical wires. The right side shows the three attachments used for the resistivity measurements.

contacts were not reliable, and this led to the development of the 3-point pressure-contact platform attachments shown in Fig. 4-6.

Referring to Fig. 4-6a and Fig. 4-6b, sections of 3 mm thick Teflon discs were removed to form these two attachments, which are then fixed to the base-plate in Fig. 4-4. In Fig. 4-6a the voltage electrodes are 0.25 mm thick phosphor-bronze strips. The two top pieces are embedded into the Teflon via two slits. The bottom electrode is fixed to a pin which is free to rotate. The screw controls the pressure exerted by the electrodes on the sample. In Fig. 4-6b the voltage electrodes are 0.4 mm thick phosphor-bronze strips, which are 1 mm wider than the Teflon base to allow for sample contact. The top two are fixed to the Teflon by the two screws. The bottom electrode is attached by the pair of screws, which are rotated simultaneously to control the contact pressure.

The attachment in Fig. 4-6c is 2.5 mm thick and made from epoxy resin (a mould was used). A rectangular copper base-plate was created for this attachment (connected via the three holes). The middle part for the sample is recessed by 1 mm. The dashed lines represent stainless tubes (ϕ1.5 mm) embedded in the epoxy, acting as guides for the three

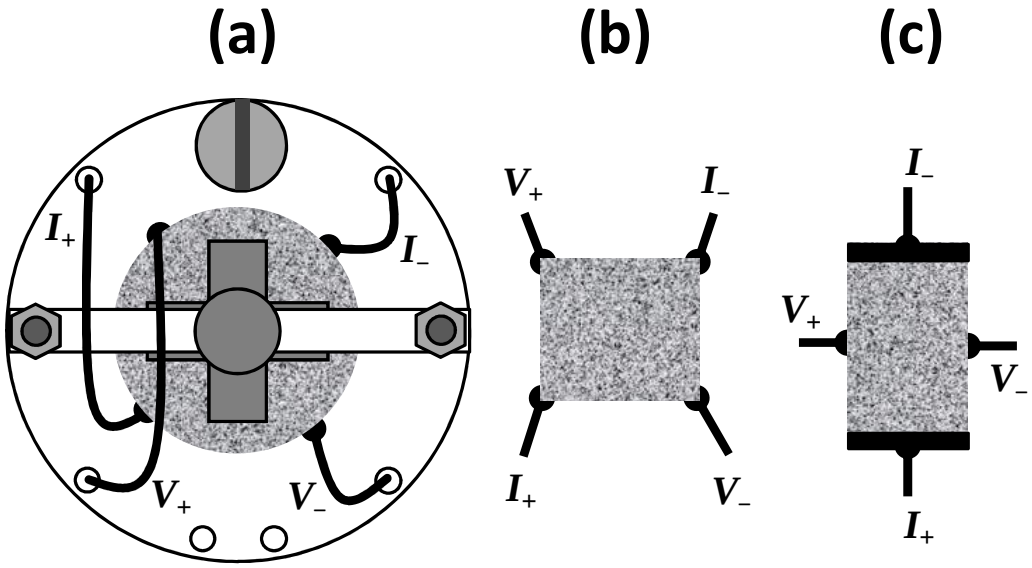

Fig. 4-5. The platform used for the 2-point Hall effect measurements. *V* and *I* refer to the voltage and current leads respectively.

gold-coated pins. The pins were pressed onto the sample's edges by the shaped phosphor-bronze strips (0.4 mm thick), which were anchored to the epoxy by the three screws. Paper was glued onto the pin heads with GE varnish to provide electrical insulation (the phosphor-bronze strips could make contact with the copper base-plate).

All the voltage leads in Fig. 4-6 were soldered to the metal electrodes. The bar samples for these platforms were thin. As indicated in the figure, the current electrodes were painted on the top surface with silver paste. (See §5.4 for more details.) The current leads were then attached by silver paste. Fig. 4-10 in the next section shows the circuit diagrams for the three types of Hall effect measurements.

Each platform had some disadvantages which produced problems for the Hall effect measurements. This was the reason for the development of several platforms. The platform in Fig. 4-6c was the most reliable. For successful runs, however, they all produced consistent results. Table 5-2 and Table 5-3 in chapter 5 indicate which platforms were used for the presented results. The following platform labels were used: 2-a, 2-b and 2-c refer to the 2–point platforms in Fig. 4-5; 3-a, 3-b, and 3-c refer to the 3-point platforms in Fig. 4-6.

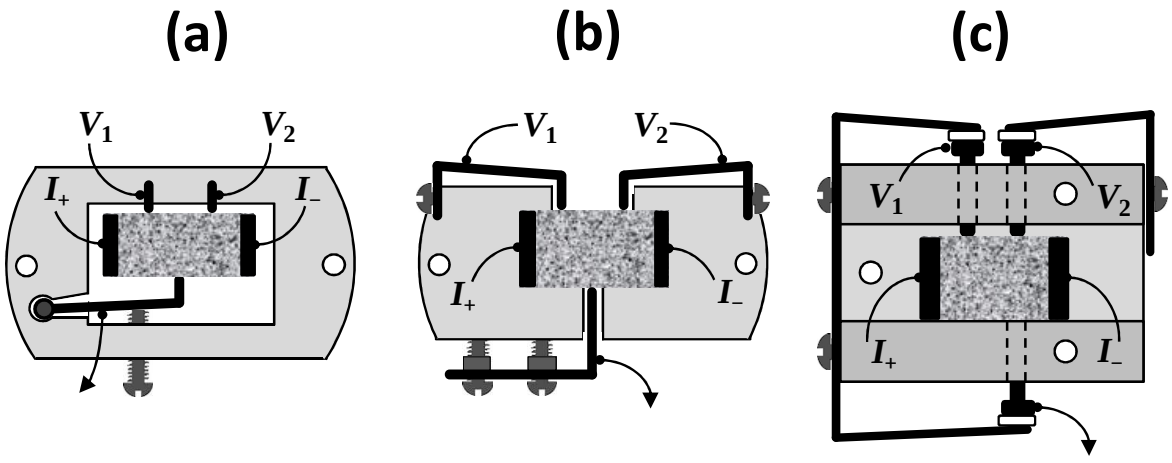

Fig. 4-6. The base-plate attachments used for the 3-point Hall effect measurements. *V* and *I* refer to the voltage and current leads respectively. The common voltage lead for the voltages V_1 and V_2 is shown by ▼.

4.2.4 The transport station

Fig. 4-7 shows the interface box constructed to provide easy access to all the electrical lines on the cryostat insert (Fig. 4-3). The front has two sets of sockets (labelled X and Y), with each set of 10 sockets connected to 10 wires of a shielded twisted-pair cable. The 2 m long cables terminate with a pair of Oxford 10–pin female connectors which attach to the top of the cryostat insert. The front panel provides access to (labels refer to the Oxford 10 – pin labels; 'G' & 'I' not used):

- 2 lines for the current supply to the heater. [Y:A – B]
- 4 unused lines. [Y: C – D and E – F]
- 4 lines for the 4-wire resistance measurements of the Allen-Bradley carbon resistor by the Fluke 8840A multimeter. [Y: H – J and K – L]
- 4 lines for the 4-wire resistance measurements of the carbon glass resistance thermometer by the Lakeshore 234D monitor. [X: A – B and C – D]
- 6 transport lines connected to the sample for the current supply and voltage measurements, which are the focus of this section. [X: E – F, H – J, and K – L] (Refer to Fig. 4-4.) Two lines are used for the current supply, while the other four are used for two voltage measurements.

The side panel of the interface box was used as part of the current supply circuitry, which is shown in Fig. 4-8. Two power supplies were used ('PS1' sockets – Lakeshore 120 current source; 'PS2' sockets – HP 6274B power supply). The current source is limited to 100 mA, and the second power supply was used to provide the larger currents required for some of the Hall effect measurements (up to 250 mA). The 'Source' switch selects the power supply. Before going to the output ('OUT' sockets), the current is measured by a Keithley 617 electrometer (used in ammeter and voltmeter modes). The 'Mode' switch selects whether an ammeter or voltmeter is connected to the 'SENSE' sockets. In I-mode the current goes directly to these sockets with the current measured by an ammeter. In

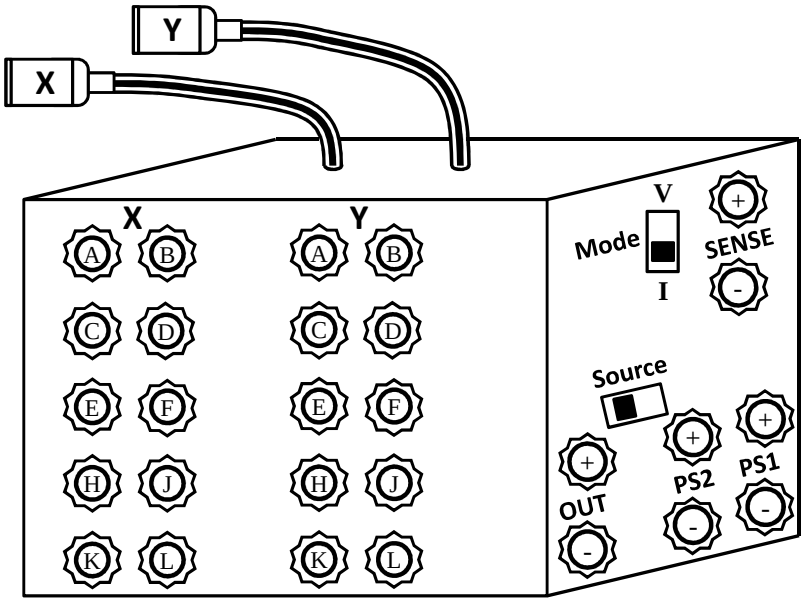

Fig. 4-7. Diagram of the interface box.

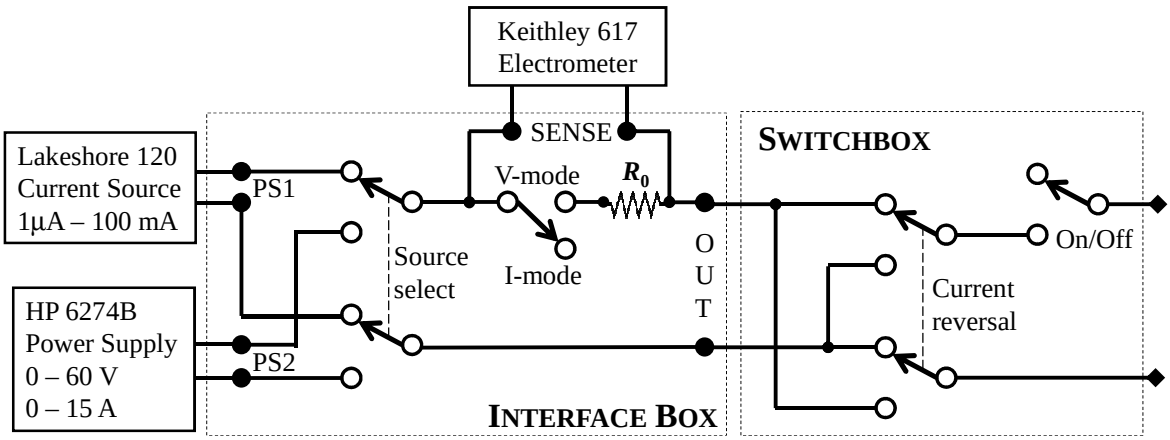

Fig. 4-8. Circuit diagram of the current supply assembly.

V-mode the current passes through a fixed precision resistor and the current is obtained from voltage measurements across the resistor (using Ohm's law $V = IR$). The V-mode was required due to the 30 mA range limit of the Keithley, although it does have the advantage of using the same pair of lines for voltage and current measurements, thereby not requiring manual re-plugging of sensor cables.

A computer-controlled switchbox was also constructed to implement 8 SPDT relay switches. The switchbox was required for software control to switch the current on or off and to reverse the current direction (Fig. 4-8), and to implement the van der Pauw method (Fig. 4-9a). The voltages were measured by an HP 3457A multimeter, which had a 10 channel HP44492 reed-relay multiplexer card. This allowed for several software controlled voltage measurements (only 2 channels were needed at a time).

Fig. 4-9 shows the circuit diagrams for the three different types of resistivity measurements employed. (Refer to §4.2.3 for sample connections and setup.) 'Current Supply' refers to the complete circuit in Fig. 4-8. The van der Pauw method (Fig. 4-9a) uses one of the software-controlled switches on the switchbox. Referring to Fig. 4-1, the

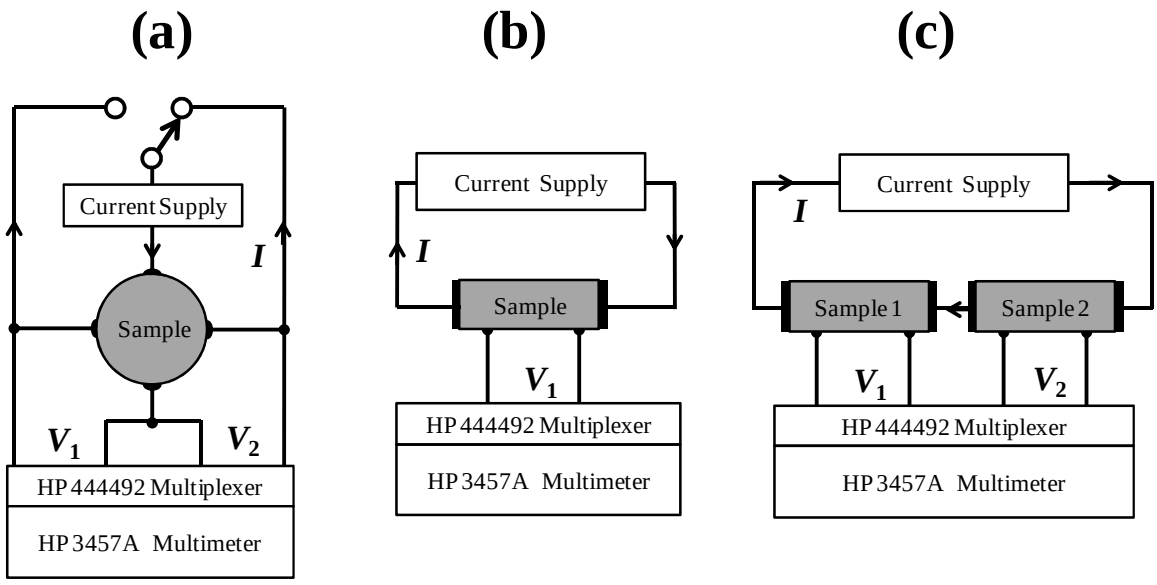

Fig. 4-9. Circuit diagrams for the various resistivity measurements: (a) The van der Pauw method. (b) The single bar-sample setup. (c) The dual bar-sample setup.

voltages V_1 and V_2 are measured for the two switch positions. Before measuring the voltage, a sufficient delay was implemented after switching the current to ensure signal relaxation. (This was also done when reversing the current and switching it on.) For the single bar-sample (Fig. 4-9b), the van der Pauw layout was maintained (the switch was kept at the position shown Fig. 4-9a and voltage V_1 measured). The dual bar-sample setup (Fig. 4-9c), which was implemented for the liquid helium runs, used a separate cable layout. Notice that the two samples are in series, receiving the same current *I*. To optimise voltage measurements, the two samples were chosen with consecutive *x* values having similar resistances. (For example, a high resistance sample 1 would require a low current due to heating effects, and this low current through a low resistance sample 2 would consequently produce too small a voltage.)

Fig. 4-10 shows the circuit diagrams for the three different types of Hall effect measurements. Fig. 4-10a shows the 2-point setup corresponding to the platform in Fig. 4-5. Fig. 4-10b shows the circuit for the 3-point platforms in Fig. 4-6a and Fig. 4-6b. Fig. 4-10c corresponds to the 3-point platform in Fig. 4-6c. Notice that the two voltages V_1 and V_2 in the 3-point circuits have a common contact which is different in the two cases.

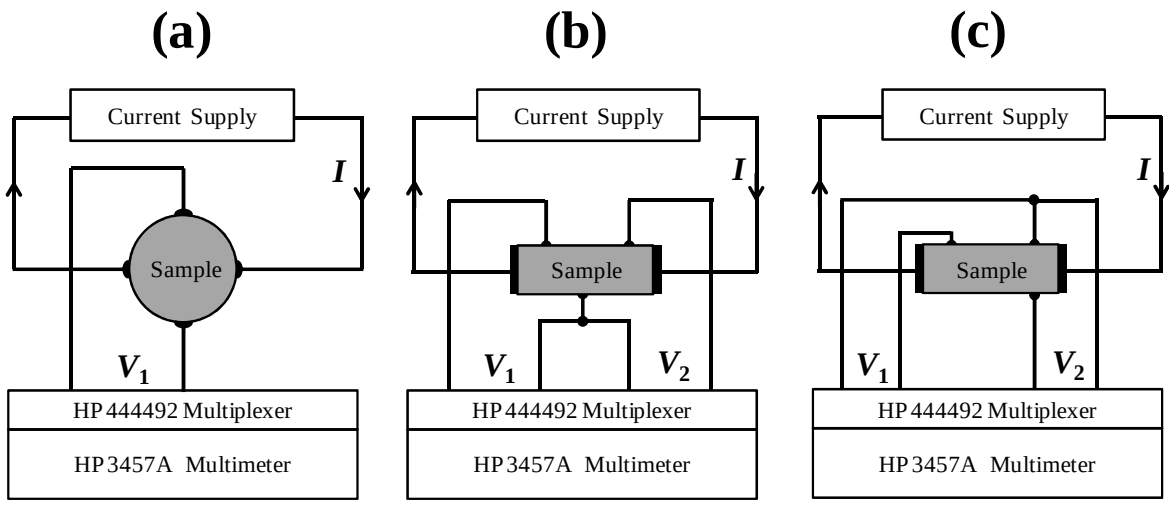

Fig. 4-10. Circuit diagrams for the various Hall effect measurements. The 2-point setup is shown in (a). The two 3-point setups, incorporating dual voltage measurements, are shown in (b) and (c).

Fig. 4-10b represents a dual 2-point Hall effect setup, with each voltage capable of independently measuring the Hall effect and magnetoresistance (see §4.1.3 and Fig. 5-4 in §5.2). In Fig. 4-10c the voltage V_1 directly measures the sample resistivity (including magnetoresistance measurements), while voltage V_2 measures the Hall effect on the oppositely positioned contacts (effectively a 2-point Hall effect setup).

A Pentium-MMX 166 MHz computer was used for the transport station. The computer's built-in 9-pin RS-232 serial interface was used to read the Lakeshore 234D temperature monitor. The eight switches on switchbox were controlled by a custom-built 3*8-bit programmable IO interface card. An IOTech IEEE488 (GPIB) interface card provided the connection to the following equipment: Lakeshore 450 gaussmeter; Oxford ITC503 temperature controller; HP 3457A multimeter; Keithley 617 programmable electrometer. The software for the transport station was written in Turbo Pascal V6.0 (Borland International Inc.) using the Turbo Vision object-oriented framework (Fig. 4-11 shows an example screenshot). In addition to the control of the hardware and the execution of the different measurement algorithms, a dynamic plotting option was included. Essential to the software was the ability to monitor the measured quantities in real-time (e.g. monitoring the signal-drift during Hall effect measurements).

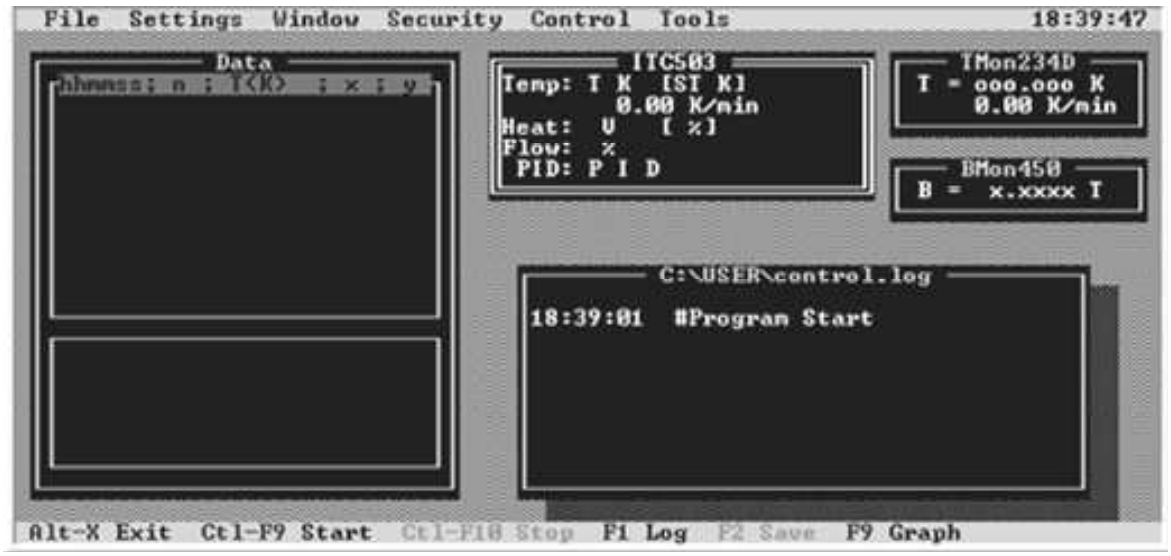

Fig. 4-11. A screenshot of the user interface from the transport station software.

4.3 Testing

This chapter concludes by describing the tests performed on the transport station to ensure proper functioning. The resistivity measurements used several switches to control the current flow, in addition to the voltage-measurement switches inside the multiplexer of the multimeter. Failure of any of these switches, or any other equipment, would lead to improper measurements. Test samples for the van der Pauw and bar-sample configurations were created to regularly check the transport station. Both test samples were attached to Oxford male 10-pin connectors (used on the cryostat insert shown in Fig. 4-3), which were plugged into the connectors of the interface box (Fig. 4-7), thereby emulating the samples inside the cryostat.

The detected Hall voltages were very small (~0.1 μV), which was near the limit of the multimeter resolution. To check that the signals were indeed due to the Hall effect in the sample, and not externally induced signals due to the magnetic field switching, a test run was performed on a piece of copper sheet. The measured Hall coefficient was compared to quoted values. A secondary test, performed several times during the measurements on the tungsten bronze samples, involved rotating the entire cryostat (to rotate the sample) while maintaining the magnetic field. A rotation through 90° is equivalent to switching the perpendicular field on or off. The same voltage signals were observed, indicating that the voltage changes were not external and could be attributed to the sample.

4.3.1 Resistivity test samples

Fig. 4-12 shows the test sample for the van der Pauw setup. The sample was a layer of silver paste painted onto a Perspex plate. The thickness d was unknown, but Eq. 4.1 shows that the measured quantity in the van der Pauw method is ρ/d. The two resistances R_1 and R_2 in Eq. 4.1 were manually measured (using a Fluke 8840A multimeter in a 4-wire resistance mode) resulting in a value of $\rho/d = 8.45 \pm 0.15$ mΩ. This value was reproduced by the transport station when the test sample was connected to the interface box, indicating correct functioning.

A test sample for the bar-sample setup was created in the same way as in Fig. 4-12. Instead of the silver paste layer, a 50 cm length of twisted-pair manganin wire was used.

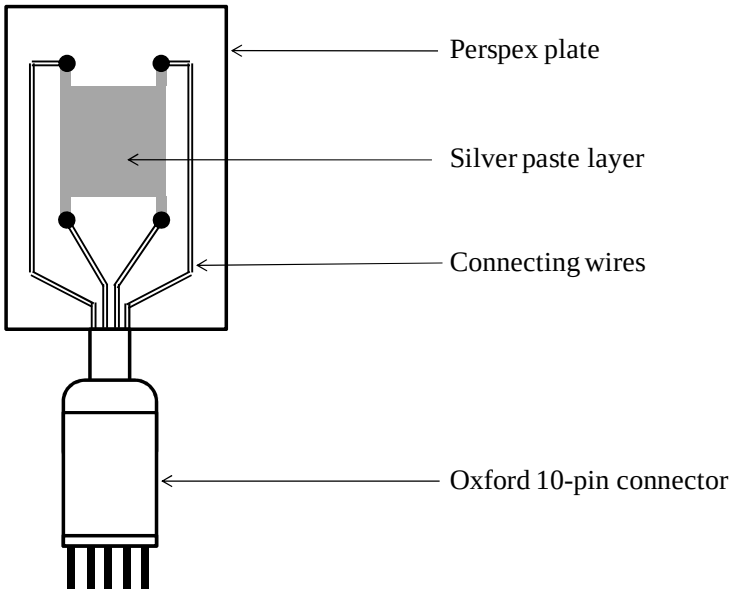

Fig. 4-12. The test sample for checking the equipment for the van der Pauw method.

Manual measurement of the wire's resistance gave R = 1.344 ± 0.003 Ω, which was used as the reference value when checking the transport station prior to measurements on bar-shaped samples.

4.3.2 Hall effect in copper

The results of room temperature Hall effect measurements on a 0.05 mm thick rectangular piece (16×4 mm) of hardened copper sheet are shown in Fig. 4-13a. The wires were attached with silver paste, with the contact placement as in Fig. 4-10b. Refer to §5.2 for a description of the measurement process, and to Eq. 5.4 for the determination of the Hall coefficient R_H = 0.051 ± 0.003 mm^2/C. The Hall concentration is then $n_H = 1/R_H e$ = 1.23 ± 0.07 × 10^{23} cm^{-3}. Quoted values are n_H/n = 1.5 and n_H/n = 1.37, where n = 8.45×10^{22} cm^{-3} is the electron concentration in copper.[62,76] The result here (n_H/n = 1.46 ± 0.09) is in good agreement, indicating proper functioning of the transport station.

Fig. 4-13b shows that the voltage noise levels are unaffected by the application of a current. This fact will be referred to later in §5.2.

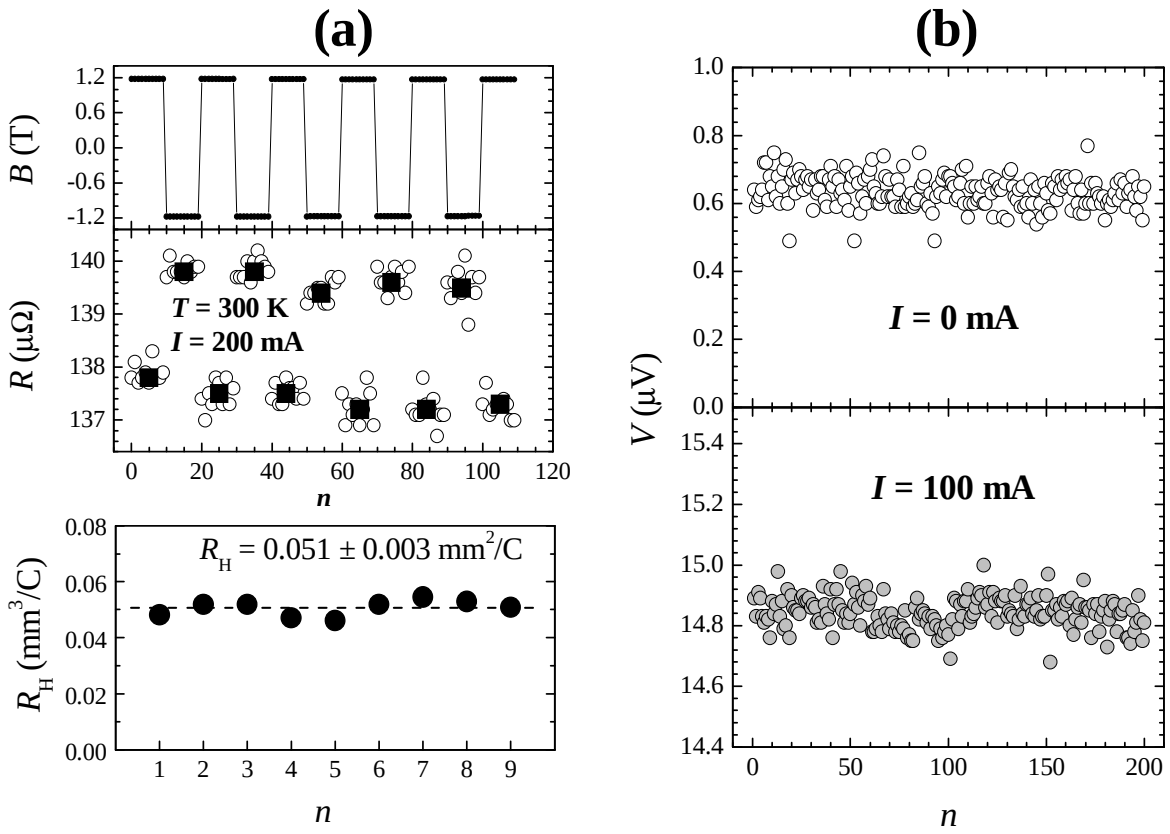

Fig. 4-13. Hall effect results for copper. (a) The magnetic field *B*, the resistance *R* = *V*/*I* (*V* is the detected voltage for the applied current *I*), and the Hall coefficient R_H. (b) The signal voltage for zero and 100 mA currents to indicate noise levels.

Chapter 5: Experimental procedures and results

This chapter presents all the Y_xWO_3 and La_xWO_3 results from the electric transport investigations down to temperatures around 2 K. The electrical conductivity, Hall concentration and magnetoresistance coefficient are obtained. The interfering effect of the magnetoresistance on the Hall voltage is revealed, as well as the methods used to isolate the magnetoresistance from the Hall effect. The magnetic field dependence of the magnetoresistance and Hall effect are investigated to validate the theoretical equations used.

5.1 Conductivity

Electrical conductivity measurements were performed on the range of Y_xWO_3 and La_xWO_3 samples using the four–wire bridge technique for bar-shaped samples. Two samples of La_xWO_3 (x = 0.100 and 0.130) were questionable and hence excluded from the low temperature investigations. The dual–sample platform discussed in §4.2.3 was used. Table 5-1 gives a summary of the Y_xWO_3 and La_xWO_3 samples used in this conductivity investigation. The donor concentration x of each bar–shaped sample is specified, including the thickness d, width w and length L. The crystal volume fraction f is included since the density–corrected conductivity is presented ($\sigma_C = \sigma_{sample}/f$ from appendix D). Note that this first–order estimate of the crystal conductivity calculated from the sample conductivity just scales the data for each x by a constant, with the temperature dependence unaffected. The current I used for each sample is included in the table, and ranged from 0.3 mA to 100 mA depending on the sample's resistance. Current reversal was used to eliminate stray voltages. The current magnitude was varied to ensure no heating effects occurred and also confirmed the ohmic behaviour of the compounds. The lowest temperature T_{min} (~2 K) obtained for each run is specified.

The van der Pauw method was used for two disc-shaped Y_xWO_3 samples (x = 0.050 and 0.200). Table 5-1 shows the diameter of each sample. The two pairs of leads were attached to the disc edge by silver paste at about 90° separations. The results for the thin $Y_{0.200}WO_3$ sample were obtained during preliminary low temperature Hall effect measurements (§5.4). The additional measurement on the $Y_{0.050}WO_3$ sample was performed to confirm that the van der Pauw and bridge methods give consistent results, and to check the distinct

Table 5-1. Sample information for the Y_xWO_3 and La_xWO_3 conductivity measurements. (See text for a description.)

	x	d (mm)	w (mm)	L (mm)	f (%)	I (mA)	T_{min} (K)
Y_xWO_3	0.050	1.20		ϕ13.3	45.0	1, 3, 10, 30	1.66
	0.050	1.66	2.46	7.9	45.0	1, 3, 10, 30	1.96
	0.060	1.51	2.45	7.2	41.3	1, 3, 10, 30	1.96
	0.070	1.25	2.30	9.2	40.2	3, 10	2.36
	0.086	1.80	2.12	6.6	44.9	30	2.24
	0.091	1.15	2.45	10.3	45.7	3, 10	2.36
	0.096	2.10	2.50	7.0	46.0	30	2.14
	0.104	2.05	2.40	6.9	46.4	30	2.01
	0.110	2.05	2.49	6.9	46.6	30, 100	1.86
	0.114	2.00	2.47	7.0	46.7	30, 100	2.43
	0.118	2.05	2.45	7.0	47.0	30, 100	3.49
	0.122	2.00	2.30	6.9	47.2	30, 100	1.85
	0.127	1.05	1.65	9.3	45.4	30	2.36
	0.132	2.00	2.43	7.3	46.3	30, 100	2.17
	0.140	2.00	2.53	7.3	46.2	30, 100	2.44
	0.148	1.90	2.45	7.1	45.8	30, 100	2.73
	0.160	1.30	2.15	9.2	43.9	30	2.36
	0.200	0.54		ϕ15.0	44.3	10, 30	2.06
La_xWO_3	0.050	1.37	2.13	8.9	44.6	0.3, 1, 3	1.98
	0.060	1.69	2.13	9.9	42.2	1, 3	1.92
	0.070	1.28	2.63	9.3	44.6	1, 3	1.92
	0.080	1.50	2.45	8.1	43.7	3, 10	1.96
	0.086	1.15	2.30	8.7	45.6	3, 10	1.96
	0.092	1.20	2.55	9.4	43.9	3, 10	2.36
	0.110	1.20	2.60	9.3	49.5	3, 10	2.36
	0.120	1.60	2.55	9.4	50.9	30	2.48
	0.150	1.65	2.55	8.8	50.7	30	2.48
	0.170	1.10	2.55	9.2	41.4	30, 100	2.45
	0.190	1.15	4.05	11.8	34.1	30, 100	2.45

conductivity behaviour observed for this lowest-concentration sample.

The contact resistance between the gold wires and sample (for voltage readings) was in the range 3 – 13 Ω, and depended strongly on the contact pressure. The contact resistance between the silver paste and sample (for the current supply) was in the range 0.2 – 5 Ω. The contact area of the silver paste was much larger, accounting for the lower contact resistances. The pressure contacts, however, provide a better contact resistance per unit area. The contact resistance increased with lower x samples (also observed in Na_xWO_3)[77], and with lowering the temperatures. Research on various techniques for electrical contacts has been conducted for single crystal Na_xWO_3.[77,90]

The results of the electrical conductivity measurements are summarised in Fig. 5-1 to Fig. 5-3. The data for both cooling and heating of the sample are shown. The experimental uncertainty in σ_C is ~9%, mostly due to dimensional uncertainties. (Uncertainty in voltage

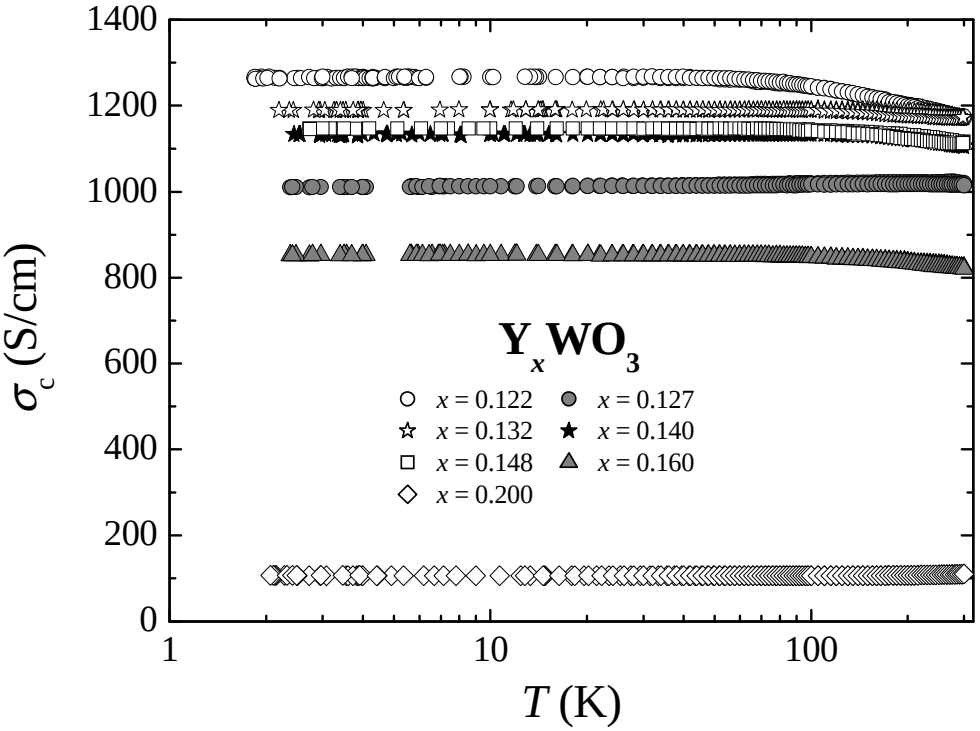

Fig. 5-1. Conductivity results for the higher concentration ($x \geq 0.122$) Y_xWO_3 samples in a linear-log plot of the density-corrected conductivity σ_C vs the temperature T.

lead separation ~0.1 mm; $\delta f/f \sim 2\%$; $\delta d \sim \delta w \sim 0.03$ mm.) The Y_xWO_3 results for $x \geq 0.122$ are shown in Fig. 5-1, and correspond to concentrations near the solubility limit and above (see Fig. 3-8a). The $x = 0.122$ sample is single-phase cubic, whereas the other samples show additional phases increasing with x (Fig. 3-2b). The $x = 0.122$ sample shows the typical metallic behaviour expected of the higher concentration tungsten bronzes (see Fig. 6-2 for a ρ vs T plot). All the other samples also show metallic behaviour with almost no temperature dependence below 100 K. The results are consistent with the "dirty metal" classification introduced in §3.3, with the impurity scattering dominating and decreasing the residual conductivity with increasing x.

Fig. 5-2 presents the conductivity results for the lower concentrations of Y_xWO_3, while Fig. 5-3 gives the results for the whole range of La_xWO_3 samples. In both figures the

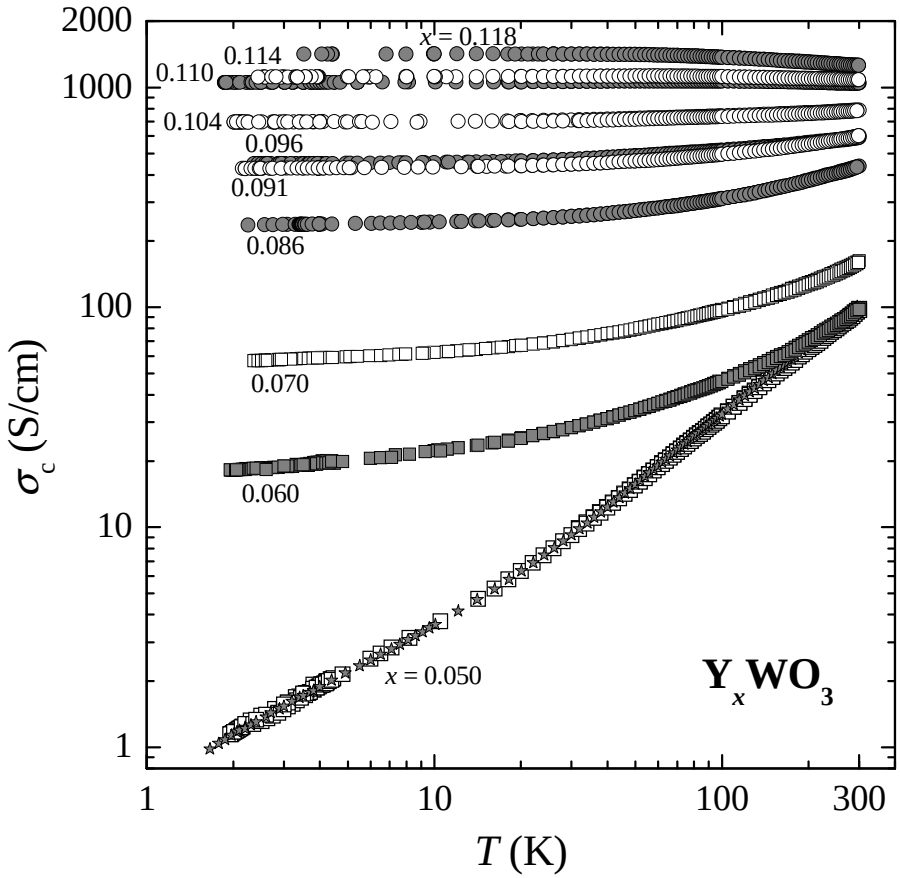

Fig. 5-2. Conductivity results for the lower concentration ($x \leq 0.118$) Y_xWO_3 samples in a logarithmic plot of the density-corrected conductivity σ_C vs the temperature T.

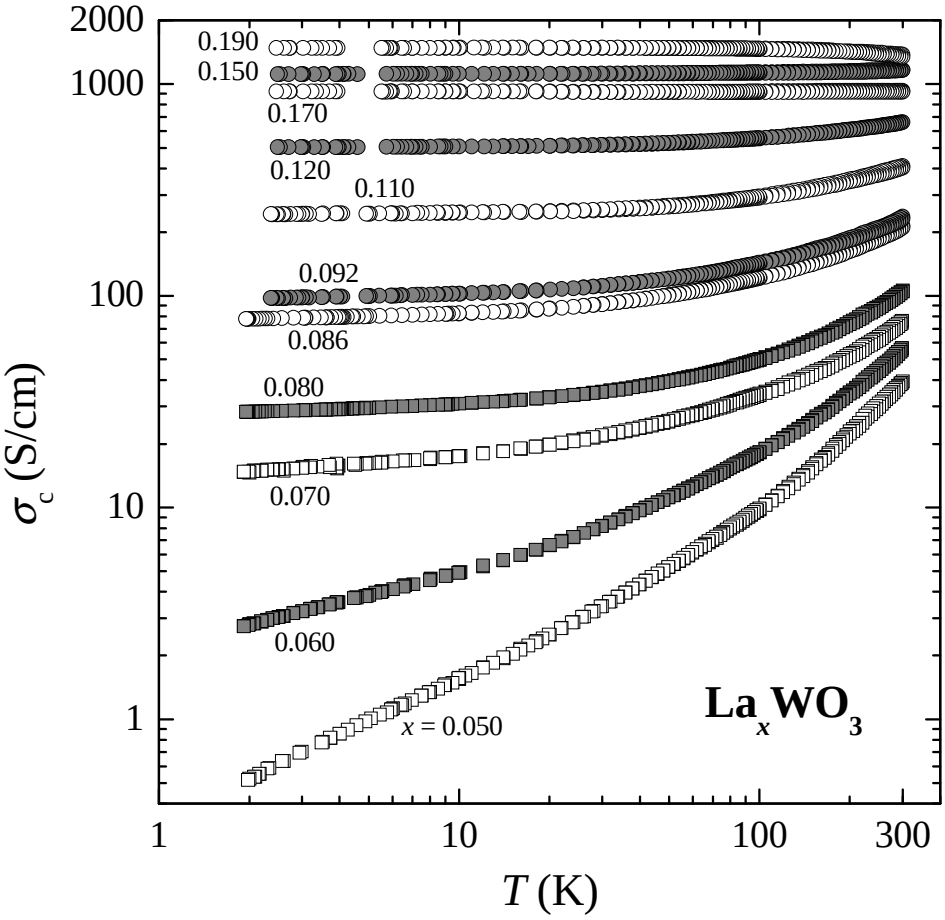

Fig. 5-3. Conductivity results for the La_xWO_3 samples ($0.05 \leq x \leq 0.19$) in a logarithmic plot of the density-corrected conductivity σ_C vs the temperature T.

single-phase cubic samples are shown by the circle symbols. All the cubic phase samples appear metallic with a finite $T \rightarrow 0$ K conductivity. For $Y_{0.050}WO_3$ the second data set (⋆) was obtained using the van der Pauw method on a disc-shaped sample, and the results clearly show that the bridge and van der Pauw methods give equivalent results.

The conductivity results for the two compounds are very similar, as expected from the results in chapter 3. The evolution with x for these polycrystalline samples is consistent with the conductivity behaviour observed in other single-crystal tungsten bronzes.[7,8,26] The family of σ vs T curves for Y_xWO_3 and La_xWO_3 shows features also found in other transition metal oxides as well as doped semiconductors.[3] With decreasing x the conductivity decreases monotonically (with a corresponding change in curvature),

changing from metallic-type ($d\sigma/dT < 0$) to semiconducting-type ($d\sigma/dT > 0$) behaviour. An exception is the $x = 0.150$ and 0.170 data for La_xWO_3, with the curvature as expected ($d\sigma/dT\,|_{0.150} > d\sigma/dT\,|_{0.170}$), but with $\sigma_{0.150}(T) > \sigma_{0.170}(T)$. Fluctuation in the absolute conductivity is expected (Fig. 2-5). The conductivity for both Y_xWO_3 and La_xWO_3 saturates at about 1400 S/cm for the two highest concentrations. This has been attributed to the limiting effect of the grain-boundary scattering. The absolute conductivity of Y_xWO_3 is larger than that of La_xWO_3 for the same x, and leads to a quicker onset of the crossover ($d\sigma/dT = 0$) and saturation with increasing x. The similarity of the $x = 0.114$ and 0.110 curves and the $x = 0.096$ and 0.091 curves for Y_xWO_3 suggests an uncertainty $\Delta x \sim 0.005$ in the nominal x values. The characterisation results in chapter 3 and the analysis in chapter 6 also support fluctuations of this magnitude.

5.2 Magnetic field effects

This section describes the effects of applying a magnetic field to the tungsten bronze samples. The general procedure used to determine the Hall coefficient is shown by looking at the results for a single sample of Y_xWO_3. In particular, the effects of magnetoresistance on the 2-point Hall effect technique are shown. The method used to separate the contributions of the Hall effect and magnetoresistance to the measured signal is presented.

The two main obstacles were signal noise and signal drift. The trick was to choose sufficiently long averaging time intervals to observe the Hall voltages, while ensuring that there was not too much signal drift during a measurement cycle. Thermal stability was crucial to minimise signal drift. For room temperature measurements the samples were left overnight with the current flowing. For most cases this was sufficient. For lower temperatures the samples were immersed in liquid nitrogen or liquid helium by flooding the vertically positioned cryostat. Pumping on the cryogen to maintain a constant pressure provided sufficient thermal stability. Changing the pumping pressure also allowed for measurements at different temperatures (2 – 4 K using liquid helium, and 64 – 75 K using liquid nitrogen). In general the temperature controller for the cryostat did not provide sufficient thermal stability, although a few measurements were successful (see temperatures in Fig. 5-6, Fig. 5-7 and Fig. 5-11).

Fig. 5-4 shows the results of Hall effect measurements on a 0.63 mm thick bar sample of $Y_{0.110}WO_3$. The plots at the top give the applied magnetic field B, which was set at 0 and ±1.2 T. The middle plots give the resistance $R = V/I$. Since the current I is fixed, the middle plots give a measure of the voltage V across the sample. The bottom plots give the rate of change in the resistance $\Delta R/\Delta B$ when changing the magnetic field. n is the data counter.

A three-point platform (platform (b) in Fig. 4-6) was used in obtaining the Hall effect data in Fig. 5-4, with the voltage measured across one pair of contacts. The contacts were unbalanced (not lying on an equipotential line) and this is seen in the zero-field resistance $R_0 \simeq 13$ mΩ. The magnetic field was cycled several times to get better estimates of the Hall voltage, and to reduce the effect of any background signal drifts (see Eq. 5.1 below).

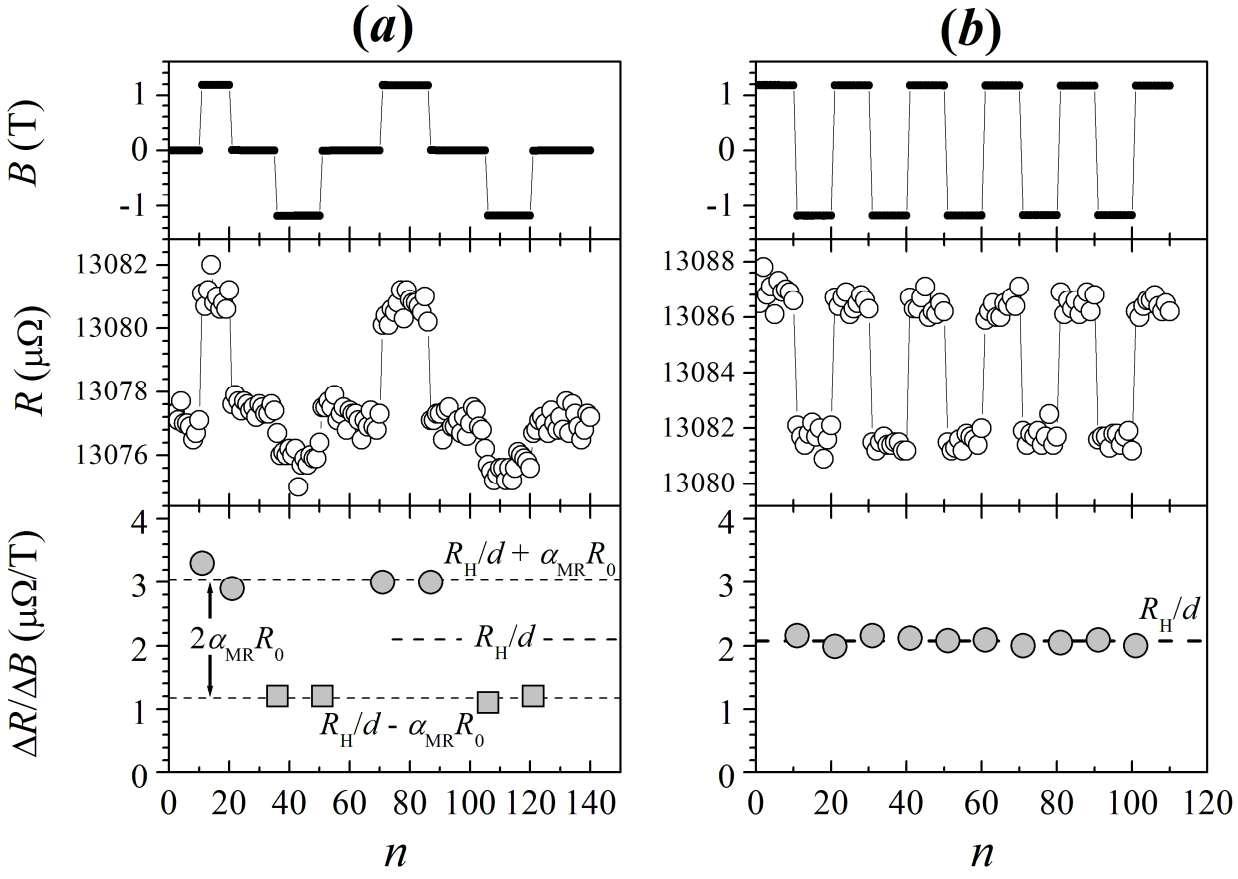

Fig. 5-4. Results from the transport station for a sample of $Y_{0.110}WO_3$ at 75 K using a Hall platform with a current of 200 mA. In (a) the magnetic field is cycled between 0 and ±1.2 T, while in (b) the field is cycled between +1.2 T and -1.2 T. (See text for a description of the plots.)

Although the signal drift during each run in Fig. 5-4 is minimal, there is evidence of significant signal drift when comparing the two runs. Each runs took about 20 min to complete, with a 30 min delay in between. During this delay R_0 changed by about 7 μΩ due to voltage drift, which is significant when compared to the field effects of 2 – 5 μΩ. Monitoring the extent of signal drift during each measurement cycle was therefore essential.

An analysis of the method used here (averaging the jumps $\Delta R/\Delta B$ by cycling the magnetic field several times) gives an uncertainty in the measured quantity $\eta = \Delta R/\Delta B$ due to signal drift as

$$\Delta\eta = \frac{1}{N\Delta B}\sum_{n=1}^{N}(-1)^n \Delta R_n \ . \qquad 5.1$$

N is the number of (even) field switches with ΔB the corresponding change in magnetic field. ΔR_n is the change in the background (B = 0) signal during the switching period (i.e. the signal drift). The expression suggests better estimates for more field cycles and using the largest field available (provided that the signal drift ΔR_n is not in phase with field switching). Due to the $(-1)^n$ term in Eq. 5.1, a uniform signal drift (constant ΔR_n) will not affect the measurements. Very large signal drifts, even when uniform, will swamp the required signals. Thermal stability is therefore crucial.

Each datum in the middle plots of Fig. 5-4 corresponds to a voltage integration time of 5 s. The long integration time was essential to reduce the noise to a level where the magnetic effects were detectable. The field was then kept constant for 10 to 20 readings (50 – 100 s) to further average the signal, and to ensure that there was no significant voltage drift. The time taken to switch the field between 0 and ±1.2 T (Fig. 5-4a) was about 45 s, while it took about 60 s to switch between +1.2 T to −1.2 T (Fig. 5-4b).

Fig. 5-4a shows different changes in R for positive and negative field directions. This difference in $\Delta R/\Delta B$ indicates magnetoresistance effects. Referring to Eq. B.19 in appendix B, the theoretical prediction to the resistance change $\Delta R/\Delta B$ for the three field changes in Fig. 5-4 is

$$0 \leftrightarrow +B_0 \qquad \frac{\Delta R}{\Delta B} = \frac{R_H}{d} + \alpha_{MR} R_0 \qquad 5.2$$

$$0 \leftrightarrow -B_0 \qquad \frac{\Delta R}{\Delta B} = \frac{R_H}{d} - \alpha_{MR} R_0 \qquad 5.3$$

$$+B_0 \leftrightarrow -B_0 \qquad \frac{\Delta R}{\Delta B} = \frac{R_H}{d} \quad . \qquad 5.4$$

Eqs. 5.2 and 5.3 clearly show the different contributions ($\pm\alpha_{MR}R_0$) the magnetoresistance makes to $\Delta R/\Delta B$. By using both field directions it is possible to extract the Hall coefficient and magnetoresistance coefficient. R_H/d is the average of the $\Delta R/\Delta B$ results, while $2\alpha_{MR}R_0$ is the difference, as shown in Fig. 5-4a. To obtain the Hall coefficient directly, referring to Eq. 5.4, the magnetoresistance effect can be avoided by using only positive and negative fields as in Fig. 5-4b. The same value for R_H is obtained. The validity of the above equations, and the electric transport theory presented in appendix B, is checked in the next two sections which present the magnetoresistance and Hall effect results.

From Eq. B.1 in appendix B the Hall voltage is proportional to the applied current. As Fig. 4-13 shows, the noise in the voltage signal is not affected by the application of the current. For the Hall effect measurements the current was therefore chosen sufficiently large to optimise the signal-to-noise ratio. This worked for the higher concentration samples, but as will be observed in the next two sections, measurements on the lowest concentrations at temperatures below 300 K were not obtained. The noise levels were too large to allow for any meaningful measurements. It was also noted that the noise levels were current induced: increasing the current to increase the Hall voltage created significant increase in the noise. The successful results on the higher concentration samples, and the test run on a copper sheet shown in Fig. 4-13, confirm that the anomalous effects on the lower concentrations are due to the samples and not some external effects. One possible explanation for this is the voltage contacts. In the tungsten bronzes creating good contacts becomes more difficult as x is lowered. It is also observed that the contact resistance increases significantly when the temperature is lowered. For the pressure-contact voltage leads the contact resistance showed about a ten-fold increase when going from 300 K to 64 K. Voltage contacts using silver paste behaved even worse.

5.3 Magnetoresistance

The magnetoresistance effect was sufficiently large at liquid helium temperatures to allow for measurements as a function of magnetic field. The first step was to confirm the validity of using Eq. B.17 in appendix B in separating the magnetoresistance from the Hall effect. The results for a bar sample of $Y_{0.091}WO_3$ (0.70×7.50×12.5 mm) and $La_{0.110}WO_3$ (0.75×7.30×11.5 mm) are shown in Fig. 5-5 which shows the magnetic field dependence of the sample resistance. The four-wire bridge method for bar samples (using platform (c) in Fig. 4-6) was used to determine the sample resistance R using a current of 100 mA.

The magnetoresistance is positive for both Y_xWO_3 and La_xWO_3, with similar magnitudes. Fig. 5-5a for La_xWO_3 suggests an increasing magnetoresistance with decreasing temperature. The sample resistance is independent of the field direction,

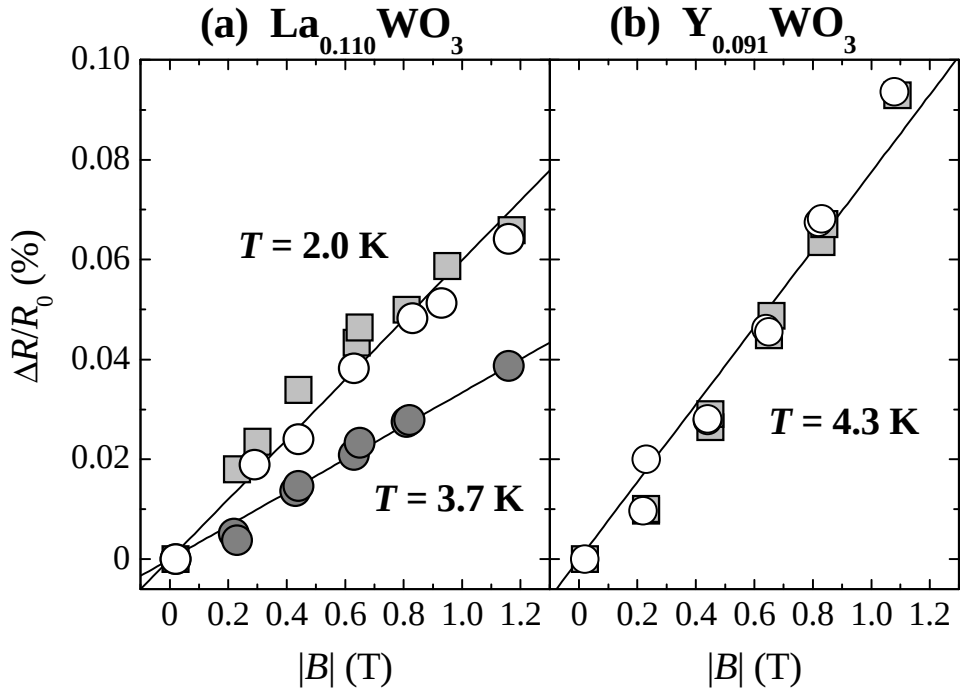

Fig. 5-5. Magnetoresistance results at liquid helium temperatures for a sample of $La_{0.110}WO_3$ (a) and $Y_{0.091}WO_3$ (b). The fractional change in resistance $\Delta R/R_0$ vs the magnetic field strength $|B|$ is shown. Results for the reversed field direction are shown by square symbols. The straight lines are linear fits of the data (forced through the origin).

consistent with the isotropic behaviour expected for these polycrystalline materials.

The resistance increases with magnetic field strength in a near-linear manner. Power law fits ($\Delta R/R_0 \propto |B|^m$) to the data give exponents $0.8 < m < 1.4$. The variation in the exponent is most likely due to signal drift, and a linear relationship with $m = 1$ is the most plausible. The straight lines in Fig. 5-5 are linear fits of the data and give a sufficient description of the magnetoresistance (considering that the uncertainty in the data is ~20%). The slope of the data, referring to Eq. B.17 in appendix B, gives the magnetoresistance coefficient

$$\alpha_{\mathrm{MR}} = \frac{\left(\Delta R / R\right)}{\Delta\left|B\right|} \ . \qquad 5.5$$

The magnetoresistance of the tungsten bronzes samples is therefore quantified here with the magnetoresistance coefficient α_{MR} by measuring the fractional change in the sample resistance in going from zero to ±1.2 T magnetic fields. Samples for which magnetoresistance measurements were successful are specified in Table 5-2. All the samples are of thin bar-shaped geometry (d – thickness; w – width; L – length). The four-wire bridge method for bar samples was used to determine the sample resistance (using the platforms in Fig. 4-6). The current I used at each temperature T ranged from 30 – 250 mA. The measurement procedure is as described in §5.2 and the setup excluded the Hall effect in the signal (using configuration 1 in Fig. B-4 of appendix B). All the measurements were made in a magnetic field of 0 and 1.2 T.

The results for α_{MR} are plotted in Fig. 5-6 for Y_xWO_3 and in Fig. 5-7 for La_xWO_3. Low temperature measurements for the lowest concentrations were not successful, as discussed in the previous section. The horizontal dashed lines in Fig. 5-6 and Fig. 5-7 show the resolution of the magnetoresistance measurements. The sensitivity was limited by signal noise and drift, and values below ~0.03 should be considered as zero or undetectable. All room temperature measurements showed no magnetoresistance effects, with detection only for $T \lesssim 75$ K which produced positive magnetoresistance for all samples. The results for La_xWO_3 are similar to those of Y_xWO_3. The magnetoresistance in Y_xWO_3 for $50\ \mathrm{K} < T < 75\ \mathrm{K}$ appears to vanish rapidly for $x \sim 0.13$. This could highlight the anomalous behaviour observed in the transport properties near the solubility limit (Fig. 3-11a and Fig. 3-14).

Table 5-2. Sample information for the Y_xWO_3 and La_xWO_3 magnetoresistance measurements. (See text for a description.)

	x	*d* (mm)	*w* (mm)	*L* (mm)	*I* (mA)	*T* (K)	Platform
Y_xWO_3	0.060	0.81	7.50	12.2	100	300	3-c
	0.070	0.81	7.50	12.8	100	64	3-c
	0.091	0.70	7.50	12.5	200	300	3-c
					100	64, 30, 4.3, 3.8, 1.9	
	0.096	0.46	5.65	14.7	250	300	3-a
					250, 200	64	
	0.104	0.57	6.70	12.7	200	300, 64	3-b
	0.110	0.56	5.45	14.5	200	300, 64	3-b
					100	30	
		0.63	5.75	12.8	200	75	3-b
	0.114	0.54	5.95	12.5	200	300, 64	3-b
	0.118	0.45	6.10	12.3	200	300	3-b
					100	64	
	0.122	0.58	6.10	12.2	200	300, 75	3-b
					100	64	
	0.127	0.41	4.75	14	200	300, 75	3-b
		0.69	7.55	12.0	100	50, 3.8, 2	3-c
	0.132	0.57	5.90	12.4	200	300, 64	3-b
	0.140	0.67	6.35	11.9	200	300	3-b
	0.148	0.58	6.00	12.4	200	300, 64	3-b
	0.160	0.54	5.50	14	200	300, 64	3-b
La_xWO_3	0.070	0.84	7.50	12.3	100	300	3-c
	0.080	0.89	7.60	12.4	100	300	3-c
	0.086	0.84	7.60	12.4	200	300	3-c
					100	64	
	0.092	0.97	7.55	12.0	100	300	3-c
		1.20	5.45	12.7	100	4, 2	
	0.110	0.75	7.30	11.5	200	300	3-c
					100	4	
					30, 100	2	
	0.120	0.80	6.50	12.3	200	300, 64, 30	3-c
	0.150	0.76	7.55	8.5	200	300, 64	3-c
	0.170	0.89	7.55	11.6	200	300, 64, 30, 4, 2	3-c

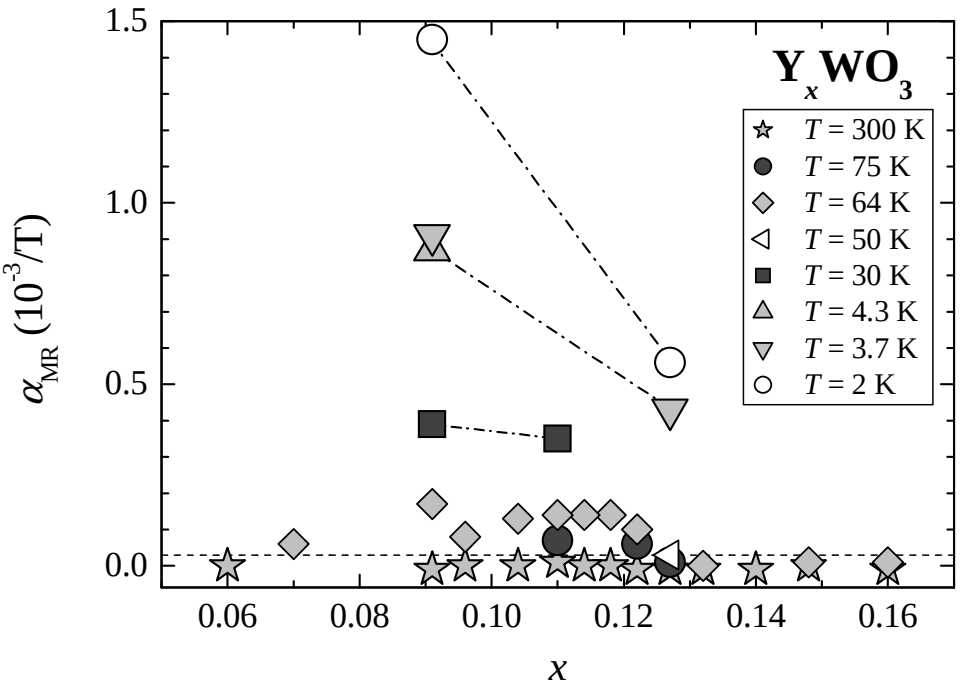

Fig. 5-6. Magnetoresistance results for Y_xWO_3 in a plot of the magnetoresistance coefficient α_{MR} vs x at various temperatures.

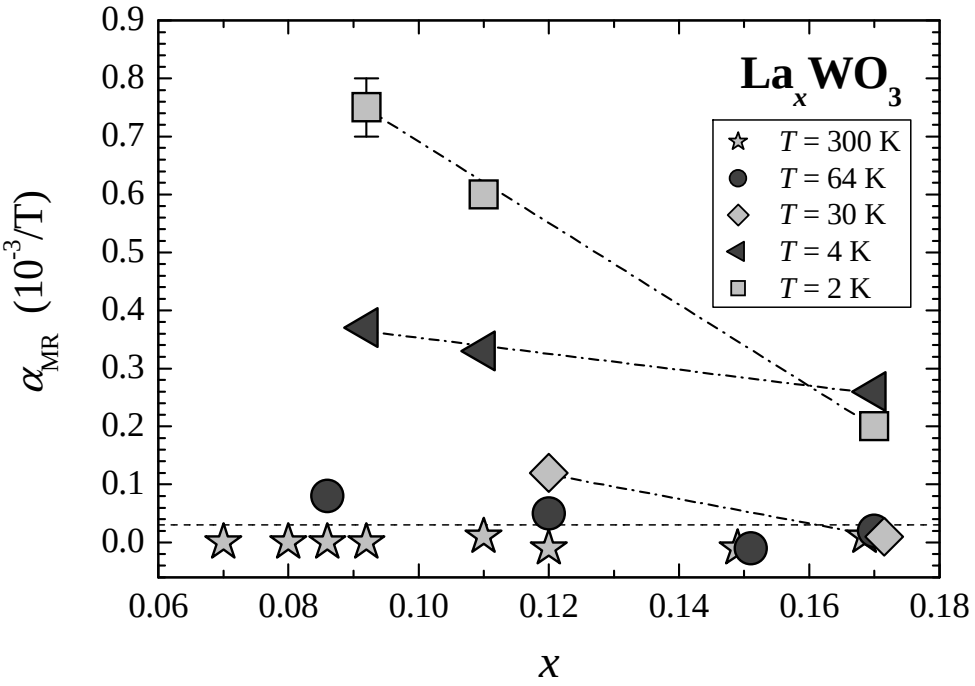

Fig. 5-7. Magnetoresistance results for La_xWO_3 in a plot of the magnetoresistance coefficient α_{MR} vs x at various temperatures.

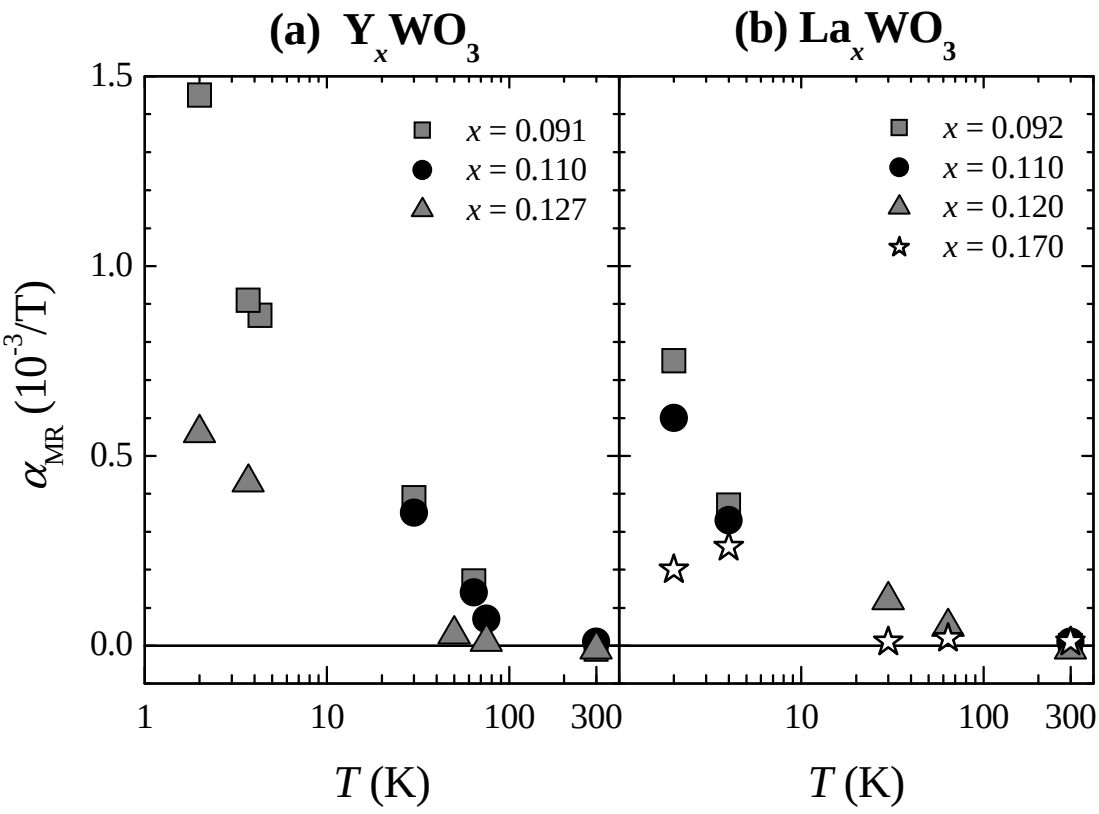

Fig. 5-8. Magnetoresistance results for Y_xWO_3 and La_xWO_3 showing linear-log plots of the magnetoresistance coefficient α_{MR} vs the temperature T for various concentrations x.

The general behaviour of the magnetoresistance for Y_xWO_3 and La_xWO_3 is summarized in Fig. 5-8 by plotting the magnetoresistance coefficient α_{MR} for selected samples. Both compounds indicate a similar behaviour. A positive magnetoresistance with similar magnitude is observed for $T < 100$ K. A monotonic increase with decreasing temperature occurs, and the magnetoresistance increases with decreasing concentration x. An exception is the highest concentration $La_{0.17}WO_3$ sample, which shows a distinctly different behaviour at the lowest temperatures.

5.4 Hall concentration

Measurements of the Hall coefficient R_H were performed on the Y_xWO_3 and La_xWO_3 samples at various temperatures. Detection of the required Hall voltage was not successful for all samples and temperatures. This was mainly attributed to poor voltage contacts, and accounts for the development of several platforms during the research (see §4.2). The failure of Hall coefficient measurements is particularly noticeable in the low x samples at low temperatures, as discussed in §5.2.

The details of the measurement procedure are specified in §5.2. All the platforms shown in Fig. 4-5 and Fig. 4-6 produced equivalent results. The platforms with pressure-contact voltage leads were more successful than using silver paste contacts. For the 3-point platforms, the 2-point technique was used on the two pairs of voltage leads (with one common lead). The second pair served as a check of the results, and the additional measurements also provided better estimates of the Hall coefficient. For Hall effect measurements the pair of voltage leads must be connected to the two sides of the sample (as shown in configuration 2 of Fig. B-4 in appendix B). The standard technique of balancing the voltages in a 3-point setup was investigated, but did not provide any additional benefits in the results.

Table 5-3 gives the details for the successful Hall coefficient measurements. All the samples were bar shaped (d – thickness; w – width; L – length), with the exception of the $x = 0.050$ disc-shaped sample (ϕ – diameter). The current I used at each temperature T is specified and ranged from 30 – 250 mA. The platform labels refer to the 2- and 3-point Hall effect platforms in Fig. 4-5 and Fig. 4-6. For several concentrations a second sample set was measured to check the results. The measured quantity is R_H/d (Eqs. 5.2 – 5.4), and the sample thickness (d ~ 0.7 mm) was made small to optimise the Hall effect signal. The width (w ~ 7 mm) was larger to provide a good surface area for the silver-paste current contacts and to reduce contact resistance. The current electrodes were placed on the top surface edges with a thickness ~1 mm (Fig. 4-6).

Hall effect results are summarised by presenting the Hall concentration $n_H = (R_H e)^{-1}$. The sign of R_H confirms negative charge carriers for both Y_xWO_3 and La_xWO_3. Uncertainties in n_H are ~8%, with $\delta d/d$ ~ 4% and the standard error of the mean ~4% for

Table 5-3. Sample information for the Y_xWO_3 and La_xWO_3 Hall coefficient measurements. (See text for a description.)

	x	*d* (mm)	*w* (mm)	*L* (mm)	*I* (mA)	*T* (K)	Platform
Y_xWO_3	0.050	1.15	ϕ = 13.3		100	300	2-a
	0.060	0.81	7.50	12.2	100	300	3-c
	0.070	0.45	9.6	13.9	100	300	2-c
					30, 100	64	
		0.81	7.50	12.8	100	300	3-c
	0.086	0.57	5.00	13.0	100, 200	300	2-c
					30, 100, 200	64	
	0.091	0.70	7.50	12.5	100, 200	300	3-c
					100	64, 30, 3.7, 1.9	
	0.096	0.39	7.00	13	250	300	2-c
					100, 250	64	
		0.46	5.65	14	100, 200, 250	300	3-a
					200, 250	64	
	0.104	0.57	6.70	12.7	200	300	3-b
		0.58	5.20	14	200	300	3-b
	0.110	0.63	5.75	12.8	100, 200	300	3-b
					200	75	
					100	64	
		0.56	5.45	14	200	300, 64	3-b
					100	30	
	0.118	0.45	6.10	12.3	100, 200	300	3-b
					100	64	
		0.59	5.35	14	200	300	3-b
					100	64	
	0.122	0.58	6.10	12.2	200	300, 75	3-b
					100	64	
		0.46	6.25	14	100, 200	300, 64	2-c
	0.127	0.41	4.75	12.0	100, 200	300, 75	3-b
		0.69	7.55	12.0	100	300, 150, 98, 50	3-c
					100	25, 10, 3.7, 2	
	0.132	0.57	5.90	12.5	100, 200	300, 64	3-b
		0.55	5.95	14	200	300, 75	3-b
	0.140	0.67	6.35	12.0	200	300, 75, 64	3-b
	0.148	0.58	6.00	12.5	100, 200	300, 64	3-b
		0.91	5.30	14	200, 250	300	3-b
	0.160	0.54	5.50	11.8	100, 200	300, 64	3-b
La_xWO_3	0.060	0.84	7.55	12.1	100	300	3-c
	0.070	0.84	7.50	12.3	100	300	3-c
	0.080	1.50	6.00	12.6	100	300	3-c
		0.89	7.60	12.4	100	300	3-c
	0.086	0.66	7.60	11.2	100	300	3-c
		0.84	7.60	12.4	200	300	3-c
	0.092	0.70	7.40	9.8	100	300	3-c
		1.20	5.45	12.7	100	300	3-c
	0.110	0.75	7.30	11.5	200	300, 64	3-c
	0.120	0.80	6.50	12.3	200	300, 64	3-c
	0.150	0.76	7.55	8.5	200	300, 64	3-c
	0.170	0.89	7.55	11.6	200	300, 64, 30, 3.8, 2	3-c

the measurements of R_H/d. The results obtained from a second sample set at both room and liquid nitrogen temperatures are consistent with the first sample set results. The fluctuations in n_H, particularly noticeable in the higher x data at 300 K, are attributed to uneven surfaces (discussed in §3.2.5).

Fig. 5-9 shows n_H vs x for Y_xWO_3 at room and liquid nitrogen temperatures. The lower temperature data are at 64 K and 75 K. The two temperatures are not distinguished in the plot since the n_H values at 64 K and 75 K are very similar. The liquid nitrogen results also show saturation for $x \gtrsim 0.13$, and support the solubility limit ideas discussed in chapter 3 for the room temperature data. All the samples show a reduction in n_H on cooling. Both temperatures show a linear behaviour in n_H at lower x. Extrapolating the low temperature results to $n_H = 0$ gives a possible estimate $x_C \sim 0.05$ for the critical concentration. This is consistent with the upper bound of 0.08 based on the stability of the cubic phase (§3.3).

Fig. 5-10 shows n_H vs x for La_xWO_3 at 300 K and 64 K. The apparent constancy of the 300 K data for $x \geq 0.12$ (also suggesting saturation) is due to experimental fluctuations, as

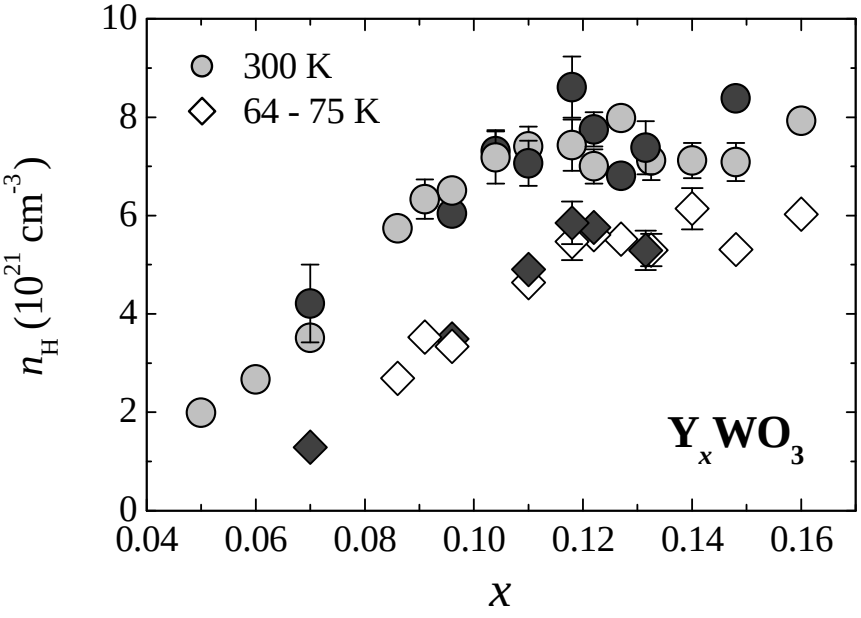

Fig. 5-9. Hall coefficient R_H results for Y_xWO_3 samples at room and liquid nitrogen temperatures in a plot of the Hall concentration $n_H = (R_He)^{-1}$ vs x. (Darker symbols represent a second sample set.)

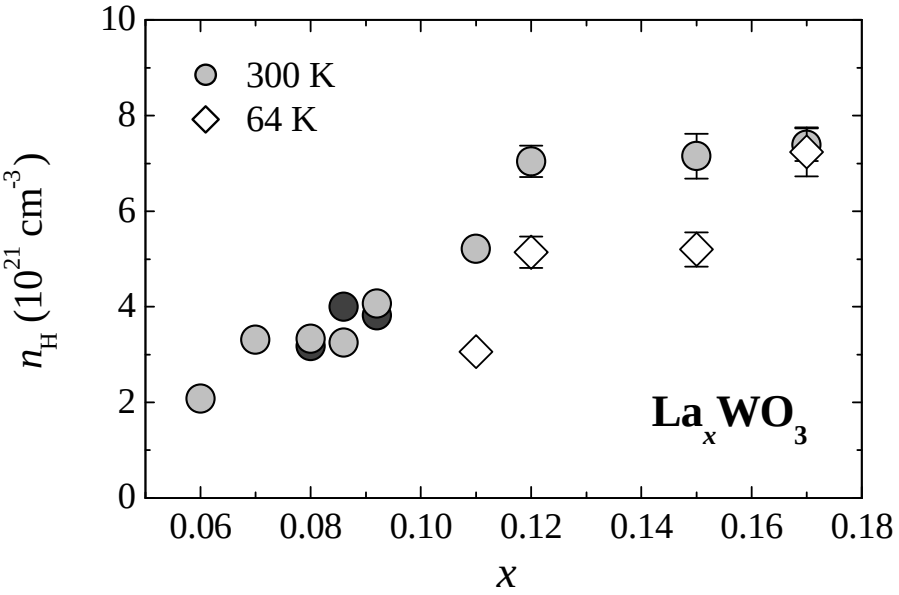

Fig. 5-10. Hall coefficient R_H results for La_xWO_3 samples at room and liquid nitrogen temperatures in a plot of the Hall concentration $n_H = (R_H e)^{-1}$ vs x. (Darker symbols represent a second sample set.)

evidenced by the 64 K data. Except for the highest concentration (x = 0.17) the Hall concentration decreases on cooling as for Y_xWO_3. As expected, the results for La_xWO_3 are comparable to those of Y_xWO_3.

Fig. 5-11 shows n_H vs T down to 2 K for the few successful Y_xWO_3 and La_xWO_3 low temperature measurements. All the samples are single-phase cubic, and show a monotonic reduction in n_H on cooling. Most of the change in n_H occurs at the higher temperatures, and for $T \lesssim 30$ K appears to plateau. The results therefore suggest a non-zero carrier concentration as $T \rightarrow 0$K. This is consistent with previous observations (chapter 3 and §5.1) that single-phase cubic samples are metallic. The extent of carrier freeze-out decreases with increasing x. This suggests, for sufficiently large x, a temperature independent Hall concentration as is found in typical metals.

Fig. 5-12 shows Hall effect results at 2 K for a disc-shaped sample of $Y_{0.20}WO_3$ (d = 0.050 mm; ϕ = 15 mm) using the van der Pauw method with a current of 100 mA. The signal drift in this case was sufficiently small to investigate the Hall effect signal as a

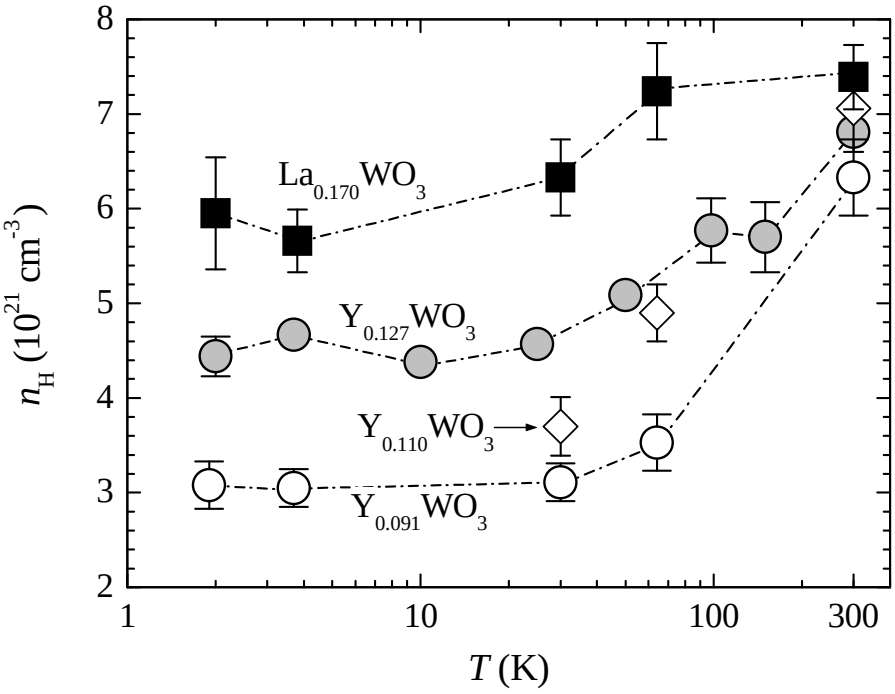

Fig. 5-11. The Hall concentration $n_H = (R_H e)^{-1}$ of Y_xWO_3 and La_xWO_3 samples as a function of the temperature T for several concentrations.

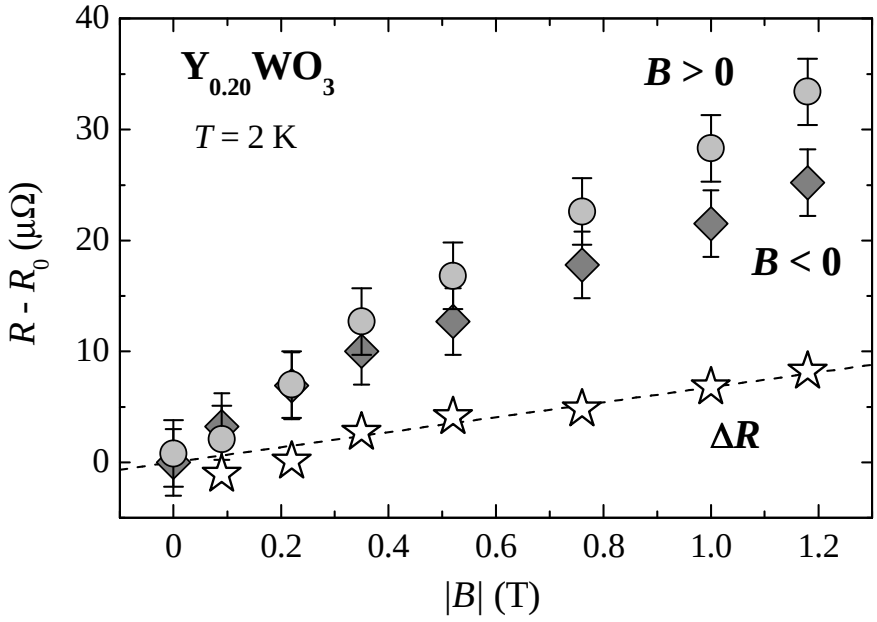

Fig. 5-12. The change in resistance $R - R_0$ at 2 K for a sample of $Y_{0.20}WO_3$ as a function of magnetic field strength $|B|$ for two field directions. ΔR is the difference in this data with the dashed line a linear fit (forced through the origin).

function of magnetic field B. The change in resistance $R - R_0$ vs the field strength $|B|$ is shown for both field directions. From Eq. B.19 in appendix B, with R_+ and R_- the sample resistances for the two field directions,

$$\begin{aligned} R_+ - R_0 &= \left(\alpha_{MR} R_0 + \frac{R_H}{d} \right) |B| \qquad B > 0 \\ R_- - R_0 &= \left(\alpha_{MR} R_0 - \frac{R_H}{d} \right) |B| \qquad B < 0 \end{aligned} \tag{5.6}$$

and hence

$$\Delta R = R_+ - R_- = 2\left(\frac{R_H}{d} \right) |B| \ . \tag{5.7}$$

The fact that $R - R_0$ is positive for both field directions shows that the magnetoresistance is dominant ($\alpha_{MR} R_0 > R_H/d$). The difference ΔR between the data, which is also shown in the plot, is due to the Hall voltage (Eq. 5.7). The above equations predict a linear dependence on the field strength, and within experimental error this is the case. The experimental results therefore show consistency with the theory in appendix B. Referring to Eq. 4.2, the results here emphasize that the van der Pauw expression for the Hall coefficient is only valid if the magnetoresistance is absent ($\alpha_{MR} = 0$ in Eq. 5.6) or if the voltage contacts are balanced ($R_0 = 0$ in Eq. 5.6).

From the slope of the fit in Fig. 5-12 and using Eq. 5.7 the Hall concentration is $n_H = 3.7 \times 10^{21}$ cm^{-3}. Referring to Fig. 5-11, the n_H value is smaller and close to that for $x = 0.127$, which is at the upper cubic limit $x_{max} \sim 0.13$. This again lends support to a solubility limit at x_{max} with the carrier concentration not increasing for $x > 0.13$, consistent with the observations in Fig. 5-9. Further evidence comes from the magnetoresistance results in Fig. 5-6 and Fig. 5-7. The 2 K data shows a significant monotonic decrease in α_{MR} with increasing x on the cubic phase range, with $\alpha_{MR} \simeq 0.56$ T^{-1} for $Y_{0.127}WO_3$ near the solubility limit. From Eq. 5.6 the magnetoresistance coefficient for $Y_{0.200}WO_3$ is obtained from the average slopes of the data in Fig. 5-12, giving $\alpha_{MR} \simeq 0.7$ T^{-1}. This is close to the value at $x = 0.127$, and not significantly smaller as expected from an extrapolation of the cubic phase behaviour.

Chapter 6: Analysis and Discussion

This chapter summarises the transport results for the Y_xWO_3 and La_xWO_3 samples. The low temperature conductivity results are analysed using available expressions for MI transition phenomena. Estimations of the critical concentration x_C are presented. Comparisons of the conductivity and Hall concentration for Y_xWO_3 and La_xWO_3 are made to Na_xWO_3 and $Na_xTa_yW_{1-y}O_3$ data. Unless stated otherwise, the density–corrected conductivity (resistivity) is presented. Measurements of the specific heat, magnetization and NMR, performed on selected samples at the Florida State University (U.S.A.), are presented. These were done to check for local moment formation based on the temperature dependence of the Hall concentration. The chapter concludes with a summary of the research results.

6.1 The solubility limit

Previous investigations have suggested a solubility limit for donor ions in the tungsten bronzes with increasing x (§2.1.1). This limit corresponds to the upper cubic phase limit x_{max}. The suggestion is supported by the experimental results for Y_xWO_3 where $x_{max} \simeq 0.13$ (§3.3). For $x > x_{max}$ the tungsten bronze phase appears to be cubic with a constant donor concentration. The cubic lattice parameter is constant for $x \gtrsim 0.13$ (Fig. 3-4), consistent with a fixed conduction band concentration, as also evidenced by the constancy of the Hall concentration on this range (Fig. 3-11a and Fig. 5-9). The solubility limit is also indirectly supported by the resistivity results. The imbalance in the reaction equation for $x > x_{max}$ results in the formation of additional compounds, as shown by the XRD results (Fig. 3-2b), and these compounds result in additional scattering centres. This leads to the increased resistivity observed for $x > 0.13$ (Fig. 3-8a), and the "dirty metal" type temperature dependence (Fig. 3-9 and Fig. 5-1). The results for La_xWO_3 also support a solubility limit with the cubic lattice parameter constant for $x \geq 0.21$ (Fig. 3-4), with additional phases for $x = 0.23$ (Fig. 3-3b).

Based on the above discussion the upper cubic limit for La_xWO_3 is taken as $x_{max} \sim 0.21$. The room temperature Hall concentration n_H vs x data for La_xWO_3 in Fig. 3-11b appears to follow that of Y_xWO_3 in Fig. 3-11a. The apparent constancy of n_H for La_xWO_3 on the cubic range ($0.12 \leq x \leq 0.17$) has been attributed to experimental error, particularly to uncertainties in sample geometry arising from fluctuations in the sample thickness d (§3.2.5). To confirm this, a plot of $n_H(64\ K)/n_H(300\ K)$ vs x is shown in Fig. 6-1. Each datum corresponds to a sample for which measurements were made at both 64 K and 300 K. Since $n_H = (R_H e)^{-1}$, with R_H the Hall coefficient, and $R_H/d = \Delta R/\Delta B$ (Eq. 5.4),

$$\frac{n_H(64\ K)}{n_H(300\ K)} = \frac{R_H(300\ K)/d}{R_H(64\ K)/d} = \frac{\frac{\Delta R}{\Delta B}(300\ K)}{\frac{\Delta R}{\Delta B}(64\ K)} \qquad 6.1$$

The last term is essentially the ratio of the measured Hall voltages at 300 K and 64 K, and does not contain the sample thickness d. The Hall concentration ratio for two temperatures therefore eliminates the need for sample geometry information.

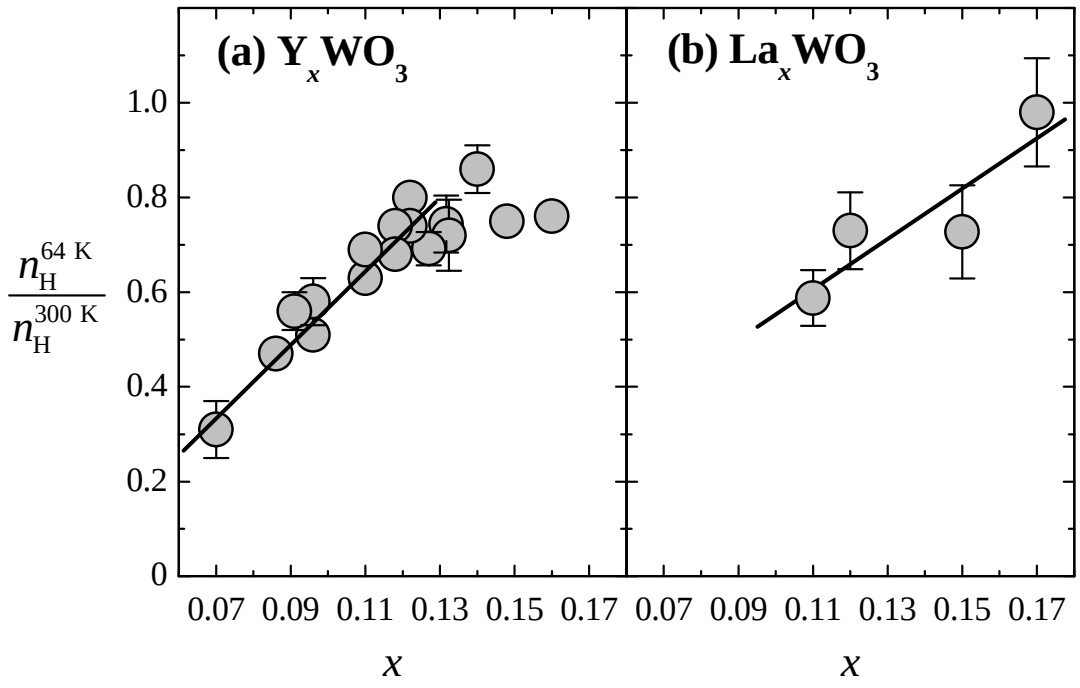

Fig. 6-1. The Hall concentration ratio $n_H(64\ K)/n_H(300\ K)$ vs x for Y_xWO_3 (a) and La_xWO_3 (b). The straight lines are linear fits ($x < 0.13$ for Y_xWO_3).

The Hall concentration ratio for Y_xWO_3 in Fig. 6-1a shows a linear increase with x for $x < 0.13$, indicated by the straight-line fit. For $x > 0.13$ the ratio appears constant at about 0.8, consistent with a solubility limit at $x_{max} \sim 0.13$. The La_xWO_3 results in Fig. 6-1b suggest an increasing ratio up to $x = 0.17$, with no indication of saturation as for Y_xWO_3. The straight line is a linear fit of the data, and within experimental error gives a sufficient description. The slope of the line is similar to that of Y_xWO_3 for $x < 0.13$. The results in Fig. 6-1 therefore do not suggest any anomalous behaviour for La_xWO_3 on its cubic-phase range. This is also supported by the La_xWO_3 conductivity results which show the expected gradual evolution with x.

The Hall concentration ratio is further discussed in §6.3 with comparison to Na_xWO_3 data. The experimental results for Y_xWO_3 show that studies of the tungsten bronze phase are only necessary up to the solubility limit x_{max}. From here on only the data in the cubic phase and below will be considered for analysis.

The temperature dependence of the resistivity for cubic Y_xWO_3 and La_xWO_3 near the solubility limit is shown in Fig. 6-2. Typical metals have a resistivity linearly dependent on temperature for $T \gtrsim \Theta_D$, attributed to thermal scattering. As $T \rightarrow 0$ K the resistivity levels off to a non-zero residual value ρ_0. This behaviour has been observed in the higher concentration cubic tungsten bronzes (Fig. 2-6) and the hexagonal tungsten bronzes[13]. The ρ vs T data in Fig. 6-2 also follows this metallic-type behaviour. The results for Y_xWO_3 and La_xWO_3 are therefore consistent with the behaviour expected in the higher concentration tungsten bronzes.

The thermal changes in the resistivity ($\Delta\rho_Y \simeq 64$ μΩ cm; $\Delta\rho_{La} \simeq 50$ μΩ cm) are similar to those observed in Fig. 2-6 for Na_xWO_3 ($\Delta\rho_{Na} \sim 20 - 40$ μΩ cm) and La_xWO_3 ($\Delta\rho_{La} \sim 40$ μΩ cm). The residual resistivity $\rho_0 \simeq 680$ μΩ cm for $La_{0.19}WO_3$ and is similar to that of single-crystal $La_{0.1}WO_3$ in Fig. 2-6 ($\rho_0 \simeq 615$ μΩ cm). $La_{0.19}WO_3$ is at almost twice the donor concentration of $La_{0.1}WO_3$, and should have ρ_0 significantly smaller. The larger resistivity is likely due to the grain-boundary contribution in the polycrystalline samples.

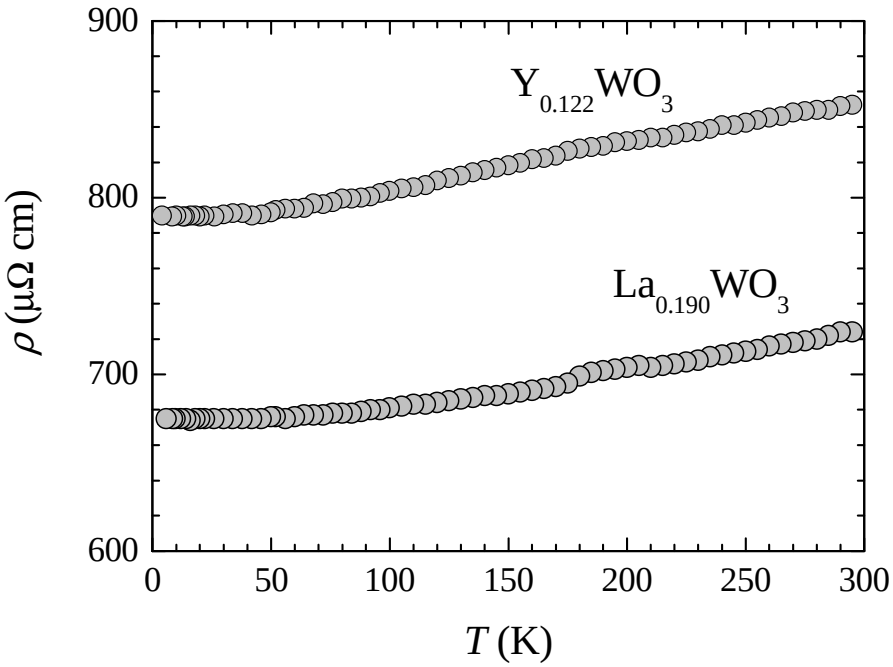

Fig. 6-2. The Y_xWO_3 and La_xWO_3 resistivity ρ vs the temperature T in a linear plot for cubic-phase concentrations near the solubility limit x_{max}.

6.2 The metal-insulator transition

In this section the conductivity data of the Y_xWO_3 and La_xWO_3 samples are analysed. The focus is on the MI transition, and several techniques are presented in an attempt to classify the samples as metallic ($\sigma_0 = \sigma(T = 0\ \text{K}) > 0$) or insulating ($\sigma_0 = 0$).

Fig. 6-3 shows the Y_xWO_3 and La_xWO_3 conductivities $\sigma(T)$, normalised to the room temperature value $\sigma(300\ \text{K})$, vs the temperature T for a range of concentrations x. For MI transition investigations the temperature dependence of the conductivity, particularly at low T, is the determining factor. Showing the relative conductivity has the advantage of focussing on the T dependence, while eliminating the absolute conductivity, which varies somewhat amongst the different tungsten bronzes. Crystal volume fraction and grain-boundary effects are also eliminated to some extent.

The similarity between Y_xWO_3 and La_xWO_3 is evident in Fig. 6-3, with the conductivity evolving in similar ways as x is reduced. The high concentration samples suggest metallic behaviour with a non-zero residual conductivity σ_0 indicated by the vanishing slope of the

low T data. This is consistent with the metallic behaviour observed in Fig. 6-2. As x is reduced there is a monotonic increase in the low T slope $d\sigma/dT$, showing features typical of other MI transition systems. For the concentrations where $d\sigma/dT > 0$, the objective is to determine the residual conductivity σ_0 from the finite temperature data in order to determine whether a MI transition is indeed occurring, and to estimate the critical concentration x_C.

The crossover from a metallic-type ($d\sigma/dT < 0$) to semiconducting-type ($d\sigma/dT > 0$) conductivity was previously believed to show the onset of the MI transition.[7,70] The results in Fig. 6-3 show this is not the case. The cubic samples (shown by the circle symbols in Fig. 6-3) all appear to be metallic in nature. This is consistent with previous results on other tungsten bronzes which show all cubic phase materials to be metallic.[26] If the

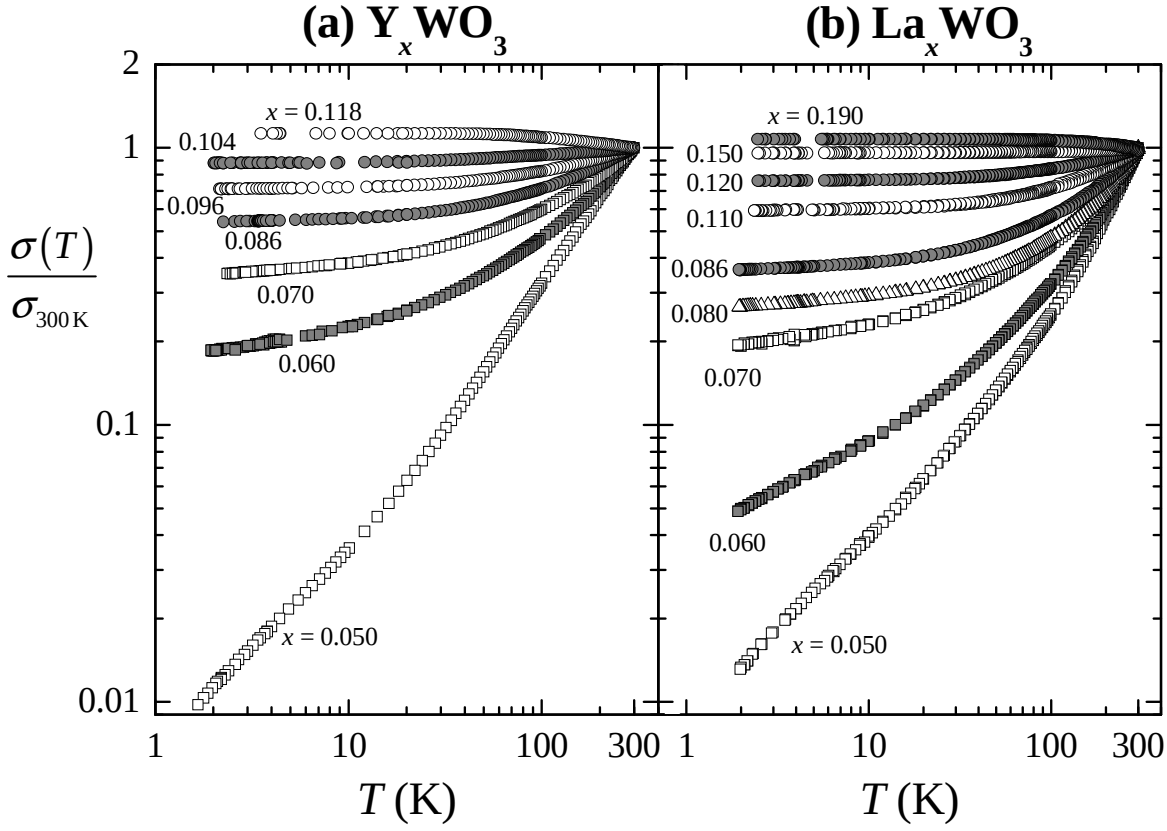

Fig. 6-3. The relative conductivity $\sigma(T)/\sigma(300\ K)$ vs the temperature T for the Y_xWO_3 (a) and La_xWO_3 (b) samples. The circular symbols correspond to x values for which the single-phase cubic structures are detected by XRD.

$x = 0.086$ cubic samples can be shown to be metallic, then it follows from Fig. 6-3 that all the cubic phase samples with $x > 0.086$ are also metallic. The analysis that follows will therefore focus on samples with $x \leq 0.086$.

The conductivity data in Fig. 6-3 for the $x = 0.050$ samples indicates a power law form ($\sigma \sim T^m$) for $T \lesssim 10$ K, with $m \simeq 0.7$ for both compounds. This suggests that $\sigma \rightarrow 0$ as $T \rightarrow 0$ K, and would classify this concentration as insulating. A MI transition is therefore suggested by the conductivity data, with the critical concentration $x_C > 0.05$. A similar temperature dependence is observed in the $Na_{0.34}Ta_{0.16}W_{0.84}O_3$ sample of Fig. 2-7, which is very near the MI transition with $\sigma \propto T$ (see also §2.4).

The question of the validity of using the nominal x values for La_xWO_3 is again evident in Fig. 6-3 (see end of §3.1). For $x = 0.050$, both compounds show a very similar behaviour. On the other hand, the temperature dependence for $La_{0.060}WO_3$ is different from that of $Y_{0.060}WO_3$, which is similar in behaviour to $La_{0.070}WO_3$. The XRD results in Fig. 3-2a and Fig. 3-3a show a very similar structural evolution as $x \rightarrow 0$. The difference therefore does not appear to be due to the presence of other phases. A small reduction in the actual x value from the nominal one for some La_xWO_3 samples (linked to the ampoule deposits – §3.1) would be consistent with the conductivity results. This is also manifested in the slightly different critical concentration values obtained for Y_xWO_3 and La_xWO_3 below.

The low temperature conductivity in the metallic phase is analysed with the expression (see §2.4)

$$\sigma(T) = \sigma_0 + \alpha T^m \qquad 6.2$$

where σ_0 is the residual metallic conductivity and α is a constant. The exponent m describes the form of the temperature dependence and is characteristic of the system under investigation. For disordered interacting systems $m = 1/2$ well into the metallic region, changing as the critical concentration is approached. Fig. 6-4 shows the conductivity of Y_xWO_3 and La_xWO_3 for $T \leq 10$ K and $x \leq 0.086$, together with fits of Eq. 6.2. The results of the fitting are summarised in Table 6-1.

The results in Fig. 6-4 show that Eq. 6.2 gives a good description of the low temperature conductivity for all the concentrations shown. The negative values of σ_0 obtained for $Y_{0.050}WO_3$, $La_{0.050}WO_3$ and $La_{0.060}WO_3$ suggests that these samples are not metallic. The higher concentrations have $\sigma_0 > 0$ consistent with metallic behaviour. The residual conductivity also decreases with decreasing x, consistent with an approach to the critical concentration. The cubic $x = 0.086$ samples for Y_xWO_3 and La_xWO_3 both have $m \simeq 0.5$, which is the value expected well into the metallic phase for disordered interacting systems. The predicted change in the exponent to a value of $m = 1/3$ as $x \rightarrow x_C$ is also suggested by the results for $x = 0.070$. Except for $Y_{0.060}WO_3$, the exponent m shows the expected changes as x is decreased. Some transition metal oxides[4] do show an increase in m ($m \rightarrow 1$) very near x_C, consistent with the larger value of m obtained for $Y_{0.060}WO_3$. The Y_xWO_3 and La_xWO_3 tungsten bronzes therefore also show signatures of electron-electron interaction effects in the metallic phase, as also observed in the $Na_xTa_yW_{1-y}O_3$ tungsten bronze (§2.4). The fitting results for σ_0 suggest a critical concentration $x_C \simeq 0.055 \pm 0.005$ and $x_C \simeq 0.065 \pm 0.005$ for Y_xWO_3 and La_xWO_3 respectively.

An alternative method that allows for the determination of the residual conductivity σ_0 in metallic samples that takes into account the changing temperature dependence from $T^{1/2}$ to $T^{1/3}$ as $x \rightarrow x_C$ has been proposed.[69] The expression for the conductivity is

$$\sigma(T) = \sigma_0 + \kappa\sqrt{\frac{T}{\sigma(T)}} \qquad 6.3$$

where κ is temperature independent. The above expression eliminates the requirement of the exponent m in Eq. 6.2, and predicts a linear relationship between σ and $(T/\sigma)^{1/2}$. Fig. 6-5 shows plots of σ vs $(T/\sigma)^{1/2}$ using the same conductivity data as in Fig. 6-4. The dashed lines are linear fits and the fitting parameters σ_0 and κ are shown in Table 6-2.

Apart from the $Y_{0.050}WO_3$ sample, the conductivity data for $T \leq 10$ K shows good agreement with Eq. 6.3. The results for σ_0 indicate metallic samples for Y_xWO_3 and La_xWO_3 when $x \geq 0.060$ and $x \geq 0.070$ respectively. This is consistent with the results from Fig. 6-4 and the values for σ_0 are also similar. For the lowest concentrations ($Y_{0.050}WO_3$, $La_{0.050}WO_3$ and $La_{0.060}WO_3$) the negative values for σ_0 again suggest non-metallic behaviour. The critical concentrations for Y_xWO_3 and La_xWO_3 from this analysis are

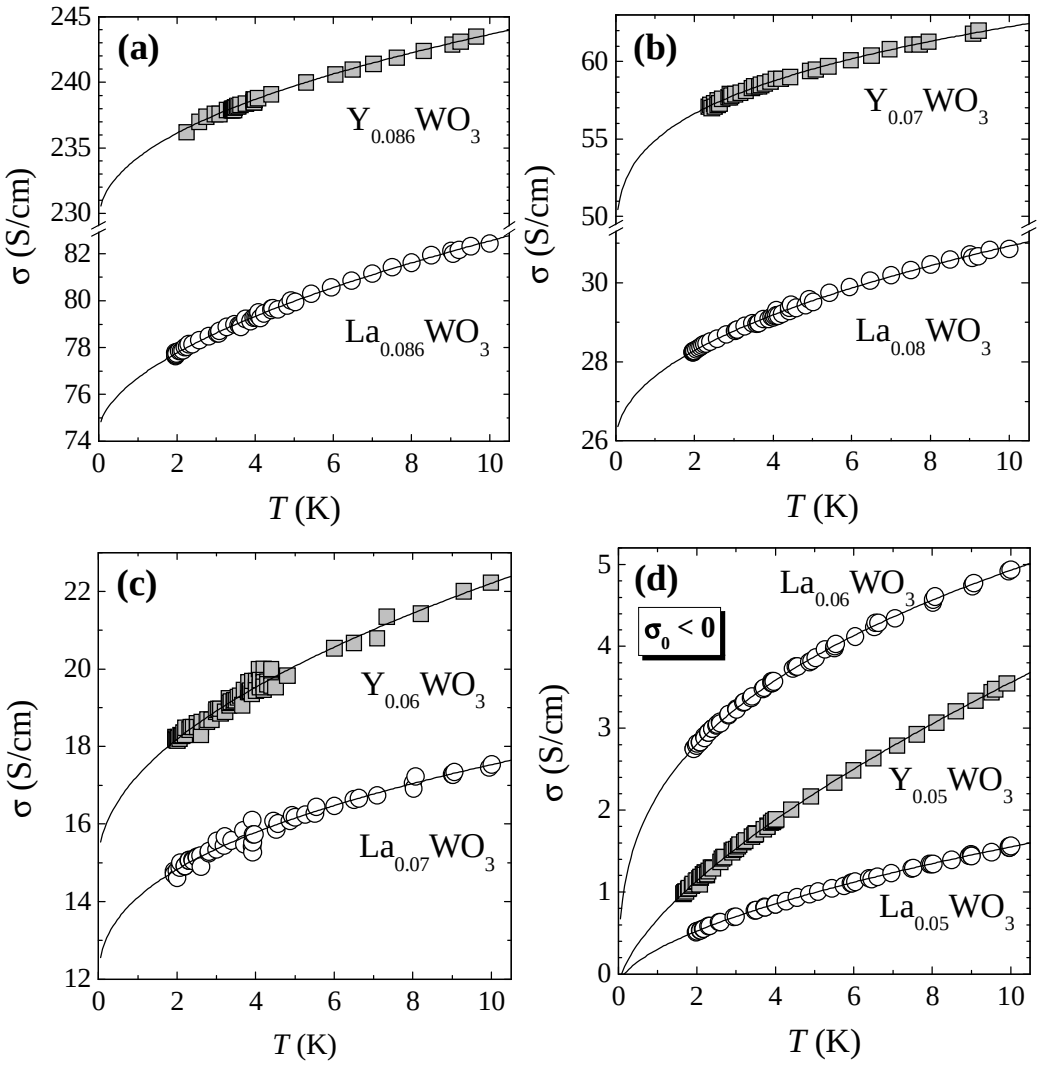

Fig. 6-4. The low temperature ($T \leq 10$ K) conductivity data of Y_xWO_3 and La_xWO_3 for $x \leq 0.086$. The curves are fits of $\sigma(T) = \sigma_0 + \alpha T^m$, with σ_0, α and m the fitting parameters, shown in Table 6-1 below. Notice the vertical axis breaks for (a) and (b), and $\sigma_0 < 0$ in (d).

Table 6-1. Parameters obtained from fitting $\sigma(T) = \sigma_0 + \alpha T^m$ to the data in Fig. 6-4.

	$Y_x WO_3$			$La_x WO_3$		
x	σ_0	α	m	σ_0	α	m
0.086	229	4.9	0.46	74	2.3	0.55
0.080				26	1.7	0.47
0.070	47	7.8	0.29	12	2.2	0.4
0.060	15	2.2	0.51	-0.26	2.4	0.33
0.050	-0.16	0.82	0.66	-0.16	0.46	0.57

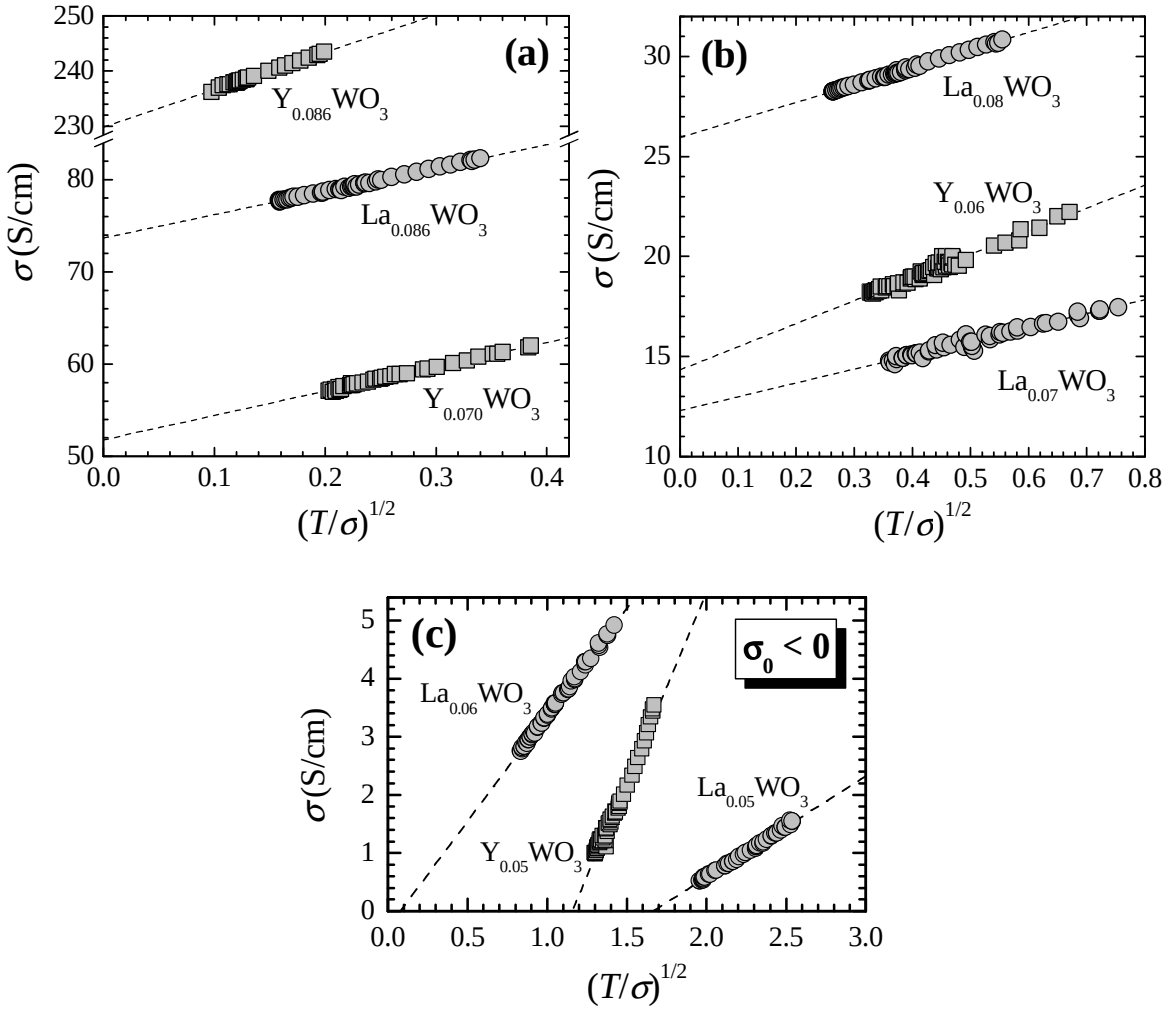

Fig. 6-5. Linear plots of σ vs $(T/\sigma)^{1/2}$ for Y_xWO_3 and La_xWO_3 ($x \leq 0.086$ and $T \leq 10$ K) used to distinguish metallic and insulating samples. The straight lines are linear fits with $\sigma(T) = \sigma_0 + \kappa\{T/\sigma(T)\}^{1/2}$. Notice the vertical axis break in (a), and $\sigma_0 < 0$ in (c). The fitting parameters σ_0 and κ are shown in Table 6-2 below.

Table 6-2. Fitting results from Fig. 6-5.

	Y_xWO_3		La_xWO_3	
x	σ_0	κ	σ_0	κ
0.086	230	68	74	25
0.080			26	8.7
0.070	52	26	12	6.9
0.060	14	12	-0.29	3.7
0.050	-7.5	6.5	-2.9	1.7

therefore the same as those obtained from Fig. 6-4 ($x_C^{Y} \simeq 0.055 \pm 0.005$; $x_C^{La} \simeq 0.065 \pm 0.005$).

The parameter κ in Eq. 6.3 is $\kappa = A\sqrt{\rho(E_F)}$, where A is a temperature independent constant and $\rho(E_F)$ the density of states at the Fermi level.[69] The fitting results for κ in Table 6-2 indicate a strongly decreasing $\rho(E_F) \propto \kappa^2$ as x is reduced. For typical metals $\rho(E_F) \propto x^{1/3}$ while for highly doped tungsten bronzes $\rho(E_F) \propto x$ (see §2.1.4). The x–dependence obtained above is significantly stronger (a fitting gives $\rho(E_F) \sim x^9$) and may signify the evolution of the pseudogap at the Fermi level with $\rho(E_F)$ eventually vanishing as the critical concentration is approached from the metallic side (see §2.4).

A convenient way of analysing the finite low temperature conductivity data from a MI transition point of view is by considering the logarithmic derivative

$$L(T) = \frac{d\log\sigma}{d\log T} = \frac{T}{\sigma}\frac{d\sigma}{dT}. \qquad 6.4$$

For a metallic system $d\sigma/dT \rightarrow 0$ and $\sigma \rightarrow \sigma_0 \neq 0$ as $T \rightarrow 0$ K, which implies that $L(T)$ vanishes at low temperatures. For an insulating system where hopping conduction describes the conductivity (Eq. 2.19), $L(T) \sim T^{-p}$ and hence diverges with lowering temperature. The logarithmic derivative can therefore be a sensitive probe of the critical concentration x_C. Fig. 6-6 gives a plot of the temperature dependence of $L(T)$ for Y_xWO_3 and La_xWO_3 for $x \leq 0.086$.

For the higher concentrations ($0.070 \leq x \leq 0.086$) $L(T)$ appears to vanish as $T \rightarrow 0$ K. This is consistent with the metallic classification obtained from the fitting results above. The $Y_{0.050}WO_3$, $La_{0.050}WO_3$ and $La_{0.060}WO_3$ samples do not show a vanishing $L(T)$, which appears to plateau at a non-zero constant value. This constant value α manifests as the $\sigma \sim T^{\alpha}$ behaviour observed at the lowest temperatures in Fig. 6-3. These samples therefore do not show metallic behaviour, but the divergence expected in $L(T)$ from insulating samples is not present. However, results for $Na_xTa_yW_{1-y}O_3$ suggest that the hopping behaviour in insulating samples occurs at even lower temperatures ($T \lesssim 1$ K – see Fig. 6-14).[7] This is further discussed at the end of the next section, which provides further support in classifying the $x = 0.050$ samples as insulating.

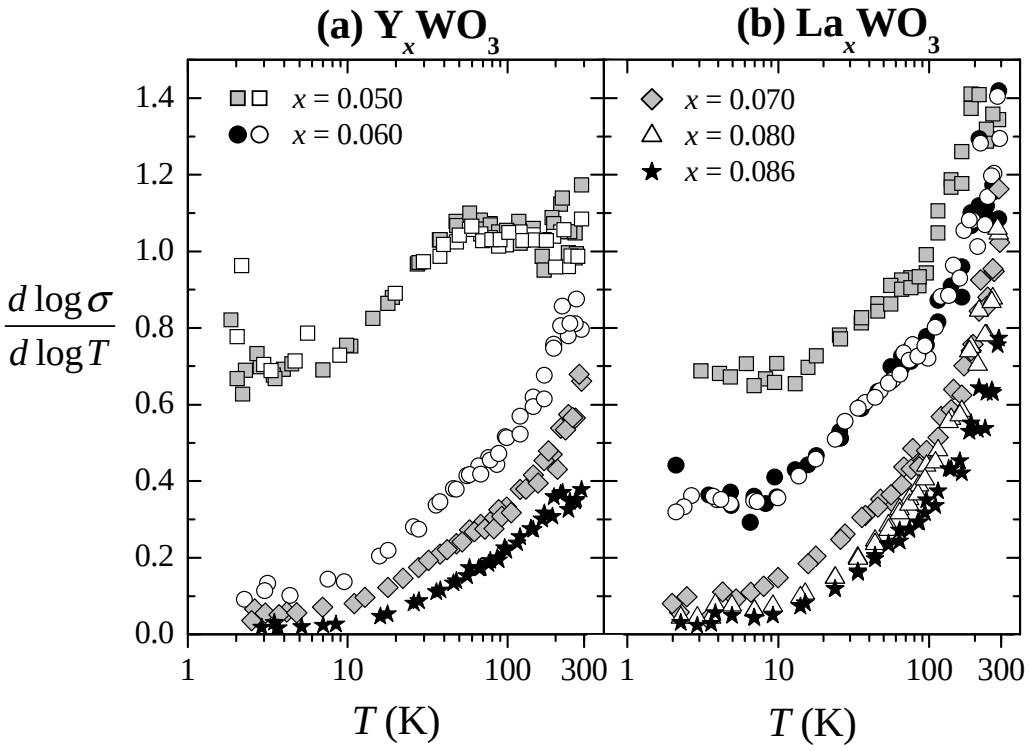

Fig. 6-6. The logarithmic derivative d log σ/d log T vs the temperature T of Y_xWO_3 and La_xWO_3 for $x \leq 0.086$. (Legends refer to both plots.)

In conclusion, the analysis of the low temperature conductivity data for Y_xWO_3 and La_xWO_3 suggests that a MI transition is occurring at a value close to the lowest concentration used. The results indicate metallic behaviour in Y_xWO_3 for $x \geq 0.060$ and La_xWO_3 for $x \geq 0.070$. Insulating behaviour is suggested for $Y_{0.050}WO_3$, $La_{0.050}WO_3$ and $La_{0.060}WO_3$. The critical concentration from the analysis in this section for Y_xWO_3 and La_xWO_3 is therefore $x_C \simeq 0.055 \pm 0.005$ and $x_C \simeq 0.065 \pm 0.005$ respectively. As mentioned above, the nominal x value for La_xWO_3 is less certain, and may account for the differences in x_C obtained for the two compounds. For the trivalent-doped tungsten bronzes the critical concentration is therefore quoted as $x_C \sim 0.06$, corresponding to an electron concentration $n_C \simeq 3.2\times10^{21}$ cm^{-3}. This x_C value is one third that found in Na_xWO_3 and $Na_xTa_yW_{1-y}O_3$ tungsten bronzes where $x_C \sim 0.18$, and corresponds to the same donor electron concentration. This finding supports claims that the MI transition is primarily driven by the conduction band electron concentration. The results also support previous observations that the cubic phase of the tungsten bronzes is metallic. The XRD results point to a mixed phase dominated by the cubic structure for lower x (Fig. 3-2a and

Fig. 3-3a). It is observed that x_C is smaller than the lower cubic limit $x_{min} \simeq 0.086$, and the MI transition therefore does not appear to be associated with the appearance of new structural features.

6.3 Comparisons to other tungsten bronze results

In this section the transport data for Y_xWO_3 and La_xWO_3 is compared to that of Na_xWO_3 and $Na_xTa_yW_{1-y}O_3$. The comparisons will be made relative to the effective donor concentration x_{eff} (or equivalently the donor electron concentration $n_d = x_{eff}/a^3$). For $Na_xTa_yW_{1-y}O_3$ the effective concentration is $x - y$. When compared in this way the trivalent-ion doped Y_xWO_3 and La_xWO_3 tungsten bronzes show remarkably similar properties to those of Na_xWO_3 and $Na_xTa_yW_{1-y}O_3$.

Fig. 6-7 shows the room temperature Hall concentration n_H vs the donor electron concentration n_d for Y_xWO_3, La_xWO_3 and Na_xWO_3. All three compounds show a similar magnitude and x-dependence for n_H. The near-linear increase with x represents the filling of the conduction band as the donor concentration is increased. The proximity of the data to the $n_H = n_d$ line lends support to the fully-ionised donor model for the tungsten bronzes, with Y^{3+}, La^{3+} and Na^+ the expected valence states of the donor atoms. (This is also supported by the NMR results in §6.4.3.) The majority of donated electrons appear to participate in the conduction process. The sign of the Hall coefficient for all three compounds confirms conduction due to the donated electrons in the conduction band. The scattering factor $A = n_d/n_H$ is obtained from linear fits of the n_H vs x data for Y_xWO_3 and La_xWO_3 in Fig. 6-7. The results $A_Y \simeq 1.2$ and $A_{La} \simeq 0.85$ are consistent with values close to unity found for most compounds (§2.1.2).

Fig. 6-8 shows the room temperature conductivity σ of Y_xWO_3, La_xWO_3, Na_xWO_3 and $Na_xTa_yW_{1-y}O_3$ vs the donor electron concentration n_d in a log-linear plot. The straight line fits give good descriptions of the Y_xWO_3, La_xWO_3 and Na_xWO_3 conductivity on the range shown, with very similar slopes (0.374, 0.380 and 0.379 respectively). Except for the lowest concentration, $Na_xTa_yW_{1-y}O_3$ also shows a similar dependence on n_d. All four tungsten bronzes therefore have similar σ vs n_d dependencies, showing a common transport mechanism in these compounds near the MI transition.

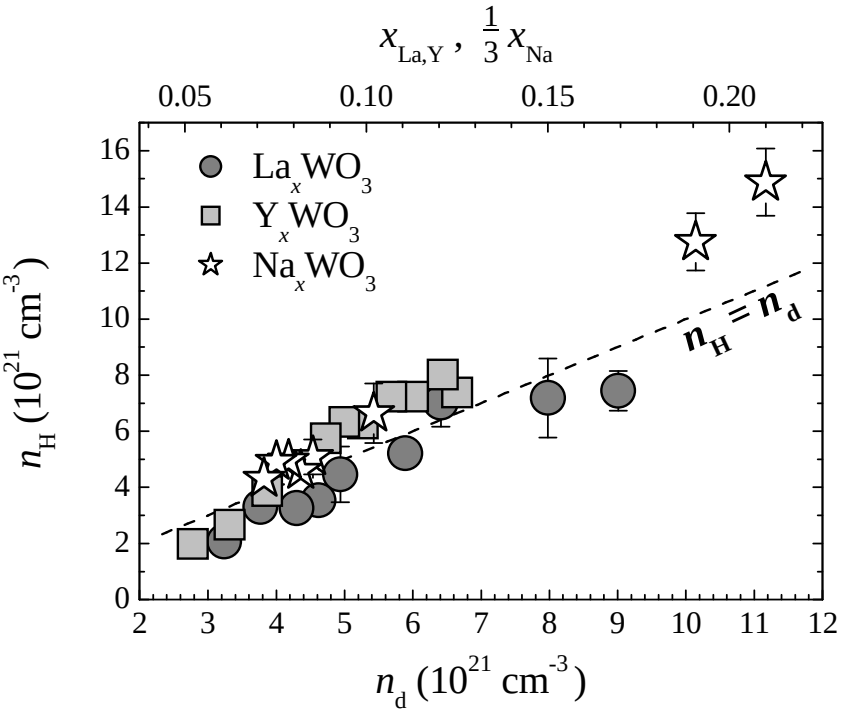

Fig. 6-7. The room temperature Hall effect results for Y_xWO_3, La_xWO_3 and Na_xWO_3. The Hall concentration $n_H = 1/R_He$ is shown vs the donor electron concentration n_d. Na_xWO_3 results are from Ref. 26. The top scale presents the donor concentration x.

The reduced conductivity of $Na_xTa_yW_{1-y}O_3$ relative to Na_xWO_3 has been attributed to the increased disorder created by the Ta substitution.[7,8] Following similar arguments, in addition to grain-boundary effects, the reduced conductivity of the polycrystalline Y_xWO_3 and La_xWO_3 samples, relative to Na_xWO_3, could be attributed to enhanced scattering associated with the higher charged trivalent Y and La ions.

The room temperature Hall effect results for the tungsten bronzes show carrier concentrations proportional to the donor concentration x. The exponential dependence of the conductivity shown in Fig. 6-8 indicates a mobility ($\sim \sigma/x$) strongly dependent on x. For Y_xWO_3 and La_xWO_3 the room temperature mobility shows a three-fold reduction in going from $x = 0.11$ to $x = 0.06$. A vanishing mobility, as well a vanishing density of states at the Fermi level, are both features occurring in MI systems as the critical concentration is approached from the metallic side (§2.2).

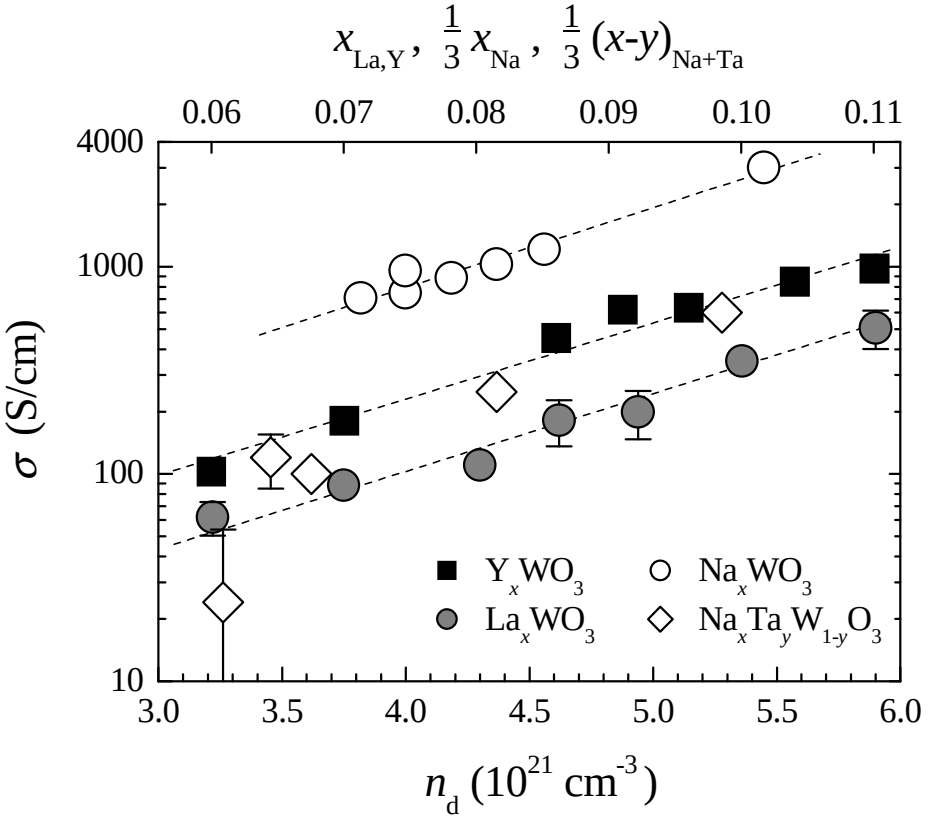

Fig. 6-8. The room temperature conductivity of Na_xWO_3 and $Na_xTa_yW_{1-y}O_3$ (reproduced from Ref. 7) and Y_xWO_3 and La_xWO_3, vs the donor electron concentration n_d. The dashed lines are linear fits of the Na_xWO_3, Y_xWO_3 and La_xWO_3 data. The top scale presents the donor atom concentrations.

The Hall concentration ratio n_H^{64K}/n_H^{300K} for Y_xWO_3, La_xWO_3 and Na_xWO_3 is shown in Fig. 6-9 as a function of the donor electron concentration n_d. The Y_xWO_3 and La_xWO_3 results are compatible, showing a near-linear increase in n_H^{64K}/n_H^{300K} with x, eventually reaching the expected saturation value of $n_H^{64K}/n_H^{300K} = 1$. The Na_xWO_3 results show a remarkably similar behaviour. The reduction in n_H on cooling suggests a partial localization of the charge carriers, with the ratio n_H^{64K}/n_H^{300K} giving an indication of the fraction of carriers still participating in the conduction process. The freeze–out effect becomes more pronounced as x is reduced, and appears to be more pronounced in Y_xWO_3 and La_xWO_3 than in Na_xWO_3. This effect may be due to the higher charge of the Y^{3+} and La^{3+} donor ions which could show stronger localization effects than the monovalent Na^+ donor in Na_xWO_3.

The behaviour of the Hall concentration ratio with temperature in Fig. 6-9 is consistent with the conductivity ratio plots in Fig. 3-14. The stronger carrier freeze out observed in lowering x indicates larger changes in the carrier concentration. This would lead to the stronger temperature dependence seen in the conductivity. The semiconducting-type behaviour, with $d\sigma/dT > 0$, observed in the lower x samples could arise from the thermal activation of charge carriers. For larger x the Hall concentration becomes temperature independent,[28,55] with $n_H^{64K}/n_H^{300K} \simeq 1$ (see also Fig. 6-10). This is consistent with the typical metallic behaviour observed in the higher concentration tungsten bronzes. It is noted that the localization effects observed in Fig. 6-9 are all for samples classified as metallic. The tungsten bronzes therefore have an atypical metallic character in the just-metallic phase.

The reduction in the Hall concentration on cooling is also observed in the hexagonal tungsten bronzes.[13,14] Hexagonal $Rb_{0.18}WO_3$ and $K_{0.20}WO_3$, with $n_d \sim 3.2\times10^{21}$ cm^{-3}, both show a Hall concentration reduction ~50% when the temperature is decreased from 300 K

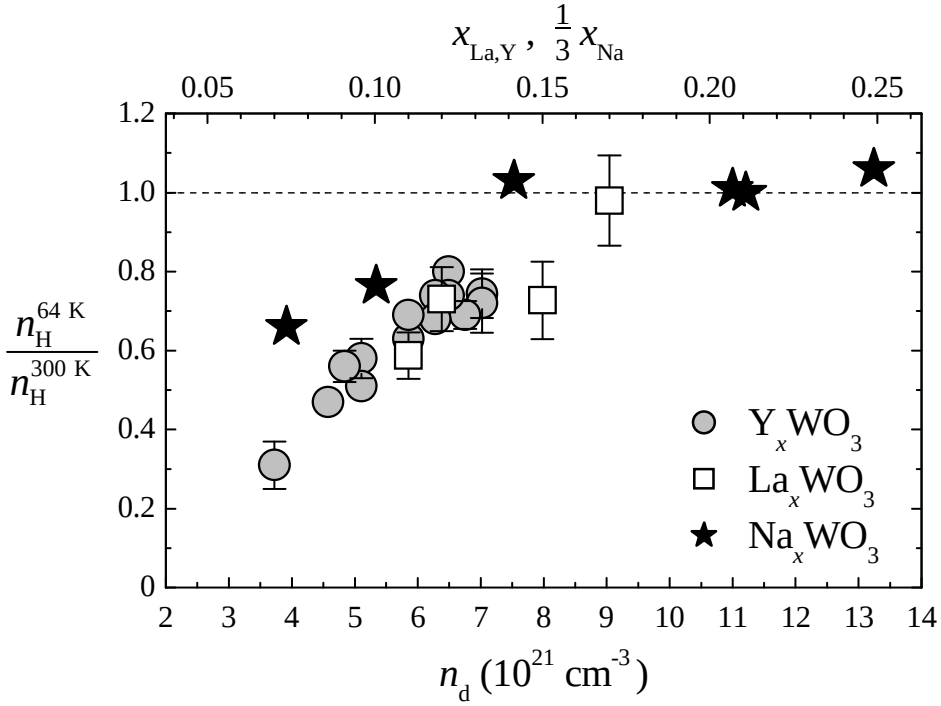

Fig. 6-9. The Hall concentration ratio n_H(64 K)/n_H(300 K) vs the donor electron concentration n_d for Y_xWO_3, La_xWO_3 and Na_xWO_3. The $NaWO_3$ results are from Refs. 26 and 55. The top scale presents the donor atom concentration x.

to below 100 K. This is similar in magnitude to the results in Fig. 6-9 for the perovskite tungsten bronzes.

Fig. 6-10 shows the Hall concentration ratio $n_H(T)/n_H(300\ K)$ as a function of temperature for cubic-phase $Y_{0.091}WO_3$, $Y_{0.127}WO_3$ and $La_{0.170}WO_3$. For comparison, the figure also shows the results for single-crystal cubic-phase Na_xWO_3 samples. All the samples are classified as metallic. For the highest concentrations the expected temperature independence of n_H is evident in the Na_xWO_3 results. As x is reduced the temperature dependence for all three compounds becomes stronger, consistent with the behaviour in Fig. 6-9. The n_H vs T behaviour for Y_xWO_3 and La_xWO_3 is very similar to that of Na_xWO_3 for equivalent concentrations. The results in Fig. 6-9 and Fig. 6-10 again highlight the common features found in the various tungsten bronzes.

The n_H vs T behaviour for Y_xWO_3 and La_xWO_3 suggests that most of the carrier freeze out occurs at the higher temperatures (30K – 300 K). For $T \lesssim 30$ K the Hall concentration appears to plateau at constant non-zero values. The conductivity results of the previous

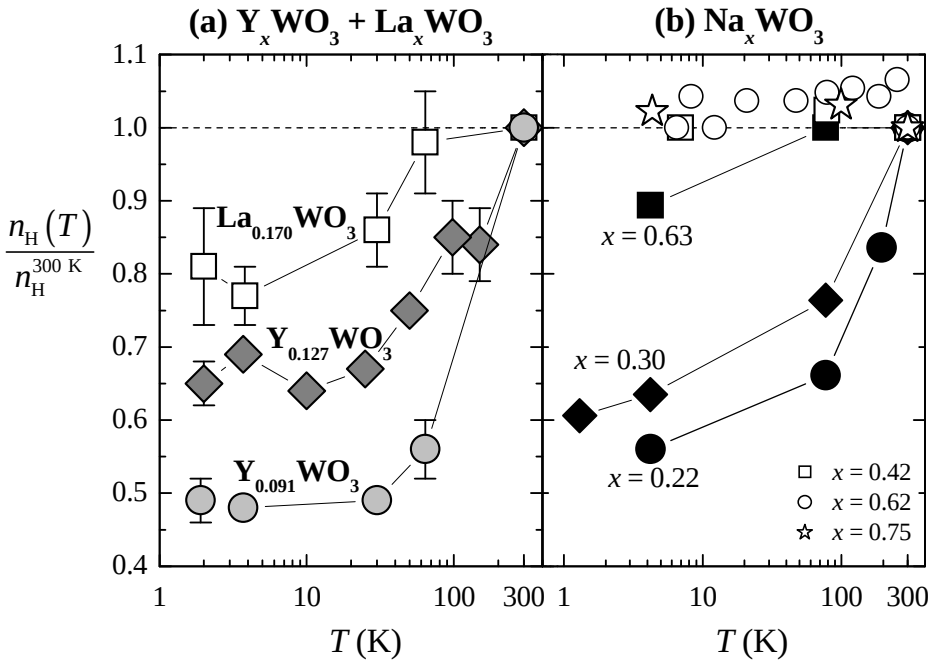

Fig. 6-10. The Hall concentration, normalised to 300 K values, vs the temperature T for Y_xWO_3, La_xWO_3 and Na_xWO_3. For Na_xWO_3 closed symbols are from Ref. 26 and open symbols are from Ref. 55.

section indicate that the samples shown in Fig. 6-10 are metallic in nature with $\sigma_0 > 0$. The temperature independence shown by n_H at low T with $n_H(T = 0\ K) > 0$ is consistent with this classification.

Theoretical calculations for the Na tungsten bronzes,[9] supported by experimental evidence,[10,82] indicate the formation of a pseudogap at the Fermi energy E_F (see §2.3 and Fig. 2-12). In the metallic phase the calculations predict localized states near E_F inside the pseudogap. The observed increase in the Hall concentration on increasing T is attributed to the thermal excitation of these localized states to accessible extended states near E_F. Increasing x reduces the pseudogap and degree of localization near E_F due to the increased screening effects of the itinerant electrons. This is consistent with the Hall results in Fig. 6-9 and Fig. 6-10. The corresponding increased mobility of the electrons with increasing x from the screening of the disorder is also evident in the room temperature conductivity mentioned earlier. The density of states at E_F and their nature (localized or extended) play a major role in determining the measured properties.

Fig. 6-11 shows a figure reproduced from Ref. 70 showing the low temperature conductivity σ vs the effective carrier concentration $x_{eff} = x - y$. The Mott minimum metallic conductivity σ_{min} is included. For comparison the $T = 2$ K conductivity of Y_xWO_3 and La_xWO_3 is also shown vs the effective concentration $x_{eff} = 3x$. The σ vs x_{eff} behaviour for Y_xWO_3 and La_xWO_3 compares well to that of the two Na tungsten bronzes. The magnitude of σ is closer to that of $Na_xTa_yW_{1-y}O_3$, consistent with the room temperature results in Fig. 6-8. For $Na_xTa_yW_{1-y}O_3$ it has been noted that metallic samples are found with $\sigma \ll \sigma_{min}$.[7] The lowest x metallic samples of Y_xWO_3 and La_xWO_3 also have $\sigma < \sigma_{min}$, indicating these concentrations to be in the critical region (see §2.2.3).

The scaling theory predicts a σ vs x relationship given by Eq. 2.15 for the residual conductivity σ_0. Fig. 6-12 shows a logarithmic plot of σ_0 vs $x - x_C$, with σ_0 the extrapolated values of the low temperature conductivity and x_C the critical concentrations for Y_xWO_3 and La_xWO_3 estimated in the previous section. Except for the lowest x, the data follows the predicted behaviour with a critical exponent $\nu_C \sim 2$ for both Y_xWO_3 and La_xWO_3. This is larger than the value of ν_C predicted by scaling theories and obtained experimentally in many other MI systems (§2.2.3). The slopes for the lowest two concentrations in Fig. 6-12 give the smaller, more expected values. The results in Fig. 6-12 may therefore suggest a

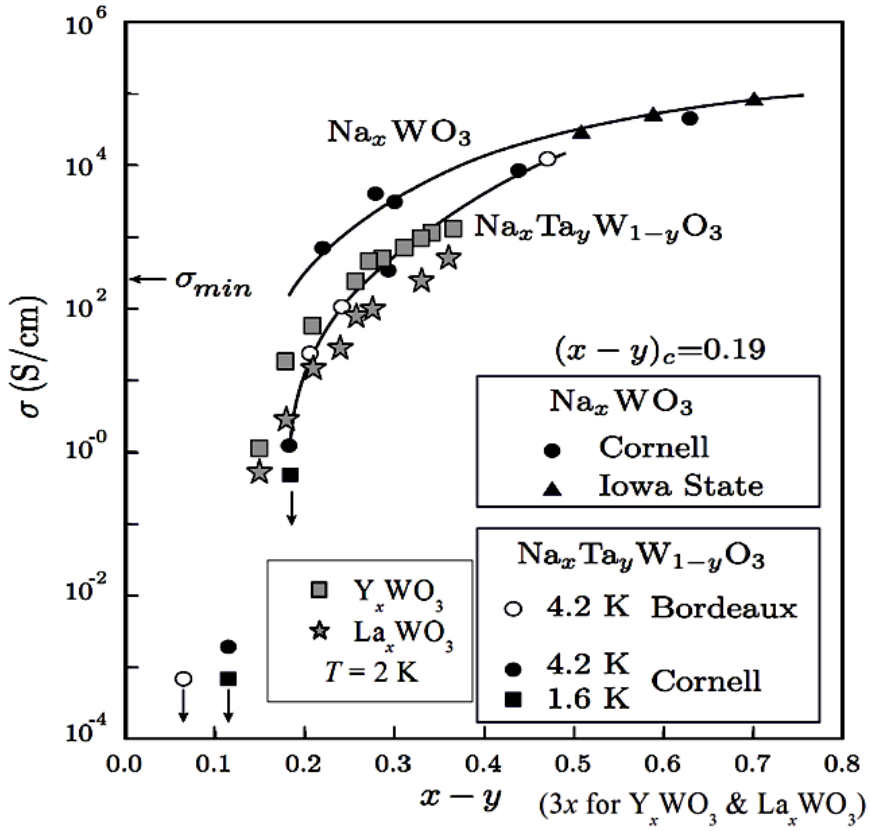

Fig. 6-11. Reproduction of a figure from Ref. 70 showing the conductivity of Na_xWO_3 and $Na_xTa_yW_{1-y}O_3$ at liquid helium temperatures as a function of the effective carrier concentration $x - y$. The conductivity of Y_xWO_3 and La_xWO_3 at 2 K has been included for comparison, with the axis showing the effective carrier concentration $x_{eff} = 3x$.

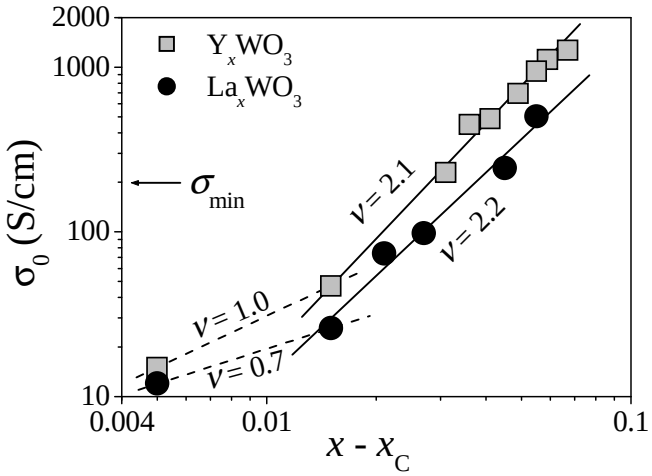

Fig. 6-12. A logarithmic plot of the residual conductivity σ_0 vs $(x - x_C)$ for the Y_xWO_3 and La_xWO_3 samples. The slopes ν of the straight lines are shown, as well as the Mott minimum metallic conductivity σ_{min}.

crossover in ν_C as the critical concentration is approached. It should however be noticed that the low x behaviour in Fig. 6-12 is strongly dependent on the value of x_C, which in this case is somewhat uncertain.

It has been noted that for the tungsten bronzes the extrapolations are obtained for data that may be too far beyond the MI transition.[71] It has also been mentioned that for transition-metal oxides the critical region persists over a larger range of compositions above the critical concentration.[4] The critical region for Eq. 2.15 is expected to go from x_C to a composition where $\sigma \simeq \sigma_{min}$.[8] This would correspond to $x - x_C \lesssim 0.03$ in Fig. 6-12. The lack of data on this range, coupled with the uncertainty in x_C, makes the critical exponent analysis inconclusive. The larger value of $\nu_C \sim 2$ has been observed in other systems, and this larger range of exponents can be explained by various percolation theories.[70,72] The actual value of the critical exponent for the tungsten bronzes, and the extent of the critical region, therefore requires more stringent investigations. Experiments on selected materials have been suggested to address this issue.[70]

The MI transition has been observed in cubic $Na_xTa_yW_{1-y}O_3$ for $x - y \simeq 0.18$. The conductivity for two samples on either side of the critical concentration is shown in Fig. 2-13. This data has been reproduced in Fig. 6-13, which also shows the conductivity of the lowest concentration samples of Y_xWO_3 and La_xWO_3. The relative conductivity $\sigma(T)/\sigma(300\ K)$ is shown to compare the temperature dependence for the compounds.

The temperature dependence and the evolution with x of the Y_xWO_3 and La_xWO_3 conductivity are very similar to that of $Na_xTa_yW_{1-y}O_3$. The $Y_{0.060}WO_3$, $Y_{0.070}WO_3$ and $La_{0.070}WO_3$ conductivity behaviour is similar to the metallic sample of $Na_{0.35}Ta_{0.16}W_{0.84}O_3$. This is consistent with the metallic classification for these concentrations obtained in the previous section. The $x = 0.050$ samples for Y_xWO_3 and La_xWO_3 both show a conductivity behaviour very similar to the insulating $Na_{0.34}Ta_{0.16}W_{0.84}O_3$ sample. The results of the previous section in classifying the $x = 0.050$ concentration as insulating is therefore supported by the comparisons in Fig. 6-13. The $La_{0.060}WO_3$ conductivity shows intermediate behaviour and lower temperature data is required to classify this sample.

The effective concentrations for the Y_xWO_3, La_xWO_3 and $Na_xTa_yW_{1-y}O_3$ samples in Fig. 6-13 are similar, and hence suggest a common mechanism for the MI transition

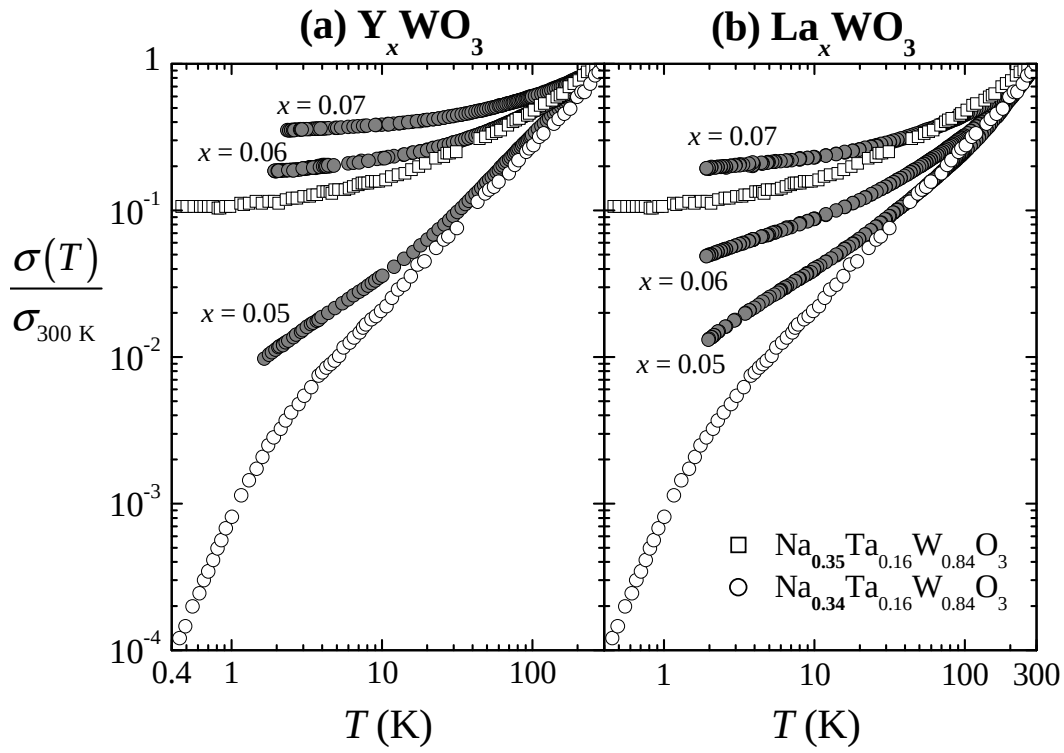

Fig. 6-13. The conductivity of the lowest three concentrations of Y_xWO_3 (a) and La_xWO_3 (b) compared to a just-insulating ($x - y = 0.18$) and just-metallic ($x - y = 0.19$) sample of $Na_xTa_yW_{1-y}O_3$. The relative conductivity $\sigma(T)/\sigma(300\ K)$ is shown vs the temperature T.

determined by the conduction band concentration. The Y_xWO_3 and La_xWO_3 samples in Fig. 6-13 are mixed phase and the XRD results indicate gradual structural variations as x is varied. The $Na_xTa_yW_{1-y}O_3$ samples maintain their cubic phase. The comparison in Fig. 6-13 therefore provides convincing support that the appearance of additional phases on lowering x has no major impact on the conductivity behaviour in the vicinity of the MI transition.

Fig. 6-14 shows the logarithmic derivative of the conductivity data in Fig. 6-13. The comparisons support the conclusions made above. The $Na_{0.34}Ta_{0.16}W_{0.84}O_3$ sample shows an increase in $d\log\sigma/d\log T$ for $T \lesssim 3$ K with a slope consistent with hopping conduction (§2.4). Although the $x = 0.050$ data for Y_xWO_3 and La_xWO_3 does show a hint of an upturn as $T \rightarrow 0$ K, lower temperatures are required to confirm the presence of hopping conduction in these two tungsten bronzes.

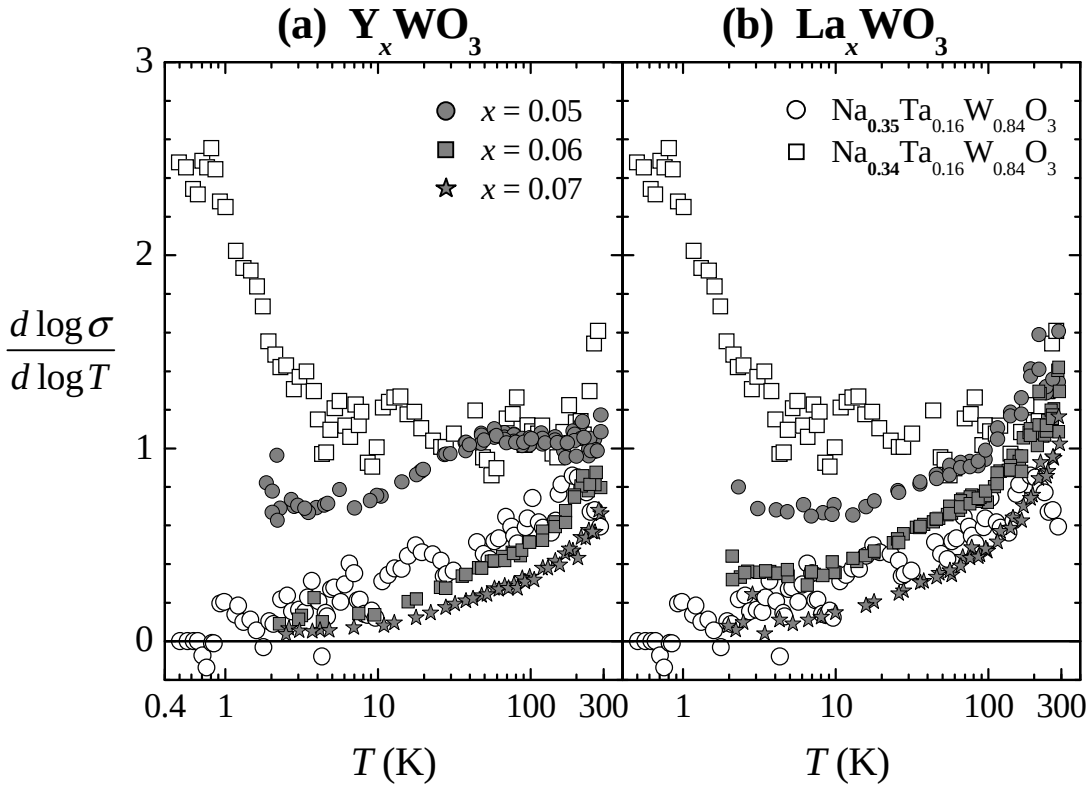

Fig. 6-14. The logarithmic derivative $d\log\sigma/d\log T$ of the conductivity data shown in Fig. 6-13 vs the temperature T. In each figure $d\log\sigma/d\log T$ for Y_xWO_3 (a) and La_xWO_3 (b) is compared to that of $Na_xTa_yW_{1-y}O_3$. (The legends refer to both plots.)

In conclusion, the results in this section show that the Y_xWO_3 and La_xWO_3 tungsten bronzes provide results similar to the Na_xWO_3 and $Na_xTa_yW_{1-y}O_3$ tungsten bronzes. When the comparisons are made with respect to the effective concentration x_{eff} (x for Na_xWO_3; $x - y$ for $Na_xTa_yW_{1-y}O_3$; $3x$ for Y_xWO_3 and La_xWO_3) all four compounds show universal behaviour for the tungsten bronzes. The differences in the physical properties are mainly attributed to the different degrees of disorder: Na^+ ions in Na_xWO_3; Na^+ and Ta^{+5} ions in $Na_xTa_yW_{1-y}O_3$; Y^{3+} and La^{3+} ions at a reduced concentration in Y_xWO_3 and La_xWO_3. In purely disorder driven Anderson localization the critical concentration for these four compounds would be different. The results, however, show the critical concentration to be governed by a similar concentration of donor electrons. Correlation effects must therefore be incorporated in a description of the MI transition in the tungsten bronzes.

6.4 Additional measurements

Specific heat and magnetization measurements were performed on samples of Y_xWO_3 and La_xWO_3 at low temperatures to check for the existence of local moments, as suggested by the temperature dependence of the Hall concentration. These measurements were done at the National High Magnetic Field Laboratory (NHMFL) of the Florida State University (U.S.A). Room temperature NMR results for La_xWO_3 are also presented.

6.4.1 Magnetization

Magnetization measurements were done on a 94 mg sample of $Y_{0.096}WO_3$ with a Quantum Design vibrating sample magnetometer (VSM) as a function of temperature T and magnetic field B. The temperature dependence was performed in a field of 0.2 T from 1.9 K to 120 K. The VSM results, shown in Fig. 6-15a, show Curie-type behaviour at the lower temperatures, which levels off to a small value of 1.5×10^{16} μ_B/g ($\simeq 6\times10^{-4}$ μ_B/donor ion) at the higher temperatures. This is consistent with a metallic-type system with local moments present. The anomaly near 50 K is attributed to the presence of paramagnetic oxygen. To estimate the local moment concentration and type, an analysis was performed on the field dependence of the magnetization at low temperature.

Fig. 6-15b shows the sample magnetization at T = 2 K as a function of the magnetic field ($0 \leq B \leq 2.55$ T). The curve is a fit of the semiclassical Langevin function for paramagnetism,[93] where the magnetization is given by $M = M_S[\coth(y) - 1/y]$, with $y = p\mu_B B/k_B T$ and $M_S = Np\mu_B$ the saturation magnetization. The two fitting parameters are p and N, where p is the effective Bohr magneton number and N the concentration of the local moments. The fitting in Fig. 6-15b gives $p = 9.4$ and $N = 6.6\times10^{16}$ g^{-1}.

The fitting results of the magnetization data indicate that the Curie-type temperature dependence is due to impurities. The large magnitude of the effective Bohr magneton number ($p \sim 9$) suggests transition and rare-earth local moments. The small concentration ($N \sim 6\times10^{16}$ g^{-1}) is consistent with the impurity concentrations found in the starting materials (donor-atom concentrations are $\sim10^{20}$ g^{-1}). The magnetization results therefore suggest no isolated local moment formation from the freezing-out of charge carriers at the concentrations suggested by the Hall data (Fig. 2-4).

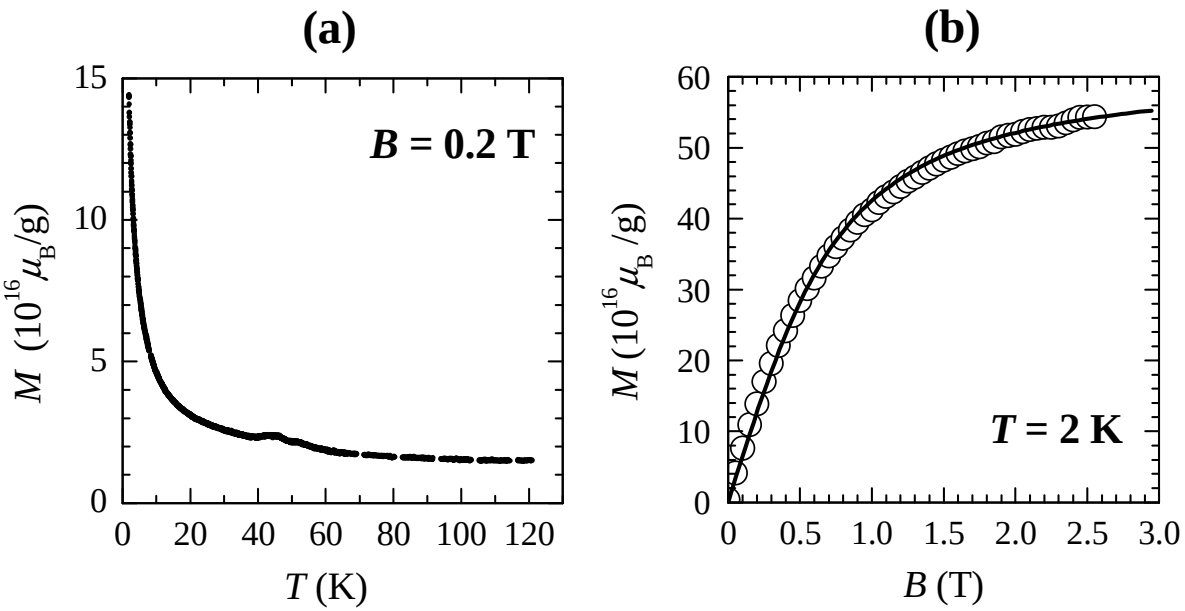

Fig. 6-15. Vibrating sample magnetometer results showing the magnetization *M* of a $Y_{0.096}WO_3$ sample. Plot (a) shows the temperature dependence for *B* = 0.2 T, and (b) shows the magnetic field dependence at *T* = 2 K. The curve is a fit of the Langevin function.

The VSM results show a temperature-independent weak paramagnetic susceptibility for $T > 100$ K, typically observed in metals.. This is also observed in $Ba_{0.12}WO_3$ and Na_xWO_3 for $0.22 \leq x \leq 0.60$.[51,57] The susceptibility near room temperature is attributed to the temperature independent diamagnetic contributions of the WO_3 lattice and donor cations, and the Pauli-type paramagnetic contribution of conduction band electrons.[51] The VSM results therefore support the metallic classification for $x = 0.096$.

VSM measurements were also performed on a sample of $Y_{0.050}WO_3$ for $B = 1$ T and 2 K $< T <$ 300 K. The results are similar to those in Fig. 6-15a for $Y_{0.096}WO_3$ (see Fig. E-5 in appendix E). For $T \gtrsim 100$ K the magnetization is constant, but negative. The diamagnetic contribution is larger as the reduced electron concentration leads to a decreased Pauli-type paramagnetism. Local moment formation is also not evident for this lowest *x* sample.

It has been stated[64] that for correlated disordered systems an enhancement of the susceptibility can occur at low temperatures. Additional evidence that the increase in

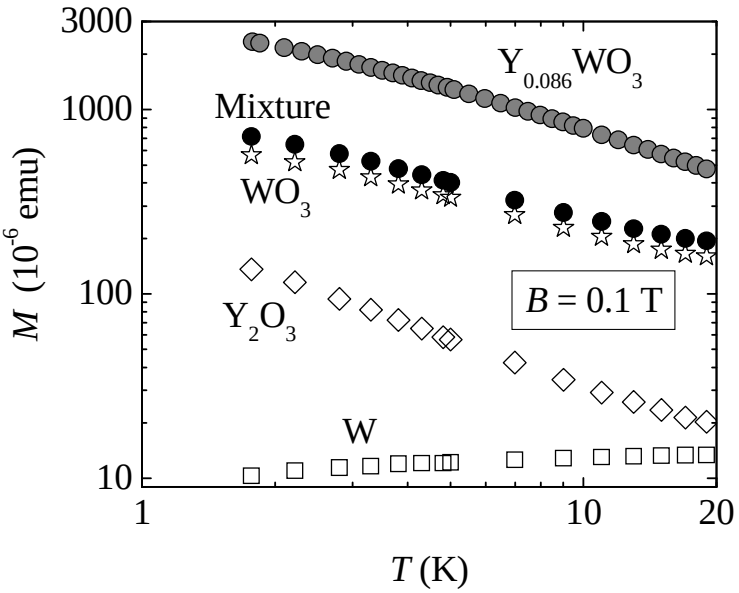

Fig. 6-16. Magnetization results for $Y_{0.086}WO_3$ showing the moment *M* vs the temperature *T* per 1 g of sample. An estimate of the moment of 1 g of the pre-sintered material (●) was obtained by measurements on the starting powders of WO_3, Y_2O_3 and W. The moment contribution of each powder to the 1 g mixture is shown.

Fig. 6-15a is due to impurities is shown in Fig. 6-16. The results indicate no significant difference (in magnitude and *T*-dependence) between the sample susceptibility and the estimate for the pre-sintered pellet. The dominant contribution to the mixture is from WO_3, which forms most of the starting materials, and provides the main source of the low temperature Curie-type susceptibility contribution. Pure WO_3 is diamagnetic, and this positive contribution would be due to the impurities.

6.4.2 Specific heat

Specific heat measurements were performed on a 10.5 mg sample of $Y_{0.096}WO_3$ using a Quantum Design heat capacity system. The measurements were taken in magnetic fields of 0 and 9 T, with temperatures ranging from 2 K to 100 K. The results are summarised in Fig. 6-17. The specific heat *C* is field-independent within experimental limits. The curve is a plot of the expression $C = \gamma T + \beta T^3$, which consists of the electronic (γT) and phonon (βT^3) contributions to the specific heat at low temperatures. The standard C/T vs T^2 plot of the data (see Fig. E-7 in appendix E) gives the fitting parameters as γ = 1.32 mJ/mol·K^2

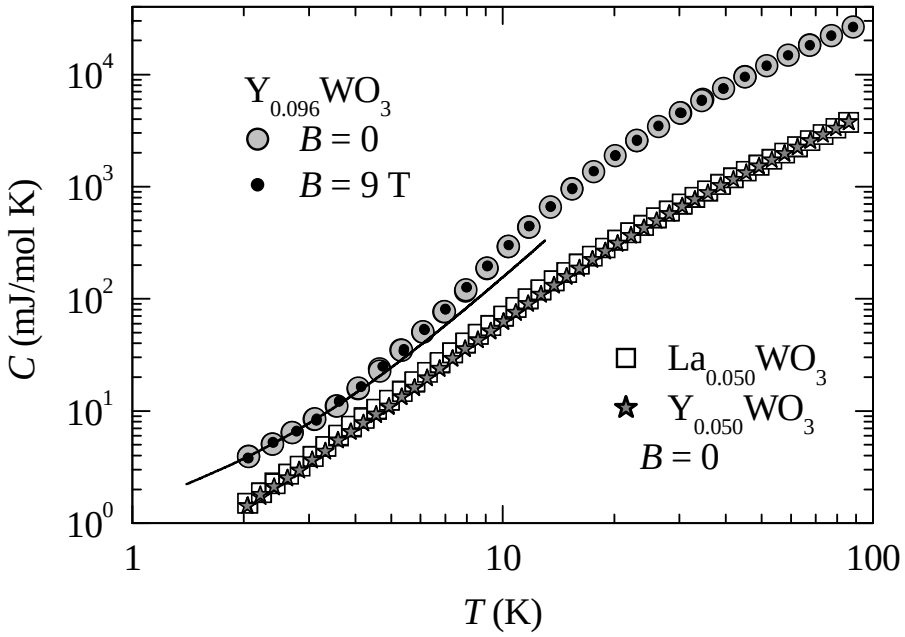

Fig. 6-17. The specific heat C of Y_xWO_3 and La_xWO_3 samples vs the temperature T for magnetic fields B = 0 and 9 T in a logarithmic plot. The curve is a low temperature fit of the expression $C = \gamma T + \beta T^3$ to the x = 0.096 data.

and β = 0.142 mJ/mol·K^4. The parameter β leads to a Debye temperature Θ_D = 239 K for the lattice. The non-zero field-independent value of γ is suggestive of a metallic system, consistent with the magnetization results.

The specific heat data shows no significant change in the specific heat when the 9 T field is applied. The difference in data is mostly due to experimental fluctuations, except for a possible very small anomaly occurring at T ~ 10 K. The position and magnitude of this anomaly is consistent with the Schottky-type specific heat obtained for impurity local moments using the parameters obtained from the VSM data. The specific heat, like the magnetization, therefore suggests no isolated local moment formation linked to carrier freeze-out in the bulk material.

The $Y_{0.096}WO_3$ electronic specific heat coefficient γ is close to metallic Na_xWO_3 values for similar effective concentrations ($x_{Na} \sim 3x_Y$) (Fig. 2-9). This indicates a similar density of single-particle states near the Fermi energy for the tungsten bronzes at similar donor-

electron concentrations. The specific heat results therefore also suggest $Y_{0.096}WO_3$ to be metallic. The Debye temperature Θ_D = 239 K for $Y_{0.096}WO_3$ is consistent with values found for WO_3 (Θ_D = 216 K) and Na_xWO_3 (Θ_D = 255 – 375 K for x = 0.23 – 0.60).[51,94]

According to the resistivity results, the x = 0.050 concentration appears to be non-metallic, having similar resistivity behaviour to the just-insulating sample of $Na_{0.34}Ta_{0.16}W_{0.84}O_3$ (Fig. 6-13). As a conclusion to this research, specific heat measurements were performed on samples of $Y_{0.050}WO_3$ and $La_{0.050}WO_3$. The results are included in Fig. 6-17 for a comparison to the specific heat data for metallic $Y_{0.096}WO_3$. As for the x = 0.096 results, measurements on the x = 0.050 samples in a 9 T magnetic field yielded no discernable difference from the zero-field data.

The coincidence of the $Y_{0.050}WO_3$ and $La_{0.050}WO_3$ data confirms the expected equivalence of the Y and La tungsten bronzes. The results also support the use of the nominal x values for the La_xWO_3 samples. A significant shift in the actual La concentration due to the sample preparation anomalies (§3.1) should have produced specific heat results noticeably different to that of $Y_{0.050}WO_3$.

The low temperature specific heat of $Y_{0.096}WO_3$ shows the typical metallic-type $\gamma T + \beta T^3$ contribution. The $Y_{0.050}WO_3$ and $La_{0.050}WO_3$ results show a distinctly different behaviour. For T < 20 K a power-law behaviour is observed in Fig. 6-17 with $C \propto T^{2.4}$. To determine the form of the low T electronic contribution the 3–parameter expression $\gamma T^k + \beta T^3$ was fitted to the x = 0.050 data. The results give $k \simeq 2$ and the fits are shown in Fig. 6-18. Including an additional linear term in the fit (for a metallic-type contribution) produces unphysical negative specific heat parameters. The values of β produce Debye temperatures Θ_D ~ 360 K, larger than the 240 K obtained for the metallic $Y_{0.096}WO_3$ sample.

The electronic specific heat may be expressed as

$$C_e = \int_0^\infty dE\,(E - E_F)\,\rho(E)\frac{\partial f_{FD}}{\partial T}\ , \qquad 6.5$$

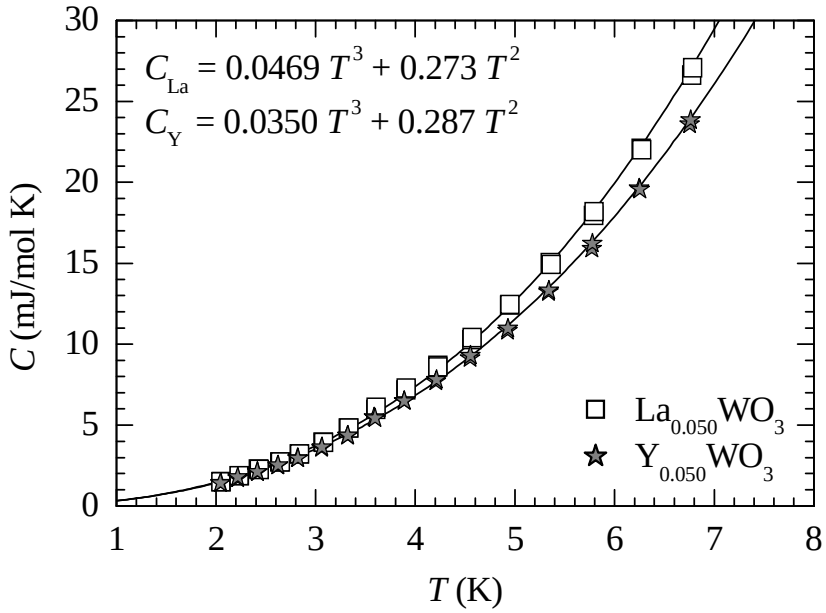

Fig. 6-18. The expression $C = \beta T^3 + \gamma T^2$ is fitted to the low temperature specific heat data of $Y_{0.050}WO_3$ and $La_{0.050}WO_3$ shown in Fig. 6-17.

where E_F is the Fermi energy, $\rho(E)$ the single-particle density of states and f_{FD} the Fermi-Dirac distribution function. Taking $\rho(E) = \rho(E_F) + \alpha|E - E_F|^n$ (see Eqs. 2.7 and 2.9), with $\rho(E_F)$, α and n constant, gives for $k_B T \ll E_F$

$$C_e = a_1 \rho(E_F) T + a_2 \alpha T^{n+1} \qquad 6.6$$

with a_1 and a_2 temperature-independent constants. The first linear term is the usual metallic contribution, arising from a non-zero $\rho(E_F)$, while the second term arises from a gap at the Fermi energy. The fitting results in Fig. 6-18 suggest a T^2 electronic contribution, which implies that $\rho(E_F) = 0$ and $n = 1$. This indicates the possible development of a linear soft gap at the Fermi level. Tunnelling conductance, which is supposed to reflect the single-particle density of states $\rho(E)$, suggests similar results for $Na_xTa_yW_{1-y}O_3$ with $x = 0.34$ and $y = 0.16$.[9,10] This is the same just-insulating sample of $Na_{0.34}Ta_{0.16}W_{0.84}O_3$ shown in Fig. 6-13 which compares well to $Y_{0.050}WO_3$ and $La_{0.050}WO_3$. The specific heat results therefore lend further support in classifying the $x = 0.05$ samples as insulating.

6.4.3 Nuclear magnetic resonance

Room temperature NMR measurements were performed on two samples of La_xWO_3 (x = 0.08 and 0.15). Both concentrations are metallic according to the conductivity results. Fig. 6-19 shows the ^{139}La Knight shift data. A reference solution of lanthanum nitrate ($La(NO_3)_2$) was used. The relaxation time T_1 was found to become long as the temperature is lowered, pointing to a phonon relaxation mechanism, while $T_2 \sim 1.0$ ms.

Within experimental error the peak positions are the same for all three compounds. The results are consistent with a trivalent La^{+3} state in La_xWO_3 and show that the La^{+3} ions have essentially the same electronic state in all three cases. Studies of the ^{183}W and ^{23}Na Knight shifts in metallic Na_xWO_3 indicate that the conduction electrons are in states of W 5*d* and not Na 3*s* character.[43,44,95] The La_xWO_3 NMR results therefore support the view that the tungsten bronze donor atoms donate their valence electrons to the tungsten 5*d* orbitals and are uncoupled from the conduction band.

An NMR study of $Na_xTa_yW_{1-y}O_3$ showed no evidence of local moment formation, even on the insulating side of the transition.[96] This is consistent with the magnetization and specific heat results for Y_xWO_3 and La_xWO_3 presented above.

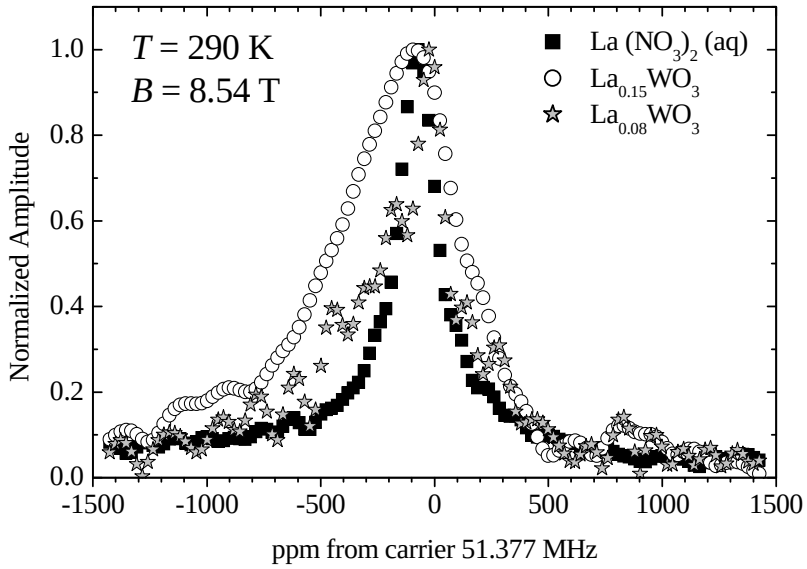

Fig. 6-19. ^{139}La Knight shift data for $La_{0.08}WO_3$, $La_{0.15}WO_3$ and a solution of lanthanum nitrate. The amplitudes are normalized for comparison.

6.5 Summary

- Polycrystalline Y_xWO_3 and La_xWO_3 have been prepared by solid state reaction and characterised by x-ray diffraction, optical reflectivity and electrical transport. The results point to universal behaviour in the metallic phase of the tungsten bronzes, governed by the donor–electron concentration in the conduction band.

- The Y_xWO_3 and La_xWO_3 electrical conductivity, measured as a function of x and T, shows a family of curves similar to other tungsten bronzes, and indicative of MI transition behaviour at low x. A crossover from metallic-type to semiconducting-type temperature dependence is observed on reducing the donor concentration x. Just–metallic samples have a low T conductivity less than the Mott minimum metallic conductivity.

- Electrical conductivity results show that a MI transition occurs for nominal concentrations between $x = 0.05$ and $x = 0.06$ in both Y_xWO_3 and La_xWO_3. A critical concentration $x_C = 0.055 \pm 0.005$, corresponding to an electron concentration $n_C = 3.0 \pm 0.3 \times 10^{21}$ cm^{-3}, is therefore quoted for these two uncompensated systems.

- The metallic nature of the single-phase cubic structure of the tungsten bronzes has been confirmed for both Y_xWO_3 and La_xWO_3. The structural changes that occur in uncompensated tungsten bronzes on lowering x do not appear to have any major impact on the conductivity behaviour in the vicinity of the MI transition.

- The Hall effect at 300 K is consistent with the fully-ionised-donor model. The Hall carrier concentration for metallic samples decreases on cooling, and plateaus at a reduced value below 30 K. These results suggest the existence of localised and extended states in a pseudogap at the Fermi energy, as predicted by electronic structure calculations.

- A small positive magnetoresistance is observed below 100 K which increases with decreasing temperature, and also increases for lower x.

- No evidence of local moment formation has been obtained from magnetization and specific heat measurements at low temperatures.

Chapter 7: Conclusions

Sintered polycrystalline samples of the trivalent-ion doped tungsten bronzes Y_xWO_3 ($0.05 \leq x \leq 0.20$) and La_xWO_3 ($0.05 \leq x \leq 0.23$) have been prepared. The resultant samples were visibly homogeneous for all x and exhibit the bluish-black colour found in other tungsten bronzes with the same donor electron concentrations. The structural and electrical transport properties are consistent with those expected for the tungsten bronzes. Density measurements indicate a crystal volume fraction ~45%. Powder XRD suggest a stable single-phase cubic perovskite phase for $0.086 \lesssim x_Y \lesssim 0.127$ and $0.086 \lesssim x_{La} \lesssim 0.210$, with a lattice constant ~3.8 Å as observed in other tungsten bronzes. Additional phases occur outside the cubic phase ranges. Diffuse reflectance spectroscopy in the visible and infrared range produces x-dependent results dominated by metallic-type reflection, accounting for the variations in colour and lustre in the tungsten bronzes.

Electric transport investigations, focussing on dc conductivity and Hall effect measurements, were performed on the Y_xWO_3 and La_xWO_3 samples. The observation and investigation of the MI transition was a principal research objective. The limitations of polycrystalline samples, evident in earlier Na_xWO_3 studies, are seen here in the higher x samples. The crystal volume fraction and grain boundary effects play important roles in certain measured properties. The solubility limit of the donor atoms in the tungsten bronzes is demonstrated for Y_xWO_3.

The conductivity σ shows a family of curves typical of MI transition systems and comparable to results for Na_xWO_3 and $Na_xTa_yW_{1-y}O_3$. A change from metallic-type ($d\sigma/dT < 0$) to semiconducting-type ($d\sigma/dT > 0$) behaviour is observed as x is reduced. All the single-phase cubic samples show metallic behaviour ($\sigma \neq 0$ as $T \rightarrow 0$ K), confirming the results obtained for the other uncompensated tungsten bronzes, and indicating a critical concentration $x_C < 0.086$. The structural changes in lowering x do not appear to significantly affect the MI transition, as the conductivity curves show a similar evolution to those of $Na_xTa_yW_{1-y}O_3$, which remains cubic through the transition.

The room temperature Hall effect suggest that both Y and La are fully ionised in trivalent states with the valence electrons donated to the WO_3 conduction band. This is also shown by NMR measurements on La_xWO_3 samples. The fully-ionised-donor model for the tungsten bronzes is therefore supported. The sign of the Hall coefficient confirms the expected negative charge carriers. The Hall concentration decreases on cooling, as observed well into the metallic phase, indicating a partial "freeze-out" of charge carriers. This supports similar results observed in Na_xWO_3. No evidence of isolated local moment formation is found from vibrating sample magnetometer and specific heat measurements at low temperatures. Magnetoresistance appeared at lower temperatures, and this effect was also measured as a by-product of the Hall investigations. The magnetoresistance is positive, only detectable below 100 K, and increases on cooling. Small resistivity changes of $0.01\% \lesssim \Delta\rho/\rho \lesssim 0.1\%$ occur in 1 T fields.

For lower donor concentrations ($x < 0.12$) the Y_xWO_3 and La_xWO_3 samples show very similar behaviour in all their properties. This shows that the donor valence and not donor type will be most important in determining the behaviour of the tungsten bronzes. Y_xWO_3 and La_xWO_3 are shown to be equivalent systems for these types of investigations. Comparison to other tungsten bronzes shows very similar results with respect to the effective donor concentration. This shows that the conduction band concentration is of dominant importance in determining the properties of interest. The comparison points to universal behaviour in the tungsten bronzes.

The MI transition was observed to occur for nominal concentrations between $x = 0.05$ and $x = 0.06$ in both the Y_xWO_3 and La_xWO_3 samples using several methods of analysis. The critical concentration $x_C \simeq 0.055$ obtained here for the two trivalent doped tungsten bronzes is about one third that obtained for $Na_xTa_yW_{1-y}O_3$ with $(x-y)_C \simeq 0.18$. This corresponds to the same electron concentration in the conduction band. The result supports claims that the MI transition in the tungsten bronzes is primarily driven by electron-electron interactions. The disorder produced by random doping will be quite different in the trivalent and monovalent donor systems, and does not appear to play a dominant role. The results also show that for $x \gtrsim x_C$ an atypical metallic phase occurs, with properties that evolve with x, such as a temperature dependent Hall concentration not observed in typical metals. This atypical behaviour is related to the presence of strong correlation effects in the

just-metallic regime. Metallic behaviour adequately described by conventional band theory is only expected well above x_C (~$3x_C$ for Na_xWO_3).

The range of concentrations investigated here includes all of the interesting conductivity features found in this class of compounds. The lowest concentration exhibits insulating behaviour ($\sigma \rightarrow 0$ as $T \rightarrow 0$ K). At somewhat higher x is the range of unconventional metallic samples ($d\sigma/dT > 0$ but $\sigma \neq 0$ as $T \rightarrow 0$ K). A crossover then occurs at the highest concentrations with the conductivity exhibiting features more typical of conventional metals.

The research here presents the first systematic transport investigation on trivalent-ion doped tungsten bronzes. The results complement the previous research done on other tungsten bronzes, and lay a foundation for further research on the Y_xWO_3 and La_xWO_3 compounds. The experimental research mentioned in chapter 2 on the other tungsten bronzes could be performed in the same manner on the trivalent-doped compounds. The conductivity results, supported by specific heat measurements, indicate the lowest concentration $Y_{0.05}WO_3$ and $La_{0.05}WO_3$ samples to be just-insulating. Further investigations on the MI transition could therefore also focus on concentrations with $x < 0.05$ for insulating–sample behaviour. Observation of hopping conduction in just–insulating samples would require temperatures well below 2 K. Preparing and investigating single crystal samples of Y_xWO_3 and La_xWO_3 should also be considered. The results here, however, show that the polycrystalline structure does not appear to significantly affect the electrical properties for the lower x samples. The details of the multiphase structural nature as x is reduced below the cubic phase range needs to be determined. The anomalous low temperature behaviour of the Hall carrier concentration in the vicinity of the MI transition is important and requires further investigation.

Appendix

The following sections are included in the appendix.

A. Gives the theoretical background for the analysis of powder x-ray diffraction data. The expressions were derived to obtain better estimates of the lattice constants than the values presented by the XRD equipment.

B. Gives the theoretical basis of the main equation used for the transport data. A detailed derivation is presented to understand the experimental observations, especially the effects of a magnetic field on the voltage measurements.

C. Describes the numerical method used to determine the van der Pauw function $F(r)$. This was required to automate the determination of the resistivity using the van der Pauw method.

D. Introduces the density–corrected resistivity used in the thesis. The anomalous behaviour in the resistivity due to crystal volume fraction effects required explanation.

E. Provides additional data in the form of figures with descriptions in the captions.

F. Presents two papers published so far based on this research.

A. Theory for powder x-ray diffraction

Fig. A-1 shows an example of a powder x-ray diffraction (XRD) recording for a sample of cubic $La_{0.21}WO_3$. The Bragg condition for the constructive interference from a set of lattice planes, which gives rise to the peaks in the XRD data, is $2d \sin\theta = n_o \lambda$, where λ is the x-ray wavelength, n_o is the order of the interference, d is the lattice plane spacing, and θ the angle between the incident beam and the lattice plane. The diffracted beam is therefore deviated by an angle 2θ, which is the quantity specified in the XRD data as seen in Fig. A-1. For a cubic lattice the Bragg condition can be expressed as

$$2a \sin\theta_m = \sqrt{m}\,\lambda. \qquad \text{A.1}$$

The cubic lattice constant is a and $m = h^2 + k^2 + l^2$ is the peak index, with (hkl) the integer Miller indices (both shown in Fig. A-1), and θ_m is the position of the corresponding peak. The positions of the peaks therefore allow for a determination of the cubic lattice constant.

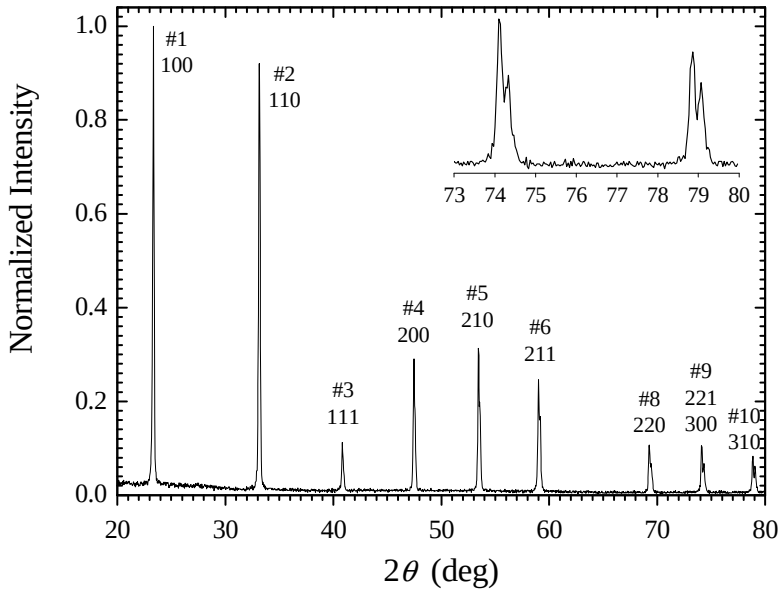

Fig. A-1. A powder XRD trace for $La_{0.21}WO_3$ showing results typical of a cubic perovskite structure. The peak labels give the peak index *m* and Miller plane indices *hkl*. The inset focuses on peaks #9 and #10, showing the peak splitting due to the $K_{\alpha 1}$ and $K_{\alpha 2}$ radiation.

The copper target in the *x*-ray tube generates $K_{\alpha 1}$, $K_{\alpha 2}$ and K_{β} radiation with wavelengths λ = 1.5405 Å, 1.5443 Å, and 1.3922 Å respectively. A nickel filter is generally used to eliminate the K_{β} radiation, as in Fig. A-1. (See Fig. 3-5 for an XRD trace without a nickel filter showing the K_{β} peaks.) As observed in the inset of Fig. A-1, the small difference between the $K_{\alpha 1}$ and $K_{\alpha 2}$ wavelengths ($\simeq$ 0.004 Å) is apparent in the peak splitting at larger angles (since $\Delta\theta_m \propto \tan\theta_m$ from differentiating Eq. A.1 w.r.t λ). For the XRD data analysis the average wavelength 1.5418 Å was used.

The angular position of the XRD spectrometer was not calibrated during each run, and this could introduce a constant shift in the presented values of 2θ. This zero-offset problem limits the accuracy with which the lattice parameter is calculated from Eq. A.1. It is therefore preferable to work with the peak separation $\theta_{mn} = \theta_m - \theta_n$ which eliminates the zero-offset θ_0 (see Fig. A-2). Using the trigonometric identities $\cos(\theta_m - \theta_n) = \cos(\theta_m)\cos(\theta_n) + \sin(\theta_m)\sin(\theta_n)$ and $\cos^2\theta = 1 - \sin^2\theta$, the Bragg condition in Eq. A.1 can be expressed as

$$\left(\frac{2a}{\lambda}\right)^2 = \frac{m + n - 2\sqrt{mn}\cos\theta_{mn}}{\sin^2\theta_{mn}}. \qquad \text{A.2}$$

The cubic lattice constant is then determined from all the peak separations θ_{mn}. The value of a was determined for each pair (m,n) of peaks and the average of these values was then presented.

The thermal expansion of a crystal is due to the changes in the lattice constant as the temperature is changed. The defining equation for the expansion coefficient α can be expressed as

$$\frac{\Delta a}{a} = \alpha \Delta T, \qquad \text{A.3}$$

where Δa is the change in the lattice constant a due to a temperature change ΔT.

Since the XRD data provides the lattice constant, it is in principle possible to determine the expansion coefficient by performing runs at different temperatures. The Bragg

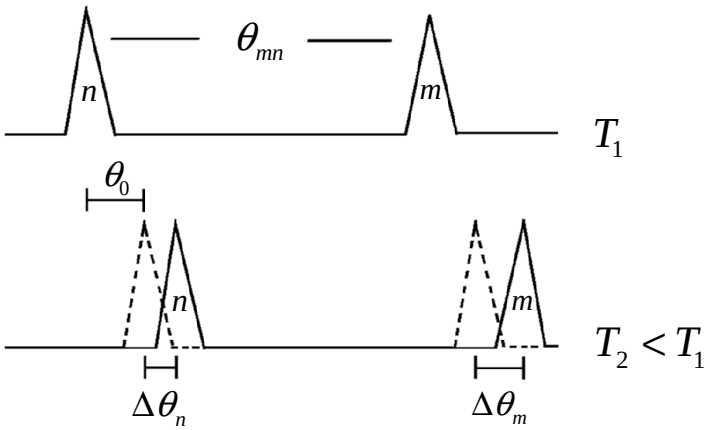

Fig. A-2. XRD recordings for two temperatures T_1 and T_2 (< T_1) showing the effects of the zero offset θ_0 and the thermal shifts $\Delta\theta_n$ and $\Delta\theta_m$. The dashed lines show the positions the peaks would have at T_1 for the second run.

condition in Eq. A.1 shows that the peak positions will shift with a changing lattice constant. Differentiating Eq. A.1 w.r.t *a* gives

$$\frac{da}{a} = -\frac{d\theta_m}{\tan\theta_m}. \qquad \text{A.4}$$

A reduction in temperature will reduce the lattice constant (da < 0 from Eq. A.3) which will shift the XRD peaks to larger angles (dθ_m > 0 from Eq. A.4). This is illustrated in Fig. A-2. Since the offset angle θ_0 is the same for all the peaks in the second run $\theta_m(T_2) = \theta_m(T_1) + \theta_0 + \Delta\theta_m^{thermal}$. Using Eqs. A.3 and A.4

$$\theta_m(T_2) - \theta_m(T_1) = \theta_0 + (-\alpha\Delta T)\tan\theta_m. \qquad \text{A.5}$$

Plotting the change in peak position $\Delta\theta_m = \theta_m(T_2) - \theta_m(T_1)$ versus tan θ_m for each peak *m* should produce a straight line graph with intercept θ_0 and slope $-\alpha\Delta T$ from which the expansion coefficient α is then be obtained. The expansion coefficient can also be obtained directly using Eq. A.3 by determining the lattice constant at both temperatures with Eq. A.2. Both methods were used to obtain improved estimates of α.

B. Theory for electric transport measurements

Referring to Fig. B-1, the main equation used in the analysis of the transport data is

$$R_{xy} = \frac{V_{xy}}{I} = \frac{\rho(B)}{d}\Gamma_{xy} + \varepsilon_{xy}\frac{R_H}{d}B \ . \qquad \text{B.1}$$

The sample of uniform thickness d has a resistivity ρ, which may depend on the magnetic field B, and a Hall coefficient R_H. When a current I flows via two contacts on the periphery, the above equation gives the general resistance $R_{xy} = V_{xy}/I$ measured between any two points x and y on the periphery (V_{xy} is the measured voltage). The switch $\varepsilon_{xy} = 1$ if the current flows through the path connecting x and y (such as a' – a in Fig. B-1), otherwise $\varepsilon_{xy} = 0$ (such as a – b in Fig. B-1). Γ_{xy} is a geometrical factor depending only on the shape of the sample and the positioning of the current and voltage leads. It is independent of the temperature T and magnetic field B. In the special case of a bar sample $\Gamma_{xy} = L/w$, where w is the sample width and L is the separation between the voltage contacts.

To derive Eq. B.1 it is necessary to study the behaviour of the voltages on the periphery

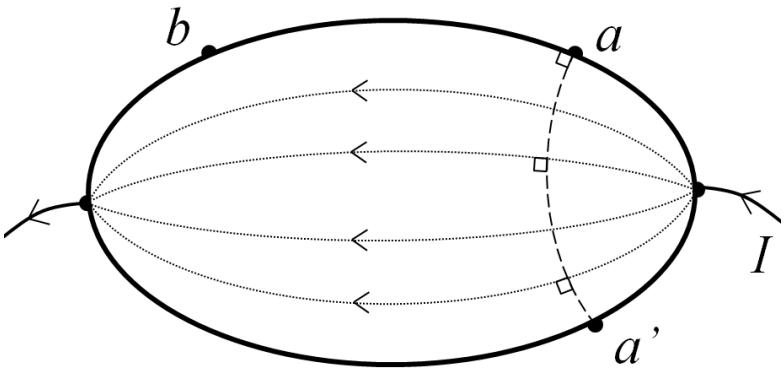

Fig. B-1. Setup for transport measurements on samples with uniform thickness and resistivity. Voltage leads are shown by *a*, *a'* and *b*, and a current *I* flows through the two points shown. The dotted lines indicated current flow lines, while the dashed line shows a path from *a'* to *a* perpendicular to the current flow. The magnetic field *B* is perpendicular to the page.

of the sample. These voltages will be determined by the electric fields produced inside the sample by the applied current. The application of a magnetic field $\vec{B}$ will generate a Lorentz force on the charge carriers ($\vec{F} = q\vec{v} \times \vec{B}$, q – carrier charge; $\vec{v}$ – drift velocity). The accumulation of charge on the periphery will then generate a Hall electric force ($\vec{F} = q\vec{E}_H$) which eventually cancels the Lorentz force. The current flow lines will remain unaffected by the application of $\vec{B}$. It is therefore convenient to decompose the total electric field $\vec{E}$ into the Hall electric field $\vec{E}_H$ and the current driving field $\vec{E}_J$. In terms of the current density $\vec{J} = qn\vec{v} = R_H^{-1}\vec{v}$, with n the carrier concentration,

$$\begin{aligned} \vec{E}_H &= -R_H \vec{J} \times \vec{B} \\ \vec{E}_J &= \rho \vec{J}. \end{aligned} \qquad \text{B.2}$$

The Hall field cancels the Lorentz force of the magnetic field, accounting for the minus sign, and is always perpendicular to the field $\vec{B}$ and $\vec{E}_J$ (which is parallel to $\vec{J}$). The second equation is Ohm's law. The voltage difference $V_{xy} = V_x - V_y$ between arbitrary points x and y on the periphery is therefore

$$V_{xy} = \int_x^y \vec{E} \cdot d\vec{l} = \int_x^y \vec{E}_J \cdot d\vec{l} + \int_x^y \vec{E}_H \cdot d\vec{l} \ . \qquad \text{B.3}$$

The first integral represents the voltage driving the current, while the second integral is the induced Hall voltage. Since the electric field is conservative, the path integral is independent of the path, which may be chosen arbitrarily to simplify the calculation of the voltage V_{xy}. Referring to Fig. B-1, there are two cases to be considered here: (1) voltage contacts where a peripheral path may be chosen to exclude the current contacts (such as *a* and *b*); (2) voltage contacts where any peripheral path will include one current contact (such as *a'* and *b*).

Considering case (1) with peripheral path $a - b$, since the current does not cross the surface, it must flow parallel to the path. The Hall field $\vec{E}_H$ is always perpendicular to the current (Eq. B.2), and hence perpendicular to the path. The second term in Eq. B.3 is therefore zero and so

$$V_{ab} = \int_a^b \vec{E}_J \cdot d\vec{l} \; = \rho \int_a^b \vec{J} \cdot d\vec{l} \; . \qquad \text{B.4}$$

The magnetic field dependence of V_{ab} only appears through the field dependence of the resistivity. The current distribution is unaffected by the magnetic field, and the integral $\int \vec{J} \cdot d\vec{l}$ is therefore constant for a fixed current *I*. The Hall voltages generated by the magnetic field do not affect the voltage V_{ab}.

Considering case (2) with voltage contacts *a'* and *b*, it is convenient to split the path from *a'* to *b* into two. Referring to Fig. B-1, the first path *a'*– *a* is chosen through the sample and perpendicular to the current flow lines, while the second path is *a* – *b* as in case (1). Then $V_{a'b} = V_{a'a} + V_{ab}$, with V_{ab} given by Eq. B.4. Since $\vec{J}$ is perpendicular to the path *a'* – *a*, the first integral in Eq. B.3 vanishes, and

$$V_{a'a} = \int_{a'}^{a} \vec{E}_H \cdot d\vec{l} \; = -R_H \int_{a'}^{a} \left(\vec{J} \times \vec{B} \right) \cdot d\vec{l} \; . \qquad \text{B.5}$$

Letting the uniform magnetic field, which is perpendicular to the surface, point into the page in the $-\hat{z}$ direction ($\vec{B} = -B\hat{z}$),

$$V_{a'b} = R_H B \int_{a'}^{a} \left(\vec{J} \times \hat{z} \right) \cdot d\vec{l} + \rho \int_a^b \vec{J} \cdot d\vec{l} \; . \qquad \text{B.6}$$

To determine the voltages along the periphery of the sample, the two path integrals in Eq. B.6 need to be calculated. The paths *a'* – *a* and *a* – *b* are uniquely determined by the points *a'* and *b*. Both the path integrals depend only on the current density, and hence the current distribution inside the sample, which in turn depends on the sample geometry. Eq. B.6 is the general formula for determining the voltages, with Eq. B.4 representing the case when *a'* = *a*.

The path *a'* – *a* is chosen such that the current crosses the path perpendicularly, with $\vec{J} \perp \hat{z}$, $\vec{J} \perp d\vec{l}$ and $d\vec{l} \perp \hat{z}$, and therefore $\int_{a'}^{a} \left(\vec{J} \times \hat{z} \right) \cdot d\vec{l} = \int_{a'}^{a} J \, dl$. The current crossing the

path element dl is $di = \vec{J} \cdot d\vec{A} = J\, d\, dl$, with the total current $I = \int_{a'}^{a} di$. The first path integral in Eq. B.6 is therefore

$$\int_{a'}^{a} \left(\vec{J} \times \hat{z} \right) \cdot d\vec{l} = \frac{1}{d} \int_{a'}^{a} di = \frac{I}{d} \ . \qquad \text{B.7}$$

The path $a - b$ for the second path integral in Eq. B.6 is along the boundary of the sample. The current does not cross the surface, so $\vec{J} \parallel d\vec{l}$ and $\int_a^b \vec{J} \cdot d\vec{l} = \int_a^b J\, dl$. Referring to Fig. B-2 and noting that the current flows parallel to the edge of the sample, the current density J along the edge from point a to b can be expressed as

$$J(l) = \lim_{N \to \infty} \left(\frac{\delta I}{\delta w(l)\, d} \right) = \frac{I}{d} \lim_{N \to \infty} \left(\frac{1}{N\, \delta w(l)} \right) \ . \qquad \text{B.8}$$

Defining

$$\Gamma_{ab} = \lim_{N \to \infty} \left(\frac{1}{N} \int_a^b \frac{dl}{\delta w(l)} \right) \qquad \text{B.9}$$

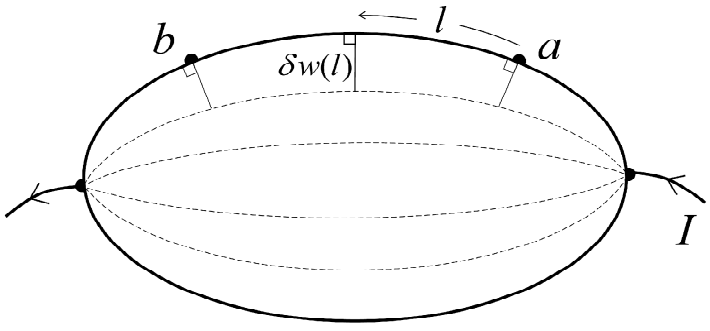

Fig. B-2. Visual aid to evaluate the path integral $\int_a^b \vec{J} \cdot d\vec{l}$. Dashed lines represent current flow lines dividing the sample into *N* sections, each carrying an equal current $\delta I = I/N$. *l* is the distance from *a* along the periphery and $\delta w(l)$ is the width of the section.

the path integral may then be expressed as

$$\int_a^b \vec{J}\cdot d\vec{l} = \frac{I}{d}\lim_{N\to\infty}\left(\frac{1}{N}\int_a^b \frac{dl}{\delta w(l)}\right) = \frac{I}{d}\Gamma_{ab} \ . \qquad \text{B.10}$$

The factor Γ_{ab} depends only on the geometry of the sample and the locations of the current and voltage contacts. Since the integrand in Eq. B.9 is the ratio of two linear lengths, Γ_{ab} is temperature independent. The factor is also independent of the magnetic field, since the current distribution would be unaffected. For a particular sample used in an experiment, with current and voltage contacts fixed, the factor Γ_{ab} is therefore a geometrical constant.

Inserting Eqs. B.7 and B.10 into Eqs. B.4 and B.6, the voltages for the two cases are

$$\begin{aligned} V_{ab} &= \rho\frac{I}{d}\Gamma_{ab} \\ V_{a'b} &= R_H B\frac{I}{d} + \rho\frac{I}{d}\Gamma_{ab} \ . \end{aligned} \qquad \text{B.11}$$

Defining the generalized resistance $R_{xy} = V_{xy}/I$ for any two points *x* and *y* on the sample's edge then gives the required result of Eq. B.1.

The preferred sample geometry for transport measurements is the bar-shaped sample shown in Fig. B-3. The sample has a constant width *w* and the current contacts are the two sides of the sample. The bar-sample setup is equivalent to the setup in Fig. B-1 for arbitrary shaped samples, and is chosen such that the current flow is uniform within the sample. All the above equations are therefore also applicable. The bar sample represents a special case where the geometric factor Γ_{ab} defined by Eq. B.9 may be easily determined. For a uniform current in Fig. B-3

$$\Gamma_{ab} = \frac{L}{w} \ . \qquad \text{B.12}$$

Referring to Fig. B-3, with points *a'* and *a* equidistant from the sample's end, and applying Eq. B.1 gives

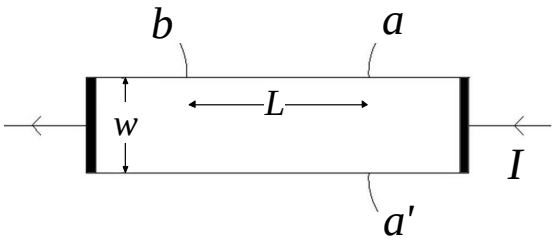

Fig. B-3. Setup for a bar-shaped sample of width *w*. The separation between the voltage contacts *a* and *b* is *L*.

$$R_{ab} = \frac{\rho L}{wd} = \rho \frac{L}{A} \qquad \text{B.13}$$

and

$$R_{a'a} = \frac{V_{a'a}}{I} = \frac{R_H}{d} B \ . \qquad \text{B.14}$$

The above two equations define the resistivity ρ and Hall coefficient R_H of a material.

In conclusion, the two configurations for two-point transport measurements on arbitrary shaped samples with uniform thickness and resistivity are shown in Fig. B-4. For configuration (1)

$$R = \frac{V}{I} = \frac{\Gamma}{d} \rho(T, B) \qquad \text{B.15}$$

and measurement of the resistance allows for a direct investigation of the temperature and magnetic field dependence of the resistivity (Γ/d is a constant – ignoring thermal changes in d). For the polycrystalline samples investigated here, the field dependence is isotropic and near-linear for fields up to 1.2 T (see §5.3). Letting R_0 and ρ_0 be the zero-field values,

$$\rho(B) = \rho_0 \left(1 + \alpha_{MR} |B|\right) \qquad \text{B.16}$$

which defines the magnetoresistance coefficient α_{MR}. Inserting this expression into Eq. B.15 gives the magnetic field dependence of the measured resistance

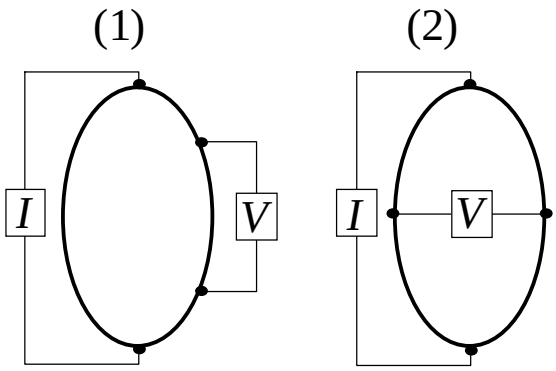

Fig. B-4. The two configurations for two-point transport measurements.

$$R(B) = R_0\left(1 + \alpha_{\mathrm{MR}}|B|\right) . \qquad \text{B.17}$$

For configuration 2 in Fig. B-4

$$R = \frac{V}{I} = \frac{\Gamma}{d}\rho(T,B) + \frac{R_H(T)}{d}B \qquad \text{B.18}$$

and resistance measurements allows for an investigation of the Hall effect by determining the Hall coefficient R_{H}. At a fixed temperature, using Eq.B.16,

$$R(B) = R_0 + (\alpha_{\mathrm{MR}}R_0)|B| + \left(d^{-1}R_H\right)B . \qquad \text{B.19}$$

For the special case when the voltage contacts are balanced ($\Gamma = 0$ in Eq. B.18 $\rightarrow R_0 = 0$ in Eq. B.19) or when there is no magnetoresistance ($\alpha_{\mathrm{MR}} = 0$), the Hall coefficient R_{H} is directly obtained from the measured resistance at any non-zero field. Otherwise, noting that the two B-dependent terms in Eq. B.19 are odd and even, the magnetoresistance coefficient α_{MR} and Hall coefficient R_{H} can be determined by also measuring the resistance in the reversed field direction. Then

$$\begin{aligned} R(+B) + R(-B) &= 2R_0\left(1 + \alpha_{\mathrm{MR}}|B|\right) \\ R(+B) - R(-B) &= 2\frac{R_H}{d}B . \end{aligned} \qquad \text{B.20}$$

C. The van der Pauw function $F(R_1/R_2)$

In the van der Pauw method, referring to §4.1.1, the resistivity ρ is given by

$$\frac{\rho}{d} = \frac{\pi}{\ln 2}\frac{(R_1 + R_2)}{2} F\left(\frac{R_1}{R_2}\right). \qquad \text{C.1}$$

The function $F(r)$ depends only on the ratio $r = R_1/R_2$ of the two measured resistances R_1 and R_2, and is defined by the equation

$$\cosh\left(\frac{r-1}{r+1}\cdot\frac{\ln 2}{F}\right) = \frac{1}{2}\exp\left(\frac{\ln 2}{F}\right). \qquad \text{C.2}$$

Since cosh is symmetric, $F(r) = F(1/r)$ and R_1 and R_2 may be freely interchanged in Eq. C.1. It can therefore be assumed that $r \geq 1$ ($R_1 \geq R_2$). A plot of F versus r is shown in Fig. C-1. Notice that $0 < F \leq 1$ is a decreasing function with $F \to 0$ as $r \to \infty$. In most geometries $R_1 \sim R_2$, and then $F \sim 1$ gives a small correction factor in Eq. C.1.

The aim is to numerically determine F for each value of $r \geq 1$. Letting $y = \ln 2/F \in [\ln 2, \infty)$ and $t = (r-1)/(r+1) \in [0, 1)$, the objective is to find y as a function of t by solving the equation $2\cosh(ty) = \exp(y)$. To get an indication about the dependence of y on

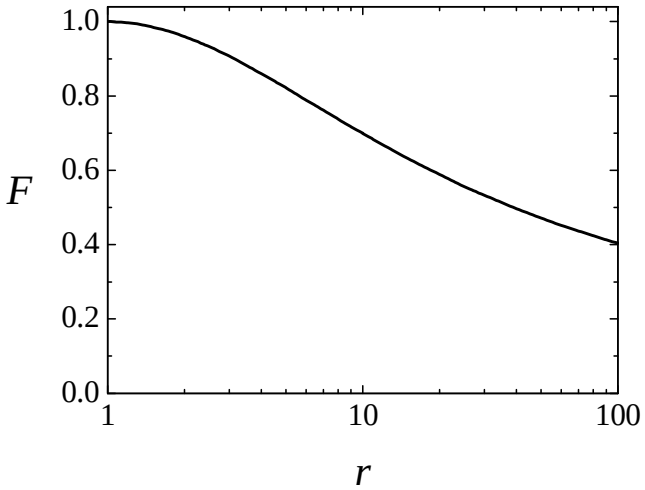

Fig. C-1. A plot of the van der Pauw function $F(r)$ as defined by Eq. C.2.

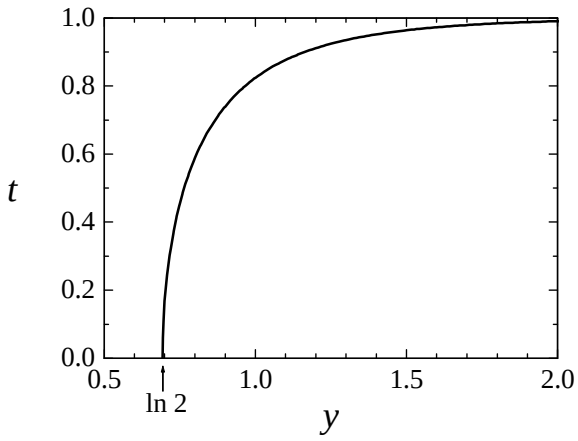

Fig. C-2. A plot of t versus y as defined by Eq. C.3.

t, it is possible to explicitly solve for *t* as a function of *y*, with

$$t = \frac{1}{y}\cosh^{-1}\left(\frac{1}{2}e^{y}\right) = \frac{1}{y}\ln\left(\frac{1}{2}e^{y} + \sqrt{\left(\frac{1}{2}e^{y}\right)^{2} - 1}\right) \qquad \text{C.3}$$

and a plot of this function is shown in Fig. C-2. Note the singularity with $y \to \infty$ as $t \to 1$. Determining *y* for a particular value of $t \in [0, 1)$ involves finding the zero of the function $G(y) = e^{ty} + e^{-ty} - e^{y}$ in the interval [ln2, ∞). For each *t* the zero of *G*(*y*) has to be solved numerically, and the bisection method can be used. However, the bisection method requires a closed interval.

For most geometries used in the van der Pauw technique the measured resistances R_1 and R_2 have similar orders of magnitude. Choosing the limit of $r = R_1/R_2 \leq 10^6$ should be safe for almost any sensible geometry. For $r \leq 10^6$, $t \leq 0.999998$ and hence $y < 5.7 \simeq 8.2 \ln 2$. Choosing the interval [ln2, 9 ln2] on which to solve the equation $G(y) = 0$ will ensure finding solutions of *y* for $R_1/R_2 \leq 10^6$. For larger resistance ratios the value of *F* will be set to zero to indicate an out-of-range ratio R_1/R_2, which should not occur in general.

The algorithm for the determination of *F*(*r*) would be:

- Determine R_1 and R_2. (Obtained by voltage and current measurements.)
- Check that the values are in range ($10^{-6} \leq R_1/R_2 \leq 10^6$). If not, let $F = 0$.

- Let $t = \left|\frac{R_1 - R_2}{R_1 + R_2}\right| = \frac{r-1}{r+1}$. The absolute value takes care of the case when $R_1 < R_2$.

- Solve $e^{ty} + e^{-ty} - e^{y} = 0$ for y using the bisection method on the interval [ln2, 9ln2].

- Let $F = \frac{\ln 2}{y}$.

The number of iterations N used in the bisection method determines the accuracy of the solution. Since $F = \frac{\ln 2}{y}$, $\frac{\delta F}{F} \approx \frac{\delta y}{y}$ and to determine F with n significant figures requires that

$$\frac{\delta y}{y} \lesssim 10^{-n}. \qquad \text{C.4}$$

In the bisection method the uncertainty in the result is just the starting interval width divided by 2^N. Using the interval [ln2, 9ln2], the uncertainty in the solution is $\delta y = \frac{9\ln 2 - \ln 2}{2^N} = \frac{\ln 2}{2^{N-3}}$. Since $y \geq \ln 2$, this implies that $\frac{\delta y}{y} \leq \frac{1}{2^{N-3}}$, and Eq. C.4 can be satisfied by letting $\frac{1}{2^{N-3}} < 10^{-n}$. This requires that $N > 3 + n \ln 10$. Below is a listing of the Pascal procedure used to determine the function $F(R_1/R_2)$. For $N = 15$ used below, the precision is about 5 significant figures.

```
function vdP_f(R1,R2: real): real;
  var
    Ly,Uy,My,t: real;
    n: byte;
  begin
    if (R2 >= 1e6*R1) or (R1 >= 1e6*R2) then vdp_f := 0   {out of range}
    else begin
      t := abs(R2-R1)/(R2+R1);
      Ly := 0.6931; Uy := 9*0.6931;  {Ly = ln2; Uy = 9*ln2}
      for n := 1 to 15 do begin
        My := (Ly+Uy)/2;
        if exp(t*My)+exp(-t*My)-exp(My) > 0 then Ly := My
                                            else Uy := My;
      end;
      vdP_f := ln(4)/(Uy+Ly);  {= ln(2)/MidPoint[Uy,Ly] }
    end;
  end;
```

D. The density–corrected resistivity

The plot of the La_xWO_3 room temperature resistivity in Fig. 3-8b shows an anomalous resistivity minimum for $x \sim 0.15$. The crystal volume fraction in Fig. 3-6b shows significant fluctuation in this region. In order to account for this behaviour in the sample resistivity, the effect of the polycrystalline porosity on the sample resistivity is investigated.

The resistance R of the bar sample in Fig. D-1a is

$$R = \rho_{\text{sample}} \frac{L}{A} \qquad \text{D.1}$$

where L is the sample length and A is the area through which the current flows. For a polycrystalline material, with a crystal volume fraction $f = V_{\text{crystal}} / V_{\text{sample}}$ (= sample density/crystal density), the sample resistivity ρ_{sample} will be larger than the crystal resistivity ρ_{crystal}, which is the quantity of interest. In general ρ_{sample} will have a complex dependence on ρ_{crystal}, determined by factors such as f and the exact nature of the polycrystalline structure. Given the limited information available on the sample microstructure with only the volume fraction f specified, the relation

$$\boxed{\rho_{\text{crystal}} = f \cdot \rho_{\text{sample}}} \qquad \text{D.2}$$

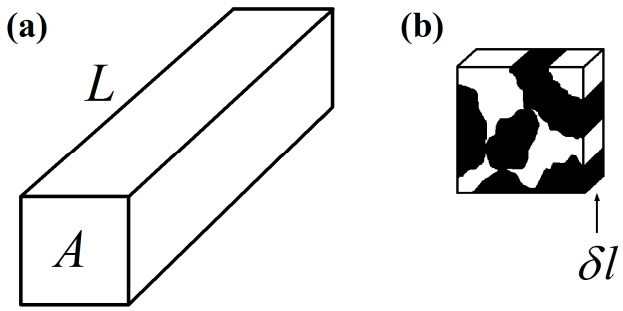

Fig. D-1. (a) A bar sample with cross–sectional area *A* and length *L*. (b) A cross-sectional slice of the sample with length *δl*. Shaded regions represent the crystallites.

may be used as a *first-order estimate* to the relationship between the sample and crystal resistivity. Notice that the sample resistivity is just scaled by a constant factor f with the temperature dependence unaffected. The above relationship is obtained by noting that the current flows only through the crystallites. Fig. D-1b shows a thin cross-sectional slice from the bar with length δl, with the shaded area representing the current carrying crystallites. The current therefore flows through an effective area $A_{\text{crystal}} < A$. The volume of the slice is $A\,\delta l$, whereas the volume occupied by the crystal is $A_{\text{crystal}}\,\delta l$, and hence

$$f = \frac{V_{\text{crystal}}}{V_{\text{sample}}} = \frac{A_{\text{crystal}}\delta l}{A\delta l} = \frac{A_{crystal}}{A} \qquad \text{D.3}$$

gives a relation between the volume fraction and the average area through which the current flows. In terms of the crystal resistivity ρ_{crystal} the bar-sample resistance is then

$$R = \rho_{\text{crystal}} \frac{L}{A_{\text{crystal}}} \qquad \text{D.4}$$

and combining with Eqs. D.1 and D.3 gives the result in Eq. D.2.

Alternatively, the equivalent expression (since $\sigma = \rho^{-1}$)

$$\boxed{\sigma_{sample} = f\,\sigma_{crystal}} \qquad \text{D.5}$$

relating the sample and crystal conductivity may also be obtained by considering variations in the crystallite content of a bar sample with fixed dimensions. Referring to Fig. D-2, the sample conductivity σ_{sample} will then be an increasing function of the crystal volume fraction $f \in [0, 1]$. It is assumed that the crystallite content is varied in such a way that the function $\sigma_{\text{sample}}(f)$ is continuous, avoiding effects such as percolation thresholds. For $f = 0$ there is no conducting medium and $\sigma_{\text{sample}}(f = 0) = 0$. Letting $\sigma_{\text{sample}}(f_0) = \sigma_0$, where f_0 and σ_0 are measured for a particular sample, and using a linear extrapolation to $f = 1$, then gives the estimate $\sigma_{\text{crystal}} = \sigma_{\text{sample}}(f = 1) = \sigma_0 / f_0$, which is Eq. D.5.

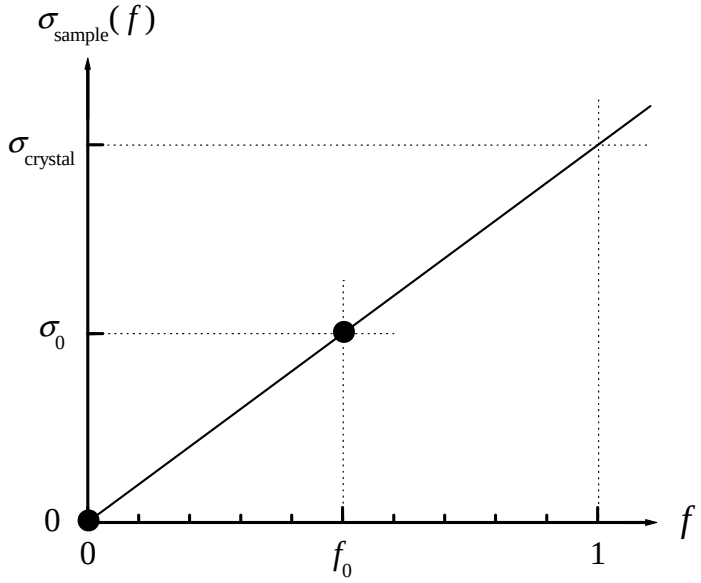

Fig. D-2. The sample conductivity σ_{sample} vs the crystal volume fraction f. The linear extrapolation to estimate the crystal conductivity $\sigma_{crystal}$ is based on the measured values σ_0 and f_0 of a single sample.

The above analysis provides a relationship between the sample and crystal resistivity based on a macroscopic analysis of the sample. On a macroscopic scale the current density will be uniform and parallel within the bar sample. On a microscopic scale at the size of the crystallites, which is implied by δl in Fig. D-1b, the direction and magnitude of the current density will not be uniform. To get better estimates for the crystal resistivity, knowledge of the microscopic structure would be required, followed by a more detailed analysis. The simple density–corrected estimate in Eq. D.2 or Eq. D.5 is however sufficient to explain the anomalies encountered in the data.

E. Gallery

Additional experimental results are presented here in the form of figures with short descriptions in the captions. These figures are referred to in the main body.

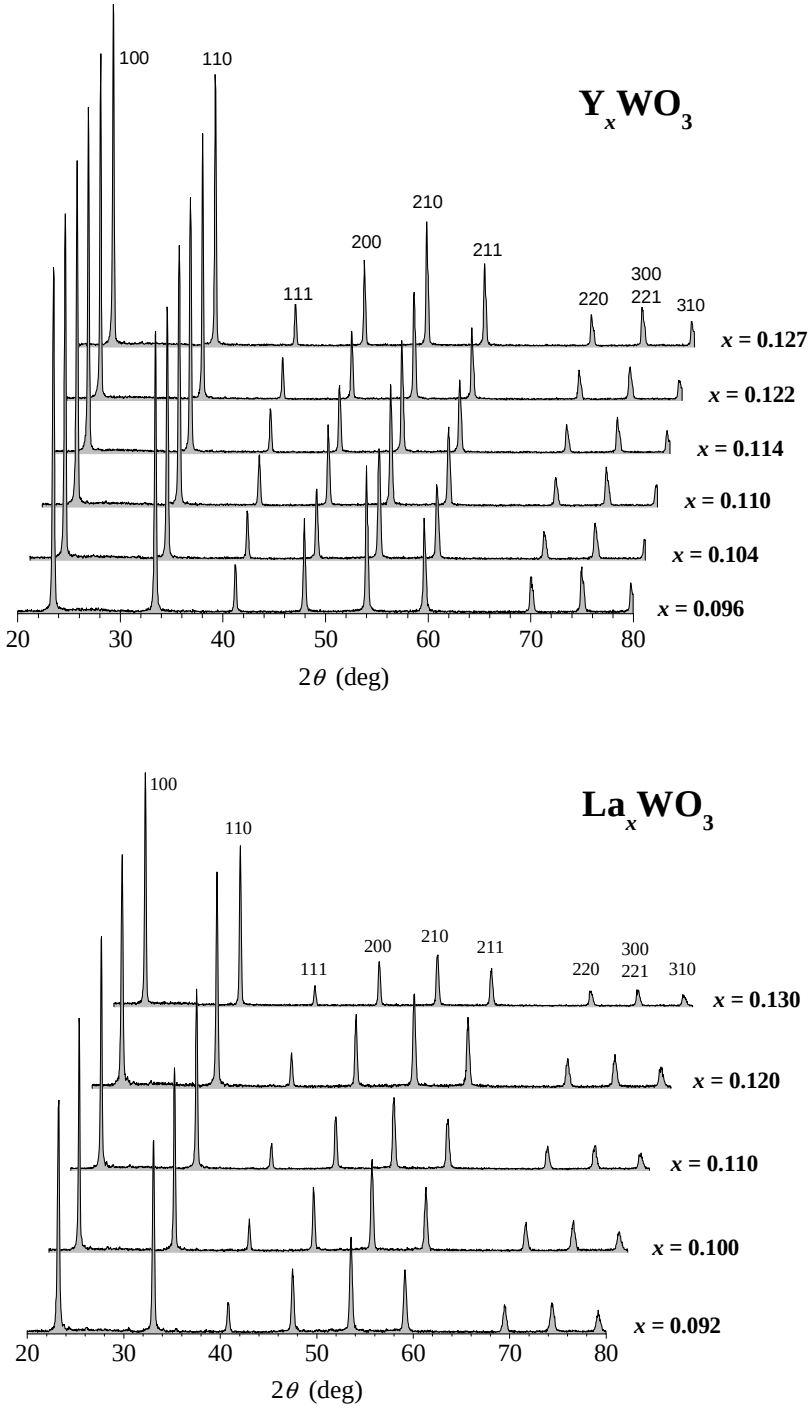

Fig. E-1. Powder x-ray diffraction results for cubic phase samples of Y_xWO_3 and La_xWO_3. The peaks are labelled by their Miller indices.

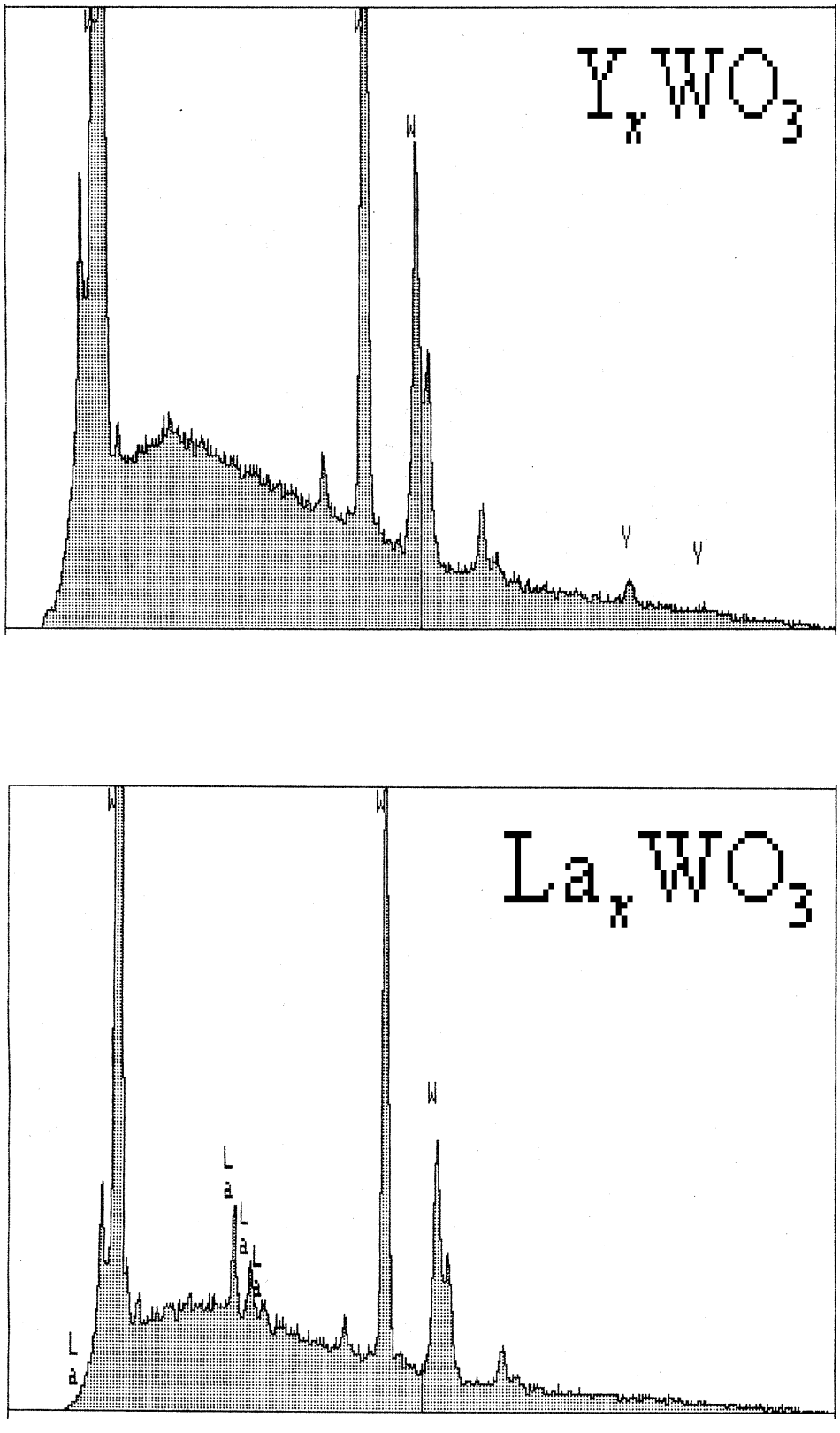

Fig. E-2. X-ray microscopy results for Y_xWO_3 and La_xWO_3 samples. The W, Y and La peaks are present, but the technique could not determine the donor concentrations with sufficient precision.

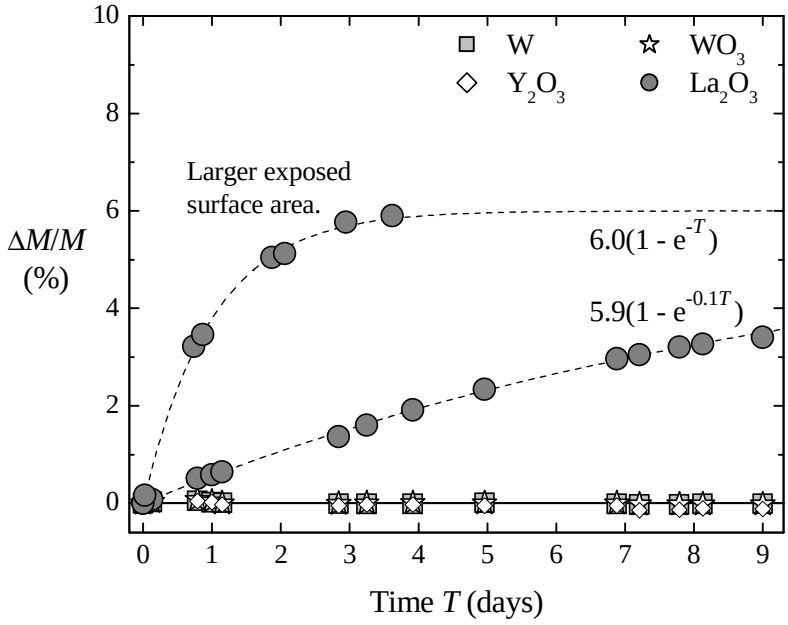

Fig. E-3. The change in mass *M* of the starting powders of La_2O_3, Y_2O_3, WO_3 and W when exposed to air. The hygroscopic nature of La_2O_3 is clearly visible, whereas the other powders show no absorption effects. The dashed curves are fits of the equation $\Delta M/M = \kappa(1 - e^{-\alpha T})$, with κ and α fitting constants.

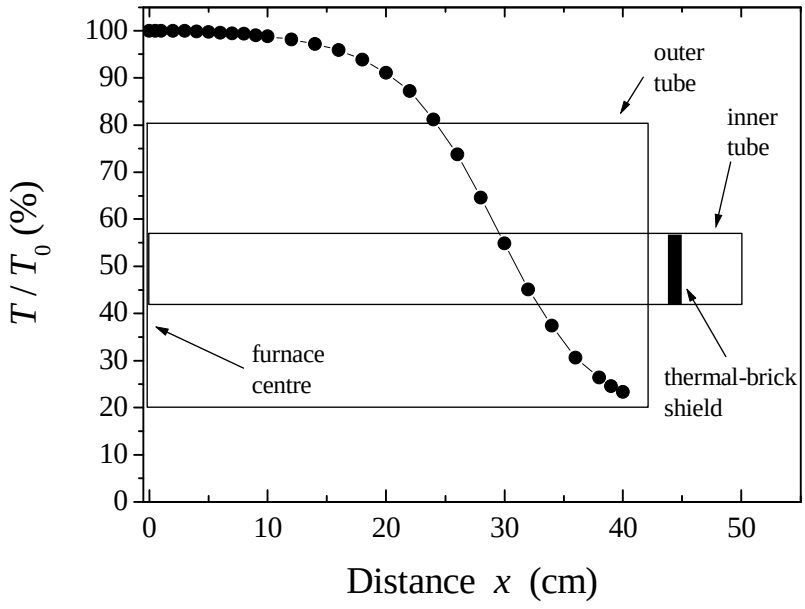

Fig. E-4. The temperature profile of the tube furnace. Also shown is the geometry of the furnace. The ampoules were about 10 cm in length, placing the pellets within about 5 cm of the furnace centre.

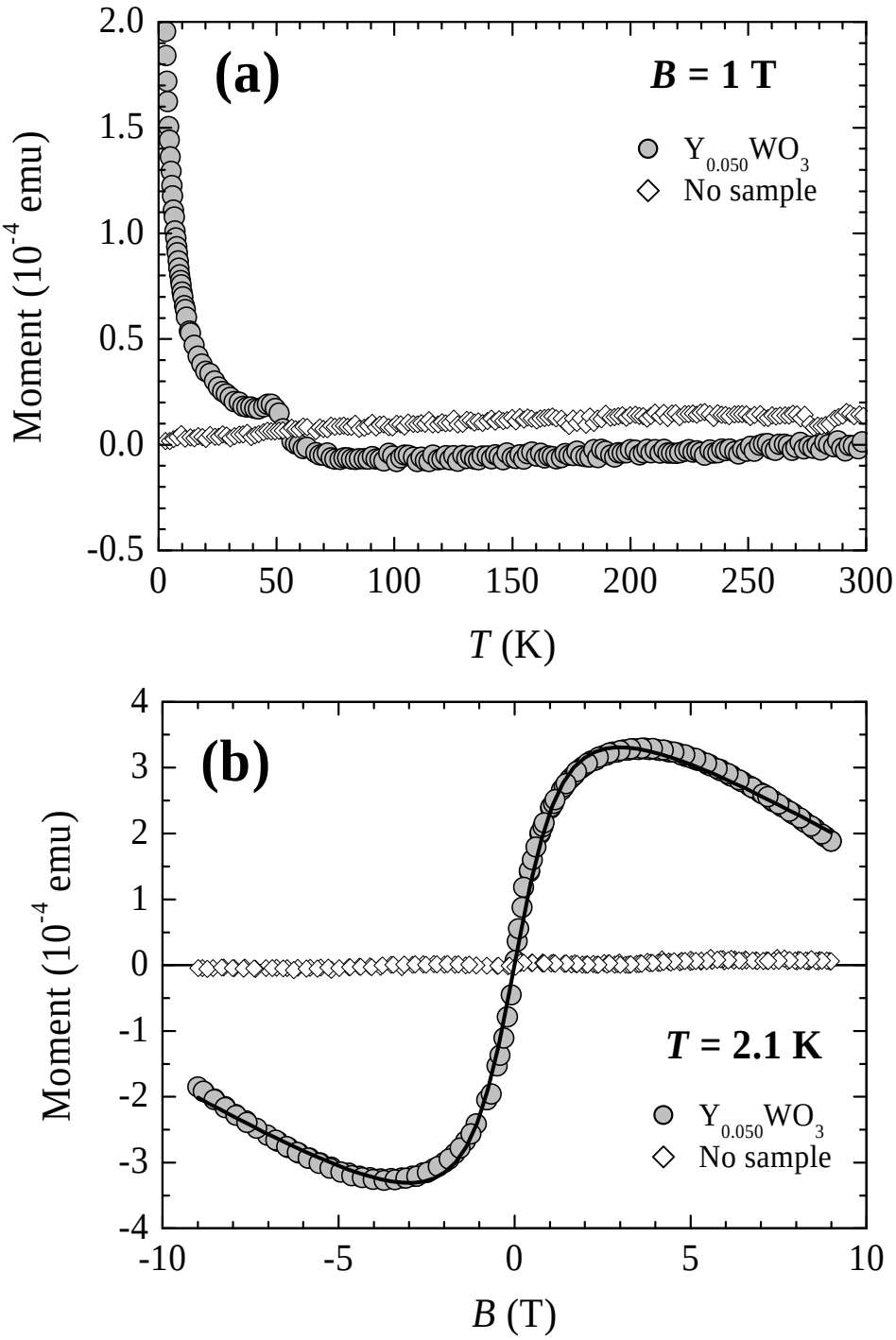

Fig. E-5.Vibrating sample magnetometer results for an 80 mg sample of $Y_{0.05}WO_3$. (a) The temperature dependence in a field of *B* = 1 T. (b) The field dependence at a temperature of *T* = 2.1 K. The curve is a fit of the paramagnetic Langevin function, together with a diamagnetic contribution (∝ –*B*) which is observed at large field strengths following the paramagnetic saturation.

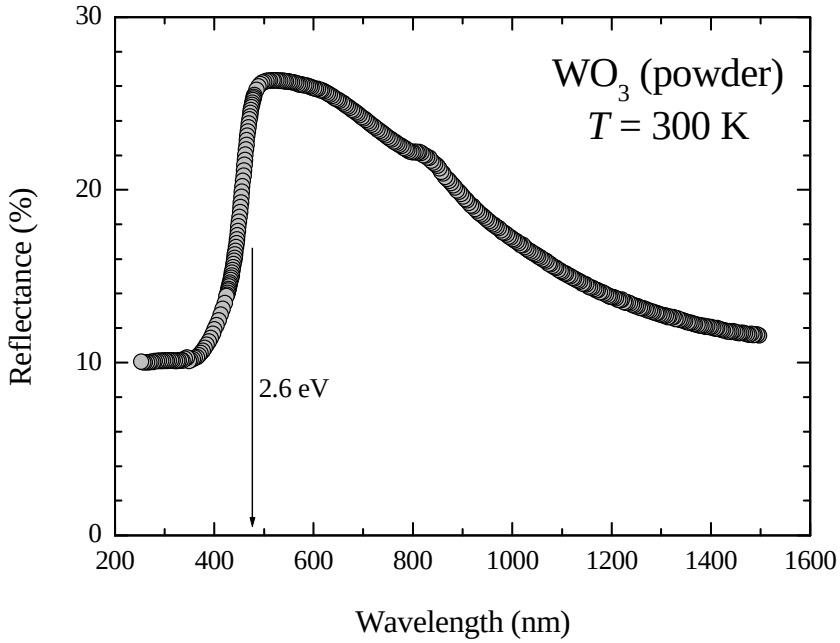

Fig. E-6. Room temperature diffuse reflectance spectrometer results for the WO_3 powder used in the sample preparation. The indirect band gap of 2.6 eV (≃ 470 nm) for WO_3 is shown.

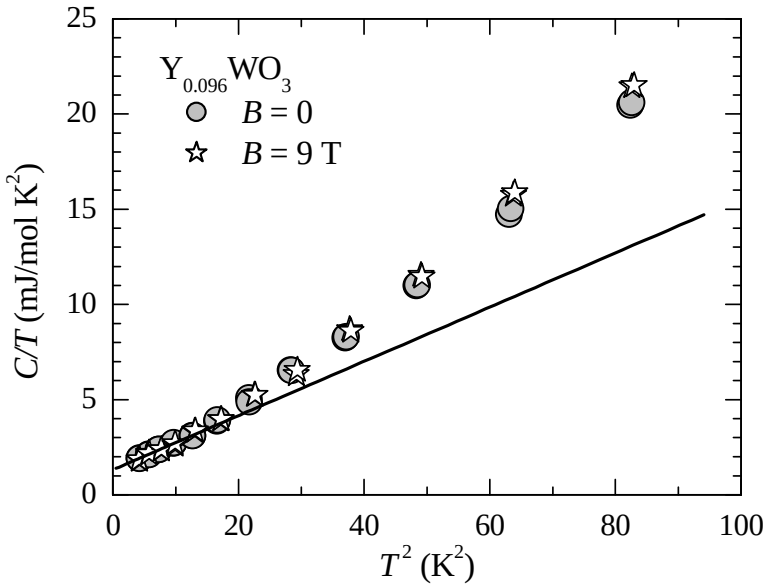

Fig. E-7. The specific heat C of $Y_{0.096}WO_3$ in a C/T vs T^2 plot for temperatures T < 10 K. The straight line is a linear fit of the low T data from which the electronic γT and phonon βT^3 contributions are obtained. The resulting Debye temperature Θ_D = 239 K, and the linear form is therefore expected for $T \lesssim \Theta_D/50$ = 4.8 K (T^2 < 23 K).

F. Publications

The following pages present two papers that have been published so far based on this research:

1. "*Effects of sample thickness on the van der Pauw technique for resistivity measurements*" published in "Review of Scientific Instruments".

2. "*Preparation and properties of the trivalent-ion doped tungsten bronze* La_xWO_3" published in "Journal of Applied Physics".

Effects of sample thickness on the van der Pauw technique for resistivity measurements

C. Kasl[a] and M. J. R. Hoch
School of Physics and Materials Physics Research Institute, University of the Witwatersrand, Johannesburg, P.O. WITS 2050, South Africa

(Received 10 November 2004; accepted 29 December 2004; published online 22 February 2005)

The van der Pauw technique is commonly used for electrical transport measurements on solid materials and is suited to thin, arbitrarily shaped samples, with the contacts placed anywhere on the periphery. Previous investigations have determined the effects of sample shape, contact size, and contact placement on the accuracy of this technique. Sample inhomogeneity effects have also been investigated. The effects of the sample thickness appear not to have been previously studied and are investigated here in order to establish precisely what is meant by a thin sample. The deterioration in the accuracy of the technique is followed as the sample thickness is increased. The results indicate that the van der Pauw technique may be used for samples where the thickness is comparable to the surface dimensions. The investigation also shows that the technique is valid for arbitrarily thick samples provided that low resistance electrodes are placed across the entire edge, perpendicular to the surface, in order to maintain an effective two-dimensional current distribution. This finding is useful for transport measurements on materials that have been prepared, for example, by solid state reaction using sintering methods. © *2005 American Institute of Physics.* [DOI: 10.1063/1.1866232]

INTRODUCTION

The van der Pauw (vdP) technique[1,2] permits the measurement of resistivity on thin samples of arbitrary shape. The requirement is a simply connected sample with a constant thickness and a uniform resistivity. The contacts should also be sufficiently small, depending on the required accuracy, and placed on the periphery of the sample.

The vdP method has been particularly useful in determining the transport properties of semiconductor wafers.[3,4] The motivation for the present investigation came from our resistivity measurements on sintered pellets of the metal–insulator tungsten bronze system, Y_xWO_3, where the thickness to diameter ratios were ~10%. Similarly, the vdP method has been used by other researchers on samples where the thickness was not much less than the surface dimensions.[5,6] The validity of using the method on "thick" samples has not previously been addressed.

THE VAN DER PAUW METHOD

Figure 1 shows the electrical contact arrangement for the implementation of the technique. The vdP resistivity of the sample is[2]

$$\rho = \frac{\pi d}{\ln 2}\left(\frac{R_1 + R_2}{2}\right) f(R_1/R_2), \tag{1}$$

where R_1 and R_2 are measured as shown in Fig. 1, and d is the sample thickness. The function $f(x)$ is defined by the equation[2]

$$\cosh\left(\left[\frac{x-1}{x+1}\right]\frac{\ln 2}{f}\right) = \frac{1}{2}\exp\left(\frac{\ln 2}{f}\right). \tag{2}$$

For certain symmetries, such as a disk with the contacts placed at 90° intervals, $R_1 = R_2$. From Eqs. (1) and (2), the resistivity is then

$$\rho = \frac{\pi d}{\ln 2} R_1, \tag{3}$$

with no switching of the current and voltage leads required.

The requirement of a thin sample stems from the fact that Eq. (1) is derived for a two-dimensional (2D) current distribution. By making samples sufficiently thin, relative to the surface dimension, the validity of the method is improved. In the four-wire method used on bar samples, the shape of the sample is chosen to ensure a uniform parallel current density distribution, whereas in the vdP method it is not necessary to know the current pattern.

The effects of contact size and placement were investigated by van der Pauw.[1,2] The results show that for disks the error in measurement $\Delta\rho/\rho \sim (t/D)^2$, where t measures the contact size or distance from the edge, and D the surface dimensions. Improved accuracy is obtained by selecting special sample shapes and contact placements. The effects of finite contact size, sample shape, contact placement, and sample inhomogeneity on resistivity measurements have been extensively investigated by Koon and co-workers.[7–11]

Precisely what is meant by a "thin sample" is investigated here, and a breakdown in accuracy of the vdP technique is shown when the thickness becomes sufficiently large. The limiting thickness to surface–diameter ratio, above which the method fails, is investigated for disk samples. Maintaining the 2D character of the current distribution by

[a]Author to whom correspondence should be addressed; electronic mail: kaslc@physics.wits.ac.za

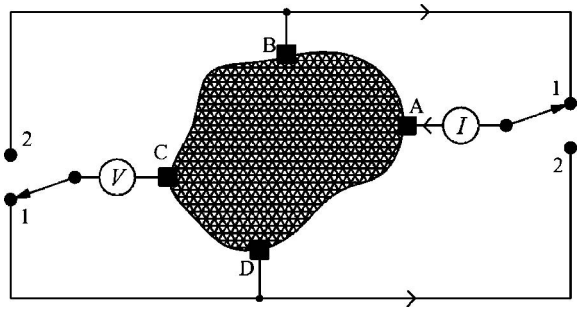

FIG. 1. The van der Pauw contact configuration for resistivity measurements. The resistances $R_1 = V_{DC}/I_{AB}$ and $R_2 = V_{BC}/I_{AD}$, used in Eq. (1), are measured by switching the current through AB and AD, and then measuring the voltages V_{DC} and V_{BC}, respectively.

placing the contacts across the entire edge of the sample, perpendicular to the surface, thereby increasing the thickness range of the method, is also investigated.

EXPERIMENT

For the purpose of the investigation, graphite rods of diameter 17 mm were used for preparing the samples. The electrical contacts were made with silver paint, which produced a specific contact resistance of about 0.3 $\Omega\,\mathrm{mm}^2$. The sample contact geometry is shown in Fig. 2. For very thin samples, geometry (a) is commonly used, with the contacts placed at the edge of the surface. In (b), the contacts are placed across the entire edge to maintain effective 2D symmetry, and hence produce a uniform current distribution across the sample. The contacts for samples 1 and 2 were created using geometry (a), while for samples 3 and 4 geometry (b) was used. The electrodes were about 1 mm wide. Bare Cu wire was embedded into the silver paint for sample 4, to reduce the resistance of these extended edge contacts. As will be shown, the resistance of the edge electrodes, relative to the sample resistance, becomes crucial in determining the range of thicknesses over which the vdP method may be used.

The sample resistivity ρ_0 was measured on several bar samples, using the standard four-wire method, giving $\rho_0 = 5.4 \pm 0.6\ \mathrm{m}\Omega\,\mathrm{cm}$ at ambient temperature. The large uncertainty in ρ_0 ($\sim 11\%$), was produced by the presence of microcracks in the graphite rods, which affected the measurements, particularly for smaller pieces. The accuracy,

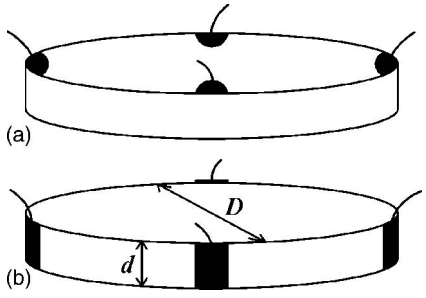

FIG. 2. The two contact geometries used. In (a) the contacts are placed on the edge of the surface, and in (b) the contacts are located across the edges to maintain an effective 2D current distribution. The disk has diameter D and thickness d.

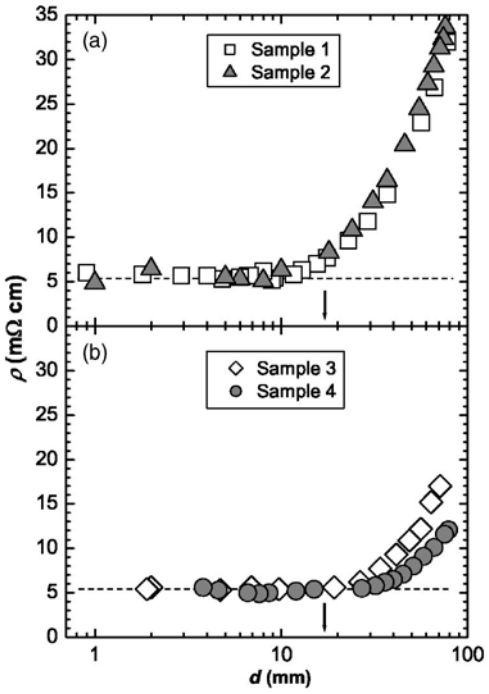

FIG. 3. The vdP resistivity ρ of the four samples vs the thickness d. The dashed lines show the sample resistivity of 5.4 mΩ cm, as measured using the four-lead bar method. The arrows indicate the diameter $D = 17$ mm of the disks. In (a) the contacts are placed on the top perimeter of the samples and in (b) across the sample edges, as shown in Fig. 2.

however, was sufficiently good to provide a reliable determination of the thickness dependence of the measured vdP resistivity.

The thickness of the samples was reduced by cutting them with a diamond wafering blade. Resistivity measurements, using the vdP method, were performed after each cut. The results are shown in Fig. 3, where the vdP resistivity ρ is plotted versus the disk thickness d.

Figures 3(a) and 3(b) show that, for sufficiently small thicknesses, the vdP method produces thickness-independent resistivity values in agreement with the four-lead bar result of 5.4 mΩ cm (indicated by the dashed curves). The vdP resistivity diverges from the known value as the thickness increases for both geometries. In Fig. 3(a), which shows the results for arrangement (a), the limiting thickness d_m is about half the diameter D of the disks. The results for (b), shown in Fig. 3(b), indicate $d_m > D$, with d_m largest for sample 4. It is also noted that for a fixed sample thickness d, method (b) gives improved accuracy and the reliability further improves with better conducting electrodes, as seen from the results for sample 4. Contact geometry (b) therefore improves the vdP method, as expected. The gradual failure of method (b) as d is increased is ascribed to the finite resistance of the electrodes. As Fig. 3(b) suggests, the resistance of the electrodes has to be sufficiently low compared to the sample resistance to give good estimates over the whole range of thicknesses.

As a further test of the method, Fig. 4 shows the resistivity of a tungsten bronze sample, $Y_{0.05}WO_3$, over a range of temperature. The vdP readings were performed on a disk of diameter 13 mm and thickness 1.2 mm, with silver paint contacts on the edges, as in Fig. 2(b). The standard four-wire

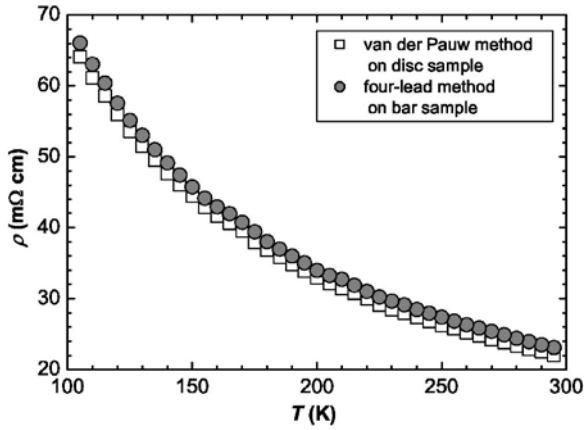

FIG. 4. The resisitivity of $Y_{0.05}WO_3$, measured by the van der Pauw and four-lead bar methods, vs the temperature.

method was used on a bar sample with dimensions 7.90 $\times 2.46 \times 1.66$ mm. The small differences in the measured resistivity values are attributed to the finite contact sizes and slight uncertainties in the dimensions. As Fig. 4 shows, the vdP method produces reliable resistivity results for a disk with a thickness to diameter ratio of 9%.

THE RESISTOR LADDER MODEL

The resistance ladder (*R*-ladder) is a dc circuit which can be used to model the experimental results. The circuit shown in Fig. 5 is an *n*-layer *R*-ladder circuit in which the number of layers represents the thickness of the sample. *R* represents the resistance of a thin slice of the sample and *r* gives a measure of interlayer resistance. Given the current *I*, the voltage *V*, and number of layers *n*, the objective is to find an estimate R_{eff} of the resistance *R*. This is equivalent to using the vdP resistivity ρ as an estimate of the sample resistivity ρ_0. The interlayer resistance *r* is an unknown, and will determine the accuracy of the estimate.

For the *R*-ladder circuit in Fig. 5, we have $R_{\text{eff}}=V/I_0$, where I_0 is the current through the top resistor. The approximation is made that the current is the same in each resistor, with $I_0=I/n$, and follows the implicit assumption in the vdP method that the current distribution is effectively 2D. Clearly the approximation will fail for either large *n* or large *r*.

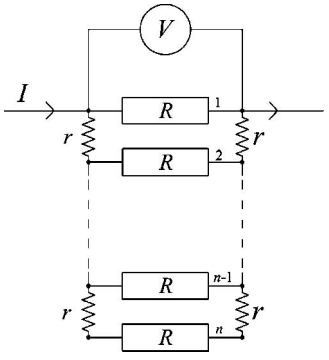

FIG. 5. The resistance ladder with *n* layers. *n* represents the sample thickness *d*, while *R* represents the resistance of a thin layer. The resistance *r* is introduced to represent the interlayer resistance.

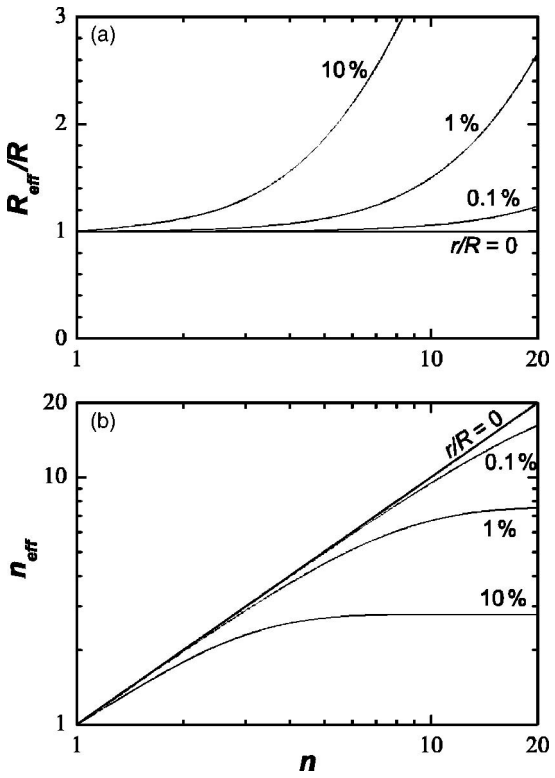

FIG. 6. Plots showing (a) R_{eff}/R [Eq. (4)] and (b) the effective number of layers n_{eff} versus the actual number of layers *n* for the *R*-ladder shown in Fig. 5. The parameter *r*/*R* gives the ratio of the interlayer resistance to the layer resistance as shown in Fig. 5.

The estimate for the resistance *R* is therefore $R_{\text{eff}}=n \times V/I$. (For $r=0$, we have a parallel circuit, and in this case $R_{\text{eff}}=R$.) The total resistance of the circuit is $R_n=V/I$, and hence

$$\frac{R_{\text{eff}}}{R} = n \cdot \frac{R_n}{R} = n f_n. \tag{4}$$

The ratio $f_n=R_n/R$ can be expressed by a recursion formula as

$$(f_{n+1})^{-1} = 1 + \left(2\frac{r}{R} + f_n\right)^{-1}, \tag{5}$$

with $f_1=1$, and the only parameter being r/R. Figure 6(a) shows a plot of R_{eff}/R versus *n*, using Eqs. (4) and (5), for various values of the parameter r/R. Except for $r=0$, the estimate R_{eff} becomes less accurate, as expected, as either the number of layers *n* or the resistance *r* is increased. The shape of the curves are very similar to the results shown in Figs. 3(a) and 3(b). The improvement in the resistivity measurements in Fig. 3(b) is equivalent to a reduction in the resistance *r*. For a particular sample thickness, the accuracy of the vdP method will therefore depend on how small the resistance of the electrodes is in relation to the sample resistance.

Given that the sample resistivity ρ_0 is known, the validity of the vdP method can also be determined by defining an effective sample thickness d_{eff} which will satisfy Eq. (1). The method is valid when $d_{\text{eff}}=d$, since from Eq. (1) we have

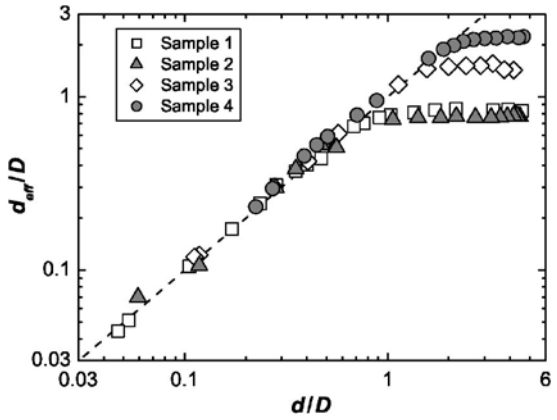

FIG. 7. The effective thickness d_{eff}, defined in Eq. (6), vs the sample thickness to diameter ratio d/D. The dashed line for $d_{\text{eff}}=d$ indicates where the vdP method is valid.

$$\frac{d_{\text{eff}}}{d}=\frac{\rho_0}{\rho}. \tag{6}$$

The effective thickness d_{eff} may be considered as a measure of the thickness through which most of the current actually flows. In a similar way, we can define an effective number of layers n_{eff}, such that $R_{\text{eff}}/R=1$ in Eq. (4). For this condition to be met, we must have $n_{\text{eff}}=(f_n)^{-1}$, and a plot of n_{eff} versus n is shown in Fig. 6(b). For $r=0$, we have $n_{\text{eff}}=n$, as expected. For $r>0$, we see that n_{eff} starts to deviate from n, as n increases, and eventually tends to a constant value. For a sufficiently large number of layers, the basic assumption of equal currents through each layer becomes unacceptable. The bottom resistor in Fig. 5 then receives a negligible amount of current, and increasing the number of layers does not change the current distribution in the circuit, leading to a constant n_{eff}.

The effective thickness to diameter ratio d_{eff}/D is plotted versus the actual ratio d/D in Fig. 7. The d_{eff} values were obtained from Eq. (6), using the sample resistivity ρ_0, and the vdP resistivity data in Figs. 3(a) and 3(b). The dashed line, where $d_{\text{eff}}=d$, indicates where the method is valid. Convergence of the data with this dashed curve gives the limiting thickness for the method. The data are similar to the curves shown in Fig. 6(b). The leveling off for large d is present for all four samples, and has the same explanation as the leveling off in n_{eff} described above. The improvement in using arrangement (b) especially with better conducting electrodes, as shown by the sample 4 results, is clear.

It may be concluded that the R-ladder model predictions show an equivalent behavior to the vdP method results on thick disk samples.

DISCUSSION

The resistivity of disk shaped samples of graphite have been measured using the van der Pauw method for a range of sample thicknesses. The decrease in reliability of this technique was studied as the thickness increased.

The following conclusions have been reached. The limiting thickness for acceptable results with electrical contacts made on the top surface is about half the sample diameter. It is not expected that these results should depend on the resistivity of the sample. The effect of the surface geometry, including square or clover-leaf shapes on the limiting thickness, requires further investigation. Results similar to those presented here are expected.

The accuracy of the method increases when the contacts are placed across the edges of thick samples, perpendicular to the top surface, to enhance the effective 2D nature of the current distribution. The electrode resistance should be much lower than the sample resistance for best results. Using this approach it is shown that reliable van der Pauw resistivity measurements can be made with thickness to diameter ratios above unity. This result is important for transport measurements on relatively thick samples prepared, for example, by solid state reaction involving sintering methods. Such pellets do not require geometric modification for resistivity measurements using the procedures described above.

ACKNOWLEDGMENTS

Financial support was provided by the South African National Research Foundation and by the University of the Witwatersrand, Johannesburg.

[1] L. J. van der Pauw, Philips Res. Rep. **13**, 1 (1958).
[2] L. J. van der Pauw, Philips Tech. Rev. **20**, 220 (1958–1959).
[3] P. M. Hemenger, Rev. Sci. Instrum. **44**, 698 (1973).
[4] D. W. Koon and T. G. Castner, Phys. Rev. B **41**, 12054 (1990).
[5] A. K. Raychaudhuri, Phys. Rev. B **44**, 8572 (1991).
[6] G. J. Snyder, T. Caillat, and J. P. Fleurial, Phys. Rev. B **62**, 10185 (2000).
[7] D. W. Koon, Rev. Sci. Instrum. **60**, 271 (1989).
[8] D. W. Koon, A. A. Bahl, and E. O. Duncan, Rev. Sci. Instrum. **60**, 275 (1989).
[9] D. W. Koon and C. J. Knickerbocker, Rev. Sci. Instrum. **67**, 4282 (1996).
[10] D. W. Koon and C. J. Knickerbocker, Rev. Sci. Instrum. **69**, 3625 (1998).
[11] D. W. Koon and W. K. Chan, Rev. Sci. Instrum. **69**, 4218 (1998).

Preparation and properties of the trivalent-ion doped tungsten bronze La_xWO_3

C. Kasl[a] and M. J. R. Hoch[b]
School of Physics and Materials Physics Research Institute, University of the Witwatersrand, Johannesburg, WITS, 2050, South Africa

(Received 28 September 2005; accepted 23 January 2006; published online 28 March 2006)

The production and characterization of lanthanum-doped tungsten oxide, La_xWO_3, sintered samples are presented for $0.05 \leqslant x \leqslant 0.23$. The x-ray diffraction results show that the cubic perovskite phase is stable for x in the range of 0.086–0.21. Outside of this range additional phases are present. Resistivity measurements made between 64 and 300 K provide information on the electronic properties. Room temperature Hall effect results show that the trivalent La ions donate their valence electrons into the WO_3 conduction band. The samples have been prepared for an investigation of the metal-insulator transition in this tungsten bronze system. © *2006 American Institute of Physics*. [DOI: 10.1063/1.2180427]

INTRODUCTION

The tungsten bronzes form a class of nonstoichiometric compounds with the general formula M_xWO_3, where M is an alkali, alkali earth, transition, or rare-earth ion. For a range of x values, the stable phase is found to be cubic, and these systems exhibit a metal-insulator (MI) transition at a critical concentration x_c close to the lower end of this range of stability.[1–3] There has been a resurgence of interest in doped perovskite materials, particularly the transition-metal oxides such as the cuprates and manganites. Many of the properties exhibited by these and other oxides are not well understood and pose challenging questions. The nature and role of the MI transitions in these systems are of fundamental importance. Reviews of the MI transition in a variety of systems, including oxides, have been given by Edwards *et al.*[4] and Imada *et al.*[5]

Recent work on the bronzes has included investigations of the rare-earth tungsten bronzes[6,7] and studies of superconductivity in the alkali tungsten bronzes.[8] Experimental and theoretical investigations of the MI transition have been carried out on the sodium tungsten bronze, Na_xWO_3, and on related systems.[1,2,9–11] Previous work,[7,12–14] carried out on La_xWO_3 has provided structural information but no systematic investigation of the x-dependent physical properties, specifically the transport properties, has been reported. The present experiments have sought to prepare and characterize La_xWO_3 samples with a range of x values suited to an investigation of the MI transition in this system.

SAMPLE PREPARATION

The solid state reaction used for the preparation of La_xWO_3, where $0 \leqslant x \leqslant 1$, is given by[13]

$$\left(\frac{x}{2}\right)La_2O_3 + \left(\frac{x}{2}\right)W + \left(1 - \frac{x}{2}\right)WO_3 \rightarrow La_xWO_3. \qquad (1)$$

The reactants, obtained from Cerac Incorporated (La_2O_3:99.999%, ~325 mesh, W: 99.95%, ~1 μm, and WO_3:99.99%, ~325 mesh), were passed through a 32 μm sieve before use. These particle sizes appeared too large for pellet production, and further grinding in the mortar during the mixing of the reactant powders was required.

The mixed reactant powders were pelletized in a 13 mm die at 6 tons using a hydraulic press. Samples were produced in batches of 5 g, creating 3–4 pellets of about 2 mm thickness. The pellets were placed in quartz tubes that were then outgassed under vacuum at 300 °C for 40 min followed by evacuation to below 10^{-5} torr before sealing. Sintering was carried out in a programmable Carbolite STF1500 tube furnace at 1100 °C for 72 h. (A ramp rate of 300 °C/h was used for the heating and cooling cycles.) The temperature stability and gradients across the ampoules are estimated to be ~10 °C.

The samples have a range of x values ($0.05 \leqslant x \leqslant 0.23$) that includes the cubic perovskite phase,[13] with the La ions occupying random[14] body-centered sites in a cubic WO_3 lattice. The sintered samples were typical of the tungsten bronzes, with a bluish-black appearance. The low x material had a navy-blue color, which darkened as x increased, and eventually became deep violet for the highest concentrations. The color changes are similar to those of Na_xWO_3 for x in the range of ~0.3– ~0.7.[15]

After sintering, white and blue deposits appeared on the inside walls of the quartz tubes. There was some evidence of a local reaction between the pellets and the quartz tubes at the points of contact, as observed with sodium bronzes.[16] Whiskers were formed in some cases, with colors similar to the sample colors, suggesting that these are tungsten bronze whiskers. For the lowest concentrations ($x \leqslant 0.080$), soft, hairlike navy-blue whiskers appeared on some pellets, and harder whisker "nests" appeared at the bottom of the quartz tubes. For the larger concentrations, violet hairlike whiskers

[a]Author to whom correspondence should be addressed; electronic mail: kaslc@physics.wits.ac.za
[b]Present address: National High Magnetic Field Laboratory, Florida State University, Tallahassee, FL 32310.

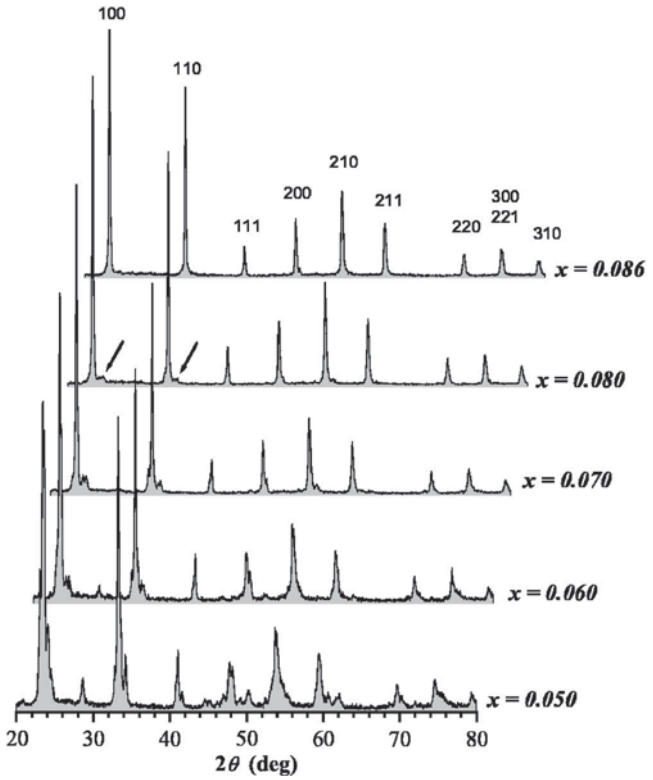

FIG. 1. The La_xWO_3 powder XRD results for the lowest x samples. For $x=0.086$ a single phase cubic perovskite structure is found (Miller indices are shown). Additional peaks appear as x is reduced, with examples indicated by the two arrows for $x=0.080$.

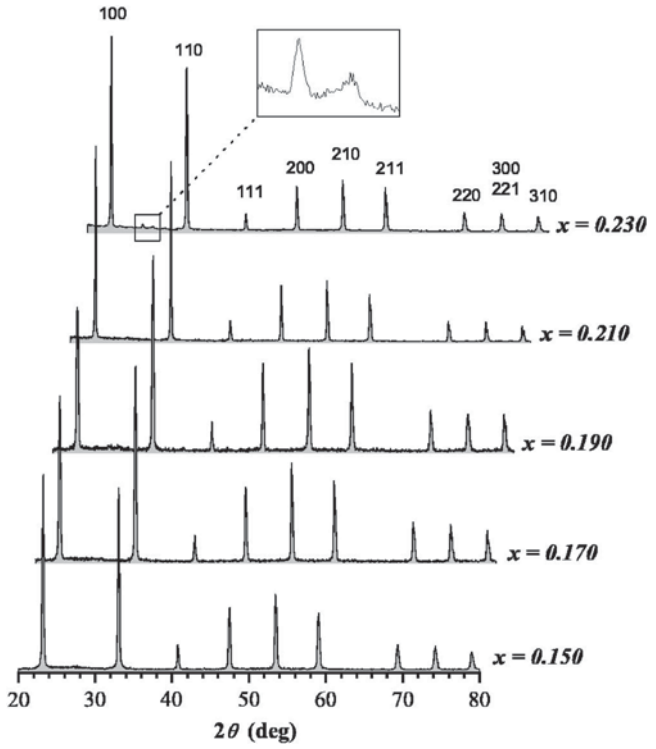

FIG. 2. The La_xWO_3 powder XRD results for the highest x samples. The cubic perovskite single phase structure is obtained up to $x=0.210$. The appearance of additional peaks is detected only for $x=0.230$, and the inset shows two of these peaks on an expanded scale.

appeared on a few pellets. Whiskerlike formations also appear on Na_xWO_3 when sintering above 930 °C.[16] An expansion of ~15% in the linear dimensions was found following the sintering, with slight warping of some pellets. The deposits and whisker formations may introduce small compositional uncertainties in the samples, and hence possible shifts in the intended x values.

La_2O_3 powder is hygroscopic, and this property produced some difficulties in sample production. Measurable expansion is observed in presintered pellets when exposed to air for several hours, and this process can eventually lead to disintegration back into powder form. To minimize moisture uptake, the pellets were kept under vacuum prior to sintering. For samples with high x values, the hygroscopic swelling effect becomes more pronounced due to the higher La_2O_3 content. This complicated good sample production above $x=0.19$. While the absorbed moisture was driven off during outgassing, the pellets with x values 0.21 and 0.23 disintegrated back into powder form inside the ampoules during handling. For these two concentrations, soft sintered-powder blocks emerged after heating to 1100 °C and only x-ray diffraction measurements were made on these samples. Following sintering, all of the samples were stable and showed no changes in physical properties with time.

RESULTS AND DISCUSSION

Powder x-ray diffraction

Room temperature powder x-ray diffraction (XRD) investigations were performed on the samples using a Philips powder diffractometer with Cu K_α radiation ($\lambda=1.54$ Å). The XRD results for the lowest concentrations ($0.050 \leqslant x \leqslant 0.086$) and highest concentrations ($0.150 \leqslant x \leqslant 0.230$) are shown in Figs. 1 and 2, respectively. The cubic phase peaks are labeled by their Miller indices. For concentrations in the range of $0.086 < x < 0.150$, the XRD patterns give a single cubic phase. For $x < 0.086$, additional peaks appear in the diffraction pattern, as shown in Fig. 1 for $x=0.080$. At $x=0.050$, much of the pattern is due to noncubic material. Similar lower limits for the cubic phase have been observed in other tungsten bronzes doped with trivalent ions.[13,17] Figure 2 shows the samples to be in the cubic phase up to $x=0.210$, with $x=0.230$ showing the emergence of extra phases in the system. The appearance of mixed phases, as seen in Fig. 1 for $x \to 0$, is not unexpected, since WO_3 exhibits either monoclinic or triclinic phases at room temperature.[18] The powder XRD patterns for the cubic phases are typical of the tungsten bronzes.[6,19] The results therefore indicate a cubic perovskite structure for La_xWO_3 from 0.086 to 0.210. This range is similar to that suggested by previous work.[13] Variations in the cubic phase ranges have been reported for other tungsten bronzes.[20]

The cubic lattice constants for La_xWO_3, as determined from the powder XRD data, are shown as a function of x in Fig. 3. The value for $x=0.05$ could not be determined with sufficient accuracy due to the marked presence of additional phases. A linear fit over the cubic range gives $a=3.807+0.21x$ Å, in agreement with values for the cubic lattice parameter obtained by others.[13,14] Although Broyde[13] suggests a nonlinear form for the x dependence of the lattice constant,

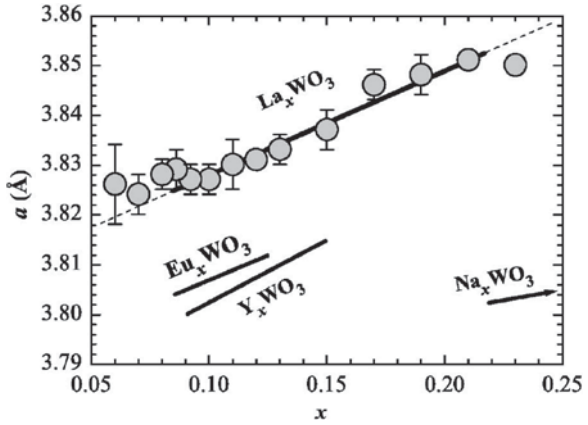

FIG. 3. The cubic lattice constant for La_xWO_3. The dashed curve is a linear fit over the cubic phase range (indicated by the solid line). Also shown are the cubic phase lattice constants for Y_xWO_3, Eu_xWO_3, and Na_xWO_3 (Refs. 13, 20, and 21).

the present results indicate a linear dependence on x over the cubic range, as observed in other tungsten bronzes.[6,20,21] The cubic lattice constants found for La_xWO_3 are similar to those of Ce_xWO_3.[6] The labeled solid lines in Fig. 3 indicate the cubic phase ranges and lattice constants of three other bronzes.[13,20,21] The arrow shown for Na_xWO_3 indicates the cubic phase exists for larger x than shown in the figure. The lattice constant in the tungsten bronzes depends on the radii of the dopant ions,[13,17] consistent with Fig. 3.

The dashed line in Fig. 3 shows extrapolated values of the cubic lattice constant beyond the cubic-phase limits. For $x>0.21$, the plotted point deviates from the extrapolated values, while, for $x<0.086$, the extrapolated linear behavior cannot be confirmed due to the structural uncertainties in this mixed phase range. The presence of the mixed phases is particularly important at the low dopant concentrations where the MI transition occurs. Previous investigations[22] have shown that the cubic phase of the tungsten bronzes is metallic, and the transition to the insulating state is preceded by lattice instability in the system. If this is the case for La_xWO_3, then we expect the MI critical concentration x_c <0.086.

Density and crystal volume fraction

Sample mass densities, measured on bar, and disk samples, are shown in Fig. 4(a). The predicted density of cubic crystalline La_xWO_3, calculated using the lattice constant values from Fig. 3, is shown by the dashed line. The density of the compressed powder pellets prior to sintering was about 5 g/cm^3. The slight expansion of the pellets during sintering is consistent with the observed reduction in pellet density. The crystal volume fraction f, which is the ratio of the sample and crystal densities, is shown in Fig. 4(b). The polycrystalline, porous nature of the sintered samples is evident from these values. The figure shows a gradual increase in f with x (from 42% to 52%) up to $x=0.15$, followed by a significant decrease in f for $x>0.15$. The decrease is attributed to the hygroscopic nature of La_2O_3 with the larger La_2O_3 content for high x samples causing a greater expansion of the pellets prior to sintering. The densities for the largest concentrations 0.21 and 0.23 are not shown. These samples were in powder form in the ampoules (sample preparation section) and formed soft sintered-powder blocks, which had even lower densities than shown in Fig. 4(a). The results reveal the importance of preparing La-doped samples in a dry atmosphere, particularly for larger x values.

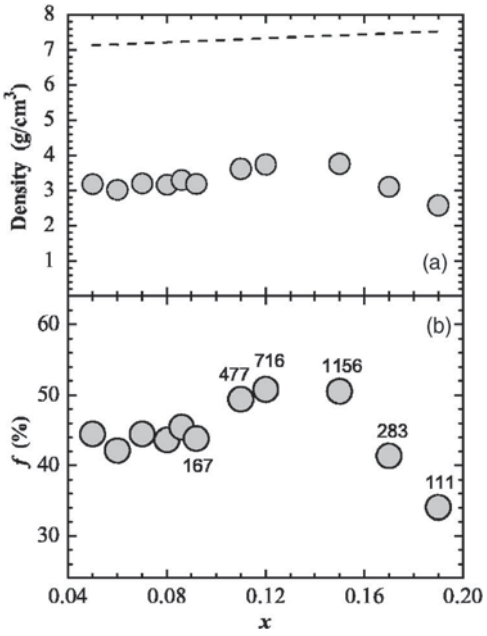

FIG. 4. The mass density and crystal volume fraction f for the La_xWO_3 samples. The dashed line in (a) shows the predicted crystal density for the cubic perovskite phase, based on the lattice constant data. Data labels in (b) give an indication of sample hardness based on the number of cutting wheel revolutions required to cut equivalent sized samples.

There is a variation in the nature of the samples, such as sample strength and texture, related to f and x. As an indication, the number of revolutions of a cutting wheel required to cut equivalent sized pieces of material are shown in Fig. 4(b) for some samples. These results show that the sample hardness is dependent on both f and x.

Resistivity

Further characterization of the material involved electrical transport measurements at temperatures between 64 K (pumped liquid nitrogen) and 300 K using an Oxford continuous flow cryostat. The samples were cut in the form of disks with thicknesses varying from 0.75 to 1.45 mm, and diameters between 11 and 15 mm. The van der Pauw technique[23,24] was used for resistivity measurement, with leads attached to the sample edges with silver paint. Offset voltages were cancelled by using current reversal, and currents were kept small to avoid heating effects.

The resistivity of a bar sample is $\rho=RA/l$, where R is the resistance, l is the length, and A is the cross-sectional area. If the material is porous, such as for these sintered polycrystalline samples for which $f\sim45\%$, there will be a difference between the sample resistivity ρ_s and crystal resistivity ρ_c, with $\rho_c<\rho_s$. Given the limited information available on the sample microscopic structure, a first order estimate of the crystal resistivity is

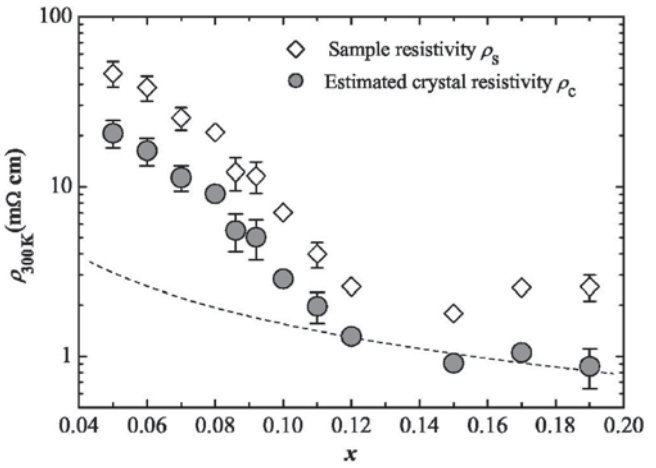

FIG. 5. The room temperature resistivity of the La_xWO_3 samples. The estimated crystal resistivity ρ_c, using Eq. (2), is also shown. The dashed line indicates metallic-type behavior with $\rho \propto 1/x$.

$$\rho_c = \rho_s \cdot f, \tag{2}$$

using the resistivity definition and the average area $A_{\text{eff}} = A \cdot f$ through which the current flows.[25]

The room temperature sample resistivity ρ_s is shown in Fig. 5 for the range of x values available. Also shown is the estimated crystal resistivity ρ_c using Eq. (2) and the measured f values shown in Fig. 4(b). Above $x=0.15$, ρ_s unexpectedly increases with x. This is attributed to the significant decrease in the volume fraction indicated in Fig. 4(b). ρ_c shows a more gradual change in this region. The dashed curve in Fig. 5, with $\rho = c/x$, shows metallic-type behavior with the conductivity proportional to the dopant (carrier) concentration. The proportionality constant $c=0.155$ was chosen to fit the curve through the $x=0.12$ point. The resistivity values for $x>0.12$ can be accounted for as conventional metallic-type behavior. The increased slope of the resistivity plot for $x<0.12$ suggests that disorder effects are important in this range. Similar resistivity changes with a dopant concentration have been observed in other single crystal tungsten bronzes such as Na_xWO_3 and $Na_xTa_yW_{1-y}O_3$.[2,22]

Previous results suggest that La appears in its trivalent oxidation state in La_xWO_3,[7,14] consistent with the view that in the tungsten bronzes, the dopant ion donates its valence electrons to the WO_3 $t_{2g}(\pi^*)$ conduction band.[9] For different bronzes it is therefore convenient to compare transport data relative to the donor electron concentration n_d. For La_xWO_3, $n_d = 3x/a^3$, with a the lattice constant, while, for Na_xWO_3, $n_d = x/a^3$. The conductivity data[2] for single crystal samples of Na_xWO_3 and $Na_xTa_yW_{1-y}O_3$ are shown in Fig. 6. The volume fraction corrected conductivity σ_c for low x La_xWO_3 samples ($0.06<x<0.11$) is also shown for comparison. The La_xWO_3 conductivity is about an order of magnitude smaller than for Na_xWO_3, but is comparable to values found in $Na_xTa_yW_{1-y}O_3$. The dashed lines in Fig. 6 indicate an exponential dependence of the conductivity on the dopant concentration for the range shown. (This is also observed in the resistivity data of Fig. 5 for $x \leqslant 0.12$.) The slopes are very similar for the three tungsten bronzes shown. This similarity

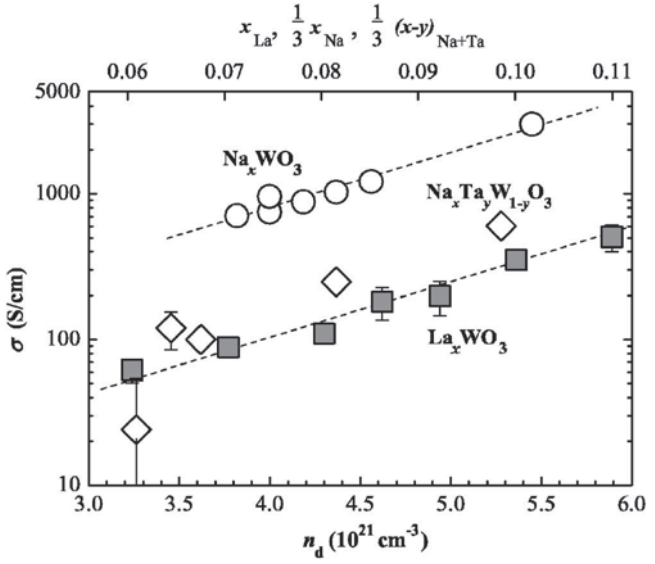

FIG. 6. The room temperature conductivity of Na_xWO_3 and $Na_xTa_yW_{1-y}O_3$ (Ref. 2) and La_xWO_3, vs the donor electron concentration n_d (x/a^3 for Na^+ and $3x/a^3$ for La^{3+} states). The dashed lines are linear fits of the Na_xWO_3 and La_xWO_3 data. Due to lattice constant variations with x and dopant (Fig. 3), the top scale is approximate.

in behavior suggests that a common mechanism is responsible for the evolution of the high T conductivity with x (or n_d) in all three systems.

The reduced conductivity of $Na_xTa_yW_{1-y}O_3$, relative to Na_xWO_3, has been attributed to the increased disorder created by the Ta substitution.[1–3] Following similar arguments, the reduced conductivity of polycrystalline La_xWO_3, relative to Na_xWO_3, is, at least in part, due to enhanced disorder effects associated with the trivalent La ions and will, in addition, involve grain boundary scattering.

Figure 7 shows the conductivity σ_c plotted versus the temperature T down to 64 K. Except for the crossover behavior of the $x=0.15$ curve, which may be due to the measurement errors of the absolute resistivity or to the slight uncertainties in x mentioned above, there is a uniform change in the behavior as x and T are varied. The uncertainties are estimated as ~7%, mainly due to uncertainties in sample dimensions and finite contact size. The samples become less conducting as x is decreased, with a marked increase in the T dependence of σ_c. At 60 K the conductivity changes by two orders of magnitude, with only a threefold change in x. For $x=0.19$, the resistivity has a linear T dependence over the range shown in Fig. 7, with a positive slope ($d\sigma_c/dT<0$). This is typical of metallic conduction, and similar behavior is observed in other bronzes.[26–28] $d\sigma_c/dT$ changes sign at $x \approx 0.17$, and then increases uniformly as x decreases. The curves in Fig. 7 show similar features to those of Na_xWO_3 and $Na_xTa_yW_{1-y}O_3$,[1,2] and are characteristic of an MI transition.

Hall effect

Hall effect measurements were performed on bar samples of length ~10 mm, width ~7 mm, and thickness ~1 mm. The width to thickness ratio was made large to optimize the Hall voltage detection. The two current contacts

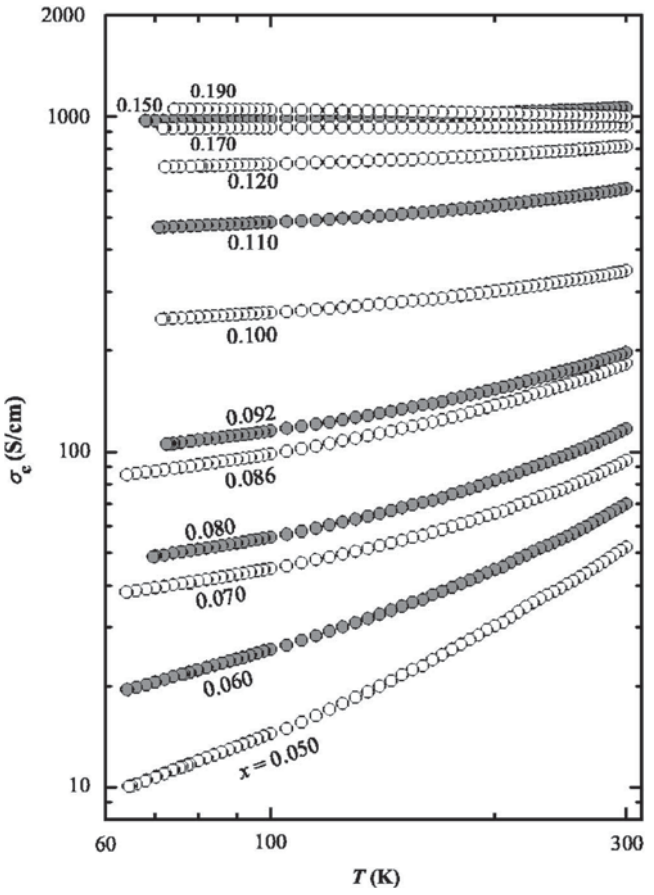

FIG. 7. The conductivity of the La_xWO_3 samples, vs the temperature T. The estimated crystal conductivity $\sigma_c = \sigma_{sample}/f$ is shown.

were attached with silver paint, while the voltage probes were pressure-contact gold-coated pins. Currents of 100 and 200 mA were used with a magnetic field up to 1.2 T supplied by a Varian magnet.

The results for the Hall effect measurements are shown in Fig. 8, which plots the Hall carrier concentration[4] $n_H = A/R_H e$ versus the donor electron concentration n_d. R_H is the measured Hall coefficient, and the scattering factor A is conventionally taken as unity. Shown for comparison are the Hall carrier concentration results for Na_xWO_3.[22] The two sets of data fall close to the $n_H = n_d$ line in Fig. 8, which, assuming $A = 1$, corresponds to all the donor electrons being involved in transport.

The sign of the Hall coefficient confirms negative charge carriers. The results in Fig. 8 are consistent with Na^+ and La^{3+} donor-ion states, with the donor electrons in the WO_3 conduction band. The slight differences between the data and the straight line in Fig. 8 may be attributed to variations in the scattering factor from unity. Assuming that $n_H = n_d$, a linear fit of the data in Fig. 8 produces scattering factors of $A_{Na} \sim 0.8$ and $A_{La} \sim 1.1$.

The relaxation time approximation for metals predicts the conventionally used value of $A = 1$. For many metals A will deviate from unity (although $A \sim 1$), and more elaborate models are required to describe the scattering factor. The alkali metals have measured scattering factors ranging from ~ 0.8 to ~ 1.2. The values for the La and Na bronzes found above show similar deviations from unity.

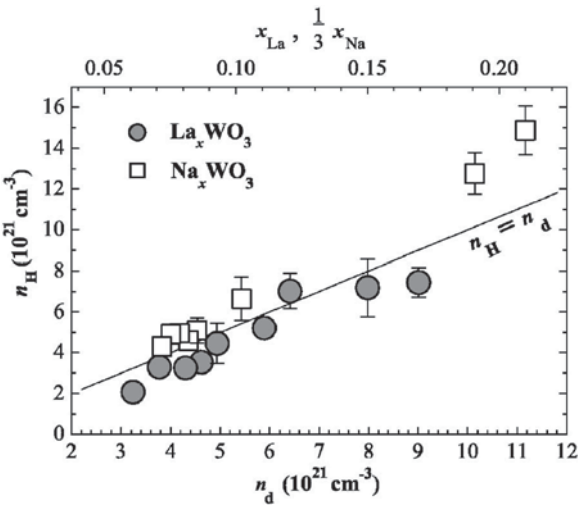

FIG. 8. The room temperature Hall concentration $n_H = A/R_H e$ for La_xWO_3, with $A = 1$ vs the donor electron concentration n_d. Also shown are Na_xWO_3 Hall results (Ref. 22).

CONCLUSIONS

Sintered polycrystalline La_xWO_3 samples have been prepared by solid-state reaction for $0.05 \leqslant x \leqslant 0.23$. Density measurements on the sintered material give a crystal volume fraction $\sim 45\%$.

The structural and electrical transport properties are consistent with those expected for the tungsten bronzes. The cubic perovskite phase exists for $0.086 \leqslant x \leqslant 0.21$, with additional phases appearing outside this range. The XRD patterns give cubic lattice constants increasing from 3.82 to 3.85 Å as x increases. The appearance of mixed phases is similar to that found in other uncompensated tungsten bronzes as $x \to 0$. This effect prevents a precise determination of the MI critical concentration in these systems.

The polycrystalline structure makes direct comparison of the La_xWO_3 conductivity to that of other single crystal tungsten bronzes somewhat uncertain. However, the T and x dependence of the conductivity corresponds to that found for single crystals of Na_xWO_3 and $Na_xTa_yW_{1-y}O_3$. The Hall effect carrier concentrations are similar to those of Na_xWO_3 when allowance is made for the different valence states of the dopant ions. The Hall effect measurements confirm negative charge carriers, and indicate that the donor valence electrons are donated to the WO_3 conduction band and participate in conduction at room temperature.

The MI transition for Na_xWO_3 is estimated at $x_c \approx 0.19$,[1,2,9] corresponding to $n_d \approx 3.4 \times 10^{21}$ cm^{-3}. If the MI transition is mainly determined by the donor electron concentration, then for La_xWO_3 we would expect $x_c \sim 0.063$. This is consistent with the upper bound value of 0.086 based on the stability of the cubic phase as given by XRD. The present results suggests that the critical concentration is also governed by the electron density in the conduction band and not simply by the donor density x, as expected in some site percolation models.

This paper presents the properties of La_xWO_3 over a range of x values, with comparisons to other tungsten bronzes. The temperatures used here, however, are not suited to a detailed analysis of the MI transition in this system. The investigations down to liquid He temperatures are in progress and the results will be presented elsewhere.

ACKNOWLEDGMENTS

Financial support provided by the National Research Foundation of South Africa and by the University of the Witwatersrand, Johannesburg is gratefully acknowledged. We thank Professor D.F. Holcomb of Cornell University for his many important contributions to the work.

[1]M. A. Dubson and D. F. Holcomb, Phys. Rev. B **32**, 1955 (1985).
[2]A. K. Raychaudhuri, Phys. Rev. B **44**, 8572 (1991).
[3]A. K. Raychaudhuri, Adv. Phys. **44**, 21 (1995).
[4]P. P. Edwards, R. L. Johnston, F. Hensel, C. N. R. Rao, and D. P. Tunstall, Solid State Phys. **52**, 229 (1999).
[5]M. Imada, A. Fujimori, and Y. Tokura, Rev. Mod. Phys. **70**, 1039 (1998).
[6]K. Wassermann, M. T. Pope, M. Salmen, J. N. Dann, and H. Lunk, J. Solid State Chem. **149**, 378 (2000).
[7]C. Grenthe and M. Sundberg, J. Solid State Chem. **167**, 412 (2002).
[8]R. Brusetti, P. Haen, and J. Marcus, Phys. Rev. B **65**, 144528 (2002).
[9]H. Dücker, W. von Niessen, T. Koslowski, M. A. Tusch, and D. E. Logan, Phys. Rev. B **59**, 871 (1999).
[10]A. K. Raychaudhuri, K. P. Rajeev, H. Srikanth, and N. Gayathri, Phys. Rev. B **51**, 7421 (1995).
[11]M. Kielwein, M. Saiki, G. Roth, J. Fink, G. Paasch, and R. G. Egdell, Phys. Rev. B **51**, 10320 (1995).
[12]H. R. Shanks and G. C. Danielson, J. Appl. Phys. **38**, 4923 (1967).
[13]B. Broyde, Inorg. Chem. **6**, 1588 (1967).
[14]P. J. Wiseman and P. G. Dickens, J. Solid State Chem. **17**, 91 (1976).
[15]P. A. Lightsey, Ph.D. thesis, Cornell University (1972).
[16]M. A. Dubson, Ph.D. thesis, Cornell University (1984).
[17]W. Ostertag, Inorg. Chem. **5**, 758 (1966).
[18]E. Salje and K. Viswanathan, Acta Crystallogr., Sect. A: Cryst. Phys., Diffr., Theor. Gen. Crystallogr. **31**, 356 (1975).
[19]J. Wang, G. Lui, and Y. Du, Mater. Lett. **57**, 3648 (2003).
[20]C. S. Dimbylow, I. J. McColm, C. M. P. Barton, N. N. Greenwood, and G. E. Turner, J. Solid State Chem. **10**, 128 (1974).
[21]D. P. Tunstall, Phys. Rev. B **11**, 2821 (1975).
[22]P. A. Lightsey, D. A. Lilienfeld, and D. F. Holcomb, Phys. Rev. B **14**, 4730 (1976).
[23]L. J. van der Pauw, Philips Tech. Rev. **20**, 220 (1958).
[24]C. Kasl and M. J. R. Hoch, Rev. Sci. Instrum. **76**, 033907 (2005).
[25]The expression $\sigma_{\text{sample}}=f\sigma_{\text{crystal}}$ relating the sample and crystal conductivities may also be obtained as follows. The sample conductivity $\sigma_{\text{sample}}(f)$ depends on the crystal volume fraction f, with $\sigma_{\text{sample}}(0)=0$. Putting $\sigma_{\text{sample}}(f_0)=\sigma_0$, where f_0 and σ_0 are measured for a particular sample, and using a linear extrapolation to $f=1$, we have the estimate $\sigma_{\text{crystal}}=\sigma_{\text{sample}}(1)=\sigma_0/f_0$.
[26]L. E. Conroy and T. Yokokawa, Inorg. Chem. **4**, 994 (1965).
[27]B. W. Brown and E. Banks, Phys. Rev. **84**, 609 (1951).
[28]W. R. Gardner and G. C. Danielson, Phys. Rev. **93**, 46 (1954).

Bibliography

1. M. Imada, A. Fujimori and Y. Tokura, Rev. Mod. Phys. **70**, 1039 (1998).
2. N. F. Mott, *Metal-insulator transitions*, 2nd ed. (Taylor and Francis, 1990).
3. P. P. Edwards, R. L. Johnston, F. Hensel, C. N. R. Rao and D. P. Tunstall, *Solid State Physics* Vol. 52 (Academic Press, 1999).
4. A. K. Raychaudhuri, Adv. Phys. **44**, 21 (1995).
5. P. A. Lee and T. V. Ramakrishnan, Rev. Mod. Phys. **57**, 287 (1985).
6. P. G. Dickens and M. S. Whittingham, Quart. Rev. Chem. Soc. **22**, 30 (1968).
7. A. K. Raychaudhuri, Phys. Rev. B **44**, 8572 (1991).
8. M. A. Dubson and D. F. Holcomb, Phys. Rev. B **32**, 1955 (1985).
9. H. Dücker, W. von Niessen, T. Koslowski, M. A. Tusch and D. E. Logan, Phys. Rev. B **59**, 871 (1999).
10. A. K. Raychaudhuri, K. P. Rajeev, H. Srikanth and N. Gayathri, Phys. Rev. B **51**, 7421 (1995).
11. J. H. Davies and J. R. Franz, Phys. Rev. Lett. **57**, 475 (1986).
12. S. Raj, H. Matsui, S. Souma, T. Sato, T. Takahashi, A. Chakraborty, D. D. Sarma, P. Mahadevan, S. Oishi, W. H. Mc-Carroll and M. Greenblatt, Phys. Rev. B **75**, 155116 (2007).
13. R. K. Stanley, R. C. Morris and W. G. Moulton, Phys. Rev. B **20**, 1903 (1979).
14. L. H. Cadwell, R. C. Morris and W. G. Moulton, Phys. Rev. B **23**, 2219 (1981).
15. H.R. Shanks, Solid State Commun. **15**, 753 (1974).
16. P. A. Lightsey, PhD Thesis, Cornell University (1972).
17. Q. Zhong, J. R. Dahn and K. Colbow, Phys. Rev. B **46**, 2554 (1992).
18. S. F. Cogan, T. D. Plante, M. A. Parker and R. D. Rauh, J. Appl. Phys. **60**, 2735 (1986).
19. K. Wassermann, M. T. Pope, M. Salmen, J. N. Dann, and H. J. Lunk, J. Solid State Chem. **149**, 378 (2000).
20. A. A. Bessonov, A. M. Fedosseev, J. C. Krupa, I. B. Shirokova and N. A. Budantseva, J. Solid State Chemistry **169**, 182 (2002).
21. K. M. Kim and K. Y. Kim, J. Power Sources **173**, 917 (2007).
22. B. Broyde, Inorg. Chem. **6**, 1588 (1967).

23. H. R. Shanks and G. C. Danielson, J. Appl. Phys. **38**, 4923 (1967).
24. C. Grenthe and M. Sundberg, J. Solid State Chem. **167**, 412 (2002).
25. P. J. Wiseman and P. G. Dickens, J. Solid State Chem. **17**, 91 (1976).
26. P. A. Lightsey, D. A. Lilienfeld and D. F. Holcomb, Phys. Rev. B **14**, 4730 (1976).
27. E. J. Huibregste, D. B. Barker and G. C. Danielson, Phys. Rev. **84**, 142 (1951).
28. W. R. Gardner and G. C. Danielson, Phys. Rev. **93**, 46 (1954).
29. C. Kasl and M.J.R. Hoch, J. Appl. Phys. **99**, 063711 (2006).
30. W. Ostertag, Inorg. Chem. **5**, 758 (1966).
31. C. S. Dimbylow, I. J. McColm, C. M. P. Barton, N. N. Greenwood and G. E. Turner, J. Solid State Chem. **10**, 128 (1974).
32. M. Campagna, G. K. Wertheim, H. R. Shanks, F. Zumsteg and E. Banks, Phys. Rev. Lett. **34**, 738 (1975).
33. B. Ingham, S. C. Hendy, S. V. Chong and J. L. Tallon, Phys. Rev. B **72**, 075109 (2005).
34. A. Hjelm, C. G. Granqvist and J. M. Wills, Phys. Rev. B **54**, 2436 (1996).
35. M. G. Stachiotti, F. Corà, C. R. A. Catlow and C. O. Rodriguez, Phys. Rev. B **55**, 7508 (1997).
36. A. D. Walkingshaw, N. A. Spaldin and E. Artacho, Phys. Rev. B **70**, 165110 (2004).
37. B. W. Brown and E. Banks, J. Am. Chem. Soc. **76**, 963 (1954).
38. H. R. Shanks, J. Cryst. Growth **13–14**, 433 (1972).
39. X. Yang, C. Li, M. Mo, J. Zhan, W. Yu, Y. Yan and Y. Qian, Journal of Crystal Growth **249**, 594 (2003).
40. J. Guo, C. Dong, L. H. Yang and G. C. Fu, J. Solid State Chem. **178**, 58 (2005).
41. E. K. H. Salje and K. Viswanathan, Acta Cryst. **A31**, 356 (1975).
42. R. Clarke, Phys. Rev. Lett. **39**, 1550 (1977).
43. A. T. Fromhold and A. Narath, Phys. Rev. **152**, 585 (1966).
44. B. R. Weinberger, Phys. Rev. B **17**, 566 (1978).
45. M. D. Hill and R. G. Egdell, J. Phys. C **16**, 6205 (1983).
46. T. Wolfram, Phys. Rev. Lett. **29**, 1383 (1972).
47. J. F. Owen, K. J. Teegarden, and H. R. Shanks, Phys. Rev. B **18**, 3827 (1978).
48. W. A. Kamitakahara, B. N. Harmon, J. G. Taylor, L. Kopp, H. R. Shanks and J. Rath, Phys. Rev. Lett. **36**, 1393 (1976).

49. G. Hollinger, F. J. Himpsel, B. Reihl, P. Pertosa and J. P. Doumerc, Solid State Commun. **44**, 1221 (1982).
50. L. D. Muhlestein and G. C. Danielson, Phys. Rev. **160**, 562 (1967).
51. F. C. Zumsteg, Phys. Rev. B **14**, 1406 (1976).
52. H. Dücker, T. Koslowski, W. von Niessen, M. A. Tusch and D. E. Logan, J. Non-Crystalline Solids **205-207**, 32 (1996).
53. D. W. Lynch, R. Rosei, J. H. Weaver and C. G. Olson, J. Solid State Chem. **8**, 242 (1973).
54. P. A. Lightsey, Phys. Rev. B **8**, 3586 (1973).
55. L. D. Muhlestein and G. C. Danielson, Phys. Rev. **158**, 825 (1967).
56. W. McNeill and L. E. Conroy, J. Chem. Phys. **36**, 87 (1962).
57. L. E. Conroy and T. Yokokawa, Inorg. Chem. **4**, 994 (1965).
58. J. Guo, C. Dong, L. Yang, G. Fu and H. Chen, Mater. Res. Bull. **42**, 1384 (2007).
59. B. W. Brown and E. Banks, Phys. Rev. **84**, 609 (1951).
60. J. Guo, C. Dong, L. H. Yang, G. C. Fu and H. Chen, Mater. Res. Bull. **41**, 655 (2006).
61. A. S. Ribnick, B. Post and E. Banks, Adv. Chem. Ser. **39**, 246 (1963).
62. C. Kittel, *Introduction to solid state physics*, 7th ed. (Wiley, 1996).
63. R. S. Popovic, Sensors and Actuators **17**, 39 (1989).
64. A. K. Raychaudhuri, K. P. Rajeev, H. Srikanth and R. Mahendiran, Physica B **197**, 124 (1994).
65. Y. Xue, Y. Zhang and P. Zhang, Phys. Rev. B **79**, 205113 (2009).
66. E. Hecht, *Optics*, 2nd ed. (Addison Wesley, 1987).
67. J. D. Jackson, *Classical electrodynamics*, 3rd ed. (Wiley, 1998).
68. J. D. Greiner, H. R. Shanks and D. C. Wallace, J. Chem. Phys. **36**, 772 (1962).
69. M. Watanabe, Y. Ootuka, K. M. Itoh and E. E. Haller, Phys. Rev. **58**, 9851 (1998).
70. D. F. Holcomb, Ann. Phys. (Leipzig) **8**, 649 (1999).
71. A. A. Likalter, Physica B **315**, 252 (2002).
72. T. Thsepe, C. Kasl, J. F. Prins and M. J. R. Hoch, Phys. Rev. B **70**, 245107 (2004).
73. B. I. Shklovskii and A. L. Efros, *Electronic properties of doped semiconductors* (Springer-Verlag, 1984).
74. P. P. Edwards and C. N. R. Rao, *The metallic and non-metallic states of matter* (Taylor & Francis, 1985).

75. T. F. Rosenbaum, R. F. Milligan, M. A. Paalanen, G. A. Thomas, R. N. Bhatt and W. Lin, Phys. Rev. B **27**, 7509 (1983).
76. N. W. Ashcroft and N. D. Mermin, *Solid state physics* (Saunders, 1976).
77. M. A. Dubson, PhD Thesis, Cornell University (1984).
78. J. Hubbard, Proc. R. Soc. A **281**, 401 (1964).
79. A. L. Efros and B. I. Shklovskii, J. Phys. C **8**, 49 (1975).
80. B. L. Altshuler and A. G. Aronov, Solid State Commun. **30**, 115 (1979).
81. P. W. Anderson, Phys. Rev. **109**, 1492 (1958).
82. G. Hollinger, P. Pertosa, J. P. Doumerc, F. J. Himpsel and B. Reihl, Phys. Rev. B **32**, 1987 (1985).
83. H. Srikanth and A. K. Raychaudhuri, J. Phys.: Condens. Matter **5**, L551 (1993).
84. J. G. Massey and M. Lee, Phys. Rev. Lett. **75**, 4266 (1995).
85. C. Grenthe, M. Sundberg, V. P. Filonenko, and I. P. Zibrov, J. Solid State Chem. **154**, 466 (2000).
86. V. P. Filonenko, C. Grenthe, M. Nygren, M. Sundberg and I. P. Zibrov, J. Solid State Chem. **163**, 84 (2002).
87. R. Azimirad, A. Khademi, O. Akhavan and A. Z. Moshfegh, J. Phys. D: Appl. Phys. **42**, 205405 (2009).
88. L. J. van der Pauw, Philips Res. Rep. **13**, 1 (1958).
89. C. Kasl and M. J. R. Hoch, Rev. Sci. Instrum. **76**, 033907 (2005).
90. D. A. Lilienfeld, MSc Dissertation, Cornell University (1976).
91. C. Rosen, B. Post and E. Banks, Acta Cryst. **9**, 477 (1956).
92. J. F. Smith and G. C. Danielson, J. Chem. Phys. **22**, 266 (1954).
93. S. Blundell, *Magnetism in condensed matter* (Oxford University Press, 2004).
94. S. A. Wender and N. Hershkowitz, Phys. Rev. Lett. **29**, 1648 (1972).
95. D. P. Tunstall, Phys. Rev. B **11**, 2821 (1975).
96. M. A. Dubson and D. F. Holcomb, Phys. Rev. B **34**, 25 (1986).